Study of optical and optoelectronic devices based on carbon nanotubes

Elena Durán Valdeiglesias

université
PARIS-SACLAY

NNT : 2019SACLS100

UNIVERSITÉ PARIS SUD
Comprendre le monde, construire l'avenir

Study of optical and optoelectronic devices based on carbon nanotubes

Thèse de doctorat de l'Université Paris-Saclay
préparée à l'Université Paris-Sud

École doctorale n°575 Electrical, optical, bio : Physics and engineering (EOBE)

Spécialité de doctorat : Physique

Thèse présentée et soutenue à Palaiseau, le 7 mai 2019, par

Elena Durán Valdeiglesias

Composition du Jury :

Olivier Gauthier-Lafaye Directeur de recherche, LAAS (UPR 8001)	Rapporteur
Yannick Dumeige Maître de Conférence, FOTON (UMR 6082)	Rapporteur
Jean Sébastien Lauret Professeur, LAC (UMR 9188)	Examinateur
María Pilar Bernal Artajona Directrice de recherche, Femto-ST (UMR 6174)	Présidente
Arianna Filoramo Chercheure, LICSEN,CEA Paris-Saclay	Examinatrice
Laurent Vivien Directeur de recherche, Université Paris-Saclay (UMR 9001)	Directeur de thèse
Carlos Alonso Ramos Chargé de recherche, Université Paris-Saclay (UMR 9001)	Invité
Xavier Le Roux Ingénieur de recherche, Université Paris-Saclay (UMR 9001)	Invité

C2N

cnrs

Thèse de doctorat

Résumé en français du manuscrit de thèse

Titre :

Etude de composants optiques et optoélectroniques à base de nanotubes de carbone

Par :

Mme. Elena Durán Valdeiglesias

Directeur de thèse :

M. Laurent Vivien

L'objectif de cette thèse est d'exploiter les remarquables propriétés optiques des nanotubes de carbone pour le développement de dispositifs optoélectroniques intégrés sur la plateforme photonique silicium.
Les résultats présentés dans ce manuscrit ont été possibles grâce à la collaboration de mon équipe avec divers chercheurs de groupes européens, notamment Arianna Filoramo du CEA-Saclay (France), Massimo Gurioli de l'Université de Florence (Italie), Charles Baudot de STMicroelectronics à Crolles (France) et Nicolas Dubreuil au laboratoire Charles Fabry de l'Institut d'Optique (France). La fabrication des dispositifs photoniques et hybrides a été réalisée au sein de la centrale de nanotechnologies du C2N avec l'aide de Xavier Le Roux.

INTRODUCTION

La photonique silicium est reconnue comme une technologie émergeante pour les applications de transmission de données de nouvelle génération. Le principal avantage de la photonique silicium est son faible coût dû à sa fabrication à grande échelle dans les fonderies CMOS développées pour l'industrie de la microélectronique. L'utilisation de substrats silicium sur isolant (SOI) offre de bonnes caractéristiques pour l'optique intégrée grâce en particulier au fort contraste d'indice de réfraction entre le silicium et la silice permettant ainsi la réalisation de composants compacts avec des dimensions inférieures au micromètre. L'utilisation de la plateforme silicium sur isolant permet également l'intégration sur un même circuit de composants optiques, électriques et de systèmes micro-électromécaniques (MEMS). Malgré de nombreux avantages dans l'utilisation du silicium pour la photonique, plusieurs inconvénients majeurs rendent le développement de la photonique silicium un réel défi. En effet, en raison de la bande interdite indirecte du silicium, le silicium est un mauvais émetteur de lumière, avec l'impossibilité aujourd'hui d'en faire un laser pompé électriquement. La large gamme spectrale de transparence (1100 nm$<\lambda<$8000nm) fait du silicium un bon matériau pour le guidage de la lumière et donc un mauvais détecteur car aucune absorption à ces longueurs d'onde. De plus, le silicium est un semiconducteur centrosymétrique, ne présentant pas d'effet Pockels, l'effet électro-optique le plus connu pour la modulation optique.

Pour surmonter les limitations intrinsèques au silicium, différents schémas d'intégration ont été proposés. Pour la génération de lumière sur silicium, la solution dominante est l'intégration hybride de matériaux III-V sur Si. Pour la photodétection, deux approches différentes ont été envisagées. La première consiste en une intégration hybride de matériaux III-V sur du silicium, ce qui permet d'obtenir des photodétecteurs efficaces et à haute vitesse. Cependant cette approche reste complexe. La seconde approche est basée sur l'hétéro-épitaxie de germanium (Ge) sur silicium. Cette approche, utilisant un matériau compatible avec la technologie silicium, permet une intégration simple, peu coûteuse et très performante. Enfin, la modulation dans le silicium peut être réalisée en utilisant la variation de porteurs dans le Si. En effet, l'indice de réfraction du matériau sont modifiés en modifiant la concentration en électrons et en trous dans le guide d'onde. Cette modification de concentration de porteurs engendre ainsi une variation de phase de l'onde guidée exploitable à l'aide d'un interféromètre pour obtenir une variation d'intensité lumineuse. L'intégration de tous ces matériaux sur silicium est techniquement possible, mais l'utilisation de procédés technologiques différents et parfois incompatibles rend le développement de circuits photoniques complexes. Dans ce contexte, l'idée originale de la thèse est d'utiliser les nanotubes de carbone pour la réalisation de sources lasers, de modulateurs optiques et de photodétecteurs sur la plateforme photonique silicium. De plus, de nombreux travaux ont montré le potentiel des nanotubes de carbone pour la nanoélectroniques, permettant ainsi d'envisager la démonstration de circuits photoniques et électroniques à base de nanotubes de carbone.

L'objectif principal de cette thèse est l'utilisation des nanotubes de carbone pour le développement de tous les dispositifs optoélectroniques sur la plateforme silicium afin d'adresser les challenges de multitude d'applications : capteurs, dataCom, quantique....

Dans ce travail, nous proposons l'utilisation de nanotubes de carbone à mono-paroi (SWCNT). Les SWCNT sont des matériaux très polyvalent, présentant des propriétés électroniques et optiques remarquables. Ils présentent une forte photoluminescence et électroluminescence dans la gamme de longueurs d'onde du proche infrarouge (NIR), ainsi qu'une forte photostabilité thermique. La longueur d'onde d'émission peut être ajustée en sélectionnant un diamètre de nanotube (ou chiralité) précis. La possibilité d'utiliser l'injection électrique pour la génération de lumière est très prometteuse pour la réalisation de lasers optiques à pompage électrique. Des études théoriques ont également prédit de forts effets Stark et Kerr, qui pourraient également être utilisés pour obtenir des effets de modulation. Enfin, les nanotubes présentent plusieurs bandes d'absorption en fonction de leurs chiralités permettant ainsi la réalisation de photodétecteurs. Toutes ces propriétés optiques et optoélectroniques reposent sur des mécanismes physiques intrinsèquement rapides, conduisant à des dispositifs hautement efficaces, à haute vitesse et large bande passante, sur une très large plage spectrale. Par conséquent, les nanotubes de carbone sont très prometteurs pour le développement de la photonique.

Cette thèse est organisée en cinq grandes parties :

- Matériaux : développement et l'optimisation d'un procédé de purification des nanotubes de carbone
- Intégration hybride dans des structures photoniques silicium
- La démonstration d'une source de lumière pour aller vers une émission laser
- Le développement de composants optoélectroniques : sources pompées électriquement et photodétecteurs
- L'étude des effets nonlinéaires du troisième ordre des nanotubes de carbone.

MATERIAUX : EXTRACTION DES NANOTUBES DE CARBONE SEMICONDUCTEURS

Tous les procédés de préparation des SWCNT connus donnent des mélanges de chiralités, de diamètres et de longueurs de nanotubes. Par conséquent, la nécessité d'un processus spécifique et efficace permettant la sélection de la chiralité et plus particulièrement la sélection des SWCNT semiconducteurs est une des premières conditions pour utiliser les SWCNT en photonique. Dans cette

thèse, nous utilisons le processus d'ultracentrifugation assisté par polymère. La technique commence par la préparation de la solution initiale, composée par les SWCNTs, le polymère et le solvant. Cette solution de départ est soumise à un processus de sonication, généralement composé de deux étapes : sonications douce et forte. La sonication douce améliore la solubilité et la sonication forte pour homogénéiser la solution en cassant les faisceaux de nanotubes (bundles). Le processus se termine par le processus d'ultracentrifugation où les s-SWCNT sont séparés des m-SWCNT et des impuretés, donnant ainsi une solution pure en nanotubes semiconducteurs.
Dans cette thèse, trois types de solutions ont été développés pour couvrir l'ensemble du spectre de 1 µm à 1,6 µm. Une première solution avec une longueur d'onde d'émission de 1 µm à base de SWCNT CoMoCAT. La seconde avec une longueur d'onde d'émission centrée autour de 1,3 µm basée sur les SWCNT HiPco et la dernière couvrant la bande télécom à 1,5 µm réalisée à partir de SWCNT à ablation au laser. Les deux premières solutions ont été optimisées pour une excitation optique car les s-SWCNTs obtenus sont trop courts pour réaliser des contacts électriques. La solution par ablation Laser a été développée pour réaliser des dispositifs avec une injection électrique car la longueur des s-SWCNT est supérieure à 6 µm. La figure 1 montre les spectres de photoluminescence normalisés pour les trois solutions développées dans ce travail.

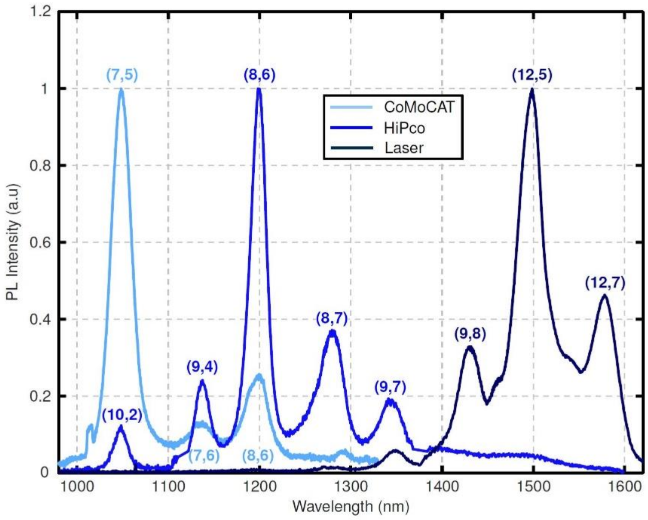

Figure 1 : Spectre de photoluminescence normalisé pour : Solution d'ablation au laser s-SWCNT en bleu foncé, solution HiPco s-SWCNT en bleu et solution de CoMoCAT s-SWCNT en bleu clair.

INTEGRATION HYBRIDE AVEC DES STRUCTURES PHOTONIQUES

Nous avons étudié plusieurs types de résonateurs en anneau et de cavités afin d'améliorer l'interaction de la lumière entre le mode optique et les nanotubes de carbone :

- Guides d'onde rubans et guides d'onde à fente. De notre analyse théorique visant à étudier la capacité des deux structures, guide rubans et guide à fente, à interagir avec le milieu environnant (les s-SWCNT dans notre cas), nous avons conclu que, dans toutes les configurations étudiées, les guides d'onde à fente en polarisation TE présente une sensibilité plus grande que les guides d'onde rubans en polarisation TM. Nous avons confirmé expérimentalement que les résonateurs en anneau à base de guide à fente donnaient des intensités aux résonances améliorées de plus de 60% par rapport aux résonateurs avec des guides rubans. La figure 2 présente les émissions lumineuses mesurées par les s-SWCNT dans les mêmes conditions expérimentales dans trois scénarios différents. La ligne bleu foncé représente la PL pour une excitation hors résonateur. La ligne bleu présente la PL collectée du résonateur en anneaux sous excitation lumineuse pour des guides rubans. Des pics étroits apparaissent superposés à l'émission des s-SWCNTs. Ces pics sont induits par résonance à l'intérieur du micro-anneau. Enfin, en trait bleu clair, nous représentons la PL mesurée lorsque nous avons concentré le laser de pompe sur le résonateur en anneaux à fente. Fait intéressant, malgré leur plus grande perte de propagation, les résonateurs à anneau à fentes présentent de forts pics de résonance. Cela indique que l'interaction lumière – matière entre les s-SWCNT et le mode guide d'onde optique est nettement améliorée avec des guides à fente.

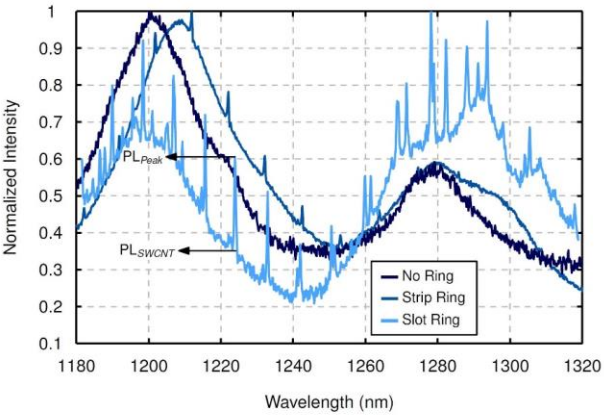

Figure 2 : Intensité de photoluminescence normalisée en fonction de la longueur d'onde lorsque : le faisceau d'excitation est focalisé sur une région Si non structurée (ligne bleu foncé), un micro-anneau à guides rubans (ligne bleue) et un micro-anneau à guide à fente (ligne bleu clair). La longueur d'onde de la pompe est de 735 nm.

- Nous avons également analysé l'effet de polarisation de la lumière sur les guides d'onde. Contrairement aux précédentes publications selon laquelle la polarisation TE est la polarisation adéquate pour exciter les SWCNT parallèlement à la surface de la puce. Nous avons théoriquement analysé et démontré expérimentalement qu'il est possible d'utiliser la composante de champ électrique longitudinal du mode TM pour interagir efficacement avec les s-SWCNT alignés parallèlement à la surface. En outre, une nouvelle stratégie est proposée pour améliorer l'interaction sélective du mode optique avec une chiralité unique de s-SWNTs en utilisant un schéma de couplage asymétrique. Enfin, nous avons réduit les pertes optiques des dispositifs hybrides en créant des fenêtres d'interaction localisées ce qui a permis d'améliorer le taux d'extinction de 11 dB. La figure 3 compare le spectre de photoluminescence d'un résonateur à anneaux avec un intervalle de G = 250 nm et un rayon de R = 5 µm, dans la région d'optimisation de la photoluminescence pour une longueur d'onde de 1300 nm, lorsque la polarisation du laser d'excitation est alignée soit perpendiculaire au guide d'onde ou selon la composante E_z longitudinale (alignée le long du guide d'onde).

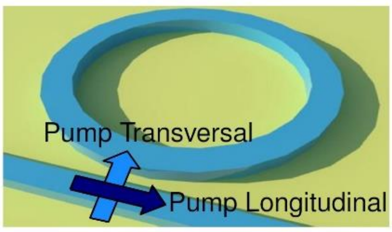

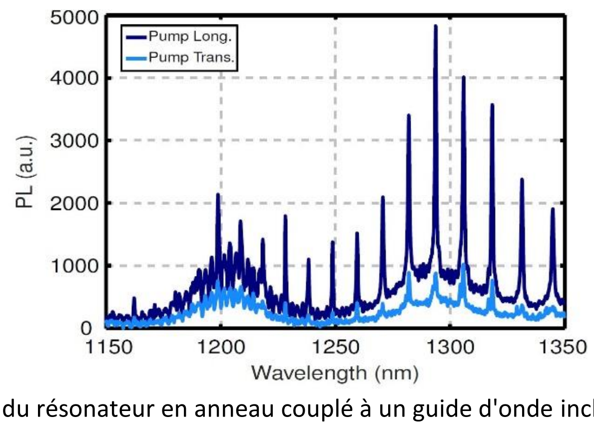

Figure 3 : À gauche : vue schématique du résonateur en anneau couplé à un guide d'onde incluant les deux schémas de polarisation du laser de pompe : transversal (aligné avec la composante E_x) et longitudinal (parallèle à la composante E_z). A droite : spectre de photoluminescence pour un résonateur en anneau de rayon R = 5 µm et un intervalle bus-anneau G = 250 nm. L'excitation est effectuée à partir de la surface de la puce avec une longueur d'onde de 735 nm et le signal de photoluminescence généré couplé au guide d'onde est collecté à partir de la facette de la puce, en bout de guide d'onde.

- Notre objectif était de travailler avec une cavité à petit volume de mode. Nous avons présenté la première démonstration expérimentale couplant l'émission de s-SWCNT dans une cavité à cristal photonique à fente. Nous avons montré une réjection hors résonance supérieure à 5 dB. La figure 4 montre le spectre de photoluminescence collecté lorsque la longueur d'onde d'excitation est de 735 nm (correspondant à la transition excitonique S_{22} de la chiralité (8,7)). Le spectre de photoluminescence montre deux pics nets, aux longueurs d'onde d'environ 1285 nm et 1271 nm. Ces pics ont une largeur totale de 0,35 nm et 1,75 nm, correspondant à des facteurs de qualité (estimés à partir de l'ajustement lorentzien) de Q ≈ 3600 et Q ≈ 700, respectivement.

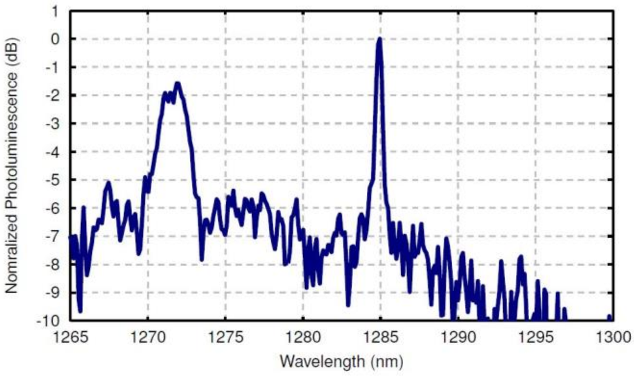

Figure 4 : Signal de photoluminescence normalisé obtenu pour une longueur d'onde d'excitation de 735 nm.

- Nous avons présenté les résultats préliminaires en excitation colinéaire. Avec cette méthode proposée, il est possible de maximiser l'interaction entre le signal de pompe et les s-SWCNT. En raison de la longueur d'onde de la pompe (735nm), il est nécessaire d'utiliser la plateforme nitrure de silicium sur isolant. La figure 5-a présente la section transversale latérale des coupleurs à réseau avec les deux configurations de mesure. Sur la figure 5-b, la photoluminescence collectée lorsque la longueur d'onde d'excitation est de 735 nm.

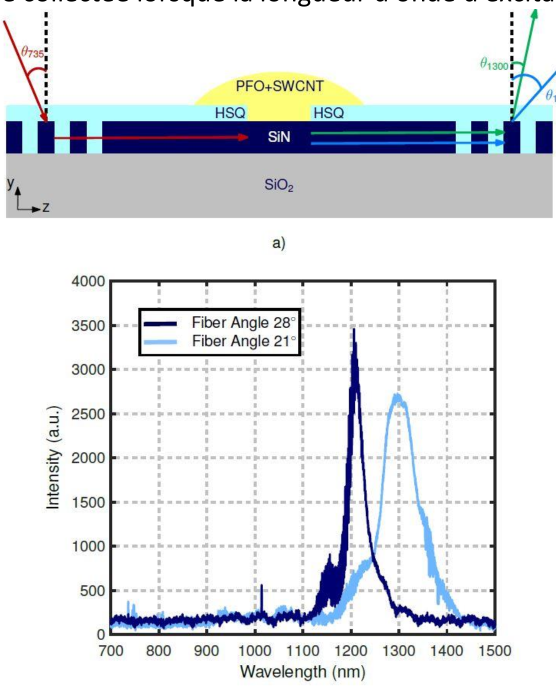

Figure 5 : a) Vue schématique avec les deux configurations d'angle de collection pour la sélection des longueurs d'onde d'émission. b) Signal de photoluminescence collecté à partir du guide d'onde SiN pour une longueur d'onde d'excitation de 735 nm

VERS UN LASER INTEGRE DE NANOTUBES DE CARBONE

Les deux principaux ingrédients pour faire un laser sont : un milieu à gain et une cavité. Depuis les premières mesures de gain optique des nanotubes de carbone en 2010, un énorme effort a été mené dans le cadre de cette thèse pour augmenter la concentration de s-SWCNT en solution et ainsi augmenter le gain optique. Une forte amélioration de la photoluminescence a ainsi été obtenue en utilisant différents types de micro-cavités avec un nouveau schéma d'intégration. Ces progrès dans la qualité de la solution, les caractéristiques de la cavité (facteurs de perte et Q) et l'intégration hybride de s-SWCNT dans des résonateurs photoniques étaient de bons indicateurs pour obtenir l'effet laser. Nous avons donc effectué, en collaboration avec l'équipe de Fabrice Raineri, des mesures en régime pulsé pour un s-SWCNT intégré dans un microdisque. Ces mesures ont montré pour la première fois que une dépendance non linéaire de la puissance en sortie de guide d'onde avec la puissance de pompe. Dans le même temps, on a observé une augmentation du facteur de qualité Q des pics de résonance, correspondant à une réduction du spectre d'émission. Ce comportement est parfaitement reproductible et aucune dégradation de l'échantillon n'a été observé. Malheureusement, ces deux éléments suivent la tendance adéquate, mais ils n'ont pas dépassé les valeurs permettant de garantir que l'effet laser est atteint. Ce comportement pourrait aussi trouver son origine dans l'effet thermo-optique ou dans l'émission spontanée amplifiée. Ces résultats prometteurs ne suffisent donc pas pour démontrer clairement l'effet laser. Des mesures de cohérence et des expériences complémentaires sont nécessaires pour conclure sur les possibilités d'obtenir un effet laser avec les NTC. Le spectre de photoluminescence en fonction de la puissance d'excitation est représenté sur la figure 6-a. La figure 6-b montre le pic d'intensité de photoluminescence pour la résonance centrale (environ 1265 nm) en fonction de la puissance de pompe à 735nm. Nous pouvons clairement distinguer deux comportements différents. Le premier, pour des puissances comprises entre 5 mW et 85 mW, un comportement linéaire est observé. Un comportement super linéaire est obtenu pour une puissance de pompe supérieure à 90 mW. En même temps, une largeur spectrale des résonances nettement rétrécit pour les fortes puissances de pompe (Fig. 6-c).

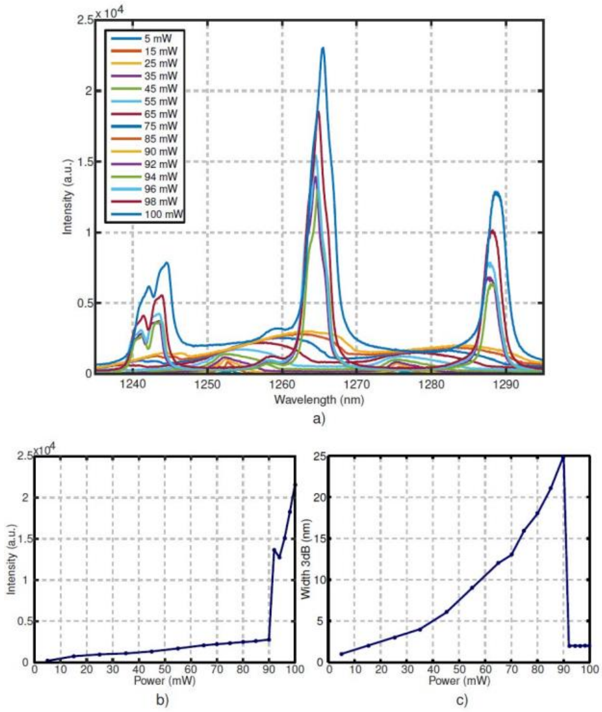

Figure 6 : a) Spectre de photoluminescence en fonction de la puissance de pompe pour un diamètre de microdisque de 5 µm. L'excitation est réalisée par la surface et la collection de photoluminescence par un coupleur à réseau en bout de guide d'onde Si. b) Intensité maximale du mode de résonance à une longueur d'onde de 1265 nm en fonction de la puissance de pompe. c) largeur à 3dB pour le mode résonant à une longueur d'onde de 1265 nm en fonction de la puissance de pompe.

ELECTROLUMINESCENCE ET PHOTODETECTION EN CNTS

Les résultats expérimentaux préliminaires pour l'émetteur et le détecteur en surface basés sur la matrice de SWCNT déposée par DEP et utilisant un contact asymétrique sont présentés. Ces résultats ont clairement démontré que l'utilisation de contacts asymétriques améliore les performances d'émission et de détection. Les mesures de photocourant présentent une forte dépendance à la polarisation de la lumière, ce qui indique le degré élevé d'alignement des nanotubes et exclut également la possibilité que le photocourant observé soit lié à un effet photo-thermoélectrique. Dans ce travail, nous montrons pour la première fois une conception, une fabrication et des mesures d'une liaison optique à base de SWCNT semi-conducteurs intégrés sur une plate-forme photonique SiN. La sensibilité du détecteur est estimée à 0,1 µA / mW. La vue SEM de l'une des liaisons fabriquées est présentés en figure 7. Cette liaison inclue la source, le détecteur et le guide d'onde. La ligne en pointillé représente la position du guide d'onde entre les deux dispositifs à base de nanotubess. La figure 7-b présente une source de lumière. Nous distinguons clairement les électrodes de platine utilisées pour effectuer la DEP et une électrode de scandium plus étroite pour effectuer les mesures avec des contacts asymétriques. La figure 7-c présente une matrice de nanotubes de carbone alignée entre des électrodes Sc et Pt.

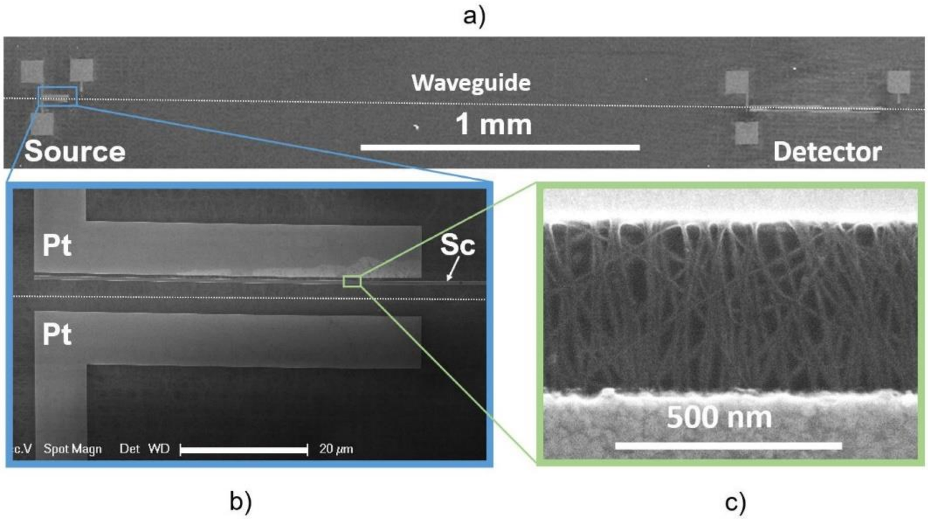

Figure 7 : Images SEM pour l'un des liens optiques fabriqués. a) Vue générale de la liaison optique réalisée. La ligne en pointillé représente la position du guide d'onde. b) Zoom de la source optique. Deux contacts symétriques (Pt-Pt) sont utilisés pour réaliser la diélectrophorèse et une troisième électrode (Sc) est conçue pour former un contact asymétrique (Pt-Sc). c) Réseau de nanotubes alignés.

EFFETS NON LINEAIRES DANS LES SWCNTS

Cette partie est consacrée à l'étude des propriétés optiques non linéaires des SWCNT semi-conducteurs. En particulier à l'effet optique non linéaire de troisième ordre, l'effet Kerr. Une approche analytique basée sur le modèle à deux bandes et le modèle de Kramers-Krönig a permis de montrer la dépendance du coefficient n2 avec la chiralité des nanotubes de carbone. Nous avons considéré 2 types de nanotubes de carbone, les CoMoCAT avec le spectre d'absorption présenté en figure 8-a et les HipCo en figure 8-b. A l'aide de modèle, on constate une évolution du coefficient n2 entre des valeurs positives et des valeurs négatives en fonction de la chiralité des nanotubes considérée.

Les SWCNT semi-conducteurs sont également des nanomatériaux très intéressants pour des dispositifs non-linéaire intégrés. Etant donné que l'ingénierie de bande interdite joue un rôle important dans les non-linéarités optiques du troisième ordre, nous sommes en mesure d'adapter la réponse optique non linéaire effective dans les guides d'ondes hybrides SWCNT-sur-SiN. Ces résultats ont été démontrés expérimentalement, montrant un bon accord avec la prédiction théorique.

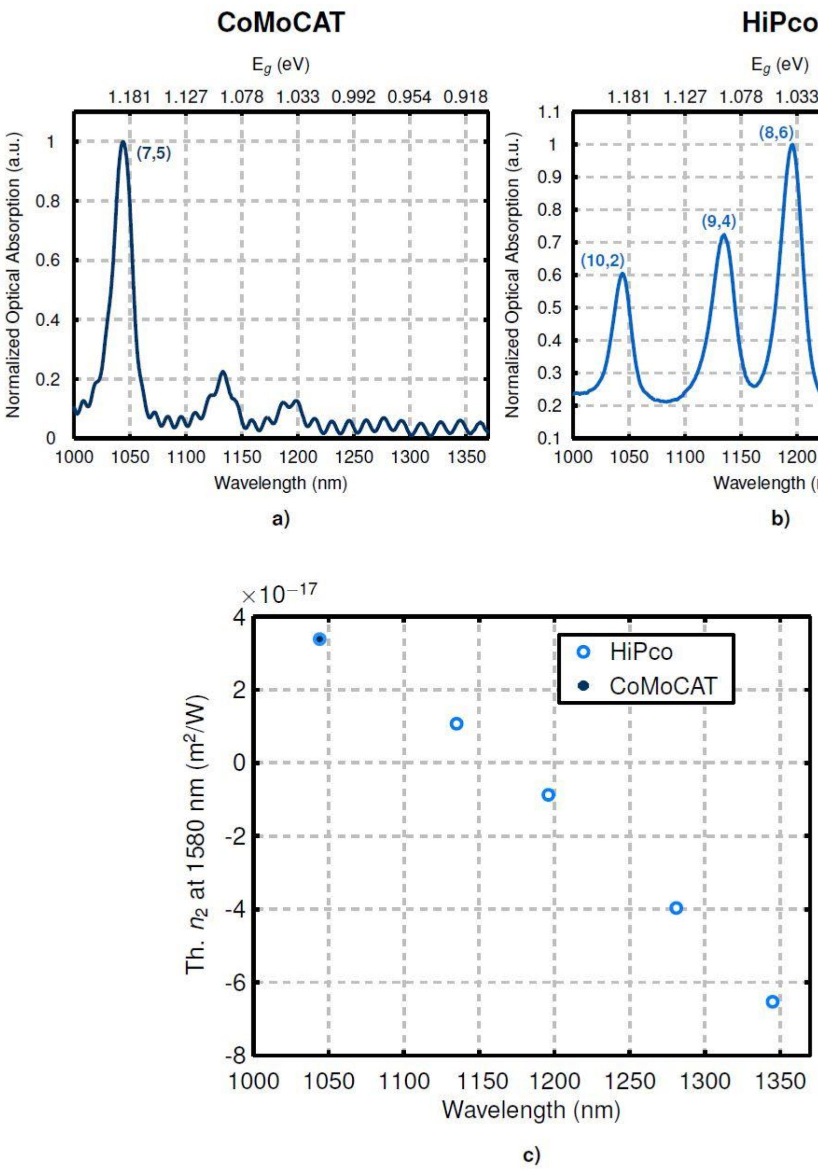

Figure 8 : Absorption optique normalisée de CoMoCAT en solution a) et de HiPco en b) préparée au cours de cette thèse. c) Estimation théorique du coefficient Kerr de chaque chiralité présente dans les solutions CoMoCAT et HiPco représentées respectivement en bleu foncé et en bleu clair.

CONCLUSIONS

Dans cette thèse, un travail complet sur l'intégration des s-SWCNT sur une plate-forme photonique silicium a été réalisé. Ce travail a commencé pour un aperçu de la structure et des propriétés optiques. Avec une mention spéciale sur les méthodes de purification et les techniques de dépôt. Un temps considérable a été consacré à l’optimisation des solutions SWCNT semi-conductrices. Différentes techniques de dépôt, schémas d'intégration et structures photoniques ont été analysés. Les premières démonstrations expérimentales de composants optiques et optoélectroniques avec excitation optique et électrique et régime non linéaire sont exposées dans le cœur du manuscrit de thèse.

Acknowledgments

First of all, I would like to begin by expressing my deepest gratitude to my thesis director, Laurent Vivien. Thank you Laurent for giving me the confidence and the freedom to explore new solutions, to participate in numerous conferences and project meetings, to collaborate with different colleagues and institutions all around the world. Even if Laurent has always a million of meetings, he always found the time to discuss with me, to support me, to encourage me, to solve my problems and to teach me. If great are his scientific qualities even greater are personal qualities. As in all theses there have been good and bad moments but, without any doubt, these years have been much easier thanks to his good humour and optimism. I would like to say that I have enjoyed every day of this thesis, even those in which I only wrote, or in which absolutely nothing worked. I can only say thank you Laurent for giving me the opportunity to do a thesis with you.

Unquestionably, the results shown in this manuscript are the result of the work of an excellent group of scientists. On the one hand, I have been very lucky to do my thesis in the MINAPHOT group where I have had total freedom to interact and discuss with all their members. Thanks Eric for the discussions, your time to answer any questions. Thank you, Delphine, for your help in both the scientific and the personal aspects. Thanks Carlos for always having time to discuss with me, and for your help to solve any problem however complicated it may seem. I would like to thank all the students of the team, many of which are great friends, for the time, parties, trips and conferences that we shared together. I would like in particular to thank Samuel, Weiwei and Cam for sharing their thesis work with me and my carbon nanotubes. I sincerely think that we made a great team working together for the CARTOON project. Without a doubt, the absolute success of my pot de soutenance is thanks to the Spanish team + Daisy. Thanks to: Alicia, Miguel, Joan, David, Marta and Daisy for organizing, buying, cooking, installing and cleaning for my party. Of course, I do not forget: Diego, Mathias and Guillaume (we started the thesis together), Dorian, Sylvain, Suuuuper Daisy, Quiankun, Papichaya, Christian, Lucas, Jianhao, Pedro, Nhung, Vladyslav, Daniel, Jerry, and Dinh. On the other hand, to the rest of the members of the European project CARTOON. Especially, I would like to thank Arianna for her time and dedication to discuss from the most basic concepts to the most complex ones and to put all her resources at my disposal. For your wise advice both professionally and personally. I would like to thank all of her students for the time we were working together. Thanks to: Matteo, Al-Saleh, Alex and Marta. I can not forget the team from Florence where I learned everything I know about PL. Thanks Massimo for sharing with me your immense knowledge of physics. Thank you Francesco Sarti for your intensive PL course. Thank you Francesco Biccari, Ughetta and Francesca for making my stay in Florence so simple. None of the devices presented in this manuscript would have been possible without the great help of a large number of professionals with whom I had the good fortune to work in the clean room of the C2N. They have managed to deal perfectly with complicated situations with good doses of scientific and human qualities. Thanks to: Jean-René, Nathalie, David, Samson, Etienne, Cédric, Fabien and Benoît. To finish, I would like to thank the person who has made all the devices presented in this manuscript come true. Thanks Xavier for teaching me nano-fabrication techniques and sharing with me part of your experience in the silicon photonics technology. Without you this work would not have been possible.

Certainly, these years have been much more bearable thanks to the great help of all the administrative staff who have explained to me the basic concepts of the French administration even when I did not speak a word of French. Thank you for your extreme patience: Carole, Bernadette, Lydia, Sylvie, Laurence, Amanda and Simon.

I do not forget my lifelong friends who although in the distance have supported me during all this work. Thanks to: Migue, Pili, Pablo, Eli, Fernan, Marina, Juanjo, Isa, Alex, Juanma, Inma, Benito, Rau, Darío and María. Without missing the craziest of them all, Dioni, who crossed half continent to be by my side.

Of course, one of the fundamental pillars of my life is my family. For that reason, this work is dedicated to each of them, those who are and those who are no longer here.

Finally, to my adventures partner. Do you remember when we arrived at our little apartment with a single suitcase?

¡Gracias a todos por todo!

Contents

1
Introduction

In 1969, Marcatili proposed for the first time a dielectric rectangular waveguide for integrated optics [1]. A waveguide consisted of a rectangular dielectric rod of refractive index n_1 surrounded by another dielectric of slightly smaller refractive index. The light is propagated by total internal reflection. Two decades later, in 1985, Soref fabricated the first all-silicon integrated-optical component working from 1.3 μm to 1.6 μm, using a highly doped silicon substrate [2]. Shortly after, in 1998, Bookham Technology Ltd began the commercialization of integrated silicon photonics devices [3]. From the end of the 1990s to the present, silicon has undergone a huge technological development, continuously expanding towards new applications. Since its inception with sensor applications [4] until today, where the most relevant areas are: photonic phased arrays [5], microwave photonics systems [6], optomechanical devices [7, 8], integrated optical gyroscopes [9], quamtum photonics [10], mid-infrared applications [11], data-communications [12], nonlinear optics [13], lidar [14] and sensing [15]. This enormous expansion has been driven by the unique properties presented by the silicon platform. The main advantage is the low cost due to its large scale fabrication using CMOS foundries, developed for the microelectronics industry. Silicon-on-insulator (SOI) wafers offer a high refractive index contrast between the silicon core and the silicon dioxide cladding, enabling submicrometer dimensions with tight bend radius. This enables high-density integration of photonic circuits. The use of silicon-on-insulator platform allows the integration not only with optical components, but also with electric circuits and micro-electromechanical systems (MEMS) [16]. However, silicon has some shortcomings. Due to its indirect bandgap, silicon is not a suitable material for light sources. Because of its transparency wavelength range (λ>1100 nm), silicon is a poor absorber in the near infrared, so it is not a suitable material for photodetectors. In addition, silicon is a centrosymmetric material leading to no Pockels effect, typically used in high-performance electro-optic modulators.

To overcome the intrinsic silicon limitations, different integration schemes have been proposed. For light generation on silicon, the dominant solution is the hybrid integration of silicon with III-V materials [17, 18]. The integration can be made in three different ways: i) III-V chips bonded on silicon with coarse alignment, ii) direct epitaxial growth of III-V layers on silicon and iii) epitaxial growth on silicon and then bond it to a SOI wafer. For photodetection two different approaches have been considered. The first consists in hybrid integration of III-V materials on silicon, resulting in high speed and efficient photodetectors [19]. In this scheme, the integration is very complex and not cost-effective reducing the interest of this technique. The second approach is based on the hetero-epitaxial growth of germanium (Ge) on silicon. This scheme provides a simple, low-cost and high performance integration scheme, that in addition is compatible with Si process [20]. Germanium-based photodetectors present bandwidth larger than 50 GHz, responsivity of ~ 1 A/W and dark current lower than 100 nA [21]. Finally, the modulation in silicon can be performed using the plasma dispersion effect. The material's refractive index and absorption are modified by changing the electron and hole concentrations in the waveguide. These kinds of devices can reach speed modulations beyond 50 GHz.

The integration of all these materials on silicon is technically possible, but as different and sometimes non-compatible processes are used, the resulting scheme is not cost-effective, and consequently compromises the use of silicon photonics for a broad application domain. The integration of laser sources, optical modulators, and photodetectors within a common material platform would be much more favourable for the emergence of photonics. Moreover, it has to be noted that the integration of carbon nanotubes onto silicon has already been demonstrated for nanoelectronic applications. The baseline for the envisioned research is the use of carbon nanotubes for all optoelectronic devices in a silicon platform in order to relax integration requirements and to address a multitude of applications.

Single-wall carbon nanotubes (SWCNTs) are a very versatile material, presenting outstanding electronic and optical properties [22, 23]. They show strong photo- and electro- luminescence, in the near infrared (NIR) wavelength range, as well as strong thermal photostability. Their emission wavelength can be tuned by selecting a precise nanotube diameter (or chirality). The possibility of using electrical injection for luminescence generation [24] is very promising for the realization of electrically pumped optical lasers. Theoretical studies also predicted Stark [25] and Kerr [26] effects, which could also be employed to modulate the light. Finally, carbon nanotubes present various absorption bands, allowing the realization of photodetectors. All these optical properties rely on intrinsically fast physical mechanisms, leading to high efficiency, high-speed and large bandwidth devices, covering a very broad spectral range. Therefore, carbon nanotubes are very good candidates for photonic applications. Furthermore, a side advantage of the use of carbon nanotubes for photonics is that the current research on their use for nanoelectronics [27] may facilitate the integration between photonics and electronics. While the use of individual SWCNTs faces the severe issues of controlled positioning and precise addressing, the collective use of SWCNTs within networks lifts such roadblocks giving access to most of the SWCNTs properties relevant for optoelectronics. This research project, based on the use of carbon nanotubes for photonics, can be widely applicable to other photonic platforms as flexible substrates [28].

The objective of this thesis is the use of carbon nanotubes for the implementation of active devices on the silicon photonics platform. First, I optimized a selective method to obtain high-purity semiconducting carbon nanotubes solutions. Thanks to the remarkable optical and electrical properties of the resulting carbon nanotubes, experimental demonstrations of optical, electrical and nonlinear properties have been performed in order to show the great potential of CNTs. This thesis is organized as follows: Chapter 2 summarizes the main properties of carbon nanotubes which help to understand the rest of the work presented in this manuscript. Chapter 3 is intended to the process involved to obtain high purity solution of semiconducting carbon nanotubes. In this work, three different solutions have been processed covering from 1 μm to 1.6 μm wavelengths. In chapter 4, different waveguide topologies are analysed to maximize the light-CNT interaction. The photoluminescence resonance enhancement has been analysed for each of them. The photoluminescence resonant enhancement for a micro-disk resonator under pulsed excitation exhibiting power emission threshold and line width narrowing is presented in Chapter 5. Chapter 6 is dedicated to results obtained under electrically excitation. More specifically, surface emitter and photodetector, as well as, the preliminary results on the first integrated optical link based on carbon nanotubes are presented. Finally, the last chapter is devoted to the study of nonlinear effects in semiconducting carbon nanotubes. We have theoretically studied and experimentally demonstrated the relation between carbon nanotube chirality and nonlinear refractive index. Finally, this thesis ends with the main conclusions and the short and long term prospects.

The results shown in this manuscript have been possible thanks to the collaboration with various researchers from European groups, including: Arianna Filoramo from CEA-Saclay (France), Massimo Gurioli at University of Florence (Italy), Charles Baudot from STMicroelectronics in Crolles (France) and Nicolas Dubreuil in the Charles Fabry laboratory of the Institut d'Optique (France).

2
Carbon nanotubes

In this chapter a brief summary of the main properties of carbon nanotubes is reported. The main objective of this chapter is to introduce the basic concepts which will help to understand the work presented in the rest of the manuscript. A detailed study of the physics of carbon nanotubes is outside of the scope of this thesis. Exhaustive studies about the physics of carbon nanotubes have been already reported with a deeper explanation in previous manuscript thesis of the group [29, 30] and some handbook texts [31, 32].

2.1. Structures of Carbon nanotubes

Since their discovery in 1991 [33] by Iijima, carbon nanotubes (CNTs) have become a material of great scientific interest. Among its properties one can highlight mechanical [34], thermal [35], electronic [36] and optical [37] that make it the material of choice for many applications. Indeed, in the recent years, in the field of applied physics, several applications based on CNTs have been reported including: bio sensors [38,39], radio frequency [40], flexible electronics [28, 41], quantum [42, 43] and transistors [44], to name a few.

Two different kinds of CNTs can be synthesized, multi walled carbon nanotubes (MWCNT) and single walled carbon nanotubes (SWCNT). In this work we only consider SWCNTs because they are the most interesting nanotubes for photonics applications. The direct band gap makes SWCNT suitable for light sources, modulators or detectors. SWCNT is a cylindrical structure of carbon atoms, about 1 nm in diameter and more than several hundred nanometers in length. Because of the very large aspect ratio, SWCNT is considered as a 1D material. SWCNT can be seen as the result of rolling graphene layer up, as shown in Fig. 2.1.

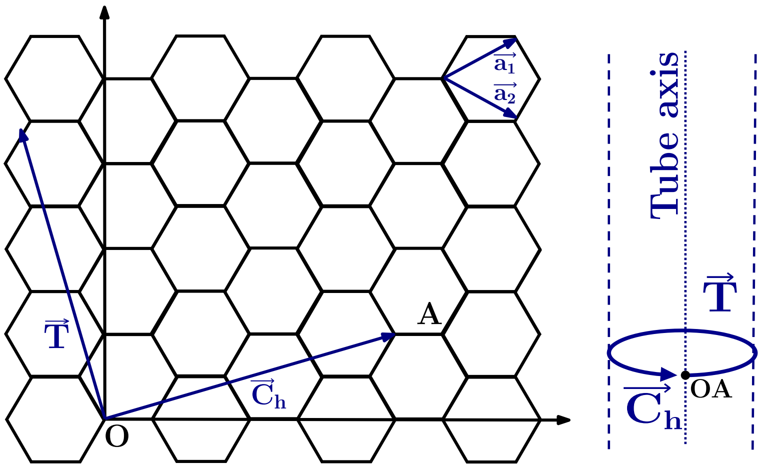

Figure 2.1.: Schematic view of a rolling of graphene sheet.

This graphene layer can be rolled in many different directions, described by the chiral vector $\overrightarrow{C_h} = n\overrightarrow{a_1} + m\overrightarrow{a_2}$, which is a linear combination of the unit vectors a_1 and a_2 of a graphene sheet with n and m integers. The chiral indices (n, m) precisely describe the chirality, diameter and nature (metallic/semiconducting behaviour) of a SWCNT. The diameter d of SWCNT with chiral index (n, m) can be expressed as:

$$d = a\frac{\sqrt{n^2 + m^2 + mn}}{\pi}, \tag{2.1}$$

where $a = |a_1| = |a_2| = 2.46$ Å. And its chiral angle as

$$\theta = arctan\frac{m\sqrt{3}}{2n + m}. \tag{2.2}$$

The SWCNTs are classified depending on their chiral angle, as follows:

- If $n = m$ then $\theta = 30°$ they are called nanotubes Armchair.
- If $m = 0$ then $\theta = 0°$ they are called nanotubes Zigzag.
- If $n \neq m$ then $0° \leqslant \theta \leqslant 30°$ and they are called nanotubes Chiral.

Figure 2.2 represents examples of SWCNTs with these three different configurations.

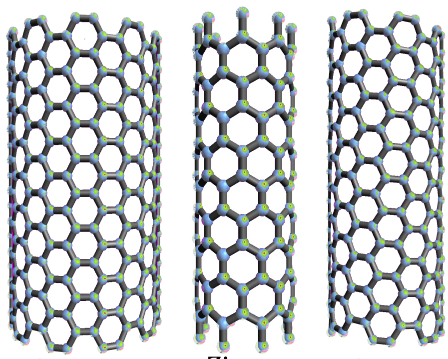

Figure 2.2.: Atomic structure for SWCNT with different chiral angles. Armchair SWCNT with chiral index of (10,10). Zigzag SWCNT with chirality of (8,0) and Chiral SWCNT with pair (8,6).

Through the chiral index of the SWCNTs it is possible to make a classification of its electronic and optical properties. The electronic properties of SWCNTs are obtained throw the zone-folding approximation of electronic structure of graphene [31]. The allowed wave vector component around the circumference of SWCNT is quantized, while the component along the nanotube axis is continuous. The zone-folding approximation consists in sectioning the graphene electronic structure as a cutting line, represented as dashed line in Fig. 2.3. If the cutting line crosses at the K point then the SWCNT is metallic (represented in Fig. 2.3.a). When the K point is not included in a quantized level, the SWCNTs is semiconducting, represented in Fig. 2.3.b. Statistically, one third of the SWCNTs meet the condition $n - m = 3p$, where p is an integer, and then are metallic (m-SWCNTs) and the other two third are semiconducting (s-SWCNTs). In Fig. 2.4 we can see a distribution of semiconducting and metallic SWCNTs.

Metallic and semiconducting SWCNTs have very different electrical and optical properties. This dissimilarity is patent in its electronic state. The density of electronic states (DOS) indicates the number of allowed electron states at a particular energy range. Figure 2.5 shows the schematic of the density of electronic states of metallic (Fig. 2.5.a) and semiconducting (Fig. 2.5.b) SWCNTs. The sharp peaks in both DOS correspond to the Von Hove singularity, coming from the 1D quantum confined electronic state in the SWCNTs. As shown in Fig. 2.5.a, the DOS of m-SWCNT presents a continuous of electronics states. Conversely, the DOS of s-SWCNTs exhibits a bandgap of hundreds of meV. The s-SWCNTs present a chirality-dependent energy gap that is inversely propor-

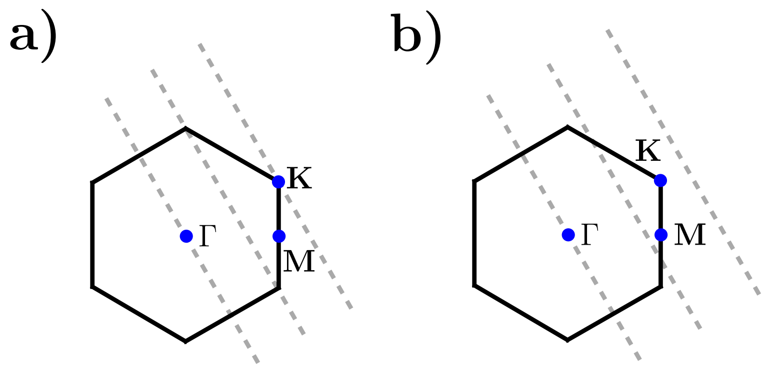

Figure 2.3.: Schematic view of the first Brillouin zone. The dashed line represents the allowed states of a carbon nanotube. a) First Brillouin zone for a metalic SWCNT, recognizable because graphene K point belongs to an allowed state of a carbon nanotube. b) When the K point is not included in a quantized level the SWCNT is semiconductor.

tional to its diameter.

m-SWCNTs present high thermal stability, high thermal conductivity, and large current carrying capability, characteristics that make them a good candidate for metallic interconnects applications. On the other hand, s-SWCNTs leverage the direct bandgap behaviour to implement diodes, transistors, LED and light sources. Thus, s-SWCNTs are remarkable nanomaterials for photonic applications.

2.2. Synthesis of carbon nanotubes

As previously explained, the properties of SWCNTs strongly depend on their chirality. For this reason the synthesis of carbon nanotubes has taken an important place in research activities. Depending on the method employed for their synthesis, it is possible to obtain a different distribution in chirality. The fabrication process also determines the number of defects in the resulting SWCNTs, which could disturb its properties. Synthesis methods can be classified according to the temperature as: high temperature (above 2000 °C) and moderate temperature (between 500 °C and 1500 °C). In high temperature methods, we can find arc discharged and laser ablation, while in moderate temperature we find chemical vapour deposition (CVD), which is the current standard method of synthesis. There are several variants of this technique depending on the catalyst used to grow nanotubes. In this work, we focus on three of them, which are used to pro-

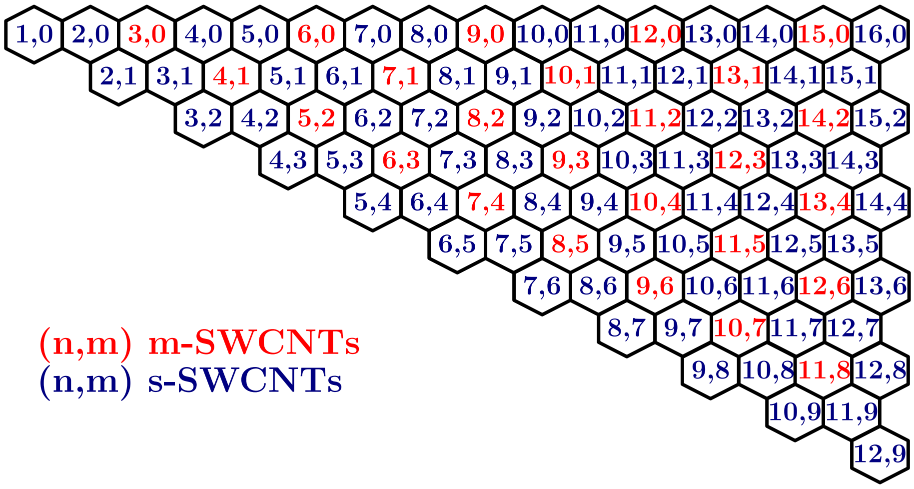

Figure 2.4.: Chiral distribution of SWCNTs. Chiralities represented in blue and red colours are semiconducting and metallic SWCNTs, respectively.

duce the SWCNTs we employed in this thesis. They are: High Pressure Carbon Monoxide (HiPco), Cobalt Molybdene Catalyst (CoMoCat) and Laser ablation. According to the method, different s-SWCNTs diameter are produced. Next, a brief summary of the most relevant methods to synthesize carbon nanotubes is presented.

- **Arc discharged.** This was the first technique employed for the synthesis of SWCNTs [45]. In this technique a continuous current of 200 A at 20 V is applied between two electrodes to generate an electric arc and produce the carbon sublimation resulting in the SWCNTs. The electrodes (anode and cathode) are graphitic carbon rods mixed with a catalyst (Ni, Fe, Co, Pt, Pd, Rh, Y) that permit to control the SWCNTs yield. This technique produces SWCNTs with diameters range of 1.2 nm and 1.6 nm [46].

- **Laser ablation.** A laser beam vaporises a graphite target in a inert chamber at high temperature. Carbon sublimation causes the generation of SWCNTs. In the same way as the previous technique, the catalyst selection favors the SWCNTs synthesis. The resulted SWCNTs have a diameter between 1.2 nm and 1.7 nm [47].

- **High Pressure Carbon Monoxide (HiPco).** For this synthesis, gas-phase carbon monoxide and iron pentacarbonyl are mixed at high pressure (∼30 atm) and temperature between 900°C and 1100°C. During the process, metallic

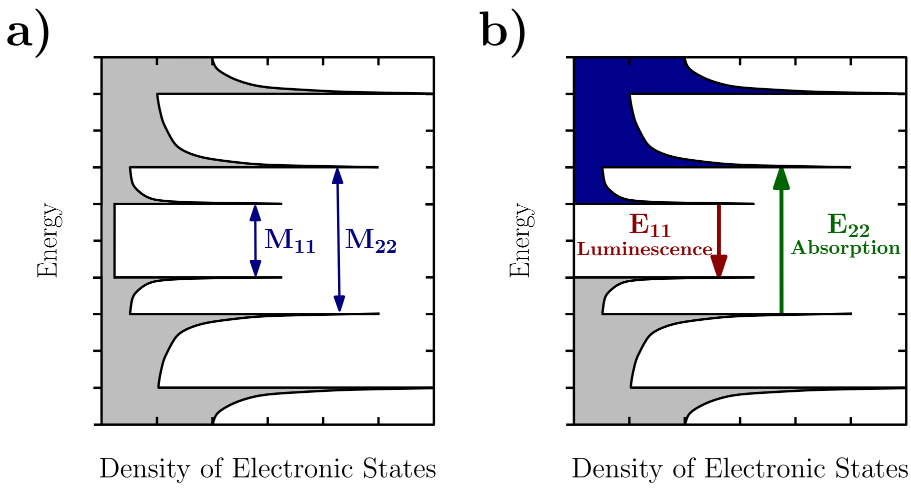

Figure 2.5.: Density of electronic states for: a) Metallic SWCNT and b) Semiconducting SWCNT.

particles break down gas molecules and form the SWCNTs. With this process, a narrow distribution of chiralities is obtained (between 0.8 nm and 1.2 nm) with a high production rate of a gram-per-day [48, 49].

- **Cobalt Molybdene Catalyst (CoMoCat).** Process similar to HiPco. In this case the catalyst is cobalt-molybdemum. The reaction is done at (∼5 atm) of pressure. In these conditions the main synthesized diameter is 0.8 nm [49].

In conclusion, high temperature synthesis methods, Arc discharge and Laser ablation, produce SWCNTs with excellent crystallinity. However, they are expensive methods due to the high power and high vacuum conditions required for the synthesis. On the other hand, the methods based on CVD are a good alternative because they are cheaper and easier to implement.

2.3. Optical properties of carbon nanotubes

In this section main optical properties of SWCNTs are analized, including photoluminescence, electroluminescence and nonlinear effects.

2.3.1. Photoluminescence

Photoluminescence (PL) is given by a physical process in semiconductor materials, where pumped photons are absorbed by the material and reemitted at a different wavelength. Absorption and emission wavelengths are mainly determined by the electronic properties of the s-SWCNT, and thus by its chirality. As a rough approximation, the PL in s-SWCNTs can be explained with the help of the tight-binding model [31]. As shown Fig. 2.5.b, in the PL phenomena the light is absorbed in the E_{22} transition, followed by a fast relaxation by emission at the E_{11} transition. The simple tight-binding calculation predicts that the energy ratio of E_{22}/E_{11} should be a near 2. However, experimental observations show a ratio of ≈ 1.8 [50]. This mismatch is due to the existence of excitons, an electron-hole pair attracted to each other by a Coulomb force, in s-SWCNTs. The first experimental demonstration of the existence of strong excitonic energy was reported by Wang et al. in 2005 [51]. This effect in SWCNT derive from their 1D character. The exciton energy is inversely proportional to the diameter of the s-SWCNTs and it is in the order of hundreds of meV. The theoretical relation between radius and energy gap in SWCNTs was summarized by Kataura in 1999 [37]. Figure 2.6 represents an excitonic diagram where the two first excitonic transitions, S_{11} and S_{22}, and the two first electronic transitions, E_{11} and E_{22}, are shown. Continuous and dashed lines indicate electronic and excitonic levels, respectively.

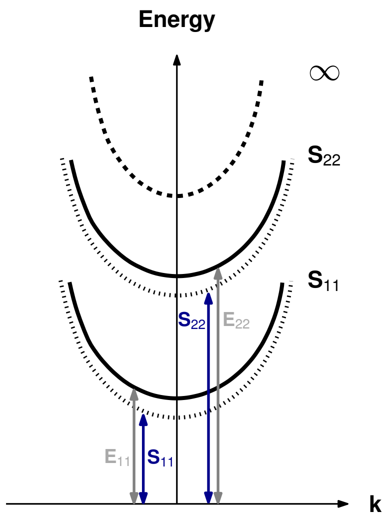

Figure 2.6.: Excitonic diagram of a s-SWCNTs. The electronic bands and excitonic levels are represented in continuous and dashed traces, respectively.

To do a fast chirality identification it is recommended to employ an empirical Kataura map [52]. Figure 2.7 depicts the theoretical and empirical Kataura maps. As shown in Fig. 2.7, nanotube diameter and energy follow an inverse relationship. Depending on the manufacturing process used to synthesize the SWCNTs, different diameters of nanotubes are obtained, with different optical and electrical properties. From Fig. 2.7, it is possible to obtain SWCNTs with emissions covering the O-Band (around $1300\,\mathrm{nm}$) and the C-Band (centered at $1550\,\mathrm{nm}$). This wideband tunability makes SWCNT a suitable material for optical applications, and especially for optical communications.

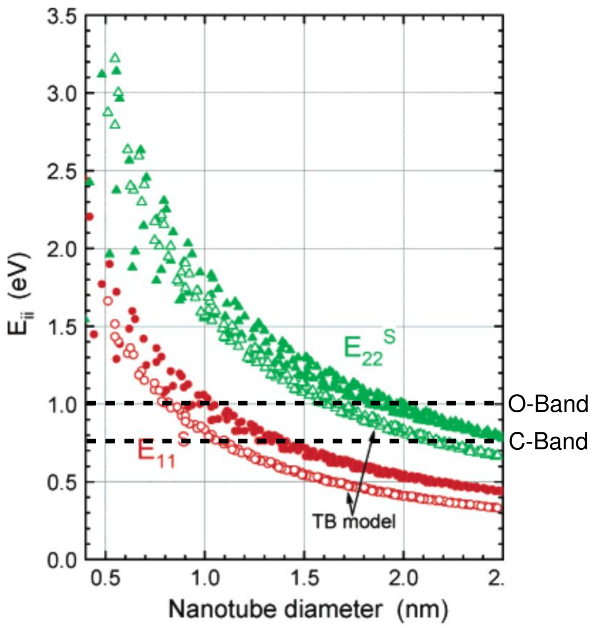

Figure 2.7.: Kataura plot. Comparison between theoretical (follow tight-binding model) and empirical values [52].

The interaction of an electromagnetic field with a one-dimensional object depends on its orientation with respect to the electromagnetic field. It is well known that the strong one-dimensional character of SWCNTs, with a typical aspect ratio of 1:1000, plays an important role in their optical properties. In 2004, Lefrebvre et al. measured for the first time the impact of the incident polarization on the absorption and PL measurements of a single SWCNT [53]. It was observed that both the absorption and the emission of a single SWCNT are maximized when the electric field of the incident light is parallel to the tube axis. As discussed in chapter 4, this strong polarization dependence plays a key role in the optimization of the interaction between SWCNT and integrated photonic waveguides.

2.3.2. Electroluminescence

The photon emission in SWCNTs can be stimulated by two different process: by absorption of photons with energy S_{22}, with the consequent emission in S_{11} energy, (process discussed in section 2.3.1), or by injection of electrons and holes at both ends of the SWCNT. This phenomenon is known as electroluminescence (EL).

The electroluminescence is generated by carrier recombinations in different electronic structures, including ambipolar FETs (field effect transistor) or by impact excitation, as observed in unipolar FET. In ambipolar carbon nanotube field effect transistors (CNTFET) the electron and hole injection is performed at the opposite ends of the SWCNT channel. A portion of the injected carriers is released as heat (phonons). Another fraction of these carriers is recombined in the channel inducing the electroluminescence [24]. This effect is schematically depicted in Fig. 2.8.

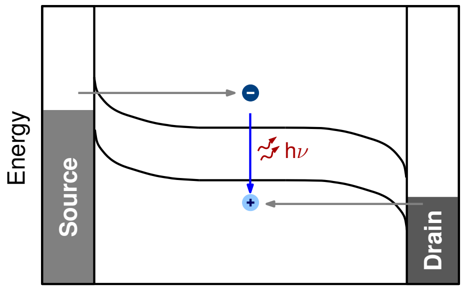

Figure 2.8.: Schematic view of carrier recombination process. Electrons and holes are injected from two metallic contacts and radiatively recombined in the channel.

This is the same mechanism that we can find in a traditional LED. The advantage of using ambipolar CNTFET is that they do not require any chemical doping, simplifying the fabrication process. The electrical behaviour of CNTFET is governed by the metal/SWCNT interaction at the contact regions. Depending on the chosen metal, p or n-type doping of SWCNTs or 1D Schottky barriers can be implemented [54]. The efficiency of the ambipolar CNTFETs emission can be optimized using asymmetric contacts [55], where each extreme of the SWCNT is connected to a different metal with a work function selected to promote the injection/extraction of electrons or holes. Near-linear relationship with the current is expected for ambipolar CNTFETs under low electric field ($2 - 3$ V/μm) [56]. In the case of impact excitation, mechanism given in unipolar transistors, the current is produced by only one type of carrier (electrons or holes). This effect dominates when using symmetric contacts [43, 57]. When the carriers (electrons or holes) are accelerated in a high electric field and impact with uncharged carbon atoms, they create excitons. The EL is produced when this exciton is radiativelly recombined emitting a photon. In this case, an exponential growth of the intensity with the current is expected [58]. Both photoluminescence and electroluminescence effects depend on the chirality of the nanotubes and the generated light is strongly polarized along the nanotube axis.

2.3.3. Optical gain in 1300 nm and 1550 nm

In 2010, Gaufrès et al. demonstrated for the first time intrinsic optical gain in s-SWCNTs with emission at a wavelength of 1300 nm [59]. The experiments were performed using the variable strip length (VSL) method in a thin film doped with s-SWCNTs. The s-SWCNTs were previously purified with ultracentrifugation assisted by aromatic polymer method [60]. The sample was excited with a nanosecond pulsed laser at 740 nm. The amplified spontaneous emission (ASE) was collected at the chip facet and measured as a function of the excitation length. Figure 2.9.a shows the ASE obtained at low fluence pump (35 mJ cm^{-2}) in blue line and demonstrates the saturation of the photoluminescence. On the other hand, when the sample is excited at high fluence pump (500 mJ cm^{-2}), represented in red line, a strong signal increase is observed, which proofs the optical gain in the material. Normalized photoluminescence spectra for the sample under study is represented in Fig. 2.9.b. The spectrum recorded corresponds to input pump fluence below the threshold (in blue) and input pump fluence above the threshold (in red). We observed a narrowing of 29% and 28% for the photoluminescence at 1300 nm and 1200 nm wavelength, respectively. Quantitative calculation of the optical gain coefficient for a nanotube thin film is estimated to be around 190 cm^{-1}.

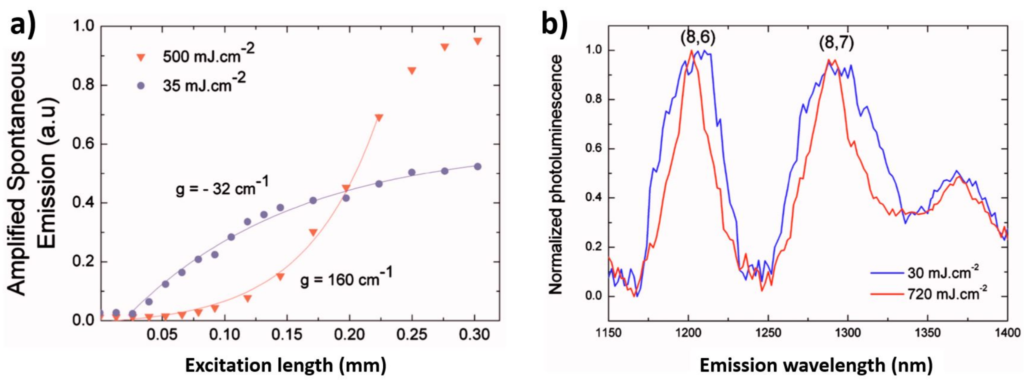

Figure 2.9.: a) Amplified spontaneous emission at 1300 nm as a function of the excitation length for low fluence pump, in blue, and high fluent pump, in red. b) Superposition of emission spectra of carbon nanotubes excited at low and high fluence pump. FWHM has been reduced 30% when the gain regime is reached. Figures extracted from [59].

In the framework of the European project Cartoon, equivalent measurements were carried out in s-SWCNTs with emission at 1550 nm wavelength (Laser ablation SWCNTs). The measurements were conducted at the University of Florence (UNIFI) and supervised by Dr. Massimo Gurioli. They employed a nanosecond pulsed laser at 532 nm wavelength. Results of first preliminary measurements are presented in Fig. 2.10, where the ASE is represented as a function of excitation length using a fluent pump of 7.5 mJ cm^{-2}. We observed under these conditions a strong signal increase which indicates optical gain in the material.

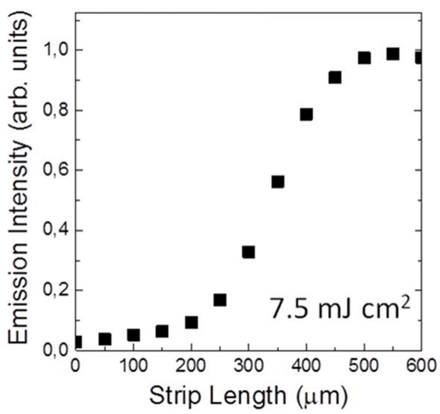

Figure 2.10.: Amplified spontaneous emission at 1550 nm as a function of the strip length. Pumping wavelength of 532 nm.

Obtaining the optical gain in the material leads us to think that reaching lasing with the integration of s-SWCNTs in photonic nanocavities may be possible.

2.3.4. Nonlinear Effects

SWCNTs present nonlinear effects that have been widely studied in the literature as it is summarized in this subsection. Nonlinear optics (NLO) is generally described by the response of the macroscopic polarization, P, to an electromagnetic field, E. A detailed study of the nonlinear effects is outside of the scope of this thesis. An exhaustive study can be found elsewhere [61, 62]. The nonlinear phenomena can be described by a series expansion of the macroscopic polarization as a function of the electric field, as

$$P = \varepsilon_0 \chi^{(1)} E + \varepsilon_0 \chi^{(2)} E^2 + \varepsilon_0 \chi^{(3)} E^3 + \cdots , \tag{2.3}$$

where ε_0 is dielectric permittivity of free space. $\chi^{(1)}$ is the first order coefficient and is the origin of linear effects. $\chi^{(2)}$ is the susceptibility of second order and it is the responsible of the Pockels effect. $\chi^{(3)}$ is the third order nonlinearity and is related with the Kerr effect. Note that Pockels effect is a characteristic of non-centrosymmetric materials [62], including lithium niobate ($\mathrm{LiNbO_3}$) used for the implementation of modulators [63]. In CNTs, second order nonlinearity of $\chi^{(2)} \sim 15 \times 10^{-6}\mathrm{esu}$ has been theoretically predicted [25]. This value is nearly ten times larger than of GaAs. Conversely, other works claim that there is not second-order nonlinearity in CNTs due to symmetry of carbon structure [64]. We can find some works were the authors experimentally observe second harmonic generation in SWCNTs [65, 66], where the authors deny that it is due to certain degree of anisotropy in SWCNTs samples. Nevertheless, no clear demonstrations have been reported yet.

In this thesis (see chapter 7), we focus the study on third-order optical nonlinearity of SWCNTs. $\chi^{(3)}$ is defined by

$$\chi^{(3)} = \chi_R^{(3)} + i\chi_I^{(3)}, \tag{2.4}$$

where the imaginary part ($\chi_I^{(3)}$) is related to the coefficient of the nonlinear absorption, β_{TPA}, as follows

$$\beta_{\mathrm{TPA}} = \frac{3\omega}{2\varepsilon_0 c^2 n_0^2} \mathbb{I}\mathbf{m}\left\{\chi^{(3)}\right\}, \tag{2.5}$$

and, its real part ($\chi_R^{(3)}$) is related to nonlinear refractive index or Kerr nonlinearity, defined as

$$n_2 = \frac{3}{4n_0^2\varepsilon_0 c}\mathbb{R}\mathbf{e}\left\{\chi^{(3)}\right\}, \tag{2.6}$$

where ω is the laser radiation frequency, ε_0 is dielectric permittivity of free space, c the speed of light in vacuum and n_0 is linear refractive index.

CNTs have garnered a great interest in the scientific community due to their exceptional high third-order optical non linearity with ultra fast recovery time and broad bandwidth [26]. Precisely, β_{TPA} is accountable for saturation absorption, area in which CNTs have been extensively developed during the last decade [67–70]. Interestingly, the nonlinear refractive index, n_2 in CNTs, was theoretically predicted to be as large as $2 \times 10^{-8}\text{cm}^2/\text{W}$, in the region where the two-photon absorption is small [26].

Here, we analyse with more detail the saturable absorption and Kerr effect.

Saturable absorption

Figure 2.11 describes passive mode-locking operation, where a saturable absorber (SA) is introduced into a laser cavity. This component absorbs the input light linearly at low optical power. After an intensity threshold, the absorption is saturated becoming transparent and modulating the light [71].

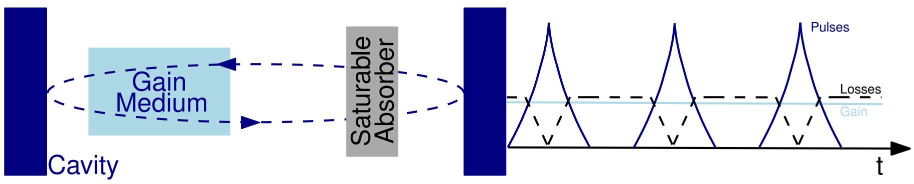

Figure 2.11.: Schematic view of a saturable absorber in a passive mode-locking of a laser. The pulses of light are created when the losses are smaller than the gain. This situation happens when the saturable absorber reaches the saturation, becoming transparent.

The most important parameters to choose the SA are: absorption spectrum, which determines the operation wavelength range, and the recovery time, which fixes the time to recover the linear absorption and start again a new saturation/absorption cycle. All the methods used for the synthesis of carbon nanotubes produce a wide distribution of chiralities where semiconducting and metallic SWCNTs are mixed. This point becomes a challenge for applications where a single chirality is desired, but it is an advantage for the fabrication of SAs based on SWCNTs. This wide distribution of chiralities will provide a broad spectrum of absorption which has a direct impact on operation wavelength range (covering all the wavelengths between 1 μm and 2 μm [72]). In addition, the presence of metallic nanotubes causes a passage of carriers through the tunneling effect of semiconductors to metal ones, resulting in a recovery time of only a few hundred femtoseconds. For comparison, well encapsulated semiconductors exhibit recovery times of 30 picoseconds [73]. The intrinsic optical saturable absorption in a broadband operation together with the fast recovery time make CNTs a suitable material for passive mode-locked laser, which makes it capable of converting a continuous laser excitation into a train of very short pulses. The main drawback of SWCNT-SAs is the high non-saturable loss which compromises their feasibility for applications in ultra fast solid-state lasers but not in fibre lasers, that tolerate high losses [68].

Nowadays we can find different materials with similar or even better nonlinear properties that could be used as saturable absorbers. For instance, graphene exhibits intrinsic wideband operation, from the ultraviolet to the far-infrared region, and ultra fast response times which are very interesting to be used as saturable absorber [68]. Despite its promising properties there are no clear and reproducible experimental results that prove the improvement compared to SA based on CNTs. In the same family as graphene, several 2D materials have been considered for SAs due to their interesting nonlinear properties. Among them black phosphorus (BP) and layered transition metal dichalcogenides (TMDs) are particularly interesting. Black phosphorus demonstrated ultra fast pulse generation ($\sim$786 fs) [74] and wideband operation, from 1μm to 2.7μm [75]. The main drawback of this material is the short stability in time and its vulnerability to optical damage when strong laser pulses are transmitted [76]. On the other hand, TMDs materials have been widely developed due to their easy fabrication and low cost. Still, these materials normally are more suitable for applications in the visible, owing to their large bandgaps [76].

Kerr Effect

The first theoretical prediction of $\mathbb{R}\mathrm{e}\left\{\chi^{(3)}\right\}$ in CNTs was made by Margulis et al. in 1998 [26]. In this work, a $\mathbb{R}\mathrm{e}\left\{\chi^{(3)}\right\}$ as high as $\sim 10^{-7}$ esu, which corresponds to a nonlinear refractive index of $n_2 \sim 2 \times 10^{-8}$ cm^2/W, was estimated under resonant conditions. This work predicts very high third-order nonlinearity compared with other optical materials, like silica glass ($n_2 \sim 3 \times 10^{-16}$ cm^2/W) and silicon $n_2 \sim 4 \times 10^{-14}$ cm^2/W. In the table 2.1 we summarized all the experimental results for nonlinear refractive index or $\chi^{(3)}$ reported to date. These experimental results were obtained pumping in the picosecond and femtosecond regimes to avoid thermal effects [77]. As we can see from the data shown in table 2.1, there is no homogeneity in the results, pump excitation or chirality of CNTs, so it is challenging to estimate the nonlinear coefficient by chirality. Hence, new experiments that clarify the contribution of each chirality to nonlinear third-order effects are required.

2.4. Purification of carbon nanotubes

As previously explained, SWCNTs are produced as a poly-disperse mixture composed of many kind of tubes of diverse lengths, diameters and chiralities, exhibiting different metallic or semiconducting behaviours. In addition, their dispersion in diameter and chirality depends also on the parameters and methods used for their synthesis and can vary from one batch to another. Thus, to use SWCNTs in real photonic devices it is highly desirable to be able to selectively extract from the pristine materials the specie with the targeted chirality i.e. targeted optical properties. A general overview of the main methods employed to select SWCNTs is provided below. This summary is not intended to be exhaustive. For a deeper information we recommend the reference [83].

Selective Destruction

These processes are conceived to remove unwanted species, as for example m-SWCNTs in a field-effect transistor. We find several examples in the literature. For example, oxidation of SWCNTs with small diameters and large chiral angles by annealing in an oxygen-rich atmosphere [84, 85]. Gas-phase reaction with fluorine gas followed by annealing shows good erosion in m-SWCNTs with diameters lower than 1.1 nm [86]. Hydrocarbonation reaction has been used for m-SWCNTs with diameters between 1.4 nm and 2 nm. Other methods are based on controlled SWCNT breakdown by current flow. A large current passes through the conductive metallic SWCNTs until they are electrically destroyed [87]. In all these methods, it is not possible to prevent the collateral damage to adjacent SWCNTs. Another disadvantage is that these methods are irreversible. Thus, the

Experiment	Laser Beam	Time Scale	n_2	CNT	Type of Sample	Ref.
Pump-Probe	1907 nm 1458 nm	Femtosecond	7.4669×10^{-12} cm^2/W $\sim 10^{-9}$ (esu)	Purified Laser Ablation	Deposite on glass substrate	[78]
Z-Scan	1460 nm	Femtosecond	$(1.1 \pm 0.5) \times 10^{-11}$ cm^2/W 1.4×10^{-8}(esu)	HipCo no purified	Thin film	[79]
Z-Scan	790 nm	Femtosecond	-5.5×10^{-11} cm^2/W No data reported in esu	Two diameters 1.41 nm and 1.58 nm	Suspension in water	[80]
Degenerate four-wave mixing (DFWM)	1064 nm 532 nm	Picosecond	No data reported in cm^2/W 6.303×10^{-14}(esu) at 532 nm 6.460×10^{-14}(esu) at 1064 nm	Solution with absorption in both 532 nm and 1064 nm; Kind of CNTs not specified.	The solvent is made by mixing polypyrrol and m-cresol with ethanol.	[81]
Z-Scan	1640 nm	Femtosecond	No data reported in cm^2/W $(1.3 \pm 0.2) \times 10^{-6}$ esu	Laser ablation, average diameter $\sim$1.41 nm	Thin film	[82]

Table 2.1.: Summary of reported $\mathbb{R}\mathrm{e}\left\{\chi^{(3)}\right\}$ and/or nonlinear index for CNTs.

eliminated SWCNTs can not be collected to be used in other applications.

Electrophoretic Separation

Separation of single SWCNTs from bundles or sorting SWCNTs by length and diameter is possible using direct current electric field, electrophoresis. Electrophoresis sorts SWCNTs according to their relative mobility through a gel or solution, i.e. the smallest molecular weight travels faster in the medium [88]. On the other hand, it is also possible to arrange SWCNTs according to their dielectric constant. To do so, an alternating current dielectrophoresis is required. Based on the dielectric constant differences between m-SWCNTs and s-SWCNTs an effective electronic sorting is achieved [89].

Ultracentrifugation

Among methods that employ ultracentrifugation, two techniques stand out. They are the density gradient ultracentrifugation (DGU) and the polymer assisted technique. The DGU sorts SWCNTs by their buoyant density [90]. The SWCNTs are introduced into an aqueous solution with a known density gradient. After the ultracentifugation, the SWCNTs are sedimented in the position where their density matches that of the gradient. With the appropriate selection of the initial gradient the different chiralities are spatially organized and can be recovered by a process known as fractionation. On the other hand, polymer assisted technique, relies on chirality-selective wrapping of the SWCNTs by polymers [91]. It was demonstrated that polyfluorene (PFO)-based copolymers were able to wrap selectively SWCNTs with certain chiral angles or diameters depending on the chemical structures of the polymers [92]. This polymer wrapping process favors the suspension of such selected nanotubes in the solvent. Then, the selectively wrapped SWCNTs are separated by centrifugation from the raw mixture and recovered (or extracted) by collecting the supernatant. The photoluminescence of SWCNTs was first reported by O'Connell et al. from individual semiconducting SWCNTs in micelles solution [93]. This is the technique used in this thesis work and it is widely discussed in chapter 3.

2.5. Deposition

In this work, we use a solution of s-SWCNTs sorted by polymer (see chapter 3). Basically, we conceived two different kinds of solutions. One is developed to work with drop casting or spin coating deposition, where the main parameter to be optimized is the concentration. In this way, the number of nanotubes that interacts with an optical device can be maximized. The main drawback of this approach is the little control over their exact position and orientation. A second solution is developed to work in dielectrophoresis, which provides improved control in position and orientation. As explained in detail in the next chapter the key feature in this strategy is the length of the resulting s-SWCNTs. The deposition techniques used in this thesis are detailed below.

Drop Casting

With this technique a volume of SWCNTs solution is deposited on the surface of the sample with a micropipette. After the solvent evaporation, the thickness of the layer is more than one micron. The SWCNTs are non uniformly distributed on the surface, following the coffee ring effect [94]. Besides, there is no control over the orientation of the tubes. In this work, we employed this technique in samples where the photoluminescence collection is done using facet coupling. The results and deeper explanation using this technique are presented in section 4.2.

Spin Coating

After deposition of the solution by drop casting, the sample is spined on a stage. Therefore, most of the solution is removed from the surface, leaving a thin layer on the substrate. The thickness of this layer depends on the spin velocity, with values in the order of the tens of nanometers. The main drawback is the lack of control in the position, orientation and distribution of SWCNTs. We used this technique when the enhancement photoluminescence is collected from the surface. These results are presented in section 4.1.

Dielectrophoresis

Dielectrophoresis (DEP) allows the alignment of SWCNTs. This technique is based on the response of SWCNTs to an oscillating electric field. Dielectrophoresis is based on the appearance of a force on a dielectric object when it is placed in a non-uniform electric field. The expression for the DEP force for cylindrical objects, as is the case of a SWCNT, is given by [95]

$$F_{DEP} = \frac{\pi}{6} r^2 l \varepsilon_m \mathbb{R}\mathbf{e} \left\{ \frac{\varepsilon_p^* - \varepsilon_m^*}{\varepsilon_m^*} \right\} \bigtriangledown |E|^2, \tag{2.7}$$

where r and l are the radius and length, respectively of SWCNT. ε_m is the real part of the permittivity of the suspending medium, E is the applied electric field. ε_p^* and ε_m^* are complex permittivities for SWCNT and medium, respectively. Where the general expression is $\varepsilon^* = \varepsilon - i\frac{\sigma}{\omega}$, being σ the conductivity, ε the real permittivity and ω the angular frequency of the applied electric field ($\omega = 2\pi f$).

In the case of an object with a high aspect ratio, such as carbon nanotubes, the dielectrophoretic force aligns the nanotubes along the electric field lines [95]. The electric field can be applied locally thanks to predefined electrodes. More

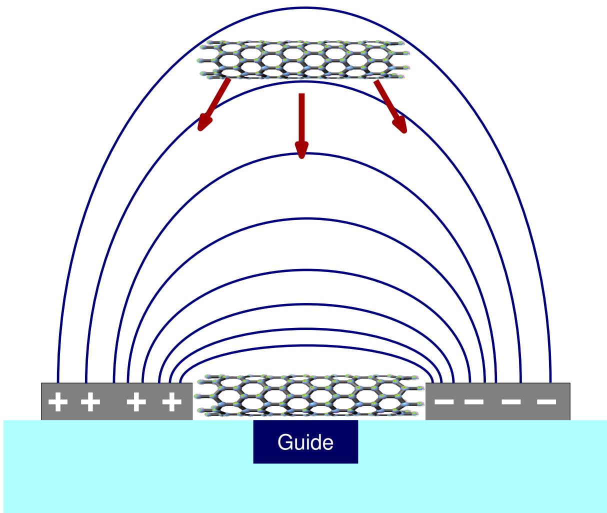

Figure 2.12.: Schematic view of a carbon nanotube subjected to dielectrophoresis.

specifically, a droplet of solution containing nanotubes is deposited onto a substrate patterned with a set of microelectrodes polarized by an alternating (AC) electric field. A schematic view of this technique is represented in Fig. 2.12. The nanotubes in the solution are trapped in the high field region between the microelectrodes forming an array of well-oriented nanotubes. The quality of the orientation depends on various parameters: the length of the nanotubes, the electrode geometry, the dielectric characteristic of both nanotubes and solvent, the concentration of nanotubes in the solution, the amplitude and frequency of the AC signal and the duration of application of the field. The main disadvantage of DEP is the highly enhanced deposition of metallic nanotubes that is detrimental for the devices envisaged in this work. For this reason, we always work with solution of s-SWCNTs with no traces of metallic nanotubes. Also the use of toluene as solvent required an accurate testing of deposition parameters and imposed a strict timing due to the fast evaporation of the solvent. Despite these disadvantages, as reported in chapter 6, we achieved the deposition of arrays of well-oriented semiconducting SWCNTs. The good electrical performance of the fabricated devices is a clear proof of the high selectivity of our s-SWCNT extraction method. On the other hand, the great advantage of DEP is that it allows integrating oriented arrays of carbon nanotubes into existing electrical and optical circuits. The specific parameters of deposition (frequency and amplitude of the applied voltage and time of deposition) are detailed in chapter 6.

2.6. Conclusions

In this chapter we presented a non exhaustive analysis of carbon nanotubes structures. We have summarized the main methods to synthesize SWCNTs. We have presented a short overview on the optical properties of SWCNTs, including: photoluminescence, electroluminescence, optical gain and non linear effects. The major purification and deposition methods have been analysed, with especial emphasis on those used in this work.

3

Material optimization and post processing

This chapter is dedicated to the process developed to obtain high purity solution of semiconducting SWCNTs. In the course of this thesis, three kinds of solutions have been developed to cover the full spectra from 1 μm to 1.6 μm. A first solution with emission wavelength at 1 μm, made from CoMoCAT SWCNTs. The second with emission wavelength centered in the region of datacom (1.3μm), based on HiPco SWCNTs, and the last to cover the telecom band at 1.5 μm, made from Laser ablation SWCNTs. The two first solutions have been optimized to work with optical excitation resulting shorter s-SWCNTs. The Laser solution has been developed to work with electrically injection, resulting s-SWCNTs larger than 6 μm.

Most of my work was dedicated to optimize the solution at 1.3 μm. Indeed, the same process was used for the CoMoCAT solution, while a soft extraction process, developed by CEA, was perform on the second solution emitting at 1.5 μm (Laser ablation).

3.1. Polymer assisted technique for semiconducting SWCNT extraction: HiPco

As explained in previous chapter, only s-SWCNTs exhibit photo- and electroluminescence. However, we had to wait a decade from the discovery of CNTs to observe their photo-luminescence for the first time [93]. So far, all known preparation processes of SWCNTs give mixtures of nanotube chiralities, diameters and length. Therefore, the need for a specific process that allows chirality selection and more especially semiconducting SWCNTs selection is the first condition to use SWCNTs for photonics. In this thesis, we used the process of ultracentrifugation assisted by polymer. This process is widely described in the bibliography [96–99]. Its main stages are represented in Fig. 3.1. The technique starts by the preparation of the initial solution, composed by SWCNTs, polymer and solvent. This starting solution undergoes a sonication process, typically comprising two steps: mild and strong sonication. The mild sonication serves to improve the solubility, and the strong sonication breaks the bundles. The precess ends with the ultracentrifugation step where the s-SWCNTs are separated from the m-SWCNTs and impurities, resulting in the purified solution.

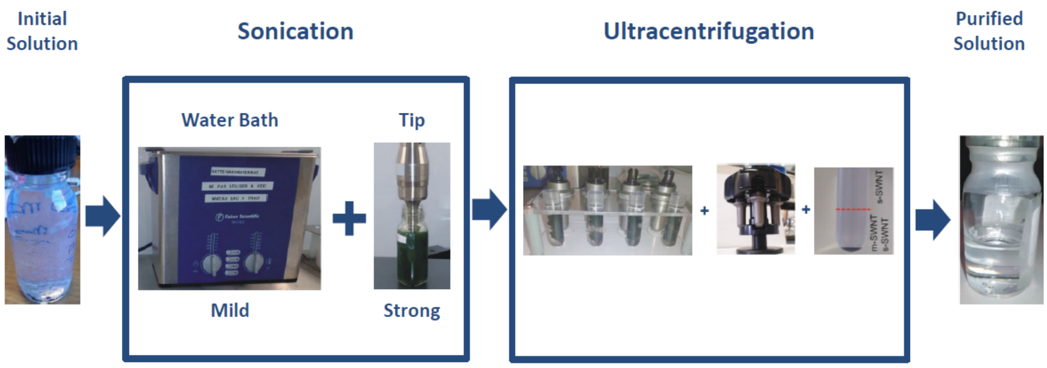

Figure 3.1.: Diagram of the polymer-assisted ultracentrifugation purification process for s-SWCNTs solution.

Specifically, we exploit the ability of polyfluorene (PFO)-based copolymers to wrap SWCNTs with certain chiral angles or diameters. This wrapping depends on the chemical structure of the polymer. This polymer wrapping favors the suspension of such selected nanotubes in a solvent. Then, the selectively wrapped SWCNTs are separated by ultracentrifugation from the raw mixture and recovered (or extracted) by collecting the supernatant solution. This technique was first developed in the group by Dr. Nicolas Izard. The complete process is described in [60, 100]. Figure 3.2 summarizes the main results obtained by Dr. Nicolas Izard and Dr. Etienne Gaufrès. In Fig. 3.2-a the absorption spectra for the same solution before (black line) and after (red line) of the purification process are shown. We can observe a clear reduction of metallic peaks (M_{11}) and the absorption background level after the ultracentrifugation process, which indicates a reduction in metallic SWCNTs and impurities [100]. Figures 3.2-a and 3.2-b present the photoluminescence excitation (PLE) map for the solution before and after the selection process. We observe a reduction of chiralities after the purification process [100].

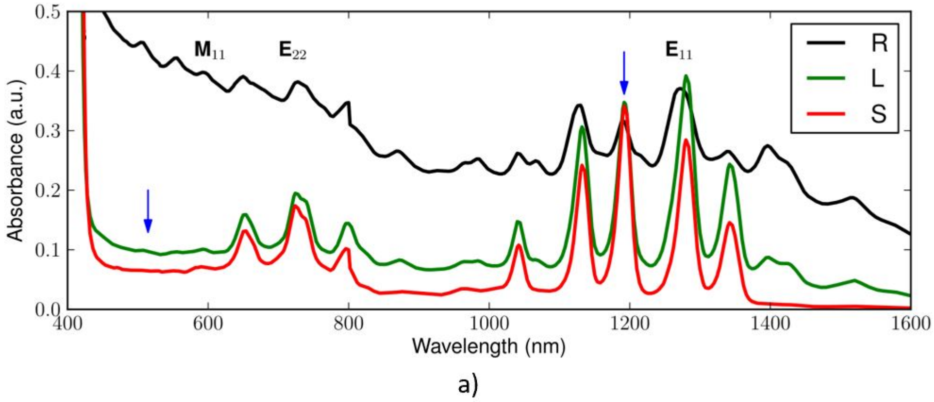

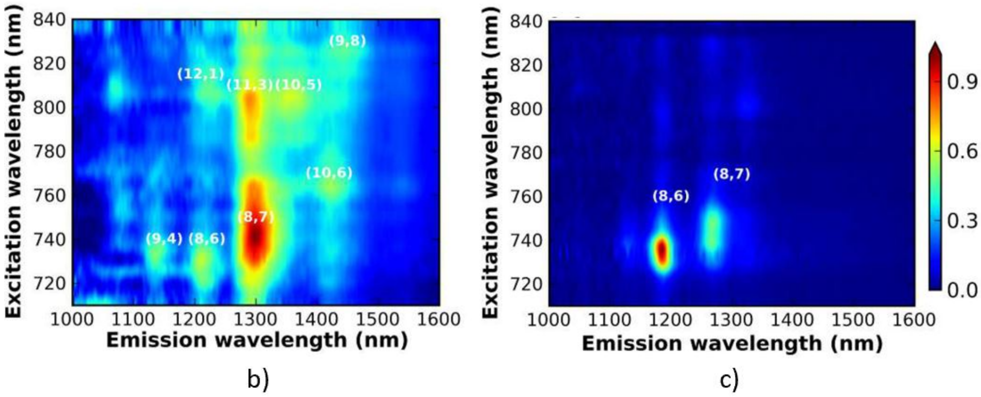

Figure 3.2.: a) Absorption spectra illustrating the effect of the polymer assisted technique. The spectrum for the raw solution is represented in black line. The spectrum for the processed solution are represented in green (10000 g, 15 minutes) and red (150000 g and 2 hours) lines, respectively. Photoluminescence excitation map for the same solution before (in b)), and after (in c)) the selection process. Figures extracted of [100].

In this thesis I optimized the process developed in the group to increase the concentration and improve the emission behavior.

The main steps of this technique are summarized below:

- **Selection of SWCNTs and polymer.** As it is well know in the literature, each process used to synthesize SWCNTs produces a mixture with different diameter distribution and thus different electrical and optical properties. For example, Laser ablation process produced SWCNTs with typical diameter between 1.2 nm and 1.4 nm. High Pressure Carbon Monoxide (HiPco) technique yields diameter comprised between 0.8 nm and 1.2 nm and Cobalt Molybdene Catalyst (CoMoCat) technique results in diameters lower than 0.9 nm. Polymer are macromolecules with structures that closely match with the surface of certain kinds of s-SWCNTs. On the other hand, the polymer assisted technique inhibits the selection of metallic chiralities, mainly due to the charge transfer from metallic SWCNTs that provokes changes in the conformation of the polymer [96]. Thus, the selection of the synthesis method together with the polymer choice provide a solution with clear dominance of certain chiralities [96].

- **Sonication process.** The sonication step is used to improve the solubility and break bundles the SWCNTs from their natural state and to promote the interaction with the chosen polymer. As we can see in the literature, two sonication steps are typically performed [96, 101]. The first one is a mild sonication with a typical value of 60 minutes to achieve maximum solubility [101]. The second one is a strong sonication, conceived to break the SWCNTs bundles [101]. On the other hand, this sonication process implies a strong mechanical excitation that will break the SWCNTs reducing their length. This could be a drawback in the case that these SWCNTs were intended to contact two electrodes. The solution based on HiPco SWCNTs was obtained by employing mild and strong sonication, providing high purity of separated s-SWCNTs to the detriment of their length. For Laser Ablation SWCNTs only mild sonication is used to keep SWCNTs long enough to perform electric contact at each end of SWCNT. In subsections 3.1.1 and 3.1.2 the sonication process is analyzed in detail.

- **Ultracentrifugation step.** This step is used to remove nanoparticles and unwrapped SWCNTs by polymer, mainly m-SWCNTs and non polymer selected s-SWCNT. During this process, the SWCNTs not wrapped by the polymer and the impurities are precipitated to the bottom of the cuvette. We keep the ultracentrifugation force of 150000 g, optimized in previous thesis works [29]. In subsection 3.1.3, the ultracentrifugation time is optimized.

At the beginning of this thesis, two different processes were already published to select SWCNTs high chirality selection in the range of $1.3\,\mu$m without detectable traces of m-SWCNTs and impurities [60, 100]. In both cases, authors employ SWCNTs powders (HiPco, Carbon Nanotechnologies Inc.), Poly-9,9-di-n-octyl-fluorenyl-2,7-diyl (PFO, Sigma-Aldrich) as a polymer and toluene as solvent, with a ultracentrifugation force of 150000 g. The main parameters of both solutions are summarized in table 3.1.

Name	SWCNT (mg)	PFO (mg)	Toluene (ml)	Water Bath Time (min)	Tip Sonication Time (min)	Ultracentrifugation Time (min)	Ref.
A	5	5	30	60	5	60	[60]
B	5	20	30	60	15	120	[100]

Table 3.1.: Summary of the main parameters of initial process for s-SWCNTs extraction based on ultracentrifugation assisted by polymer extracted from [60, 100].

The first step for the solution optimization is to reproduce the results already published. To do that, we used HiPco SWCNTs and PFO distributed by the same providers. The water bath sonication is made using a standard ultrasonic bath (Fisherbrand FB 15051) keeping the temperature under 30° during the process. The tip sonication is performed employing Vibra-Cell processor (Bioblock Scientific, 500 W), with a pulsed sonication (2 seconds ON, 5 seconds OFF) with an amplitude of 20%. The ultracentrifugation is made using Micro-Ultracentrifuge SORVAL MX 150 (Thermo scientific) with a temperature fixed at 22°.

As a major drawback, the use of polymer-assisted technique as a purification process complicates knowing the semiconducting SWCNTs concentration in the solution. We know the concentration of the starting solution but it is challenging to know the exact semiconducting SWCNT quantity in the supernatant solution. Therefore, we are going to use the absorption intensity as the figure of merit to compare different solutions, because this parameter is proportional to the concentration [101].

Figure 3.3 represents the absorbance of two solutions prepared with the processes summarized in table 3.1. The absorbance was measured using a Shimadzu UV-3600 spectrophotometer in a quartz cell using the same path length and corrected with a toluene reference solution. The sharp peaks that appear in the range between 1000 nm and 1400 nm correspond to the first electronic transition (E_{11}) of the s-SWCNTs. The main chiralities present in this solution are (8,6) and (8,7). Peaks between 600 nm and 900 nm are the second electronic transition (E_{22}) for the same chiralities. Peaks in the range of 500 nm and 600 nm correspond to the absorption band of metallic SWCNTs [100]. As demonstrated in [100], the background level in the range between of 500 nm and 600 nm is massively reduced after the ultracentrifugation process, demonstrating that there is almost no trace of m-SWCNTs. It is important to mention that the peak close to 1400 nm, marked with a red rectangle, corresponds to an artifact in the measurement equipment. Although it is not mentioned again, this peak will be present in all the absorption diagrams presented in this chapter. The measurement also presents a problem in the baseline at low wavelengths. This problem occurs several times in the measurements presented in this chapter, we still do not know its origin. As we clearly see from Fig. 3.3 the absorption level for process B is higher than the obtained with process A, which means that the concentration of s-SWCNTs is higher in solution B. Hereinafter we consider the parameters for process B as starting point to optimize the purification method. First, we checked the impact of reducing the centrifugation time from two hours to one hour. As shown in Fig. 3.4, in both cases the solution quality remains almost unchanged. So, for simplicity we choose one hour centrifugation time for the optimization of other parameters.

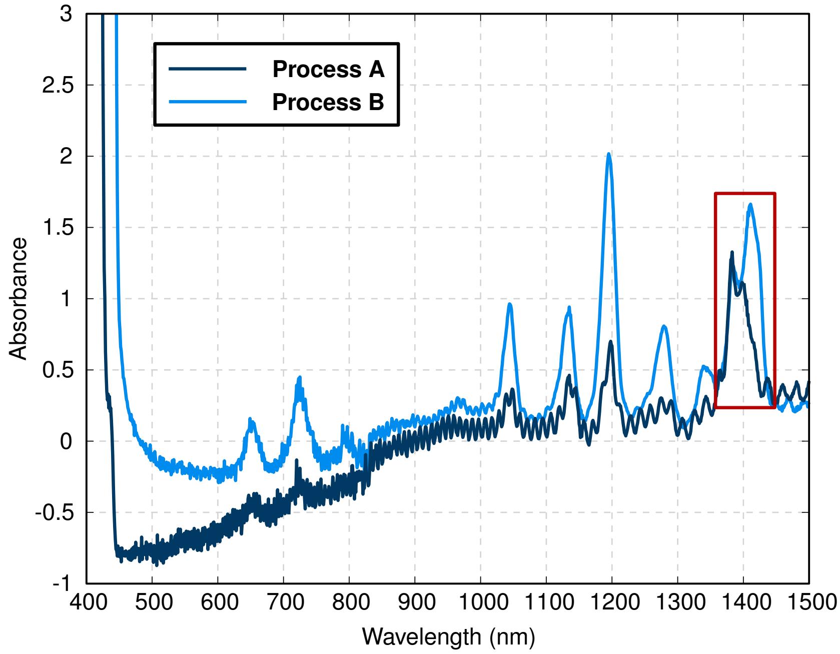

Figure 3.3.: Comparative absorption spectra of HiPco solution prepared with the initial processes (parameters summarized in table 3.1). The peak close to 1400 nm, marked with a red rectangle, corresponds to an artifact in the measurement equipment.

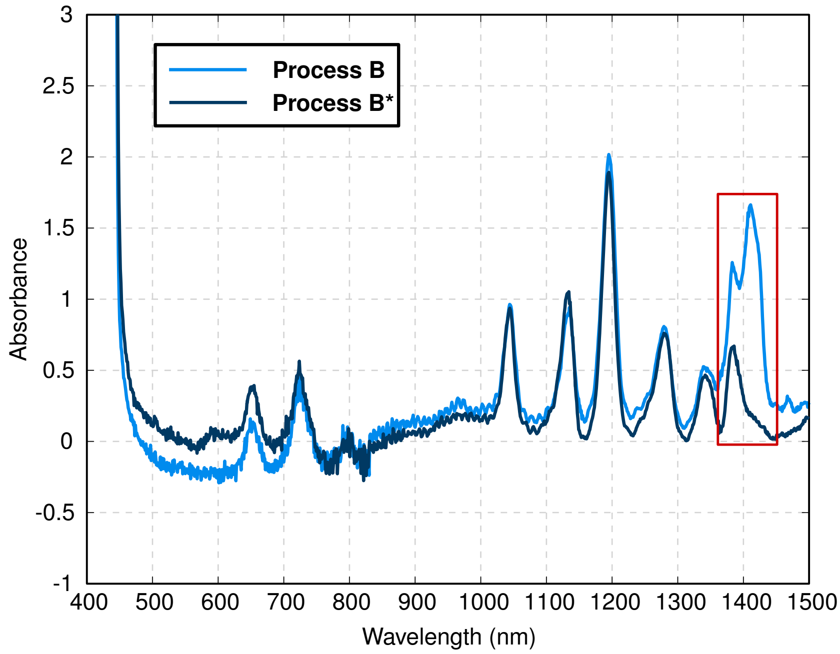

Figure 3.4.: Comparison of absorption spectra from HiPco solution prepared with two hours centrifugation (light blue) and one hour of ultracentrifugation (dark blue) at 150000 g. The peak close to 1400 nm, marked with a red rectangle, corresponds to an artifact in the measurement equipment.

3.1.1. Optimization of the sonication step

As it was previously explained, the sonication step is used to break the bundle of SWCNTs, leading to the major drawback of this approach, which is the reduced length of SWCNTs. First, we decided to introduce a new 10 minutes mild sonication step just after tip sonication process to increase the interaction between polymer and SWCNTs. In this case, we introduced a new mild sonication step just after of tip sonication process. Following this recipe, a new solution is prepared (solution C) for comparison with the modified version of solution B called B* with one hour of ultracentrifugation (see in table 3.2).

Name	SWCNT (mg)	PFO (mg)	Toluene (ml)	Water Bath Time (min)	Tip Sonication Time (min)	Water Bath Time (min)	Ultracentrifugation Time (min)
B*	5	20	30	60	15	No	60
C	5	20	30	60	15	10	60

Table 3.2.: Summary of the main parameters for s-SWCNTs extraction for a solution with two sonication steps, B*, and three sonication steps, C.

Figure 3.5 shows the absorption spectra for a solution prepared with two sonication steps (water bath + tip) solution B* versus a solution prepared with three sonication steps (water bath + tip + water bath) solution C. As we can observe in Fig. 3.5 the incorporation of a new sonication step increases the concentration of s-SWCNTs in the solution (represented in dark blue) by a factor of two respect to the case with only two sonication steps (represented in light blue). This effect is similar for all the chiralities present in the solution.

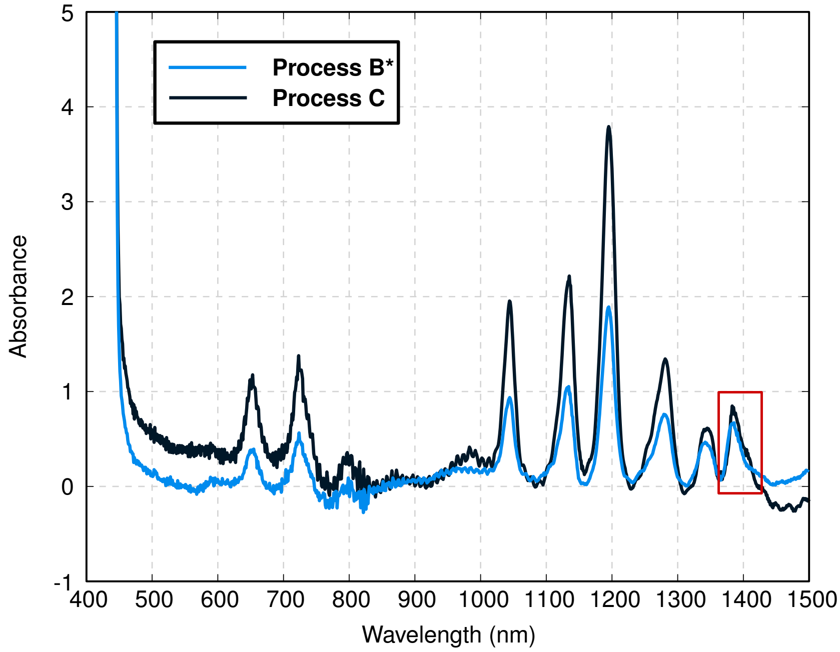

Figure 3.5.: Comparative absorption spectra for HiPco SWCNTs solutions. In light blue the solution prepared using two sonication steps (water bath + tip). In dark blue solution employing three sonication steps (water bath + tip + water bath). The parameters for both solutions are summarized in table 3.2. The peak close to 1400 nm, marked with a red rectangle, corresponds to an artifact in the measurement equipment.

3.1.2. Effect of the tip sonication time

As we concluded from the previous subsection, the incorporation of a new sonication step improves the concentration of semiconducting SWCNTs in the solution by a factor of two. We also analyzed the effect of the time for the tip sonication (strong sonication). To do that, we prepared a new solution (solution D) where all the parameters are kept as in the precedent solution (solution C) and the time for the tip sonication is doubled, increasing from 15 minutes to 30 minutes.

All the parameters involved in this comparison are summarized in the table 3.3.

Name	SWCNT (mg)	PFO (mg)	Toluene (ml)	Water Bath Time (min)	Tip Sonication Time (min)	Water Bath Time (min)	Ultracentrifugation Time (min)
C	5	20	30	60	15	10	60
D	5	20	30	60	30	10	60

Table 3.3.: Parameters for solutions with tip sonication of 15 minutes and 30 minutes.

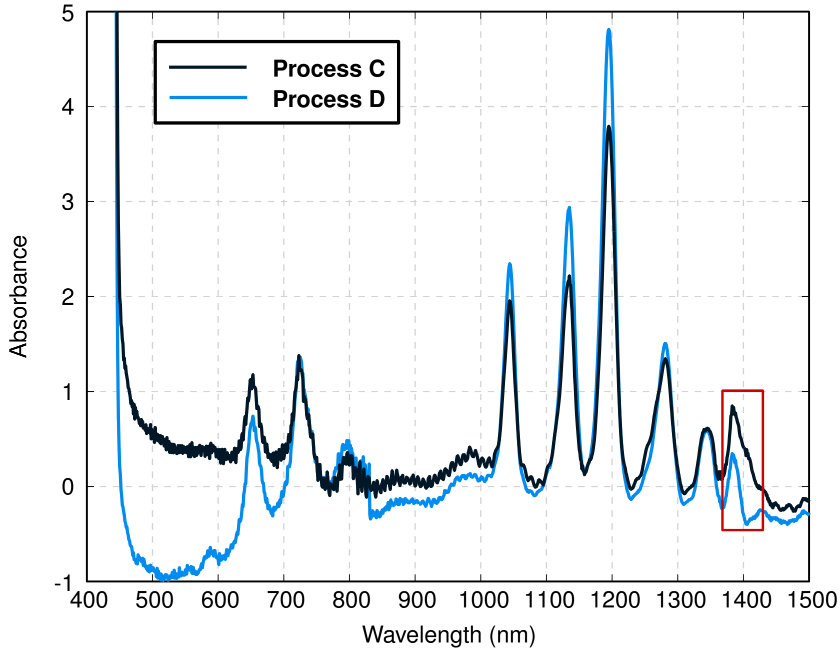

Figure 3.6.: Absorption spectra for HiPco SWCNTs solution prepared with short tip sonication time (15 minutes), in dark blue, and long tip sonication time (30 minutes), light blue, using the parameters summarized in table 3.3. The peak close to 1400 nm, marked with a red rectangle, corresponds to an artifact in the measurement equipment.

Figure 3.6 shows the comparison between the solutions obtained using 15 minutes of tip sonication (solution C) and using 30 minutes of tip sonication (solution D). As we can see from the absorption spectrum, the SWCNTs concentration in solution D (light blue) is 1.25 times higher than in solution C (dark blue). Further increasing the sonication time may improve the SWCNTs concentration in the solution with the inconvenience of reducing their length. However, it was not possible to determine the s-SWCNTs length due to the polymer wrapping. Considering that the increase in concentration obtained during this optimization, from solution B to solution D, is around 2.5 times, we decided to fix these parameters as optimized process.

3.1.3. Optimization of ultracentrifugation time

Once we have finished with the optimization for the sonication parameters in the process, we are ready to optimize the ultracentrifugation time. Polymer (PFO) has an unique interaction with s-SWCNTs with a specific chirality. Hence, m-SWCNTs, impurities and s-SWCNTs with different chiralities are not properly wrapped by the PFO leading to a weak solubilization in toluene. Wrapped s-SWCNTs behave differently in the presence of a centrifugation force. Therefore, after applying a proper centrifugation force, wrapped s-SWCNTs can be collected by recovering the supernatant solution. Too long ultracentrifugation time could cause precipitation all the SWCNTs present in the solution (including semiconducting SWCNTs well wrapped by the polymer). For this reason it is essential to find the optimal centrifugation time that allows separating m-SWCNTs and impurities from s-SWCNTs. To study the centrifugation time impact, four new solutions have been prepared following the optimized ratio SWCNT:PFO:Toluene and sonication steps reported in recipe D. In all the solutions under study the ultracentrifugation is done at 150000 g, optimized parameter in the previous thesis works. The ultracentrifugation times considered are 30 minutes, 1 hour, 2 hours and 3 hours.

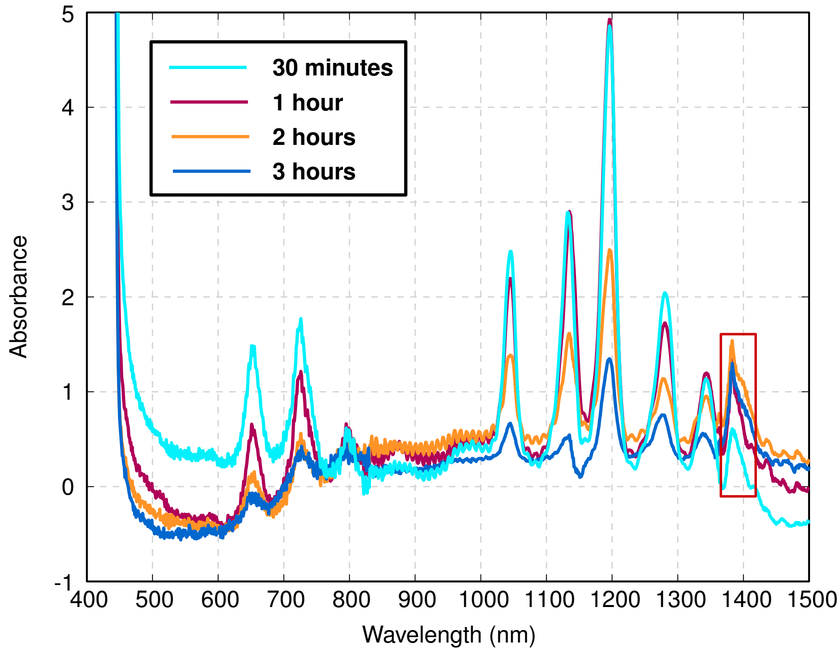

Figure 3.7.: Comparative of absorption spectra of HiPco solution prepared with the concentration and sonication time in solution D and ultracentrifugation times varying between 30 minutes and 3 hours. The peak close to 1400 nm, marked with a red rectangle, corresponds to an artifact in the measurement equipment.

Figure 3.7 shows the absorption spectra for the aforementioned solutions. As we can observe from the data represented in Fig. 3.7, the optimum centrifugation time is between 30 minutes and 1 hour. In both cases the concentration of s-SWCNTs is almost identical. In contrast, as ultracentrifugation time is further increased, the concentration of s-SWCNTs in the solution decreases. Reaching the minimum concentration for ultracentrifugation time of 3 hours. So, we can conclude that the optimum parameters to obtain high quality s-SWCNTs solution are those of solution D, detailed in table 3.3.

Once we found the optimum parameters in terms of concentration, we measured the evolution of the photoluminescence (PL) intensity before and after the optimization of s-SWCNTs extraction. These experiments were carried out by Dr. Francesco Sarti from University of Florence, partner in the European project (FP7-ICT CARTOON). Figure 3.8 shows a comparative PL spectra for a drop of a solution prepared with the process used at the beginning of this thesis (in dark blue) compared to a drop of the optimized solution. Both depositions were made on a quartz substrate. The measurements were carried out with CW Titan:Sapphire laser at 735 nm and 10 mW of power. The photoluminescence is recorded using a Princeton spectrometer with InGaAs detector. We clearly observe that the improvement in concentration of s-SWCNTs in the solution directly increases the photoluminescence intensity. The new solution developed during this work shows two times more photoluminescence. This result is very promising for the development of integrated devices based on CNTs.

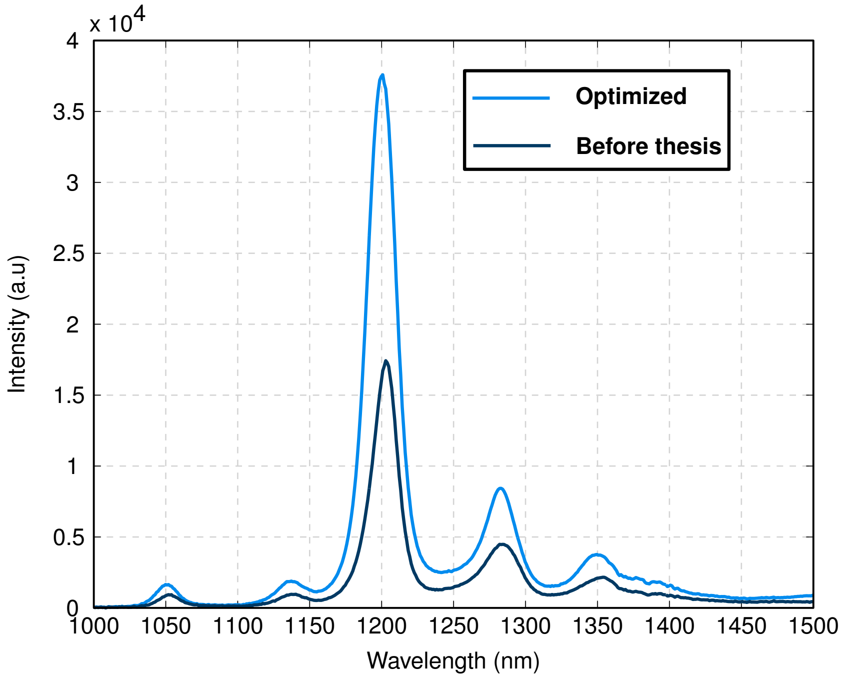

Figure 3.8.: Photoluminescence spectrum onto a quart substrate of a s-SWCNTs solution developed before this thesis versus the optimized solution elaborated in this work, represented in dark and light blue, respectively.

The optimized solution exhibits a substantial concentration improvement. However, it is difficult to further reduce the amount of polymer and increase the maximum achievable s-SWCNT concentration. In the following section, we present the post processing technique that we used to further increase the concentration s-SWCNTs, while also reducing the concentration of polymer.

3.2. Post processing. Ultra concentrated solutions

Aiming at further increasing the concentration of s-SWCNT in solution, we employed a post precessing technique. This technique is based on re-processing of the solution using an additional ultracentrifugation step, with higher speed and longer time that the one performed before. This new ultracentrifugation step induces the precipitation of the previous suspended s-SWCNTs that form a pellet on the bottom. After the processing, two products are collected: the supernatant solution that in this case is mainly composed of polymer and the precipitated s-SWCNTs. The supernatant is discarded and we collected the pellet that is dispersed in a new solvent. It is important to mention that the concentration of s-SWCNTs in the new solution can be modulated by choosing the quantity of added solvent. The post-processing of the solution was realized at the Commissariat à l'Énergie Atomique et aux Énergies Alternatives (CEA-Saclay) in the group of Dr. Arianna Filoramo (senior expert researcher). First, we started this process with an optimized solution (as solution D Fig. 3.6). The solution was ultracentrifugated at 260000 g during 4 hours in a Beckman Coulter Optima MAX XP equipped with a TLA-110 rotor system.

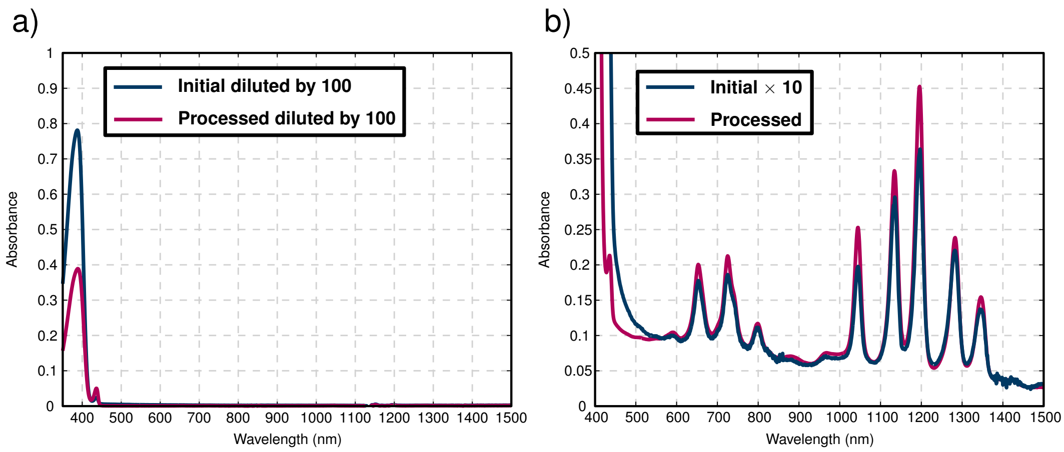

Figure 3.9.: Absorbance spectra illustrating the effect of the induced precipitation and re-dispersion with fresh solvent. a) Spectra of solution diluted by factor of 100. The light blue represents the post-processing solution showing that the polymer concentration is reduced by a factor of two. b) Comparison between the spectra before and after of post-processing step.The light blue represents the post-processing solution that shows that is more than 10 times larger that the started solution.

Figure 3.9.a shows the absorption spectra for initial and post-processed solutions diluted by a factor of 100 to avoid the saturation of the polymer peak around 400 nm. That enables to evaluate the effectiveness of the process in removing the polymer. From the measurements, we can conclude that the polymer concentration is reduced by a factor of 2. Figure 3.9.b shows the comparative absorption

spectra for the initial solution and the solution obtained after the post-processing. The light blue curve represents the post-processed solution, illustrating that the concentration of s-SWCNTs is increased by a factor of ten.

As discussed before, the PL is an intrinsic characteristic only from s-SWCNTs. Therefore, PL measurements can not be determinant for estimating the purity of the s-SWCNTs solution. Raman spectroscopy is the most powerful tool to determinate the presence of m-SWCNTs. The two main characteristics of a Raman spectrum are signatures of radial breathing modes (RBM) at low frequencies and longitudinal modes (G- and G + band) at higher energies. The main property of RBMs is that their frequency is inversely proportional to the diameter of the nanotubes. The difficulty lies in the exact determination of the relationship, since this frequency is highly dependent on the mechanical and chemical environments of the nanotubes. Interestingly, by analyzing the diameter of the nanotube according to the energy of the excitation laser in the Kataura diagram (Fig. 3.10), the metallic or semiconductor characters of the SWCNT are easily recognized.

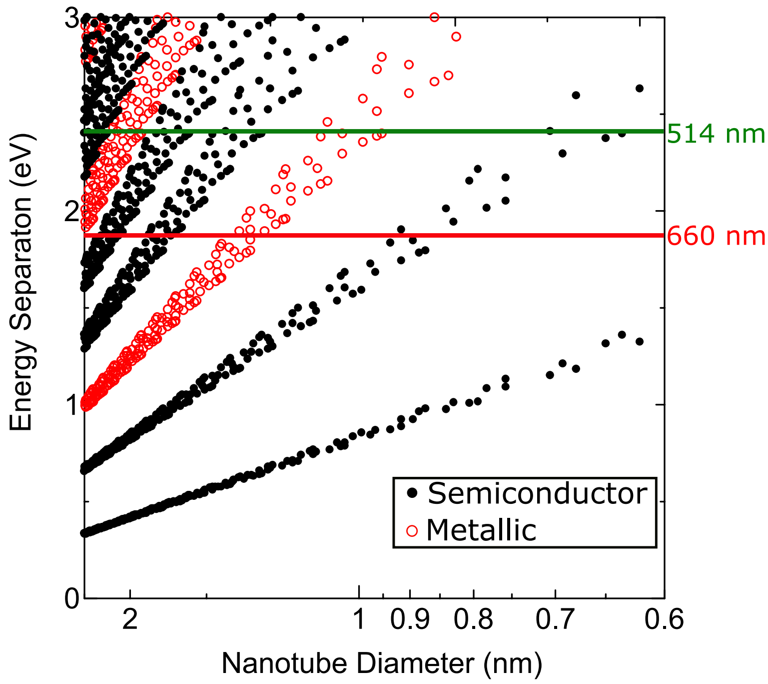

Figure 3.10.: Kataura plot extracted from [102].

The G band which is common to all sp^2 carbon form. In the case of carbon nanotubes, due to the curvature effect, multiples peaks appear in the G band

[103], doing G band a probe also for the tube diameter. In our case, due to the Raman peak for the polymer, superimposed to the G band range, the diameter analysis is done exclusively with the RBMs.

To know the quality of our solution we performed Raman spectroscopy in pristine SWCNTs HiPco powders and in the ultraconcentrated solution. The pristine powders have been deposited on a quartz substrate, while the ultraconcentrated solution has been deposited by dielectrophoresis on a quartz substrate with predefined electrodes. The Raman measurements have been performed by Dr. Arianna Filoramo and Dr. Marta Reig at CEA-Saclay. The Raman spectrum is recorded using a triple Raman spectrometer (T64000 Jobin-Yvon) at the excitation wavelength of 660 nm and 514 nm, enabling the observation of metallic and semiconducting SWCNTs.

Figure 3.11 shows the Raman shifts for the polymer alone, pristine and ultra-concentrated solutions, measured using excitation wavelengths of 660 nm and 514 nm. As shown in the inset of Fig. 3.11-d, the polymer presents a strong peak in the G-band. This signal may hide the signature of SWCNTs, hampering the analysis their nature using this range. Conversely, as presented in the inset of Fig. 3.11-c, the polymer exhibits no significant signal in the range between $140\,\mathrm{cm}^{-1}$ and $340\,\mathrm{cm}^{-1}$. Then, we focus on the analysis of the RBM of the SCWNTs. Using the empirical equation proposed in [103]:

$$\omega_{\mathrm{RBM}} = \frac{227}{d_t}\sqrt{1 + C_e d_t^2}, \tag{3.1}$$

the Raman shifts can be related to a SWCNT diameter. The Raman spectrum of the pristine solution presents a large variety of signals that correspond to semi-conducting and metallic SWCNTs with different diameters. Interestingly, the Raman spectrum for the ultra-concentrated solution only presents two peaks near $265\,\mathrm{cm}^{-1}$ and $290\,\mathrm{cm}^{-1}$ for excitation wavelength of 660 nm. From Fig.3.10 and Eq 3.1 these two peaks can be associated to semiconducting SWCNTs with a diameter of 0.85 nm and 0.78 nm, respectively. The same experiment was repeated at several positions in the sample with processed SWCNT solution. In all cases, only the signatures of s-SWCNT were found. The lack of any other Raman signals in this frequency range is a sound evidence of the absence of metallic SWCNT in the processed solution.

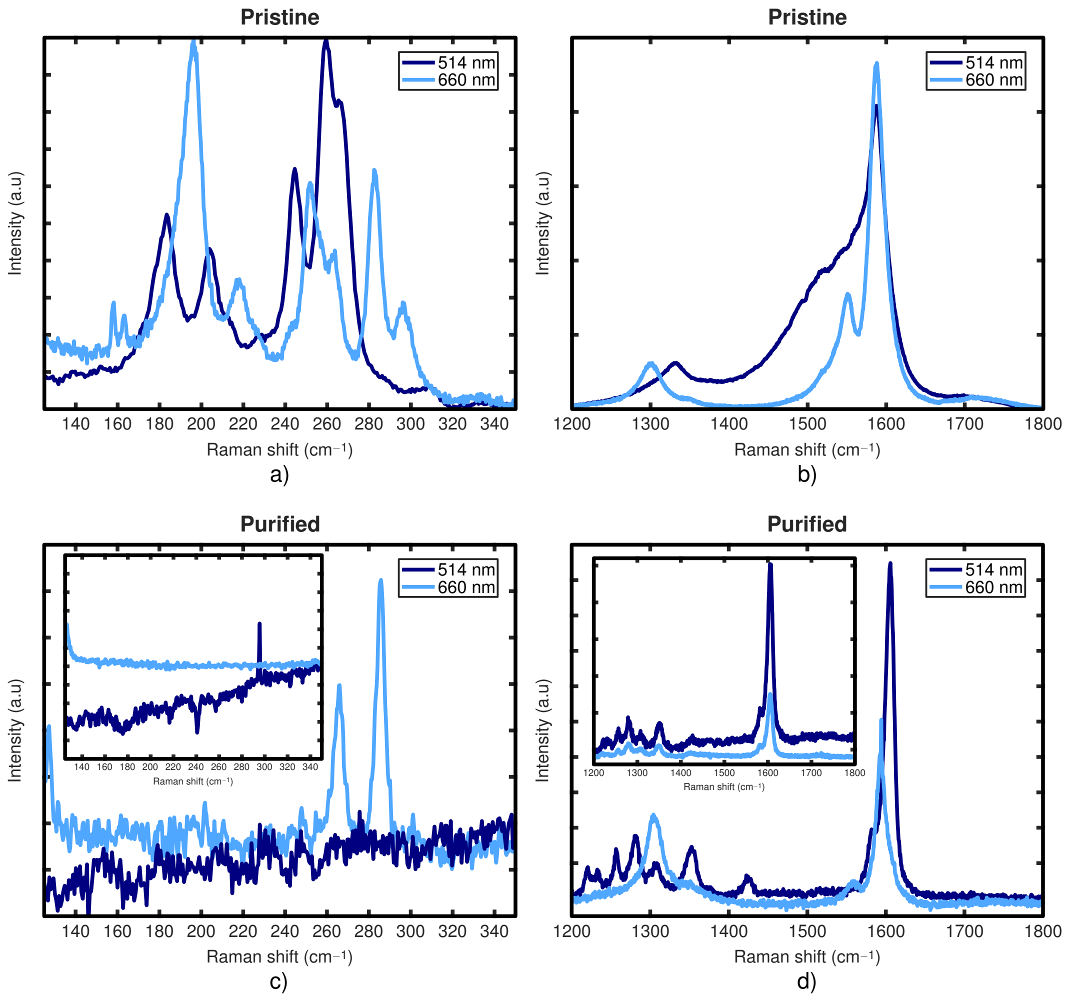

Figure 3.11.: Raman spectra for a pristine SWCNTs powder on a quartz substrate: a) RBM band and b) G band for excitation wavelength of 514 nm and 660 nm. Raman spectra for a ultraconcentrated solution deposited by dielectrophoresis on a quartz substrate: c) RBM band and d) G band for excitation wavelength of 514 nm and 660 nm. Inset: Raman spectra for a PFO solution at the same bands.

3.3. Conclusions

Figure 3.12 summarizes the PL spectrum of the three different s-SWCNTs solutions developed in this thesis. Each solution covers a different portion of the near-infrared spectrum, and has been optimized for a different purpose:

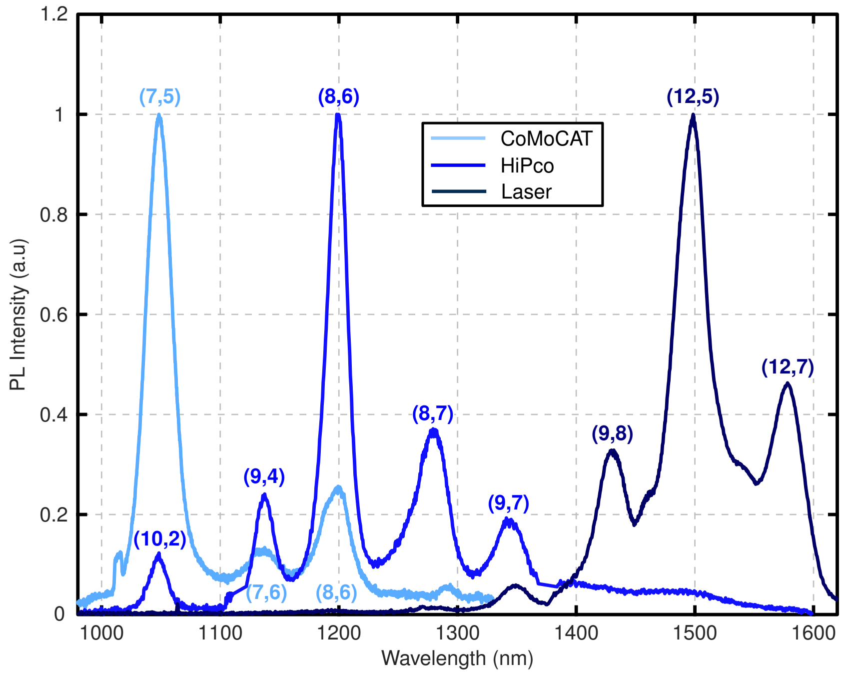

Figure 3.12.: Normalized photoluminescence spectra for: Laser ablation s-SWCNTs solution in dark blue, HiPco s-SWCNTs solution in blue and CoMoCAT s-SWCNTs solution in light blue.

- **HiPco Solution.** The largest effort of this thesis has been devoted to optimize this solution. The objective was to obtain a very highly concentrated solution of s-SWCNTs emitting in O-band of the telecomunication window (around 1,3 μm wavelength) with no trace of m-SWCNTs inducing unwanted absorption. This solution is conceived to work with spin coating or drop casting deposition on photonics structures. For this reason, the main parameter was the concentration of s-SWCNT. As it was explained in this chapter, several steps have been tested achieving as a result a solution free of m-SWCNTs where the concentration of s-SWCNTs has been doubled. To verify this important accomplishment PL and Raman measurements have been performed. Achieving a totally reproducible method. Within this work a post-processing method has been presented in which the concentration of s-SWCNTs has been improved by a factor of ten, with a reduction of the polymer concentration by a factor of two. Table 3.4 summarizes the parameters of the HiPco solutions that will be used in this work. Figure 3.13 shows the evolution of the concentration of HiPco carbon nanotubes achieved in this work. We have represented the absorbance for the predominant chirality, around 1200 nm wavelength, for the HiPco solution developed in this work. I began this work with solutions optimized in previous thesis works [29, 30], labeled as solution A and solution B. At the end of this thesis we have managed to increase the concentration by a factor of ~ 45. The optical results obtained with this solution will be presented in the following chapters.

Name	SWCNT (mg)	PFO (mg)	Toluene (ml)	WB (min)	Tip (min)	WB (min)	150000g (hours)	260000g (hours)
A	5	5	30	60	5	No	1	No
B*	5	20	30	60	15	No	1	No
C	5	20	30	60	15	10	1	No
D	5	20	30	60	30	10	1	No
E	5	20	30	60	30	10	1	4

Table 3.4.: Parameters for HiPco solutions developed in this work.

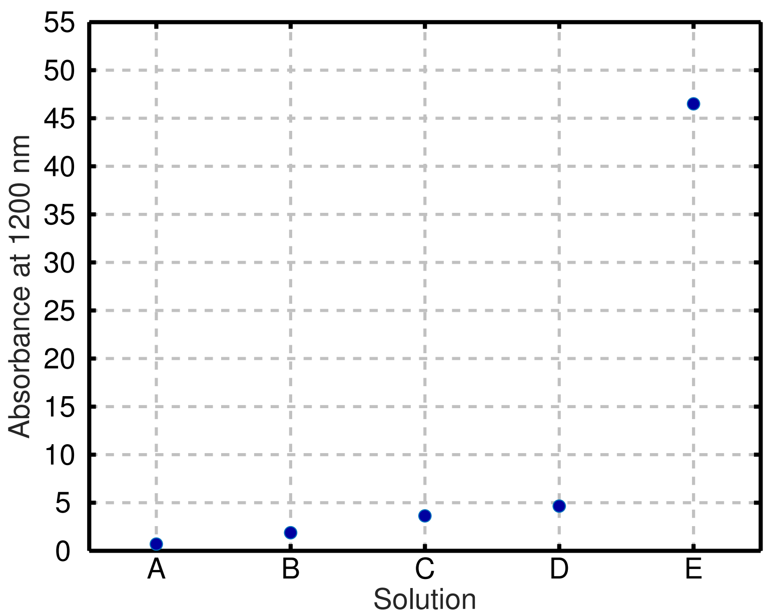

Figure 3.13.: Absorbance peak at 1200 nm (subtracting background) for each solution prepared in this work.

- **CoMoCAT Solution.** The objective was to obtain a single chirality solution for nonlinear optical characterizations. The objective was to determine the influence of s-SWCNTs chirality on the third order nonlinearities. These results are presented in chapter 7. For this s-SWCNTs solution we follow the same optimized process than for HiPco. We prepare a starting solution composed of 5 mg of CoMoCAT SWCNTs, 20 mg of PFO and 60 ml of toluene. This solution is mildly sonicated during 1 hour, followed by 30 minutes of tip sonication and 10 minutes of mild sonication. The resulting solution is ultracentrifugated during 1 hour at 150000 g. The supernatant solution is collected, forming the purified solution. As we can observe in Fig. 3.12, in light blue line, the main contribution at 1050 nm corresponds with the (7,5) chirality [96].

- **Laser Ablation Solution.** This solution has been optimized by Dr. Arianna Filoramo from CEA-Saclay. As it was mentioned at the beginning of the chapter, this solution must cover the C-band telecommunication window (around 1.55 μm wavelength). The main target of this solution is to implement electrically pumped source and detector. In the envisaged source, two metallic contacts are used to: i) aligned s-SWCNTs by DEP and ii) inject electrons and holes into the s-SWCNT. Hence, the main parameter is the s-SWCNTs length to make sure that all s-SWCNTs can be contacted by the metals. To prepare this solution we employed laser ablation SWCNT synthesized by Dr. Oliver Jost from Technische Universität (TU) in Dresden. SWCNTs are first dispersed in toluene with PFH-A, followed by 30 minutes of mild sonication and 15 minutes of ultracentrifugation at 150000 g [104]. The PL emission is represented in Fig. 3.12.

To conclude, we obtained a wide range of s-SWCNTs solutions emitting from 1 μm to 1.6 μm with high concentration of semiconducting SWCNTs and no trace of metallic SWCNTs. These solutions are very promising for photonics applications as I will show in the following chapters.

4

Hybrid integration with photonic structures

This chapter is dedicated to the analysis of different kinds of photonic ring resonators and cavities aiming to improve the light SWCNT interaction. With this goal, we study:

- **Waveguide geometry**. We analyzed the strip waveguide in TM polarization and the slot waveguide in TE polarization. Both structures have been widely used in photonics, especially in biosensing, that also requires high interaction between optical waveguide mode and the surrounding medium. A theoretical study and experimental results of the interaction of each topology with s-SWCNTs are carried out.

- **Polarization effect**. We analyzed the effect of the light polarization in strip waveguide in order to maximize absorption and emission from CNT.

- **Small mode volume cavities**. To further improve the light matter interaction we used small mode volume cavities. Their compact size and their high spontaneous emission coupling factor make them interesting as a low noise and low threshold lasers. In this work, we employed slot photonic crystal cavities which can enhance the light matter interaction through the combination of the resonant recirculation and slot confinement.

- **Collinear excitation**. With the purpose of maximizing the interaction between pump and s-SWCNTs we developed collinear excitation. Due to the pumping wavelength in the visible range, we used silicon nitride on insulator platform, where both excitation and PL are guided by the waveguide.

All the results shown in this chapter are obtained with solutions processed and optimized during this thesis work, following the process described in the chapter 3.

During the course of this chapter different strategies for the excitation and collection are used. We present results using excitation-collection on surface-surface (Fig. 4.1-a), surface-waveguide (Fig. 4.1-b) and waveguide-waveguide (Fig. 4.1-c) configurations. The choice of excitation scheme depends on the photonic platform and the employed solution.

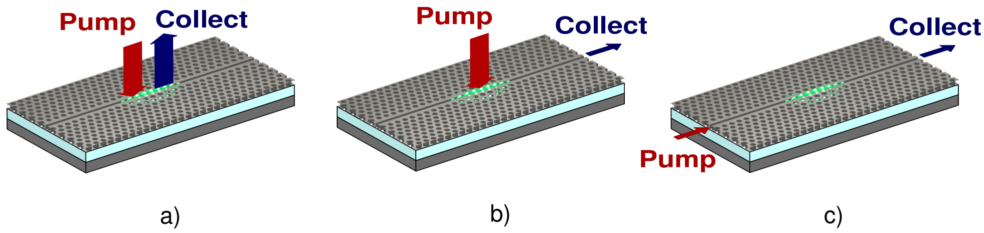

Figure 4.1.: Excitation-collection schemes: a) surface-surface, b) surface-waveguide and c) waveguide-waveguide.

This chapter is organized as follows. In the first section, the study of waveguide geometry is presented. The second section is dedicated to study the polarization effect. In this case, results on ring resonators are presented. The third section is dedicated to small mode volume cavities. Specifically, 2D slot photonic crystal cavities on SOI platform are discussed. To conclude this chapter, preliminary results using collinear excitation are shown. In this situation silicon nitride waveguides are considered, because optimum excitation wavelength for s-SWCNTs is situated in the silicon absorption region.

4.1. Waveguide geometry: strip vs slot ring resonators

In this section, a theoretical study about two different waveguide topologies is carried out. We analyzed the interaction of the optical mode propagating through strip and slot waveguides and the surrounding media where the s-SWCNTs are dispersed. Then, the fabrication process is presented. Finally, the experimental PL results using surface-surface strategy are discussed.

To favor the interaction between s-SWCNTs and optical modes, we have to study waveguides in order to maximize the overlap between optical mode field and the surrounding media (where the s-SWCNTs are deposited or dispersed) while minimizing the propagation losses. In this subsection we consider Si strip and slot waveguides exhibiting high interaction with the surrounding medium (Fig. 4.2) and low propagation loss [105].

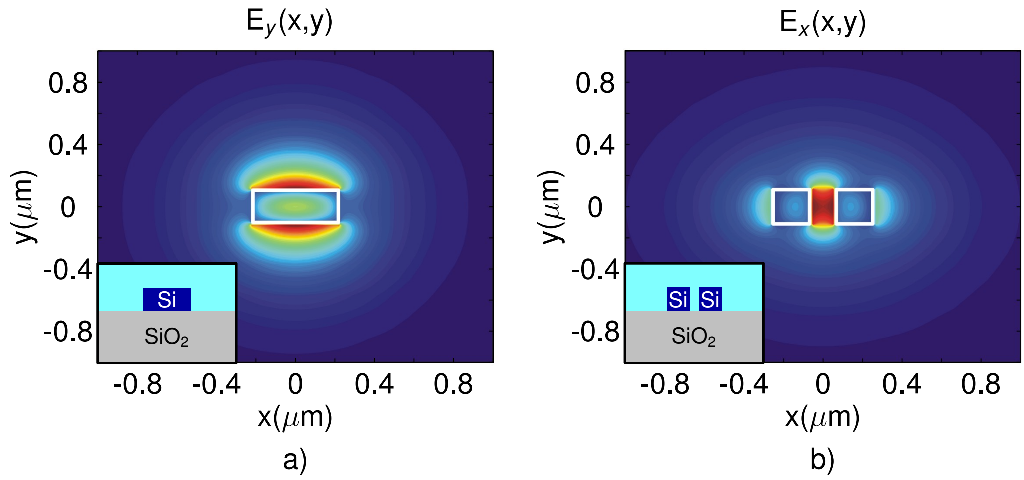

Figure 4.2.: Electric field distribution at a wavelength of 1300 nm for: a) TM mode (Electric field E_y) of strip waveguide and b) TE mode (Electric field E_x) of slot waveguide. Inset: schematic view of the simulated structures for strip a) and slot b).

We analyzed the modal properties of two silicon-on-insulator (SOI) optical waveguide configurations: strip waveguides operating with a transverse magnetic (TM) polarized light [106] and slot waveguides operating with a quasi-transverse electric (TE) polarized light [107]. For strip waveguide, TM mode has stronger evanescent field than TE mode. While, TE modes in slot waveguide yield stronger evanescent field than TM modes. This feature arises from the strong discontinuity of the normal component of the electric field at the interfaces between the silicon core and the surrounding medium. Hence, as shown in Fig. 4.2, the electric field of strip-TM mode (E_y) is confined inside the waveguide core with large intensity fields on the top and bottom boundaries. On the other hand, the electric field of slot-TE mode (E_x) funnels most of the field in the lower index material between the two silicon rails. This feature makes the slot an ideal geometry to sense the waveguide surroundings. In this subsection, we exploit this ability to maximize the interaction between the waveguide mode field and the s-SWCNTs.

This work began when the s-SWCNTs solution was not optimized yet. In this sample the solution A, presented in table 3.4 in page 42, was used. As it is explained in previous chapter, the HiPco solution is created to work in drop casting or spin coating deposition. A detailed explanation of these two techniques can be found in section 2.5. Remember that using the spin coating technique the s-SWCNTs results in layer in the order of a few nanometers. On the other hand, using the drop casting technique, the SWCNTs layer is in the order of a few micrometers. We consider these thickness to analyze the interaction with the optical mode of the two proposed types of waveguides.

To theoretically compare the interaction capability of the strip and slot waveguides, we have considered two different simplified scenarios that model these two different deposition techniques. First, we have considered a bulk scenario, depicted in Fig. 4.3-a, where we assumed that the waveguide is surrounded by a thick (semi-infinite) layer of s-SWCNTs solution, corresponding to drop casting deposition configuration. On the other hand, we have also analyzed a surface scenario described in Fig. 4.3-b, being the waveguide covered with a thin ($t_{SWCNT} = 10$ nm) s-SWCNTs layer that assessed the spin coating deposition configuration. The solution of s-SWCNTs is considered as a polymer solution doped with nanotubes. Hence, we model the deposited polymer-wrapped s-SWCNTs as a homogeneous medium with refractive index of 1.6 similar to that of the polymer [108].

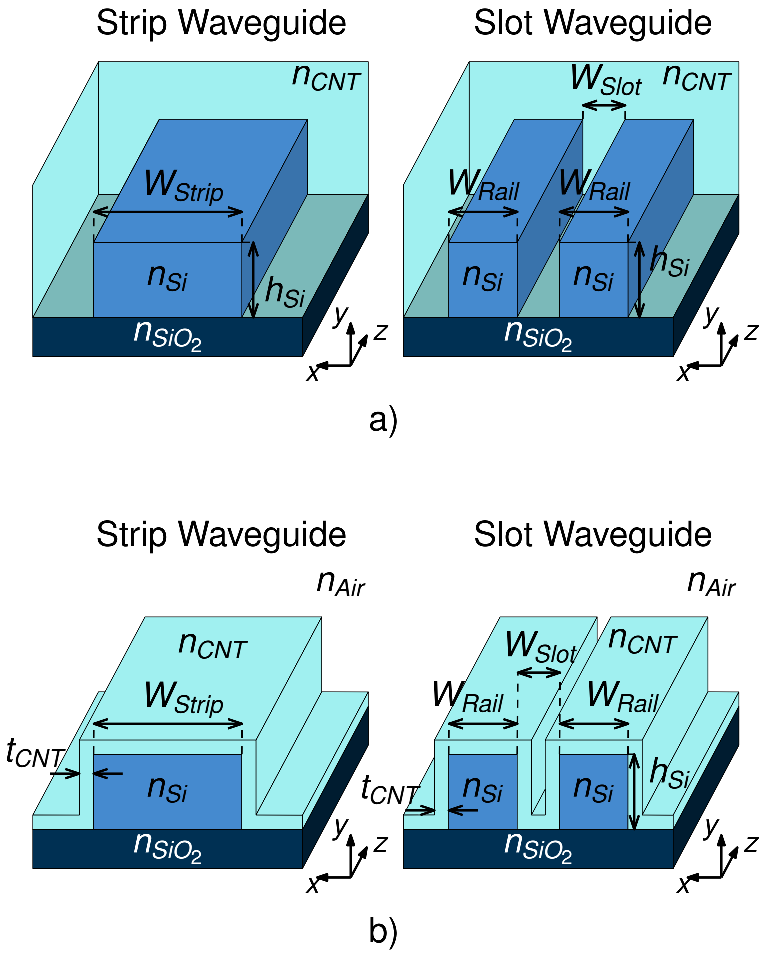

Figure 4.3.: Schematic views of strip and slot waveguides in: a) bulk scenario, corresponding to drop casting s-SWCNTs deposition and b) surface scenario, corresponding to spin coating s-SWCNTs deposition.

As a figure of merit to compare the interaction with s-SWCNTs, the sensitivity parameter, typically used in photonic biosensors [106], is calculated. As performed in previous works [109], we defined bulk and surface sensitivities, respectively, corresponding to the two considered bulk and surface scenarios. Bulk sensitivity in equation 4.1, measures the change in the effective index of the guided mode (n_{eff}) upon a change in the refractive index of the cover layer (n_{SWCNT}). Surface sensing (S_s) in equation 4.2, relates the effective index change of the guided mode (n_{eff}) to an increase in the thickness of the surrounding material (t_{SWCNT}).

$$S_B = \frac{\partial n_{eff}}{\partial n_{SWCNT}} \left[RIU/RIU \right], \tag{4.1}$$

$$S_S = \frac{\partial n_{eff}}{\partial t_{SWCNT}} \left[RIU/nm \right], \tag{4.2}$$

where ∂n_{eff} is the variation in the effective index of the waveguide mode produced either by a modification of the refractive index of the surrounding media (∂n_{SWCNT} in bulk scenario) or a change in the thickness of the waveguide covering layer (∂t_{SWCNT} in surface scenario). High sensitivities are directly related to strong interaction with the surrounding media [106, 109], which in this case corresponds to the s-SWCNT-rich layer. Analyzed strip and slot waveguides are implemented on SOI platform with 220 nm thick Si, widely used in state-of-the-art Si photonics. The two previously mentioned sensitivities have been calculated as a function of the main geometrical parameters of the strip and slot waveguides (described in Fig. 4.3). Strip sensitivity is analyzed as a function of the waveguide width (W_{Strip}). For simplicity, in the case of slot waveguides, we have represented slot sensitivity as a function of slot width (W_{Slot}) for rail widths of W_{Rail}= 200 nm and W_{Rail}= 250 nm that maximize sensitivity at the bulk and surface scenarios, respectively. Wavelength of 1300 nm is chosen for this analysis as it corresponds to the maximum photoluminescence (PL) peak wavelength from HiPco/PFO nanotubes (see in chapter 3, Fig. 3.12 page 41). For drop casting deposition of s-SWCNTs (bulk scenario in Fig. 4.4-a), slot waveguide sensitivity reaches a plateau around W_{Slot}= 80 nm, while strip waveguide sensitivity increases for thinner waveguides. Minimum strip width (and thus maximum sensitivity in this case) is limited by the light leakage towards the substrate due to the mode deconfinement with the reduction of W_{strip}. For drop-casting deposition, slot waveguide sensitivity is inversely proportional to the slot width, being the maximum achievable value limited by the minimum feature size that can be faithfully fabricated. Nevertheless, in all studied cases slot waveguides operating with TE polarized light exhibited larger sensitivity than strip waveguides with TM polarized light. This phenomenon can be qualitatively understood looking at the strip and slot mode field distribution (Fig. 4.2). Indeed, the optical mode in the slot waveguide is much more localized outside silicon (i.e. in the SWCNT-rich layer), while for strip waveguides, the mode is more confined inside the silicon core. These results indicate that the slot waveguide can provide larger field overlap with the SWCNT-rich layer.

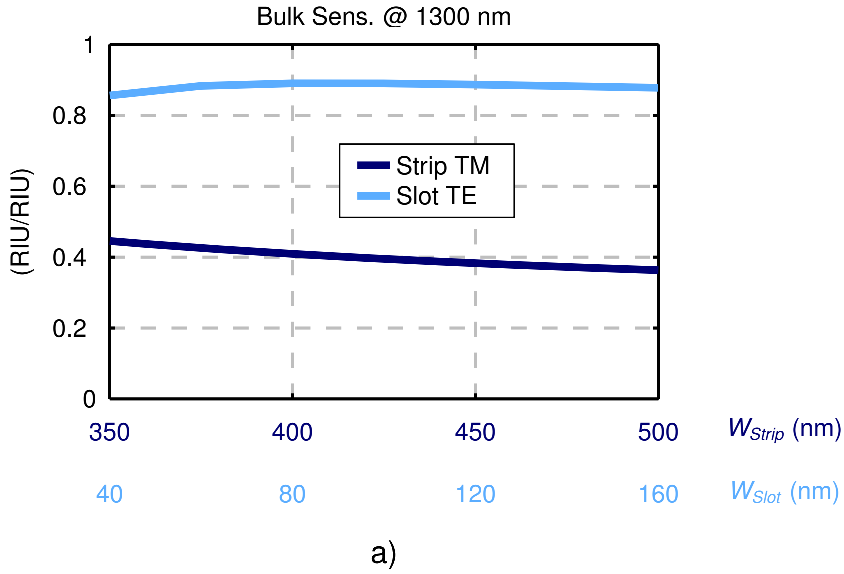

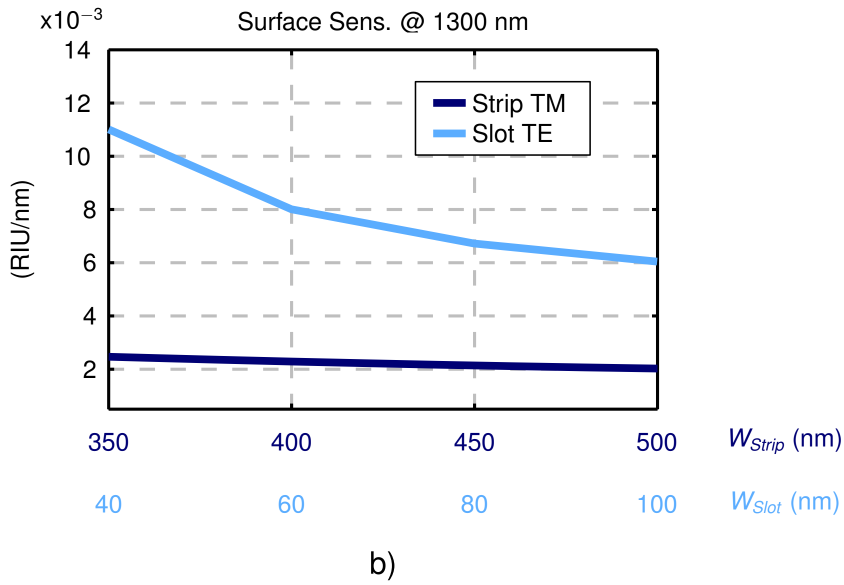

Figure 4.4.: Calculated sensitivity at the wavelength of 1300 nm for strip and slot waveguides in a) bulk scenario (drop casting SWCNTs deposition) and b) surface scenario (spin coating SWCNTs deposition).

This field overlap is a key parameter to achieve resonant enhancement of SW-CNT photo-luminescence (PL) in micro-ring resonators. It is tightly related to the overlap between the s-SWCNTs layer and the waveguide propagation loss [110, 111]. Larger s-SWCNTs-mode overlap and lower propagation losses yield improved resonant enhancement. Hence, to experimentally compare the ability of both strip and slot waveguides to effectively interact with s-SWCNTs, micro-ring resonators have been fabricated to compare their PL resonance enhancements.

Strip and slot ring resonators with a radius of 5 μm (to ensure a free-spectral-range discernible with our spectrometer) have been fabricated. The strip width of 350 nm has been chosen to ensure the maximum sensitivity, as it is shown in Fig. 4.4-a and -b. For the slot waveguide we changed the slot size between 100 nm and 200 nm with a fixed rail width of 280 nm. The ring resonators have been fabricated in the platform of Micro-Nano-Technology/C2N. SOI wafers with 220 nm thick silicon film and 2 μm of buried silica layer are used. Electron beam lithography (Nanobeam NB-4 system, 80 kV) is used to define the micro-rings employing positive resist (ZEP 520-A). A dry etching process with an inductively coupled plasma etcher (SF_6 and C_4F_8 gases) transferred the patterns in the top Si layer. Following, a dry oxidation process was adopted at 1000° C for 30 minutes to form a $\sim$ 10 nm thick silica surrounding silicon rails. The deoxidation process is performed by dipping the sample for 7 s in a 3% HF acid solution at 25 ° C in order to smooth the sidewall roughness of the waveguide. In Fig. 4.5, a scanning electron microscope (SEM) images shows transversal geometry of a slot waveguide (Fig. 4.5-a). Figure 4.5-b presents the SEM of a slot micro-ring resonator. For fabrication convenience all the structures have a concentric Si micro-disk of 2 μm with the micro-ring.

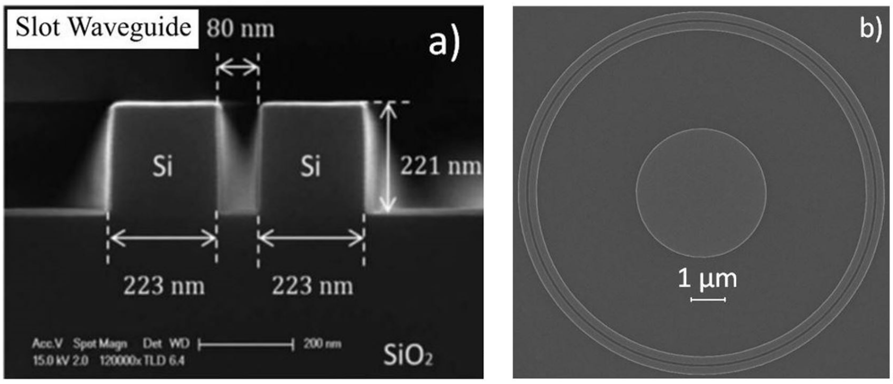

Figure 4.5.: Scanning electron microscope (SEM) image of: a) transversal geometry of a slot waveguide and b) top view of a slot waveguide ring.

Being a solution of s-SWCNTs with very low concentration we can consider it as a polymer solution with a few s-SWCNTs inside. For this reason it is necessary that the nanotubes present in the solution are as close as possible to the waveguide, maximizing the interaction between the s-SWCNTs and the optical mode. So, the preferred deposition technique is the spin coating, resulting in a deposited layer of few nm thickness, thereby ensuring the interaction of all s-SWCNTs with the optical mode. Semiconducting SWCNTs layers are deposited by spin coating at 1000 rpm during 60 s, finishing by a thermal annealing of 15 minutes at 180 $^\circ$C. Due to this the spin coating process is repeated 3 times to improve the thickness of the layer. This deposition technique was developed by A. Noury, previous PhD student on this topic.

In Fig. 4.6-a a schematic view of the setup used to characterize the resonant enhancement of these structures is presented. A Titanium-Sapphire (Ti:Sa) laser, pumped by a continuous wave solid state laser, is used as pump source. The deposited s-SWCNTs are excited at a wavelength of 735 nm, in the middle of the S_{22} transition bands of (8,6) and (8,7), predominant chiralities in the HiPco solution. The optical power was 1 mW (measured just before of objective). The Ti:Sa excitation beam passes through a λ/2 waveplate followed by a polarizing beam-splitter cube that provides a continuous control of the input power. A second λ/2 waveplate controls the polarization on the sample followed by a low-pass wavelength filter to remove higher order harmonics of the laser. First, the optical pump is focused on the region of interest in the Si sample, using a 50x (NA 0.55) microscope objective. Then, the same microscope objective collects the s-SWCNT emission, directing it to a high-pass wavelength filter to remove the excitation beam, before entering to the spectrometer. The photoluminescence (PL) is recorded with a 320 mm spectrometer with a 950 lines/mm grating, using a nitrogen-cooled 512-pixel linear InGaAs array. The PL characterization is performed at room temperature.

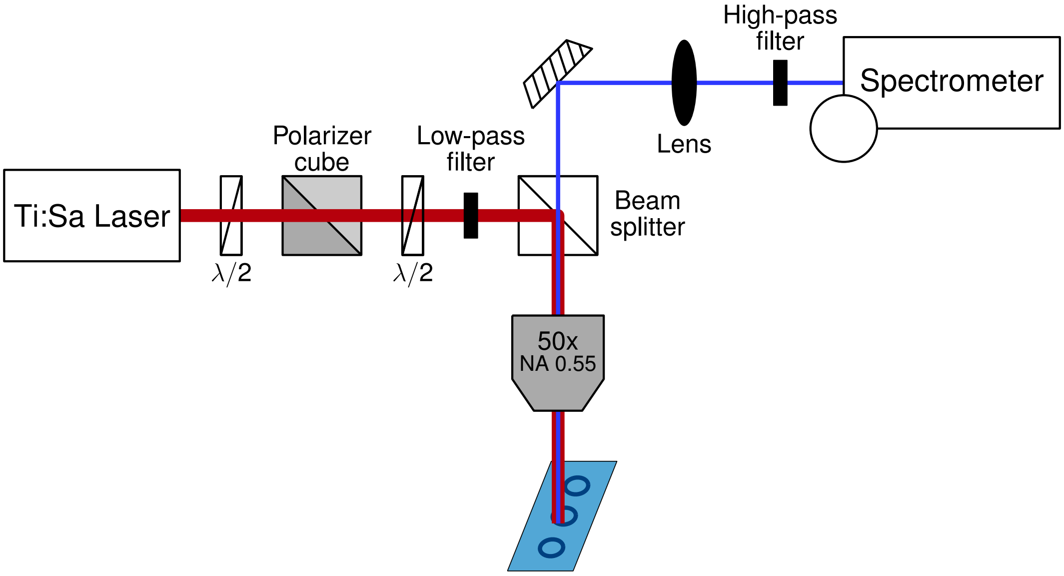

a)

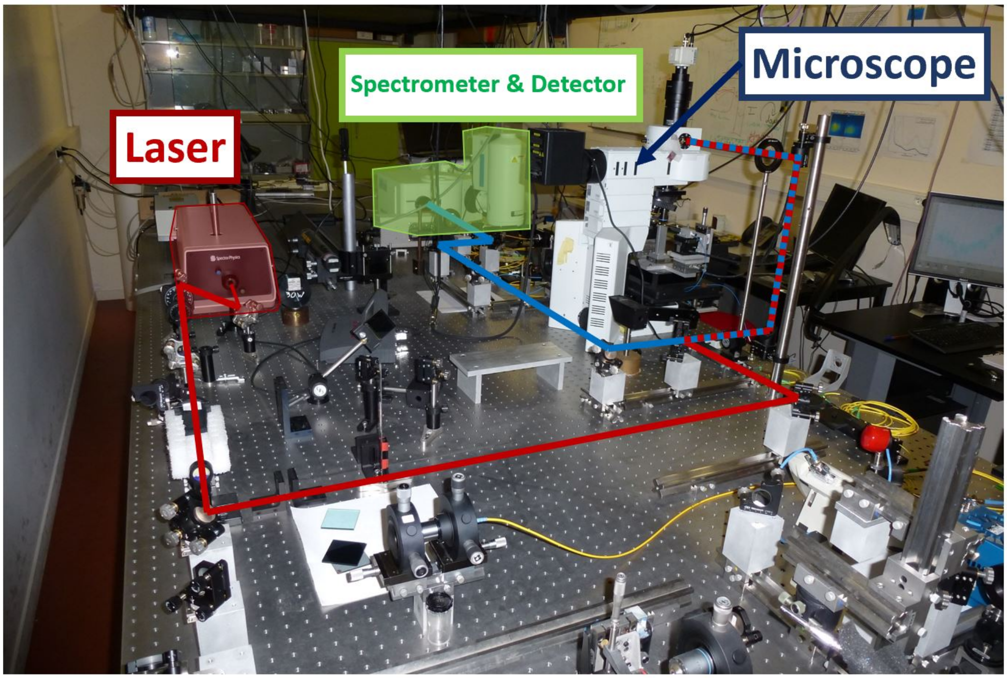

b)

Figure 4.6.: Photoluminescence setup in top-top configuration: a) schematic view and b) photography. This setup was built by N. Izard, A. Degiron and A. Noury.

Figure 4.7 presents the measured light emission from s-SWCNTs under the same experimental conditions in three different scenarios. The PL for an excitation outside of the ring area is presented in dark blue line. As we can observe two wide-band emission peaks occur around 1200 nm and 1280 nm wavelengths corresponding to the emission from s-SWCNTs with chiralities of (8,6) and (8,7), in good agreement with the results of the polymer-assisted selection technique. [60]. In blue line, the collected PL for a pump focused on top of the strip micro-ring resonator. A 350 nm wide strip waveguide is chosen because it presents the maximum sensitivity (Fig. 4.4). Narrow peaks appear superimposed onto the s-SWCNT′s emission. These peaks are induced by resonance inside the micro-ring [110]. Concurrently, a PL emission shift occurs around 1200 nm. It could be attributed to the non uniform deposition process that could produce different strain conditions shifting the SWCNTs emission [112]. Finally, in light blue line, we represent the measured PL when we focused the pump onto the slot micro-ring resonator under the same measurement conditions. Please notice here, that both, TE and TM, modes inside the ring resonators can be excited during optical pumping, resulting in two sets of resonance peaks. Interestingly, despite their larger propagation loss, slot ring resonators exhibit better resonant-enhancement peaks. This indicates that the improved interaction between s-SWCNTs and optical waveguide mode overcomes the additional loss.

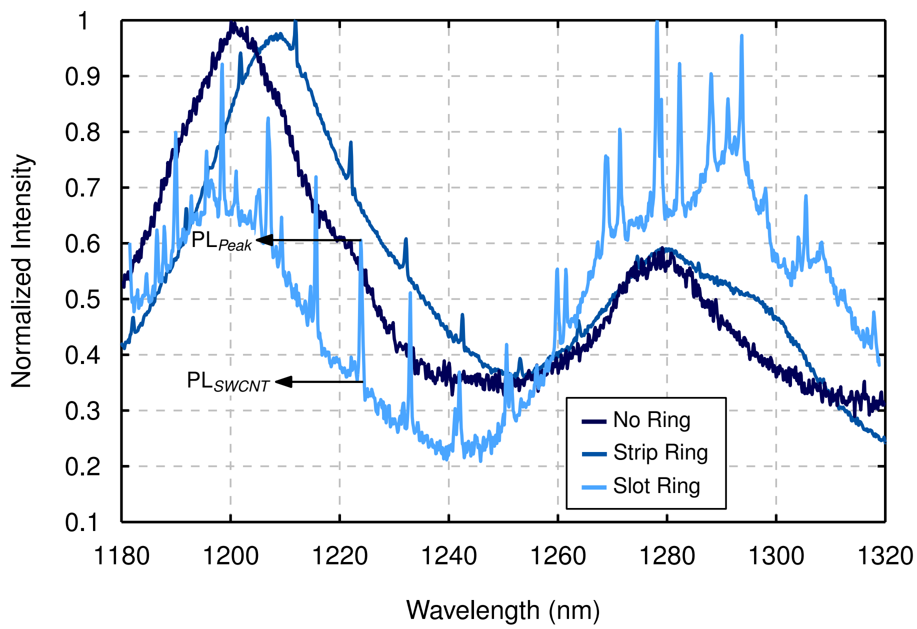

Figure 4.7.: Normalized photoluminescence intensity as a function of the wavelength when: excitation beam is focused onto un-patterned Si region (dark blue line), strip micro-ring (blue line) and slot micro-ring (light blue line). The pump wavelength is 735 nm.

In order to demonstrate the coupling of the s-SWCNTs with the photonic modes, three different PL spatial maps for a Si strip micro ring of 5 μm (reported in Fig. 4.8) have been performed. This part of the work has been possible thanks to the collaboration with the group of Dr. Massimo Gurioli in Florence University, Italy. The measurements presented here were carried out by Dr. Francesco Sarti in the framework of the European project CARTOON. The pump wavelength was 735 nm. The PL spectra with a spatial scan in a region of 9 μm x 10 μm at step of 200 nm is recorded from 1 μm to 1.4 μm wavelengths. Each spectrum is processed to obtain the different contributions. By fitting the s-SWCNTs emission at 1200 nm and 1300 nm by Lorentzians line-shapes we plot the integrated s-SWCNTs emission in Fig. 4.8-a. Bright spots in the map correspond to the regions where the s-SWCNTs are deposited, demonstrating non-uniform deposition of s-SWCNTs by spin-coating technique. We performed the same calculation over the resonant peaks onto the silicon PL emission around 1100 nm, represented in Fig. 4.8-b. We clearly distinguish the resonance peaks due to the ring and the internal disk. Finally, in Fig. 4.8-c, the resonance peaks over the s-SWCNTs PL emission at 1300 nm are shown. We clearly see that the enhanced s-SWCNTs PL emission is limited to the region where the deposited s-SWCNTs are overlapped to the silicon ring. Eventually, this proves the coupling between s-SWCNTs and the photonic modes of the silicon micro-ring resonator.

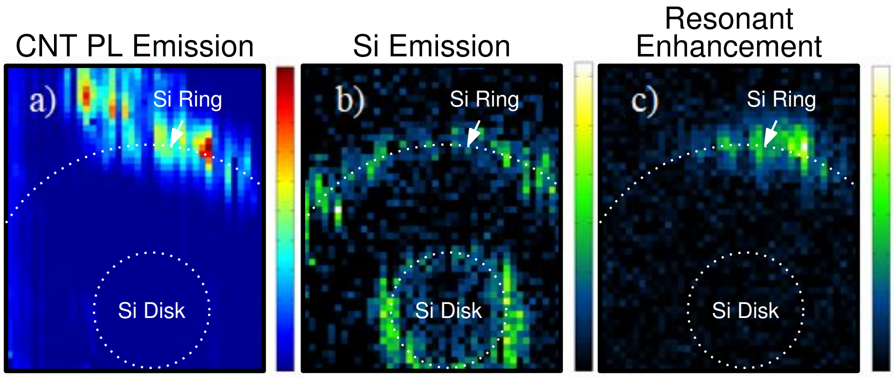

Figure 4.8.: Spatial maps of a Si strip micro-ring of 5 μm with an inner micro-disk of 2 μm. The pump wavelength was 735 nm. The maps are 9 μm $\times$ 10 μm in size. a) Spatial map of the integrated s-SWCNT PL signal from 1290 nm to 1310 nm. b) Spatial map of the enhanced silicon photoluminescence at 1150 nm. c) Spatial map of the enhanced s-SWCNT photoluminescence at 1300 nm.

To quantitatively compare strip and slot micro-rings, we define here the PL resonance enhancement factor (Γ) as the ratio between the peak PL at micro-ring resonance (PL_{Peak}) and the background PL from s-SWCNT emission (PL_{SWCNT}):

$$\Gamma = \frac{PL_{Peak}}{PL_{SWCNT}}. \tag{4.3}$$

Slot micro-ring resonators exhibited a resonance enhancement factor of $\Gamma \sim 1.8$ larger than the strip micro-rings factor ($\Gamma \sim 1.1$), proving an improved performance of slotted structures for the integration of s-SWCNTs on silicon. This result is in good agreement with the theoretical analysis previously presented, and can be explained by the fact that the light interaction in slot waveguides is stronger than in strip waveguides, overcoming the typically larger propagation loss.

Finally, Fig. 4.9 shows wavelength PL map of a typical fabricated slot micro-ring resonator as a function of the excitation wavelength. It is possible to distinguish the micro-ring resonance enhancement of the PL (sharp peaks along the emission wavelength) as well as the effect of excitation wavelength of the s-SWCNTs in and out of their absorption band, around 730 nm for (8,6) chirality with emission around 1200 nm.

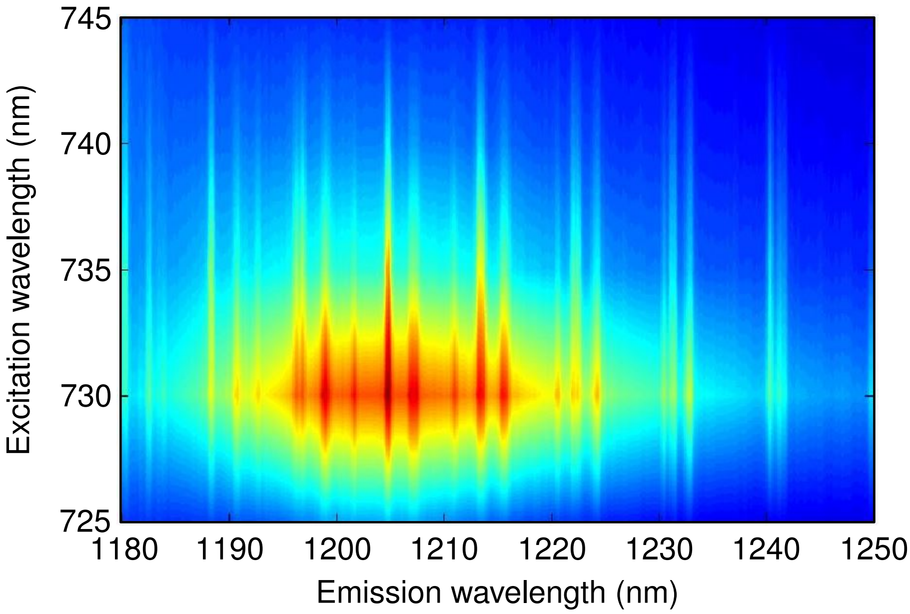

Figure 4.9.: Photoluminescence intensity of Si slot micro-ring resonator with 5 μm radius and 170 nm slot width as a function of the excitation and emission wavelengths.

In this part, two types of Si waveguides have been analyzed to improve the interaction between s-SWCNTs and optical resonators. We theoretically and experimentally analyzed and compared the ability of Si strip and slot waveguides to interact with s-SWCNTs deposited onto Si photonic chip. We have characterized the photoluminescence enhancement provided by Si strip and slot micro-rings fabricated on SOI platform. Slot micro-ring resonators showed an improvement of the resonance enhancement of 60 % in comparison with results from strip waveguide micro-resonators. Despite the advantages shown in this section, the fabrication of slot waveguides in standard pilot lines is technologically challenging. For this reason, in the following sections we focus on strip waveguide and study different strategies to maximize light-SWCNT interaction.

4.2. Polarization effect in strip silicon ring resonators

In this section the photoluminescence enhancement from ring resonators coupled to a silicon waveguide is presented.

Due to s-SWCNTs excitation wavelength of about 735 nm and the absorption of silicon at this wavelength, the surface-waveguide configuration is considered (see Fig. 4.1-b). Using the surface-waveguide configuration both spin-coating and drop casting deposition techniques can be used. First, design and characterization of ring resonators are presented. The resonators employed in this section were developed in the thesis work of Dr. Weiwei Zhang.

Interaction between s-SWCNTs and Si photonics waveguides is governed by the s-SWCNT geometry and the waveguide mode field distribution. The large aspect ratio of s-SWCNTs, with nanometer-scale diameters and micrometer-scale lengths, makes them behave like dipoles. This means that the maximum emission (and absorption) occurs for an electromagnetic field aligned to the long s-SWCNT axis [24, 113]. Therefore, Si waveguides aiming to efficiently interact with s-SWCNTs should support modes with a large evanescent field parallel to the s-SWCNTs. Conventional Si waveguides support quasi-transverse electric (TE) modes, with electric field (transversal to the light propagation) oriented parallel to the Si layer, and quasi-transverse magnetic (TM) modes, with transversal electric field perpendicular to the Si surface. Most of the s-SWCNT deposition methods (drop casting, spin coating, dielectrophoresis) result in networks of s-SWCNTs arranged along the Si surface (i.e. SWCNTs parallel to the surface). For this reason, previous works of the integration of SWCNTs in Si structures are based on the use of TE mode. We can find several demonstrations where s-SWCNTs have been efficiently coupled to the TE modes of conventional strip waveguides [114], slot [115] micro-ring resonators and strip [110] micro-ring resonators or 1-D [116] and 2-D [117] photonic crystal cavities. However, the main drawback of the TE modes is that most of the evanescent field is concentrated in the vertical waveguide walls (see Fig. 4.10-a), having a strong interaction with the sidewall roughness arising from the etching process, thus resulting in comparatively high propagation loss. Conversely, TM modes concentrate most of the evanescent field in the horizontal walls (see Fig. 4.10-b), thereby allowing lower propagation loss. In addition, for the same waveguide dimensions, e.g. 220 nm thick and 350 nm wide waveguide, TM modes are typically more delocalized, having a larger overlap with the surrounding medium. The problem is that optimizing the interaction between s-SWCNTs and the dominant component of the electric field in TM modes (perpendicular to the chip surface) would require placing the s-SWCNTs vertically on the waveguide top surface (see inset in Fig. 4.10-b). This ideal scenario, although possible, is technologically challenging and compromises the feasibility of the approach. In this part, the study of a new route to circumvent this limitation by exploiting the hybrid nature of the optical modes in SOI waveguides with sub-wavelength scale core dimensions is considered. The proposed approach exploits the longitudinal electric field component in TM modes to interact with SWCNTs aligned parallel to the chip surface, thereby obviating the need for technologically challenging vertical SWCNT deposition. Owing to the vast index difference between Si and SiO_2 and the ultra-tight confinement in 220-nm-thick SOI nanowires, (quasi-)TM modes can have a strong electric field component longitudinal to the light propagation. This longitudinal mode field component, parallel to the chip surface, can be advantageously exploited to interact with s-SWCNTs. Indeed, first by simulating, it is proved that TM modes can provide a longitudinal electric field on top of the Si waveguides (where the s-SWCNTs are placed), equal or even larger than the transverse electric field in TE modes. Then, a theoretical study of s-SWCNTs interaction with SOI micro-ring resonators is carried out. The strip waveguides is optimized to maximize the longitudinal TM component and to yield resonant-enhancement at specific wavelength ranges corresponding to either (8,6) or (8,7) s-SWCNT chiralities.

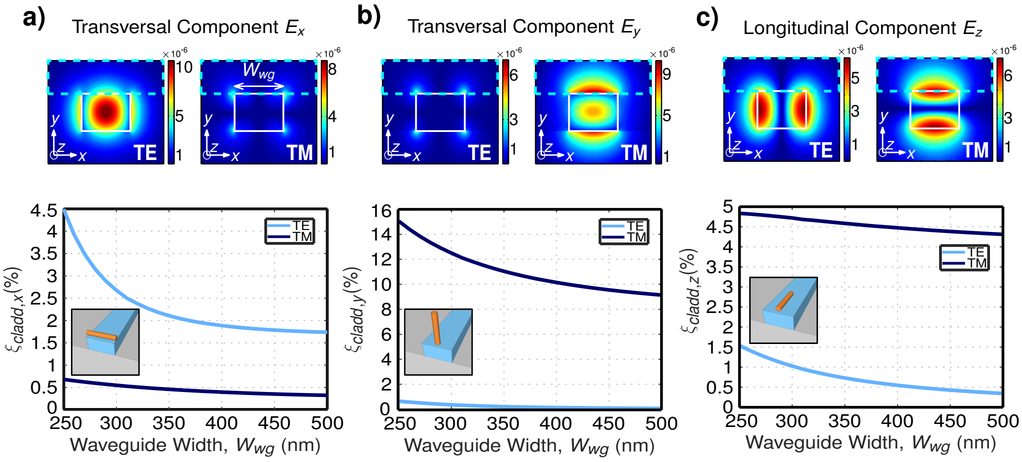

Figure 4.10.: Electric field distribution for waveguide width of W_{wg}= 350 nm, normalized to the total mode power, and figure of merit $\xi_{cladd,p}$ as a function of waveguide width for (a) transversal E_x, (b) transversal E_y and (c) longitudinal E_z components of both fundamental TE and TM modes at wavelength of 1300 nm. Insets schematically show preferred SWCNTs orientation for maximized light-SWCNTs interaction for each component of the electric field.

First, the waveguide cross section is optimized to maximize the longitudinal TM component, i.e. E_z component, on top of the waveguide. Following the conventional approach in hybrid Si photonics devices, we have calculated the dielectric energy confinement [118]. This parameter indicates the % of the mode confined in the active region. We defined the figure of merit $\xi_{cladd,p}$, which accounts for the percentage of the dielectric energy confinement on top of the Si waveguide (slashed region in Fig. 4.10). We calculated $\xi_{cladd,p}$ for each electric field component (E_p with $p = x, y, z$) for the E_x, E_y and E_z components respectively as

$$\xi_{cladd,p} = \frac{\int_{cladd} \varepsilon(\mathrm{x,y}) \left|E_p(\mathrm{x,y})\right|^2 \mathrm{dxdy}}{\int_{total} \varepsilon(\mathrm{x,y})[\left|E_x(\mathrm{x,y})\right|^2 + \left|E_y(\mathrm{x,y})\right|^2 + \left|E_z(\mathrm{x,y})\right|^2]\mathrm{dxdy}}, \quad (4.4)$$

where ε is the medium permittivity. As conventionally done when modeling these polymer-sorted SWCNTs [111, 115, 117], we considered an homogeneous top cladding with a refractive index of 1.6 (similar to that of polyfluorene [108]), which emulates the scenario of drop casting deposition. We fixed the Si waveguide thickness to 220 nm, and varied the waveguide width from 250 nm to 500 nm (W_{wg} in Fig. 4.10). Figure 4.10 shows the $\xi_{cladd,p}$, calculated with an eigenmode solver tool [119], as a function of the waveguide width for a wavelength of 1300 nm. The transversal E_y component from the TM mode has the largest figure of merit, $\xi_{cladd,y} \sim 12\%$. However, optimal interaction with the E_y field would require vertically aligned s-SWCNTs (see inset of Fig. 4.10-b), which makes this solution technologically challenging. Conversely, for both, transversal E_x and longitudinal E_z components, the preferred s-SWCNTs orientations are parallel to the chip surface (see inset of Figs. 4.10-a and 4.10-c), which makes them very interesting for scenarios relying on planar deposition techniques (drop casting and spin coating). According to the calculations, the figure of merit for the E_z component in the TM mode can be larger than that of E_x component in the TE mode, which is conventionally optimized for hybrid s-SWCNT integration. A waveguide width of W_{wg}= 350 nm is chosen, that presents a figure of merit of $\xi_{cladd,z} \geq 4.5\%$ (with $\xi_{cladd,x} \sim 0.5\%$ and $\xi_{cladd,y} \sim 12\%$), close to the maximum for TM mode with a total dielectric energy confinement in the cladding of $\sim 20\%$. Moreover, this waveguide width provides single-mode operation and good optical confinement that keep low losses and sharp bending. Electric field distributions for all components of TE and TM modes for the selected waveguide are shown in the top panels of Fig. 4.10.

Then we shaped up the TM response of micro-ring resonators implemented with the optimized waveguide. The goal was to yield a strong light matter interaction in a specific bandwidth, matching the emission range of a given s-SWCNT chirality. By adjusting the geometry of the micro-ring, it was then possible to tune the optimal resonant wavelength, releasing an extra degree of freedom to selectively promote light s-SWCNT interaction for either (8,6) or (8,7) s-SWCNT chirality present in the HiPco solution, with emission around 1200 nm and 1300 nm, respectively. As schematically depicted Fig. 4.11-a, we used an all-pass ring-resonator configuration where the ring resonator waveguide, with waveguide width of W_{ring}, was evanescently coupled to an access strip waveguide (width of W_{bus}), separated from the ring by a gap distance G.

The resonant behavior of a coupled micro-ring resonator is strongly dependent on the coupling between the ring and the bus waveguides. Light recirculation inside the ring (hence energy storage, and electric field enhancement) is maximal when coupling between the ring and the bus equals the loss inside the ring (critical coupling condition) [120]. Aiming to yield selective resonance enhancement of the s-SWCNT emission, we decided to implement an asymmetric coupling scheme. To do this, we set a bus waveguide width of W_{bus}= 270 nm and ring waveguide width of W_{ring}= 350 nm (providing strong $\xi_{cladd,z}$). As the bus and

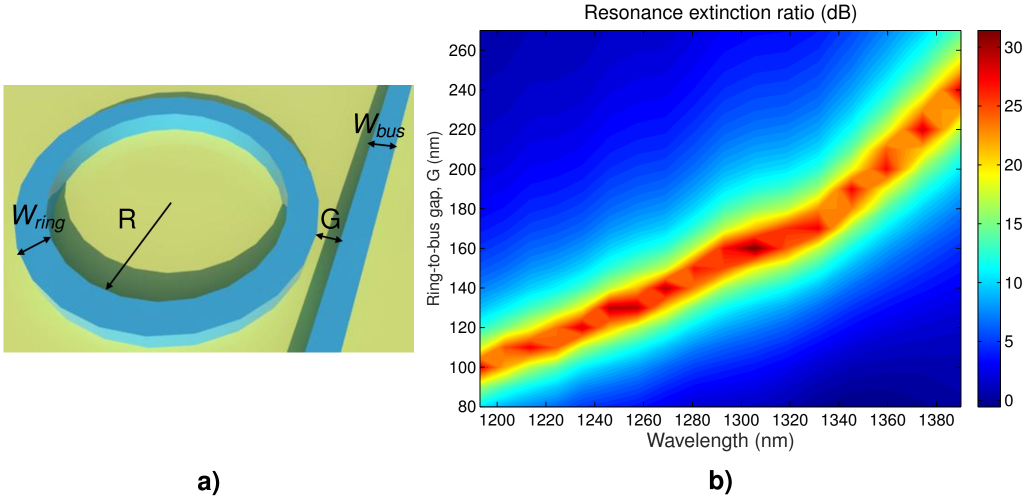

Figure 4.11.: a) Schematic view of micro-ring resonator with bus waveguide. b) Simulated resonant extinction ratio for TM modes, defined as the ratio between on-resonance and off-resonance transmission, considering G between 80 nm and 260 nm.

ring waveguides have different widths, modes propagating through them have different phase propagation constants, precluding perfect phase matching. This results in a lower power coupling between the waveguides and a shorter beat-length (distance for maximum power transfer between the waveguides). For the ring resonators used here, the coupling strength is directly proportional to the overlap between the modes of the bus and ring waveguides. The mode profile is more deconfined for longer wavelengths, resulting in larger overlaps, therefore stronger coupling. On the other hand, it can be shown that the bandwidth of the coupler is related to the beat-length dispersion [121]. Thus, this asymmetric configuration yields a strong chromatic dispersion of the bus-to-ring coupling ratio, i.e., for a given bus-to-ring gap (G), critical coupling condition is achieved for a comparatively narrow bandwidth. Hence, we can choose the wavelength range where resonant light recirculation (thus light-SWCNT interaction) is maximized just by properly choosing the gap G between the ring and the bus waveguide. We chose a ring radius of R= 5 μm, that yields a free spectral range (wavelength separation between consecutive resonances) of $\sim$12 nm, easily discernible with our spectrometer. Figure 4.11-b shows the resonance extinction ratio for TM modes, calculated with the finite difference time domain (FDTD) tool [119]. It can be seen that critical coupling condition (corresponding to deep resonances with extinction ratio greater than 30 dB) was achieved for narrow wavelength ranges of ~10 nm, with optimum range moving towards shorter wavelengths for decreasing gap widths.

The ring resonators are fabricated following the same fabrication process that the last example (section 4.1). Different ring resonators varying the bus-to-ring gap (G) between 80 nm and 270 nm have been fabricated. Tapered waveguides are used to inject/extract light through the chip facet, with a coupling loss of $\sim$ 10 dB. Propagation loss of the Si waveguides have been estimated in the 3-5 dB/cm. After the fabrication of the device, hydrogen silses-quioxane (HSQ) cladding, with refractive index of $\sim$1.45 and thickness of $\sim$800 nm, is deposited by spin coating and an additional lithography step is performed to form small circular aperture in the coupling regions between the micro-ring resonators and the bus waveguides. The HSQ cladding isolated the waveguide from the deposited s-SWCNTs everywhere except in the interaction windows where the s-SWCNTs interacts with the optical pump beam from Ti:Sa laser. Figure 3 shows an SEM image of the final device including the cladding of HSQ. It is possible to distinguish the interaction windows, which have a diameter of 3 μm, matching the size of the Ti:Sa excitation spot for pumping. This scheme ensured that all s-SWCNTs interacting with the Si micro-resonators are under the excitation illumination, minimizing extra losses arising from unwanted absorption from non-excited s-SWCNTs.

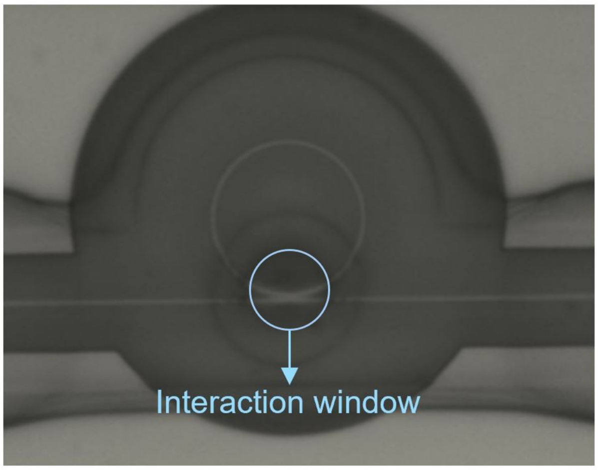

Figure 4.12.: SEM image of one of the fabricated ring with HSQ cladding. Interaction windows of 3 μm is clearly discernible in the coupling region between ring resonator and bus waveguide.

For this sample the solution E (see table 3.4 in page 42) was used. The deposition technique employed is drop casting followed by annealing at 180°C during 20 minutes.

After the s-SWCNTs deposition the linear response of the micro-ring resonators is characterized by injecting the light from a tunable Yenista laser source (1260 nm - 1350 nm wavelength). Because of the limited range of our tunable source it is not possible to inspect the region around 1200 nm wavelength, corresponding to the emission of (8,6) chirality present in HiPco s-SWCNT solution. The transmitted signal is collected with polarization maintaining lensed fiber through output tapered waveguides at the chip facets. The response of the devices is collected using an automatic data acquisition system, CT400 from Yenista. Polarization of the light injected into the chip is controlled with a polarization rotator and a polarizer at the input. As schematically is depicted in Fig. 4.13.

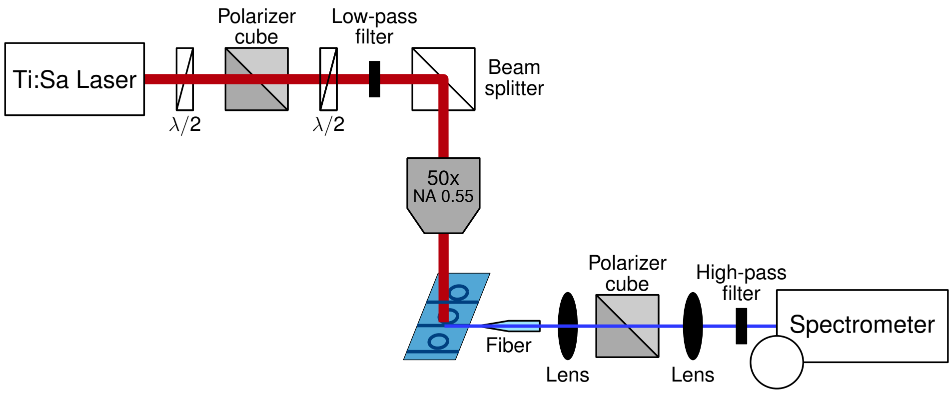

Figure 4.13.: Schematic view of photoluminescence setup in top-waveguide configuration.

Figure 4.14-b shows the measured resonance extinction ratio in our micro-rings with drop-casted s-SWCNT, as a function of the wavelength for different bus-to-ring gaps. The optimum wavelength range shifts to shorter wavelengths for decreasing gaps. Results in Fig. 4.14 show that the critical coupling condition is met for a narrow wavelength range, with optimum wavelength that increases with the gap, in good agreement with our calculations. The ring resonators with s-SWCNTs yield quality factors for TM modes of $Q \sim 4000$ and extinction ratio of ~ 10 dB at around 1300 nm wavelength for a bus-to-ring gap between 200 nm and 250 nm. On the other hand, the best quality factor for TE polarization is around $Q \sim 4000$, with a gap of 100 nm. The difference with calculated values shown in Fig. 4.11, can be attributed to scattering losses due to sidewall

roughness and absorption in the s-SWCNT, not considered in the simulations. Similar ring resonators without s-SWCNT typically yield quality factor, Q, up to 10000. The small interaction window, of 1.5μm radius used for the deposition of SWCNTs did not induce excess loss to the ring transmission. However, the perturbation produced by the presence of the s-SWCNTs (mainly due to absorption loss) is enough to reduce the quality factor of the resonances.

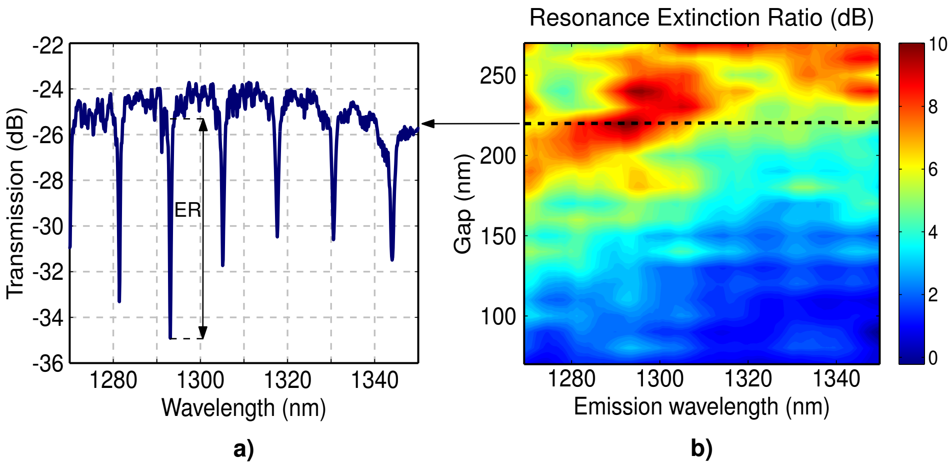

Figure 4.14.: Measured linear spectral response for TM mode of Si micro-ring resonators with bus waveguide width of W_{bus}= 270 nm, ring waveguide width of W_{ring}= 350 nm, ring radius of R= 5 μm for (a) fixed bus-to-ring gap of G= 220 nm, and (b) bus-to-ring gap varying between 80 nm and 270 nm. Dashed line indicates position of spectrum for gap G= 220 nm, shown in (a).

From this linear characterization, the resonant enhancement of the s-SWCNTs photoluminescence in the ring resonators can be studied. For comparison, Fig. 4.15-b shows the normalized photoluminescence of the s-SWCNTs solution deposited onto an unpatterned SOI sample under pumping excitation at wavelength of 735 nm with a surface-surface configuration (Fig. 4.15-a). As already reported, the s-SWCNTs emission presented two wideband emission regions around 1200 nm and 1300 nm wavelengths corresponding to the two main s-SWCNT chiralities available in the sample, (8,6) and (8,7), respectively. The characterization of the photoluminescence response of the Si micro-ring resonators is performed by pumping the s-SWCNTs layer from the surface, focusing the light coming from a Ti:Sa laser with an objective. We used an objective microscope with a magnification of 50x and numerical aperture (NA) of 0.55 that generated an excitation beam with an estimated beam waist of ~3 μm. We collected the generated photoluminescence at the facet of the chip using a polarization-maintaining lensed fiber and polarization splitter to discern contribution from TE and TM modes. An schematic view of the set-up is depicted in Fig. 4.13. We compared the photoluminescence spectrum of a micro-ring resonator with gap of $G = 250$ nm, in the optimal photoluminescence enhancement region for 1300 nm wavelength, when the polarization of the excitation beam is aligned with the transversal component (perpendicular to the waveguide) or longitudinal E_z component (aligned along the waveguide) as it is represented in Fig. 4.15-c. As shown in Fig. 4.15-d, tuning the pump beam polarization from transversal (E_x) to longitudinal (E_z) components, it is possible to favor the excitation of the TM modes in the ring. These results are in good agreement with near-field scanning experiments that exploited a similar effect to image TM modes in Si micro-ring resonators [122]. In the following experiments we kept the pump beam aligned with the longitudinal E_z component.

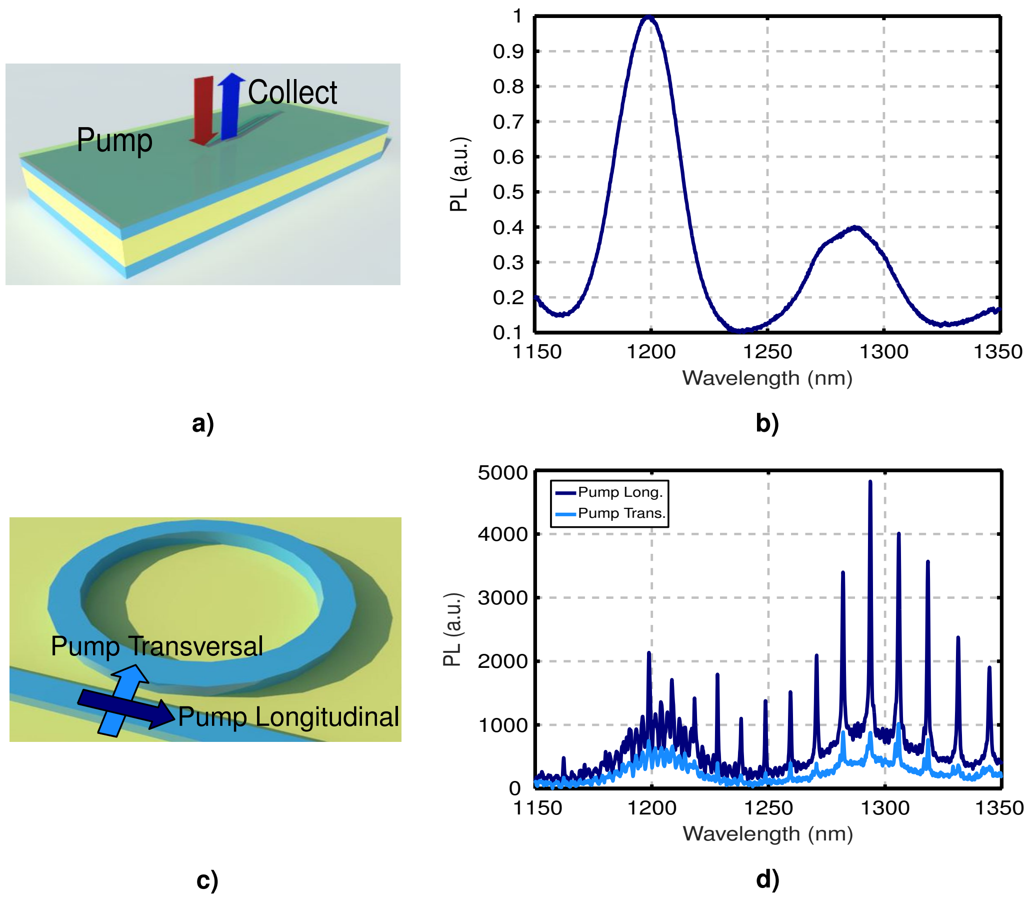

Figure 4.15.: (a) Schematic view unpatterned SOI sample with a scheme of excitation of SWCNTs and collection of the PL from the surface. (b) Normalized photoluminescence signal of SWCNTs solution drop casted on unpatterned SOI sample. Excitation wavelength of 735 nm with vertical excitation/collection. (c) Schematic view of ring resonator coupled to a bus waveguide with both polarization schemes for the pump laser: transversal (aligned with the E_x component) and longitudinal (parallel to E_z component). (d) Photoluminescence spectrum for a ring resonator of radius R= 5 μm and bus-to-ring gap G= 250 nm. The excitation is performed from the chip surface with a wavelength of 735 nm and the generated photoluminescence signal coupled to bus waveguide is collected from the chip facet. Collected photoluminescence signal when pump laser is transversal and longitudinal with respect to the propagation axis are represented in light blue and dark blue lines, respectively.

In Fig. 4.16-a we plot the upper envelope of the photoluminescence signal collected at the output bus waveguide for different gaps between the ring and the bus waveguides. As each of the rings has slightly different resonant wavelengths (mainly arising from small fabrication variations), we have reported the upper envelope to remove this spurious effect, yielding smoother plots that make the gap effect clearer. In Figs. 4.16-b and c we show two examples of measured spectra and calculated upper envelope. From Fig. 4.16-a, it is apparent that, as expected from the micro-ring design, smaller gaps yield stronger photoluminescence signal from (8,6) s-SWCNTs, while larger gaps promote emission coupling from (8,7) chirality. Note here that the photoluminescence signal around 1250 nm wavelength is weak, compared to 1200 nm and 1290 nm wavelength where (8,6) and (8,7) chiralities emit. Thus, it is not possible to clearly see the smooth resonant wavelength shift predicted by simulations in Fig. 4.11.

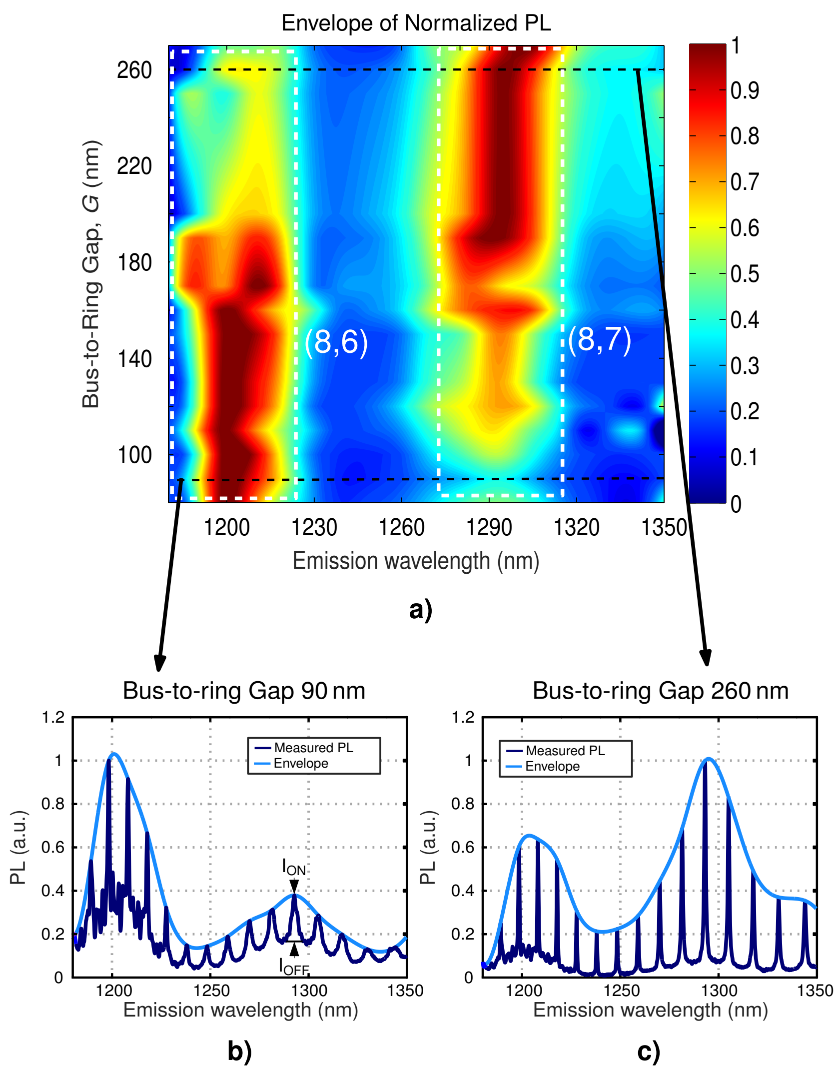

Figure 4.16.: (a) Normalized photoluminescence spectrum of SWCNTs deposited on Si micro-ring resonators with bus waveguide width of $W_{bus} = 270$ nm, ring waveguide width of $W_{ring} = 350$ nm, ring radius of $R = 5\ \mu$m, and bus-to-ring gap, G varying between 80 nm and 270 nm. SWCNTs are excited at 735 nm wavelength from the chip surface using a microscope objective and the generated PL is collected from the chip facet with polarization maintaining lensed fiber. Detail of collected PL for (b) G = 90 nm, and (c) G = 260 nm.

To compare the photoluminescence resonant enhancement for both (8,6) and

(8,7) chiralities, we have defined the resonance enhancement factor, α, as the ratio between on-resonance (I_{ON}) and off-resonance (I_{OFF}) intensities, as

$$\alpha = \frac{I_{ON}}{I_{OFF}}. \tag{4.5}$$

We computed this factor for wavelengths around 1200 nm, $\alpha(1200)$, and 1290 nm, $\alpha(1290)$. Then we defined the figure of merit, γ, as the ratio between the resonance enhancement factors for this two wavelengths:

$$\gamma = 10 \log \left(\frac{\alpha(1290)}{\alpha(1200)} \right). \tag{4.6}$$

In Fig. 4.17 we display the figure of merit γ, estimated from measurements, as a function of the bus-to-ring gap. Gaps bellow 150 nm favor resonance enhancement of s-SWCNTs with (8,6) chirality ($\gamma < 0$), with emission around 1200 nm wavelength, while larger gaps (above 150 nm) promote the resonant enhancement of s-SWCNTs with (8,7) chirality ($\gamma > 0$), with emission around 1300 nm wavelength. Furthermore, we can observe in Fig. 4.17 how the maximum enhancement smoothly shifts towards longer wavelengths as the gap increases, in good agreement with calculations shown in Fig. 4.11.

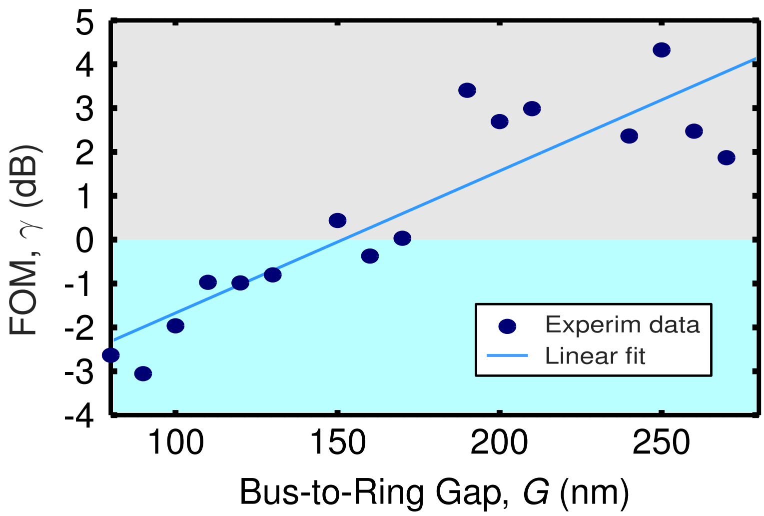

Figure 4.17.: Figure of merit estimated from measurements.

For all the measurements presented until now, the interaction window has been placed in the coupler between bus waveguide and ring resonator (as shown Fig. 4.12). In this situation the PL emission collected at the facet is from: i) PL emission directly coupled to the bus waveguide (I_{OFF} in Fig. 4.16-a) and ii) the PL emission coupled to the ring resonator (I_{ON} in Fig. 4.16-a), sum of all PL photons looping inside of the ring resonator. This configuration allows to establish the resonant enhancement factor α (equation 4.5) to analyze the resonance enhancement as a function of the wavelength.

To further exploit the comb light emission in s-SWCNTs integrated in ring resonators, it would be interesting to reduce the level of the off-resonant signal. To do so, we place the interaction window within the ring (see inset Fig. 4.18-b). In Fig. 4.18 the normalized PL emission for both configurations is represented. Figure 4.18-a reports the PL resonant enhancement when the interaction window is on the coupler region and Fig. 4.18-b presents the results when the interaction window is on the ring. In both cases, strip ring resonator with G = 250 nm have been chosen. When the interaction window is on the coupler (Fig. 4.18-a and Fig. 4.18-c), we can observe a strong background signal, corresponding with the PL emission that is directly coupled to the bus waveguide. Achieving a maximum extinction ratio of $\sim$7 dB (see Fig. 4.18-c). On the other hand, when the interaction window is on the ring (Fig. 4.18-b and Fig. 4.18-d), we observe a drastic reduction of the background signal, improving the extinction ratio by up to $\sim$18 dB as it is represented in Fig. 4.18-d.

We have demonstrated that by localizing the interaction region between s-SWCNTs and photonics structures we can improve the extinction ratio in $\sim$11 dB.

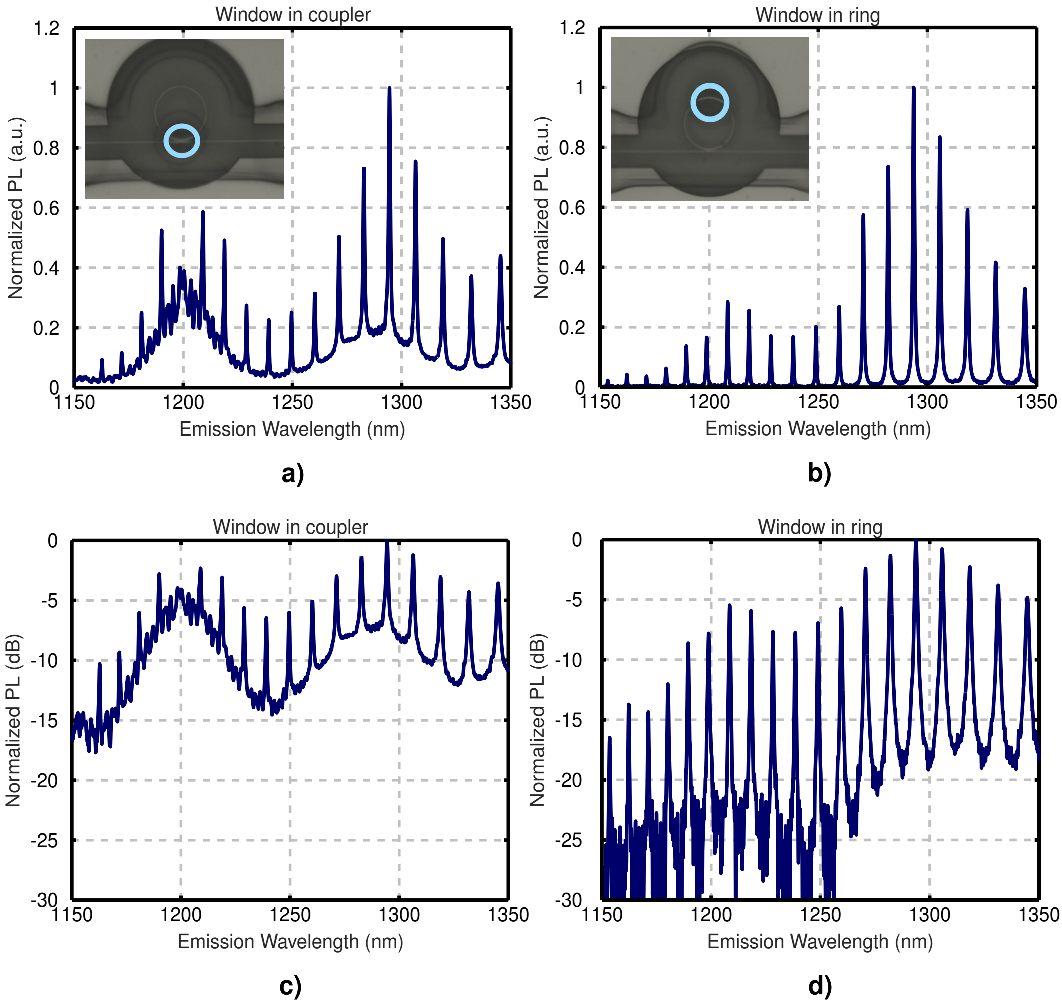

Figure 4.18.: Normalized photoluminescence emission for a strip ring resonator with gap of 250 nm in linear scale and: a) interaction window on the coupler region and b) interaction window on the ring. In log scale in c) and d), respectively.

In this subsection, we have proposed and theoretically demonstrated the use of the longitudinal electric field components in the TM modes to interact with s-SWCNTs aligned parallel to the chip surface. That allows us to have the advantages of TM modes (low propagation losses and large overlap with the surrounding medium) obviating the need for technologically challenging vertical s-SWCNTs deposition. Also, we experimentally demonstrated that by integrating the s-SWCNT onto Si micro-ring resonators, it is possible to realize s-SWCNT chirality-wise resonant enhancement of the emission, allowing an added s-SWCNT chirality selection mechanism. We experimentally show, for the first time, that with a novel selective deposition process (based on localized interaction windows and drop casting) we selectively promote the resonant enhancement of either (8,6) or (8,7) s-SWCNT chiralities present in the HiPco s-SWCNTs solution. We also show that we can reduce the back ground signal, improving the extinction ratio, yielding up to $\sim$18 dB.

4.3. Small mode volume cavities: 2D Hollow-core Photonic Crystal Cavity

The goal here is to enhance light-matter interaction and control the spontaneous emission. Thus we studied small mode volume cavities. By leveraging their small mode volumes and high quality factors, photonics crystal nanocavities have already demonstrated low thresholds or even thresholdless lasing [123,124].

In particular, we are going to use 2D slot photonics crystal cavities. This kind of cavities can enhance light matter interaction due to the combination of slot and slow light effects [125, 126] with a low index material filling the slot. The resonant light confinement in small volumes in those cavities could also be used to enhance light emission from s-SWCNTs, while their high quality factors could be exploited to spectrally narrow the wideband s-SWCNTs emission. Figure 4.19 shows a schematic view of a slot photonic crystal cavity composed by a slot region in the center part, surrounded by a 2D photonic crystal. The cavity structure (zoom in Fig. 4.19) is based on the chirp of the longitudinal lattice parameter (a_i) along the direction of light propagation, keeping the perpendicular lattice constant in order to form a photonic quantum well.

The design of the cavity is the result of the thesis work of Dr. Thi Hong Cam Hoang and Dr. Charles Caër PhD students within the group. Detailed design process can be found in [127, 128].

We report here the first experimental demonstration of resonant enhancement of the photoluminescence emission from a s-SWCNTs network coupled to 2-D hollow-core photonic micro-cavities (presented in Fig. 4.19). We exploit the strong evanescent field, the small mode volume and the high quality factors of these micro-cavities to yield narrow band light emission with high off-resonance rejection.

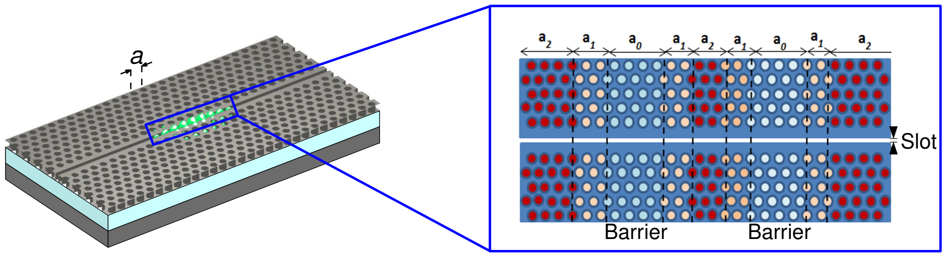

Figure 4.19.: Schematic view of 2-D hollow-core photonic crystal cavity.

Silicon hollow-core photonic crystal waveguides exploit the high index contrast and the photonic bandgap effect to funnel the mode field within the low index center slot [125]. This configuration yields mode evanescent fields two or three orders of magnitude larger than conventional waveguides with similar cross-section. Furthermore, by judiciously modulating the waveguide lattice, a defect can be introduced in the photonic bandgap that allows forming an optical micro-cavity [129, 130]. Here, we chose to adiabatically chirp the longitudinal lattice of the slot photonic crystal (a_i in Fig. 4.19) between $350\,\mathrm{nm}$ and $330\,\mathrm{nm}$ [130]. This approach allowed high quality factors and small mode volumes with a reasonable power coupling to the output waveguide [130]. Finite-difference time-domain (FDTD) tool [119] is used to design a cavity with a fundamental transverse-electric (TE) polarized mode near 1280 nm wavelength, i.e. within the photoluminescence emission range of s-SWCNTs solution. First, simulations have been carried out using spatial and temporal grids of 10 nm and 0.015 fs, respectively, with perfectly matched layer (PML) boundary conditions. A 220 nm thick Si layer (refractive index of ~ 3.5 and no absorption around 1280 nm wavelength) is used, with a silica bottom-cladding, and a top-cladding with a refractive index of 1.46 (considered constant). The optimized design comprises a slot width of 100 nm. This cavity supports two confined modes. The fundamental mode has a resonance wavelength of 1284.34 nm, a quality factor of $Q \sim 21000$ and a mode volume of $0.024(\lambda/n)^3$. The second order mode is centered at 1271.2 nm wavelength, with a lower Q factor of 6000 and larger mode volume of $0.11(\lambda/n)^3$. Figure 4.20 shows the calculated electric field distribution of the fundamental (Fig. 4.20-a) and second-order (Fig. 4.20-b) modes of the cavity. The fundamental mode is confined in the optical well formed by the two photonic barriers, while the second order mode expands within the barriers until the input and output slot photonic crystal waveguides. In both cases, more than 25% of the mode field is confined within the slot region, promoting the interaction with the surrounding medium where the s-SWCNTs will be placed. The optimization of such a cavity has been performed by Dr. Thi Hong Cam Hoang, PhD student of the group.

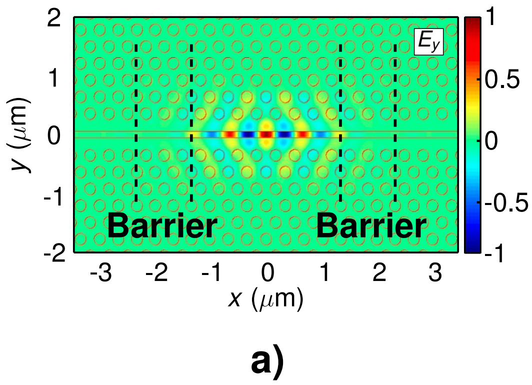

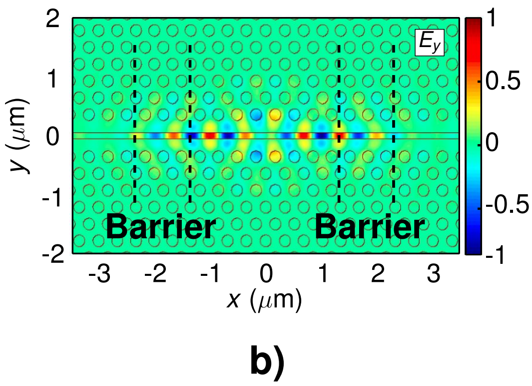

Figure 4.20.: Calculated electric field distributions of the (a) fundamental and (b) second order mode of the hollow-core photonic crystal micro-cavity.

The micro-cavities are fabricated in SOI wafers with a top Si thickness of 220 nm and buried oxide layer thickness of 2 μm. Following the same fabrication process that the previous devices. Figures 4.21-a and 4.21-b show SEM images of the fabricated cavity prior to the s-SWCNT deposition. In Fig. 4.21-a the transition from slot waveguide to slot photonic crystal waveguide is shown. The detail of the central part of the photonic crystal cavity is presented in Fig. 4.21-b. The photonic micro-cavity was terminated on both sides with slot photonic crystal waveguides, which act as input and output of the micro-cavity. Low loss transitions to tapered strip waveguides enabled efficient light collection and injection from the chip facets using lensed fibers. Detailed fabrication and design are reported in [127, 128].

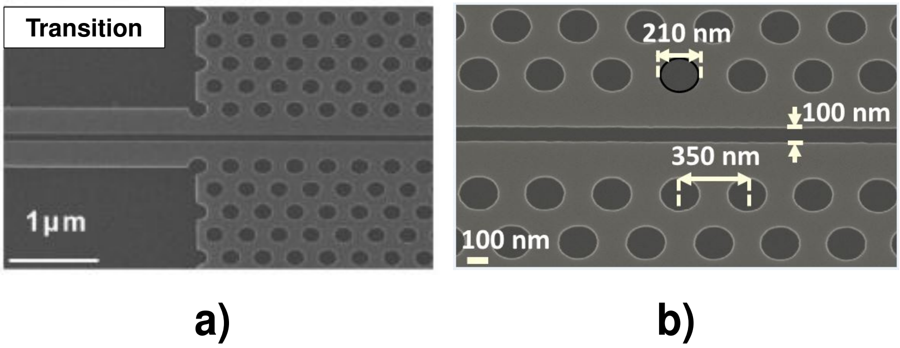

Figure 4.21.: Scanning electron microscope (SEM) images of (a) input access waveguide (transition between slot waveguide and slot photonic crystal waveguide) and (b) central part of the photonic crystal cavity.

After the devices fabrication, the s-SWCNT solution labeled as B* in table 3.4 (page 42) is deposited onto the Si micro-cavities by drop-casting followed by 15 minutes of thermal annealing at $180°\mathrm{C}$. As it was explained previously, this is the preferred deposition technique when the surface-waveguide schema is used.

The linear transmission of the cavity is characterized injecting TE polarized light from a tunable laser. Figure 4.22-a shows the measured linear spectral response of the cavity before and after s-SWCNTs deposition. In both cases, with and without s-SWCNTs, the cavity is covered with a Cargille refractive index liquid with (n=1.46) to vertically symmetrize the structure (refractive index of the silica under-cladding at $1280\,\mathrm{nm}$ is about 1.45). Note that in both cases the thickness of this layer (tens of microns) is large enough to be considered infinite for the optical mode propagation. After s-SWCNTs deposition, the quality factor of the fundamental mode (estimated from the Lorentzian fit of the resonance at 1285 nm wavelength) fell from $Q \sim 18000$ to $Q \sim 7500$, and the transmission level is reduced by more than 5 dB. This could be attributed to the absorption of the (8,7) chirality present in the s-SWCNTs purified solution, with S_{22} resonance near 1280 nm wavelength. The red-shift of the cavity resonance may arise from the slightly higher refractive index of the polymer-wrapped s-SWCNT layer (~ 1.6) compared to that of the refractive index of liquid (1.46). These results indicate a strong light-SWCNT interaction. Despite the Q reduction, the cavity with s-SWCNTs still showed a remarkably large Q/V value exceeding $300000(n/\lambda)^3$ (considering the calculated mode volume of $0.024(\lambda/n)^3$). Comparing the intensity of the transmitted light at the resonance and below the photonic bandgap (wavelength lower than $1270\,\mathrm{nm}$), a transmission efficiency of around 5 – 10% is estimated for the fundamental cavity mode. Therefore, the studied hollow-core photonic crystal cavity exhibits a large resonant light confinement with strong cavity-SWCNT interaction while at the same time providing a relatively efficient coupling to the input and output bus waveguides.

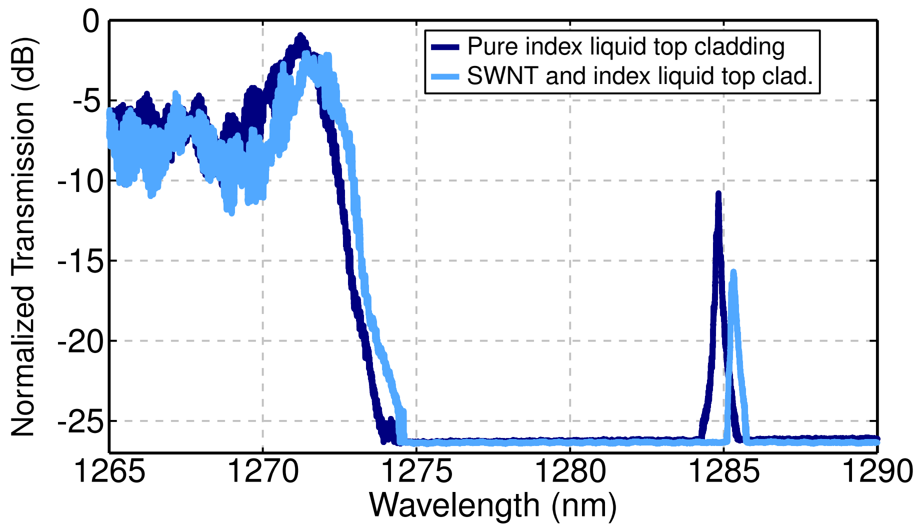

Figure 4.22.: Measured linear spectral response of optimized Si hollow-core photonic crystal microcavity before (blue line) and after (light blue line) deposition of SWCNTs.

As an illustrative example of their broadband emission, Fig. 4.23-a shows the photoluminescence excitation (PLE) spectroscopy map of the PFO-selected s-SWCNTs deposited onto a SOI substrate. The emission has a full-width half maximum (FWHM) of about 65 nm, centered at about 735 nm in excitation and 1280 nm in the emission (corresponding to the (8,7) chirality s-SWCNTs).

The photoluminescence behavior of the hollow-core photonic crystal cavity with s-SWCNTs is experimentally characterized. The PLE spectroscopy map of the s-SWCNTs deposited on the cavity, collected from the access bus waveguide, is plot in Fig. 4.23-b. The two emission peaks around 1285 nm and 1271 nm wavelengths are a clear signature of the coupling of s-SWCNT emission to the two cavity modes.

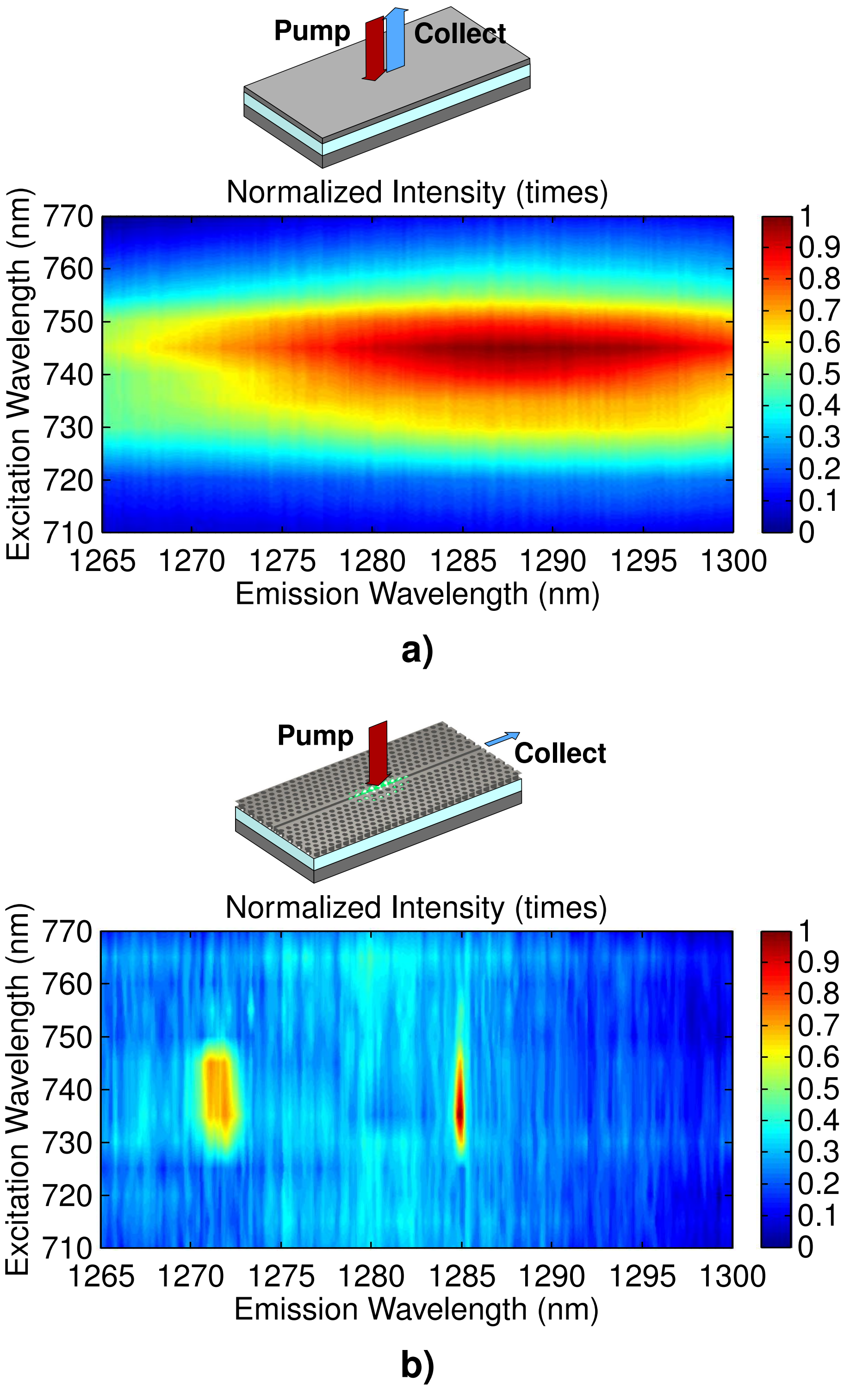

Figure 4.23.: Photoluminescence excitation map for (a) SWCNTs deposited on SOI substrate with surface excitation and signal collection, and (b) SWCNTs deposited on hollow-core photonic crystal microcavity with surface excitation and signal collected from Si bus waveguide.

Figure 4.24 shows the collected photoluminescence spectrum when the excitation wavelength is set to 735 nm (matching the excitonic S_{22} transition of (8,7) chirality). The photoluminescence spectrum shows two sharp peaks, around 1285 nm and 1271 nm wavelengths. These peaks have a full width at half maximum of 0.35 nm and 1.75 nm, corresponding to quality factors (estimated from Lorentzian fitting) of $Q \sim 3600$ and $Q \sim 700$, respectively. These results qualitatively match the FDTD calculations. Due to the fact that the cavity is formed by two photonic bandgap barriers, the optical mode is isolated to the access waveguides promoting the rejection of s-SWCNTs luminescence generated outside the cavity resonances. Indeed the off-resonance photoluminescence signal is more than 5 dB below the maximum level. It is also worth mentioning that, despite the fact that the linear transmission the micro-cavity is 10 dB lower at 1285 nm wavelength than at 1271 nm (see Fig. 4.22), the photoluminescence signal is only 2 dB larger, as we can see in Fig. 4.24. This suggests a stronger emission enhancement for the fundamental cavity mode, with higher Q/V value.

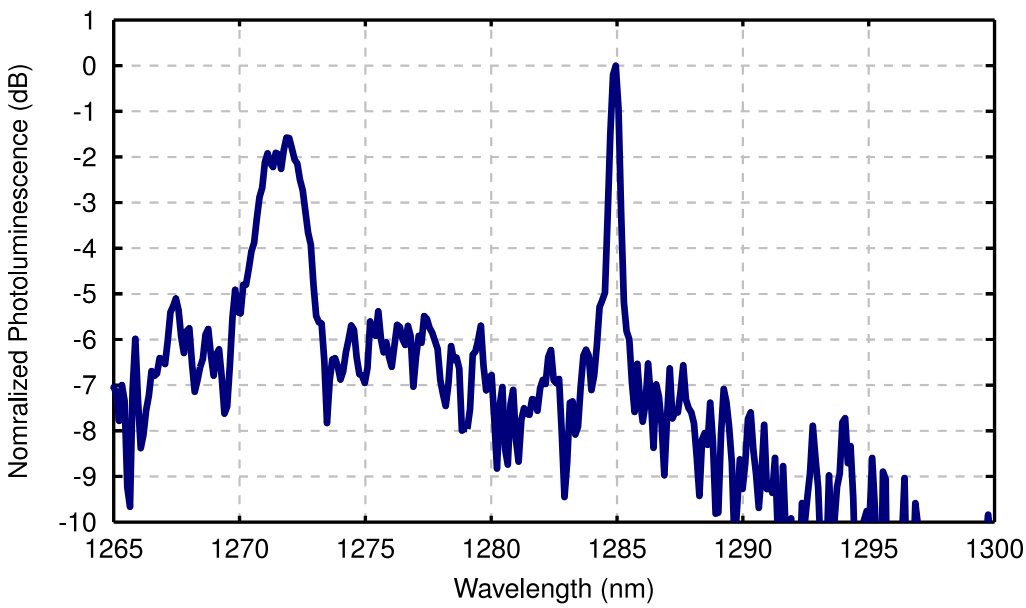

Figure 4.24.: Normalized photoluminescence signal collected from Si bus waveguide for excitation wavelength of 735 nm.

In this subsection we demonstrated the integration of a network of high-purity s-SWCNTs onto a Si hollow-core photonic crystal micro-cavity. The cavity exhibited two optical modes within the photoluminescence emission band of our polymer-sorted s-SWCNTs (around 1280 nm) with a remarkably large Q/V exceeding $300000(n/\lambda)^3$ for the fundamental mode. These peaks had a full-width half maximum of 0.35 nm and 1.75 nm and an off-resonance rejection exceeding 5 dB. This means 180 and 40 fold narrowing of the s-SWCNT emission (~ 65 nm FWHM for network of polymer sorted (8,7) s-SWCNTs on SOI substrate).

4.4. Collinear excitation: Waveguide-waveguide configuration on silicon nitride platform

With the goal to obtain PL enhancement for a given optical pump, preliminary results using collinear excitation scheme on waveguide is presented in this section. To implement a waveguide-waveguide configuration (i.e. excitation and PL guided into waveguide) it is necessary to change the photonics platform. Indeed, as the pump wavelength is in the visible range, we used silicon nitride on insulator. We can take advantage of its transparency window, from the visible to 7 μm, to properly inject the pumping wavelength (around 735 nm) and collect the s-SWCNTs photoluminescence in the band of 1300 nm.

To reach a good light injection and collection, we choose grating coupler to inject and collect both the pump and the photoluminescence signals into waveguides.

A grating coupler is a periodic structure able to diffract a radiation beam to efficiently inject/extract the light to/from an integrated waveguide through the chip surface with relaxed alignment tolerances. This ability is advantageous for the devices presented in this work because we can substantially shorten waveguide length to reduce propagation loss of both, pump and signal, and improved signal-to-noise ratio in our photoluminescence measurements. In addition, when properly implemented, grating couplers exhibit much lower back-reflections (below 1%) [131] compared to conventional facet coupling solutions (typically 15% for Si nanowires). Thus, the use of such couplers obviates the problem of the Fabry-Perot ripples in the optical measurements (due to back-reflections in the input and output interfaces), enabling a much more precise characterization of the integrated micro-cavities. On the other hand, these couplers have an intrinsically limited bandwidth, i.e. they only efficiently couple light within a wavelength range of 50 nm to 100 nm slightly varying the incident angle of the beam. This way, grating couplers designed to collect the photoluminescence from s-SWCNTs (around 1200 nm, 1300 nm wavelength) have also served as a filter for the residual pump (around 735 nm).

In collaboration with Dr. Carlos Alonso-Ramos, we have developed grating couplers to serve as an efficient fiber-chip interface for the characterization of s-SWCNTs integrated in silicon nitride platform. Due to the limited grating bandwidth and the number of wavelength ranges to explore, we have designed one grating coupler for the pump wavelength (735 nm) and one for the collection of the s-SWCNTs photoluminescence (around 1240 nm, between the two PL peaks 1200 nm and 1290 nm). In order to test the different structures, several sets of couples of grating couplers have been implemented: pump-pump, pump-PL and PL-PL.

As an example, Fig. 4.25 schematically depicts a grating coupler structure in SiN platform, describing its main geometrical parameters. Being the silicon nitride thickness fixed to 400 nm (fixed by substrate availability), only fully etched gaps in the grating region have been considered to reduce the number of technological steps. Here, Λ is the period, while l_{gap} and l_{teeth} are the lengths of the etched and non-etched sections, respectively.

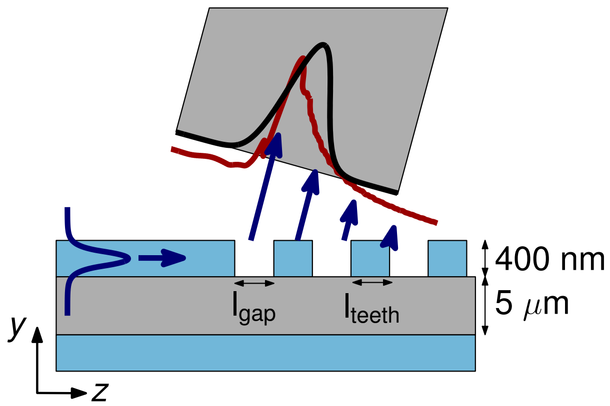

Figure 4.25.: Schematic representation of grating coupler geometry.

Radiation in the grating is mainly governed by the ratio between the period and the wavelength, through the phase-matching condition for radiation [132], that leads:

$$\sin(\theta) = \frac{n_B}{n_c} - \frac{\lambda}{n_c \Lambda}. \tag{4.7}$$

λ is the wavelength, n_B the effective index of the Bloch-Floquet mode in the periodic waveguide, θ the radiation angle and n_c the refractive index of the waveguide cladding.

Coupling efficiency to the fiber can be expressed as [131]:

$$CE = (1 - \rho) \cdot \Gamma \cdot \eta, \tag{4.8}$$

where ρ is the reflectivity of the grating interface, Γ is the directionality (ratio between power radiated upwards and total radiated power), and η is the overlap with the fiber.

From Eq. (4.7) it is possible to estimate the period that yield radiation with a positive angle for a given wavelength, thereby allowing to select the proper period ranges to study for grating optimization at 735 nm and at 1240 nm. To optimize the devices, we have calculated back-reflections and directionality as a function of the gap and teeth lengths, within the period ranges extracted from Eq. (4.7), using the finite-difference time domain simulation tool from Lumerical [119]. The complete coupling efficiency is calculated only for the devices showing good directionality and back-reflections. Finally, the dimensions providing the highest coupling efficiency are selected. To illustrate the optimization process, the radiation upwards calculated for wavelengths of 735 nm (pump wavelength) and 1240 nm (PL wavelength) are shown in Fig. 4.26-a and Fig. 4.26-b, respectively.

The optimized dimensions for 735 nm wavelength are l_{gap}= 240 nm and l_{teeth}= 380 nm, yielding a coupling efficiency to the fiber of -6.5 dB with an angle of 26°. For 1240 nm wavelength, optimal dimensions are l_{gap}= 470 nm and l_{teeth}= 620 nm, with a calculated coupling efficiency to the fiber of -4.8 dB with an angle of 25°.

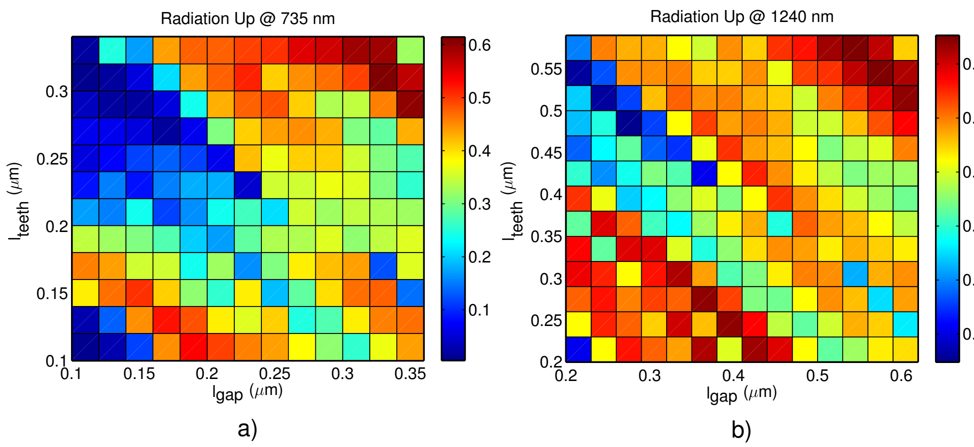

Figure 4.26.: Radiation efficiency as a function of the gap and teeth lengths in the grating region are shown for 735 nm wavelength in a) and 1240 nm wavelength in b).

A waveguide width of 750 nm has been selected to guarantee single mode behavior for the photoluminescence signal. With this waveguide width a dielectric energy confinement in the cladding of 4.90% and 7,04% for both TE and TM modes of the pump signal (735 nm) have been calculated.

Figure 4.27 shows the schematic top view of the complete structure including grating couplers and waveguide. We have fabricated several pairs of nominally identical couplers in back-to-back configuration (light is injected through one coupler and extracted with another one after the propagation in the waveguide). The devices are covered by HSQ cladding that allows to choose the interaction length, l_{int}, with the nanotubes. The devices are fabricated on wafer with 400 nm thick of SiN over a 5 μm thick buried silica.

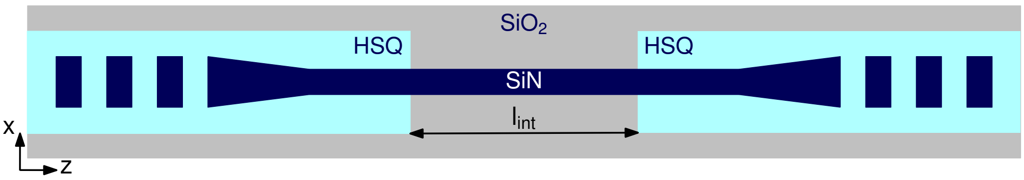

Figure 4.27.: Schematic top view of the grating coupler pairs fabricated on SiN platform. The HSQ cladding allows to choose the interaction length with the material (s-SWCNTs).

Figure 4.28 presents a scanning electron microscope images of one of the fabricated couplers before HSQ deposition. After that, a second lithography level is performed to create a cladding of HSQ where an interaction window of 400 μm length is defined on SiN waveguide.

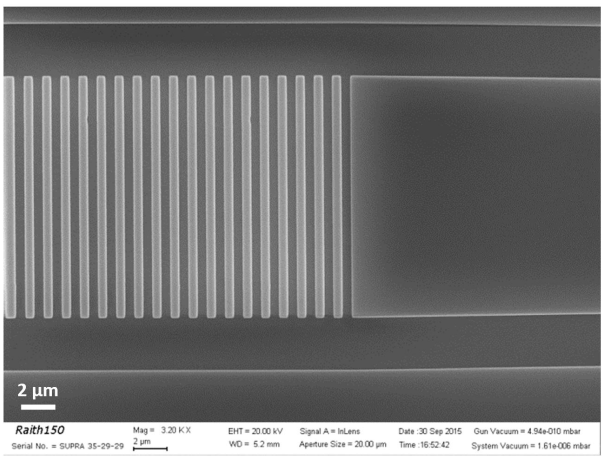

Figure 4.28.: Scanning electron microscopy image of grating coupler fabricated on 400 nm thick silicon nitride platform.

In order to estimate the quality of the fabricated devices, a new setup is built to perform the measurements. As we can see in Fig. 4.29 two goniometers are installed to control the input/output fiber angles. This setup allows several measurement configurations. The linear characterization of the devices are performed with a tunable laser from Yenista at the input. The output fiber is connected to a component tester Yenista CT-400. This configuration enables the transmission measurements in the near infrared wavelength range. For PL measurements, the light coming from a Titanium-Sapphire laser is coupled to an optical fiber and injected to the chip using an input grating coupler. An output grating, optimized at a wavelength of 1240 nm, is used to couple light into another optical fiber connected to a spectrometer with a nitrogen-cooled InGaAs detector array.

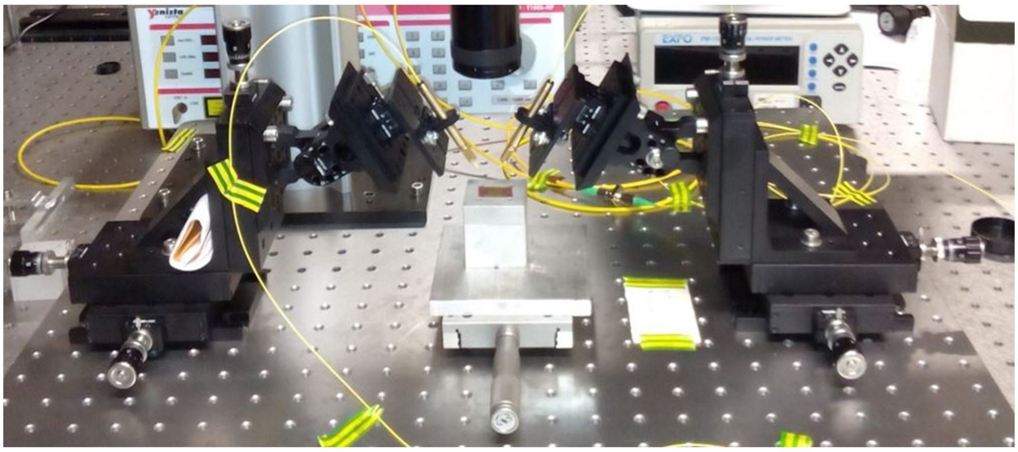

Figure 4.29.: Experimental setup for PL and linear characterization using grating couplers as input and output fiber-to-chip interfaces.

First, the linear transmission of four devices are performed for the pairs grating couplers at the PL wavelength to estimate the quality of the fabrication. The input and output angles are optimized to have the maximum efficiency at 1270 nm with an angle of 23° (Fig. 4.22). The couplers yielded an efficiency of -8 dB per coupler (total insertion loss of $\sim$16 dB) with a small Fabry-Perot ripple of $\sim$0.5 dB. This performance is comparable to that of standard grating couplers offered by photonic foundries using only one etching step [133]. Furthermore, the very small efficiency variation among the different realizations of the same geometry illustrates the very good fabrication tolerances of the structure.

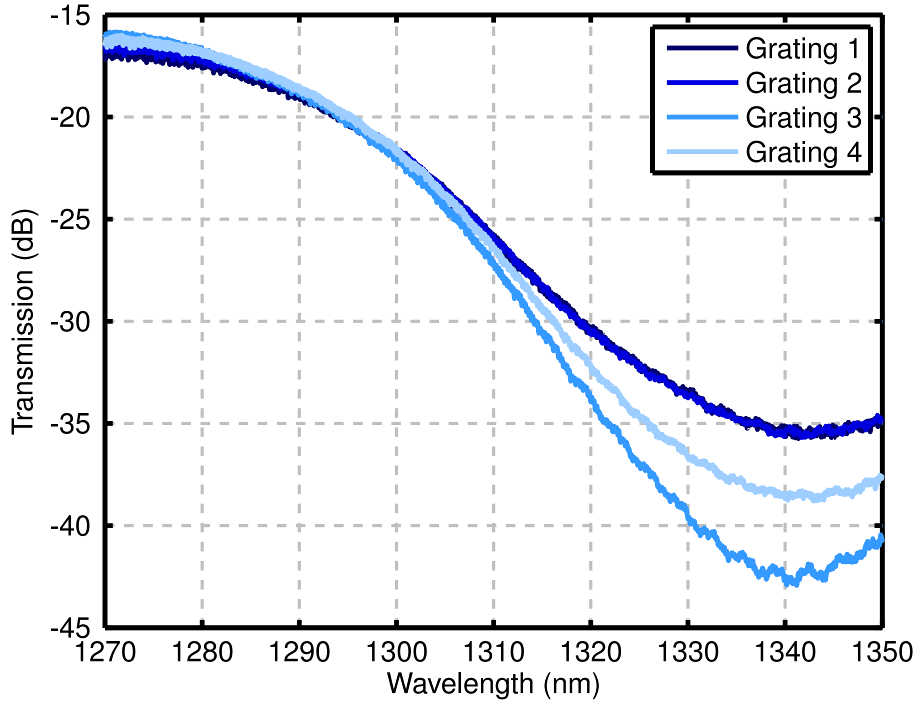

Figure 4.30.: Experimental transmission spectrum of four nominally equal pairs of grating couplers in back-to-back configuration.

After the linear characterization of the devices, the s-SWCNTs deposition is performed using drop casting technique. Figure 4.31-a represents the schematic lateral view of grating couplers with the two possible measurement configurations. In all the cases, the angle for the pump grating is adjusted to $\theta_{735} = 26°$ (red line) to properly inject the pump wavelength at 735 nm. For the PL grating, two possible angles can be employed. First, PL grating angle is set to $\theta_{1200} = 28°$, represented in Fig. 4.31-a in blue line, to efficiently collect the emission of the (8,6) chirality at 1200 nm. The PL grating angle is fixed at $\theta_{1300} = 21°$, represented in Fig. 4.31-a in green line, to collect the emission at 1300 nm corresponding with (8,7) chirality. Figure 4.31-b reports two photoluminescence spectra when the pump wavelength (735 nm) is injected in the pump grating and the s-SWCNTs photoluminescence is collected through the PL grating. In dark blue line we represent the collection when the PL grating is set to $\theta_{1200} = 28°$. The light blue line presents the photoluminescence when the angle of the grating is adjusted to $\theta_{1300} = 21°$. In the presented measurements, the output grating is also used as a pump rejection filter.

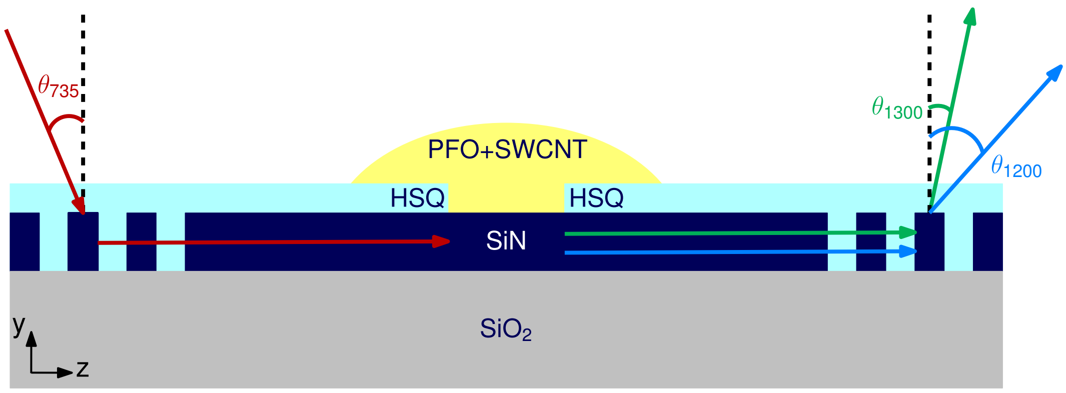

a)

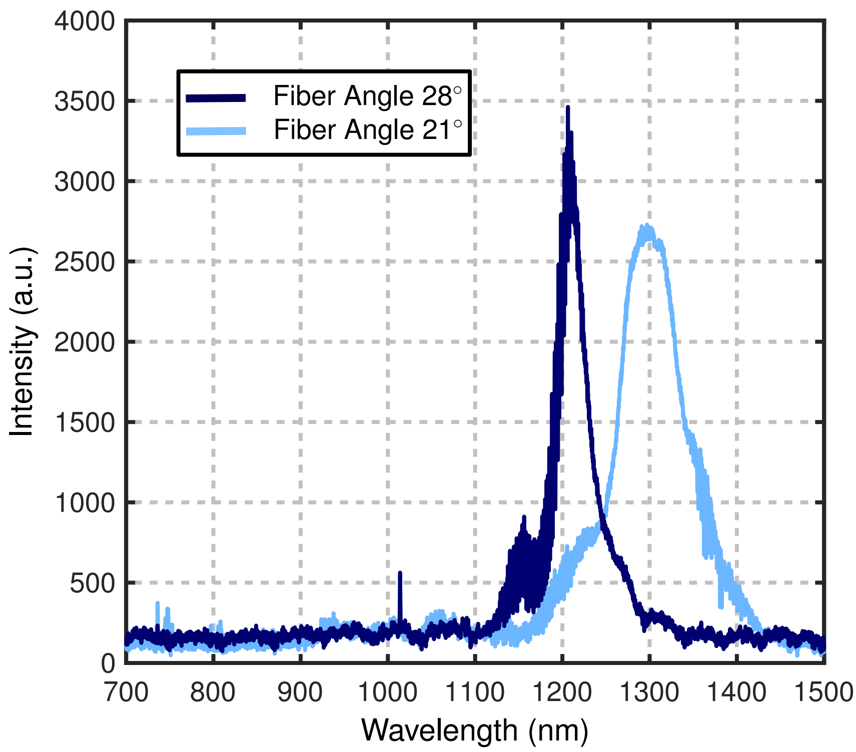

b)

Figure 4.31.: a) Schematic cross section with the two possible measurements configurations. b) Photoluminescence signal collected from SiN bus waveguide for excitation wavelength of 735 nm for the two collected PL angles for the grating.

As we can see from the results presented in this section, collinear excitation is a realistic way to enhance the interaction between pump and s-SWCNTs. These results open a new route to efficiently pump SWCNTs and collect photoluminescence.

4.5. Conclusions

In this chapter, different structures have been studied to improve the light SW-CNT interaction.

In the first section, the results using strip and slot waveguides have been reported. From our theoretical analysis to study the ability of both structures to interact with the surrounding media (s-SWCNTs in our case) we have concluded that in all configurations the slot waveguide working with TE polarization exhibits larger sensitivity than strip waveguide with TM polarization. We have experimentally corroborated that the slot ring resonator produced a resonance enhancement higher than 60 % in comparison with the strip ring resonators.

Due to technological challenge of fabricating slot waveguides, in the second section, we have analyzed the polarization effect on strip waveguides. We show that opposite to the common belief that TE polarization is the only adequate polarization to excite SWCNTs parallel to the chip surface, we show that TM polarizations is also an interesting solution. We have theoretically analyzed and experimentally demonstrated that by engineering the waveguide cross section it is possible to use the longitudinal electric field component in TM modes to interact with the s-SWCNTs aligned parallel to the chip surface. Also, a new strategy is proposed to enhance a single chirality PL based on the use of asymmetric coupling scheme. Finally, we employed localized interaction windows to tune the coupling of the generated PL signal, allowing an extinction ratio improvement of $\sim$11 dB.

In the third section, we aimed at working with small mode volume cavities. We have presented the first experimental demonstration coupling of the s-SWCNTs emission into a 2D hollow-core photonic crystal cavity. We shown an off-resonance rejection exceeding 5 dB.

Finally, in this chapter we have presented preliminary results in collinear excitation. With this method it is possible to maximize the interaction between pump signal and the s-SWCNTs. Due to the pump wavelength it is necessary to change the platform to silicon nitride on insulator where we have also demonstrated good fabrication process.

All these results are very promising to develop photonic devices based on carbon nanotubes.

5

Towards carbon nanotubes integrated laser

As widely reported in the bibliography, to do a laser it is necessary to have a gain medium with amplified light by stimulated emission and a resonator which provides feedback [134–136]. When the light passes through, backwards and forwards in the gain medium, the light is amplified by stimulation emission. If the amplification exceeds the losses in the resonator the lasing effect is reached.

The representative properties of a laser are determined by the light amplification by stimulated emission in a resonator. The laser light is generated following a coherent process. Hence, the emitted light is spatially and temporally coherent [134]. So, laser light has to verify the double coherence, spatial and temporal, and has to present the following properties [134, 137]:

- The laser presents a narrow linewidth emission. This is because the stimulated emission generates waves with the same wavelength, phase, direction and polarization.

- The output light should be a beam with a well defined phase across it, which is a good signature of spatial coherence.

- The emission has to show a clear threshold in power and linewidth. The linewidth should exhibit narrowing by factor of two.

- The emitted light presents the characteristic of the gain medium and the resonator. For this reason, if the resonator is polarization sensitive, the laser light has to be strongly polarized. It is often observed for resonators that present various modes the so-called mode competition. When increasing the excitation energy, the intensity of some laser modes grows faster than the other modes in the cavity.

As it is pointed out in chapter 2 s-SWCNTs present intrinsic optical gain. The measurements using the variable strip length (VSL) performed by Gaufrès et al. revealed an intrinsic optical gain of $g = 160\,\mathrm{cm}^{-1}$, comparable to the values of common high quality III-V laser materials [138].

After this remarkable landmark, in this thesis work a great effort has been devoted to improve the concentration, and therefore, the luminescence from s-SWCNTs. As presented in chapter 3, an improvement of the concentration of s-SWCNT by a factor of ~ 45 with respect to the previous thesis works has been obtained [29, 30].

In parallel to the work on solution optimization, several experiments have been successfully carried out in this thesis to demonstrate remarkable photoluminescence enhancement from s-SWCNTs integrated into photonic structures (chapter 4). In addition, a new strategy to selectively choose the interaction region between s-SWCNTs and photonic structures has been demonstrated, based on the definition of selective interaction windows in an HSQ cladding. With this new strategy we can reduce the extra losses for non excited s-SWCNTs.

At this point of the work, it is clear that we gather all ingredients to try to demonstrate for the first time the laser effect based on s-SWCNTs. A pulsed pump laser is chosen instead of a CW laser, which is favorable to reach the lasing effect [134]. A lasing effect requires population inversion in the gain material.Working in pulsed regime, the inversion of carriers can be ensured with a reduction of the thermal and carriers effect.

To progress in this direction, a new strategy has then been defined within this thesis based on the integration of s-SWCNTs in compact micro-disk resonators (radius of 2.5 μm). We have chosen to use micro-disk because the resonances in a micro-disk resonator are governed by the whispering gallery mode (WGM), confined by total internal reflexion. Then modes interact less with sidewall, reducing the scattering losses. Higher Q-factor and lower losses are expected. In addition, the size of the micro-disk fits with the pump beam area and all SWCNTs on top of the disk can be excited simultaneously.

All the experimental data presented in this chapter have been obtained in the setup of Dr. Fabrice Ranieri at Centre de Nanosciences et de Nanotechnologies

(C2N).

5.1. Silicon micro disk devices

In collaboration with Dr. Weiwei Zhang, PhD student, silicon micro-disk resonators with a radius of 2.5 μm and 5 μm have been designed. A bus waveguide width of 290 nm has been chosen to assure single mode operation at 1300 nm. The resonators have been fabricated in 220 nm SOI wafer following the process described in chapter 4. Figure 5.1-a shows the SEM image of one of the micro-disk fabricated before the s-SWCNT deposition. Figure 5.1-b represents a schematic view of the micro-disk. The injection and collection of the light is perform using grating couplers.

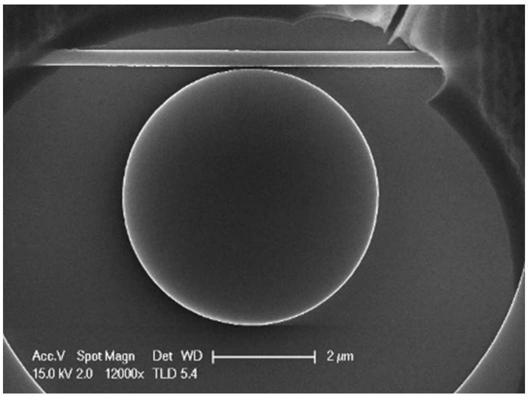

a)

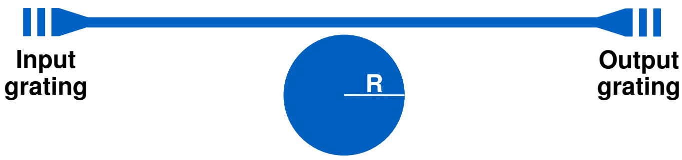

b)

Figure 5.1.: a) SEM image of one of the fabricated micro-disk before the s-SWCNTs deposition. Disk diameter 5μm and bus waveguide 290 nm. b) Schematic view of the micro-disk resonator. Grating couplers are used to inject and collect the light. For simplicity, the HSQ cladding is not represented.

First, the linear characterization of the micro-disk of 5μm diameter after the SWCNTs deposition is performed using the setup showed in Fig. 5.2-b. The setup comprises: visualization system (Navitar), two manual grating stages, tunable laser and data acquisition system (Yenista). Figure 5.2-a presents the transmission spectrum for a micro-disk resonator as a function of the wavelength for TM polarization. The measurement presents a free spectral range (FSR) of 25 nm.

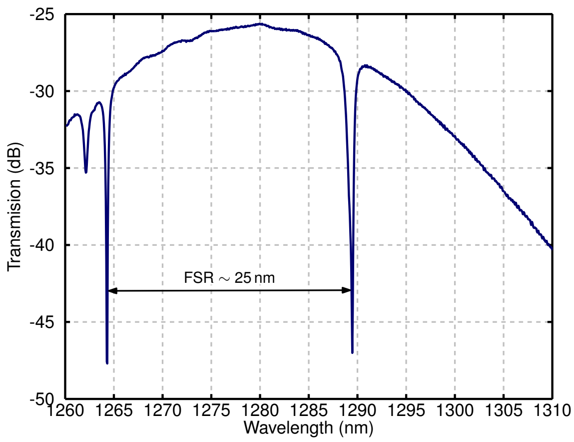

a)

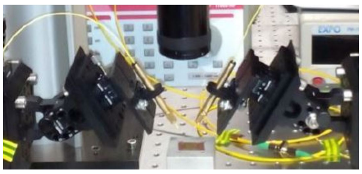

b)

Figure 5.2.: a) Linear characterization for a micro disk of 5μm of diameter. The injection and collection of the light is performed using grating couplers. b) Grating coupler setup image.

The photoluminescence collection is performed through grating couplers. The angle for the collection grating is set to collect TM resonances centered at 1300 nm. Indeed TM mode has a better mode overlaps with the SWCNTs layer deposited on the top of the micro-disk.

For this sample the solution E (see table 3.4 in chapter 3) is used. The solution is deposited by drop casting technique followed by a thermal annealing (180° during 20 minutes).

Experiments have been performed with a femtosecond laser pulse duration of 150 fs, a repetition rate 80 MHz, and a maximum average power of 100 mW (measured before the objective). The laser beam is focused on the sample surface by using a microscope objective (20x, N.A 0.40). The photoluminescence spectrum is coupled to a fiber via the grating coupler. The photoluminescence spectrum as a function of the excitation power is plotted in Fig. 5.3-a. In Fig. 5.3-b, the photoluminescence intensity peak for the center resonance (around 1265 nm) as a function of the pumping power is reported. We can clearly distinguish two different behaviors. The first one, for powers between 5 mW and 85 mW, a linear behavior is observed. A super linear behavior is obtained for pumping power larger that 90 mW. As the same time a clear linewidth narrowing occurs for the same pumping power (Fig. 5.3-c).

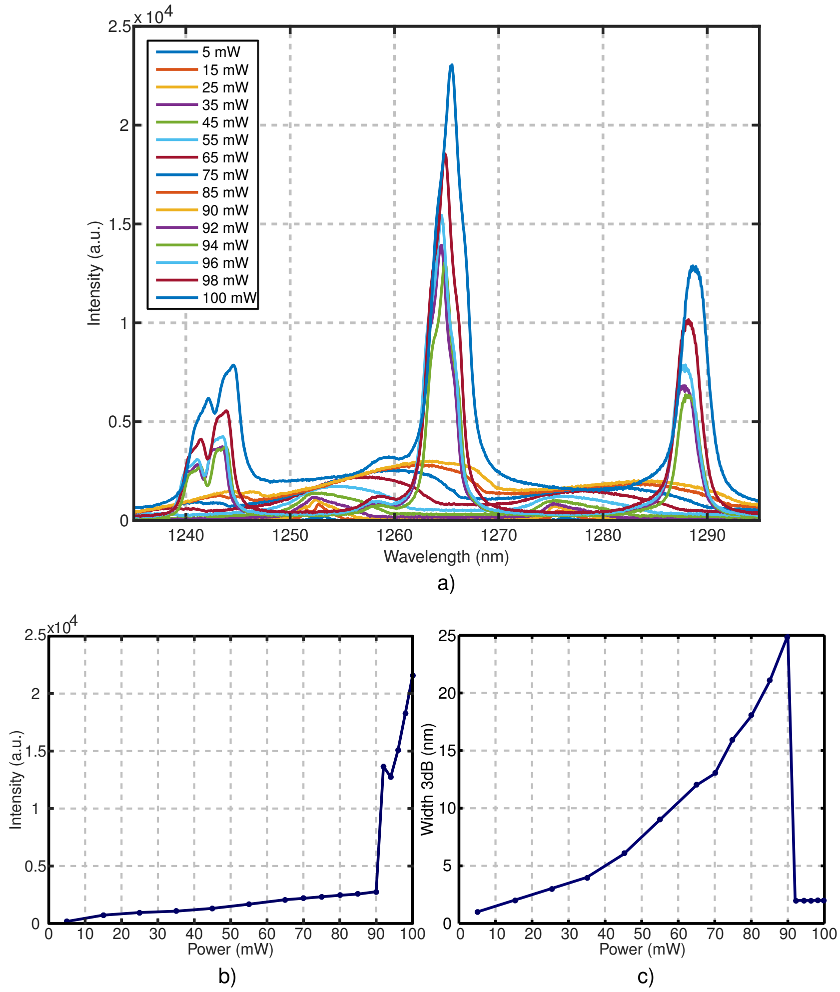

Figure 5.3.: a) Photoluminescence spectrum as a function of the pumping power for a micro-disk diameter of 5μm. The excitation is performed by the chip surface and the photoluminescence is collected using a chip-fiber grating coupler. b) Peak intensity of resonant mode at 1265 nm wavelength as a function of the pumping power. c) 3dB width for the resonant mode at 1265 nm wavelength as a function of the pumping power.

To facilitate the analysis of the photoluminescence as a function of the excitation power, we have represented in Fig. 5.4 the photoluminescence intensity evolution for "low power", "medium power" and "high power" (Figs. 5.4-a, 5.4-b and 5.4-c, respectively). At "low power" (Fig. 5.4-a), a slight shift to shorter wavelengths (blue shift) is observed. As it is showed in Fig. 5.4-d, a blue shift of about 1 nm for the two principal resonant modes (1265 nm and 1285 nm) is achieved. This phenomenon could be due to the introduction of free carriers due to the absorption of the pump, leading to increased propagation loss and quality factor reduction [139], from Q $\sim$ 1000 at 5 mW to Q $\sim$ 200 at 45 mW. For the second power range, "medium power" represented in Fig.5.4-b, a shift towards larger wavelengths (red shift) is obtained. For both resonant peaks the shift wavelength is $\sim$10 nm (see Fig. 5.4-d). This regime is characterized by strong wavelength shift accompanied by a drastic reduction of the quality factor, dropping until Q $\sim$ 50 at 90 mW. In this case it would be explained by a thermal effect in silicon [139]. Finally, at "high power" where abrupt intensity increase occurs, a clear increase of the quality factor is obtained and the red shift is still observed.

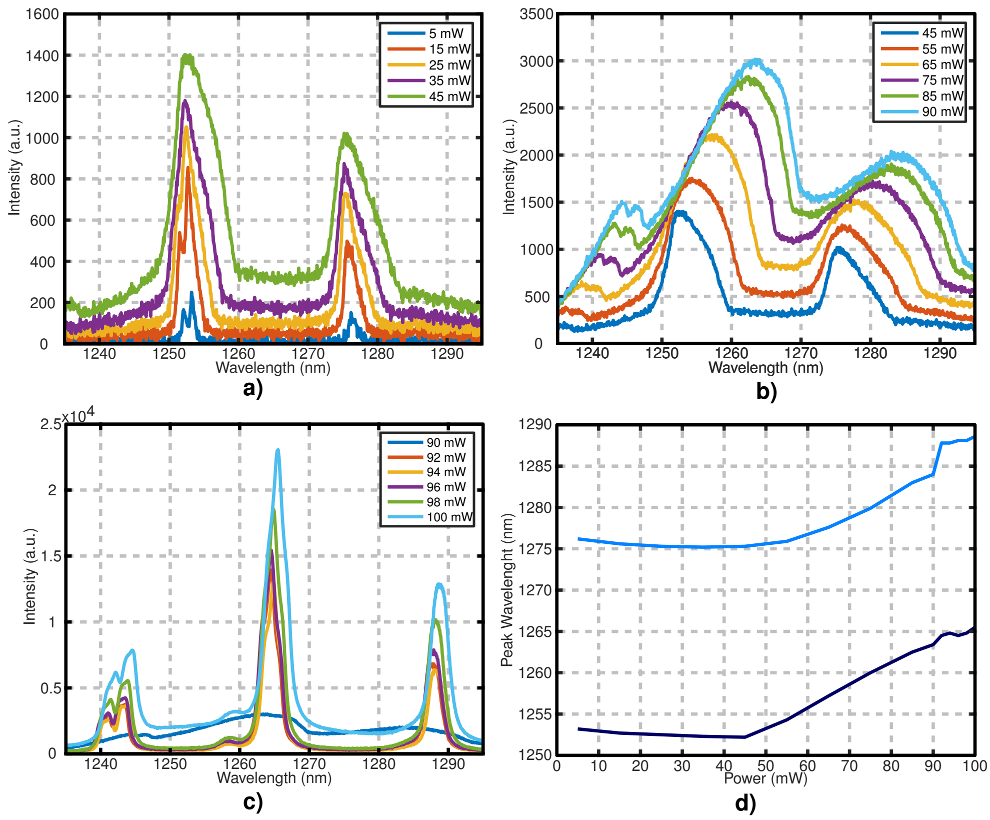

Figure 5.4.: Photoluminescence spectrum as a function of the pumping power for a micro-disk diameter of 5μm. The scheme employed for the measurements is surface-waveguide. For low pumping power, from 5 mW to 45 mW, in a), medium power, from 45 mW to 90 mW, in b) and high power, from 90 mW to 100 mW, in c) and d) wavelength shift for the resonance modes at ~1253 nm and ~1275 nm.

To verify this behavior, we performed the same experiment in another micro-disk resonator on the same sample. In this case the micro-disk resonator has a diameter of 10 μm. For a larger diameter, the resonator has lower losses and thus higher Q factor are expected. In this situation lower pumping power should be required to observe the threshold. Figure 5.5-a represents the photoluminescence spectrum as a function of the pumping power. The excitation is by surface illumination while the collection is through waveguide employing grating couplers. Two abrupt intensity increase are observed. The first for pumping power of 40 mW and the second for 90 mW. In the first case, the intensity increase, Fig. 5.5-b, is accompanied by a linewidth narrowing, 5.5-c, following the trend of a lasing threshold for a lower pumping power. Conversely, the second intensity increase happens together with an increasing of the linewidth. Such a behavior was not expected and it is not well understood. Furthermore, this power is the same that the threshold obtained in previous micro-disk resonator. However, the linewidth variation is the opposite, i.e. widening instead of narrowing.

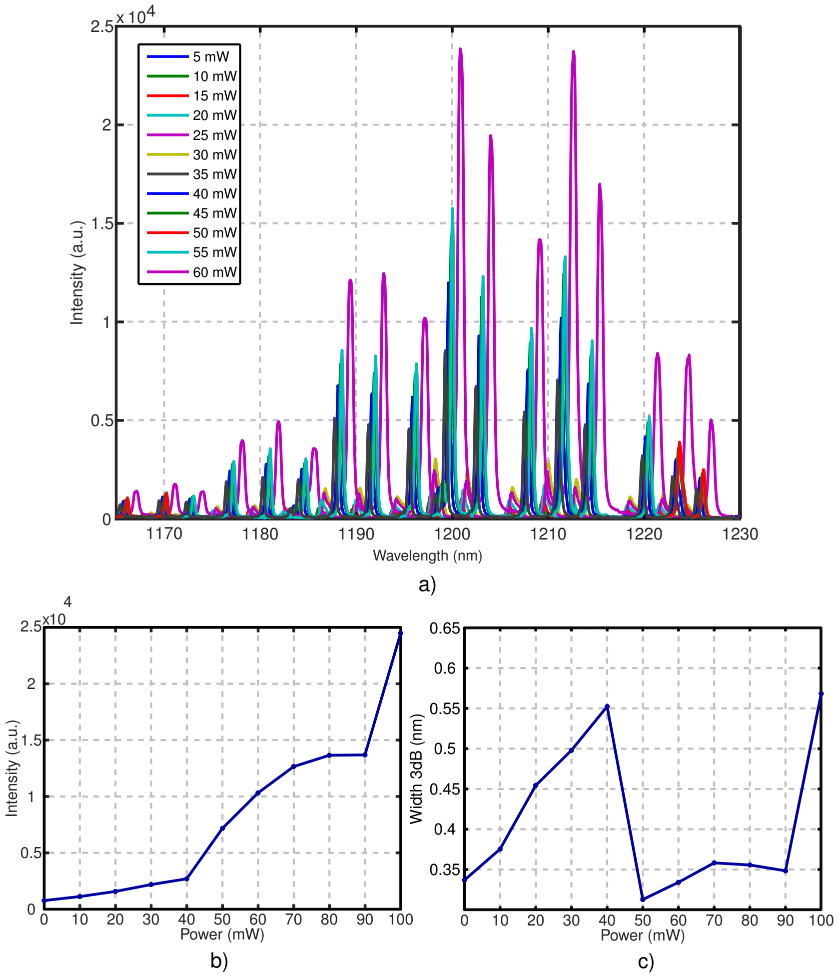

Figure 5.5.: Photoluminescence spectrum as a function of the pumping power for a micro-disk with diameter of 10μm. The excitation is performed at the surface and the photoluminescence is collected through a chip-fiber grating coupler. b) Peak intensity of resonant mode at 1213 nm wavelength as a function of the pumping power. c) 3dB width for the resonant mode at 1213 nm wavelength as a function of the pumping power.

The main question we have to ask here is: Is it a lasing effect? Let us analyze point by point:

- The intensity power has a nonlinear dependence with the pumping power, as it is shown in Fig. 5.3-b and Fig. 5.5-b . This is the first of the characteristics that we expected from a laser.

- We also observed a reduction in the linewidth after the threshold. Still, the bandwidth is never halved, compared to the low power one. It is true that the behavior of the linewidth follows a good trend, but the reduction is not equal to or greater than 2, the expected value for a laser. Furthermore, the linewidth narrowing is abrupt at the threshold which is not fully understood.

- No mode competition is observed, another of the signatures of lasing when multimode cavities are employed. This is a common trend but it is not mandatory, as we can observe similar behavior in Fabry-Perot lasing [140].

As suggested in the literature this non linear behavior in the intensity output could be produced by a thermo-optic effect [134] or by amplified spontaneous emission [137]. At this stage, it seems evident that we need to perform more experiments to further understand the origin of this behavior. A measurement of the second order photon correlation $g^{(2)}(0)$ will definitively answer to the question is it a laser?. When $g^{(2)}(0)$ remains around 2, it is indicative of thermal emission. While when $g^{(2)}(0)$ tends to unity, it denotes coherent emission and therefore lasing [137].

5.2. Conclusions

As explained at the beginning of this chapter, the two principal ingredients to implement a laser are: a gain medium and a cavity. Optical gain in carbon nanotubes was experimentally demonstrated in 2010. A great effort has been made within this thesis to increase the concentration of s-SWCNTs in solution and thus, increase the optical gain. Remarkable photoluminescence enhancement has been obtained employing different types of micro-cavities with a new integration scheme. These advances in the quality of the solution, cavity characteristics (loss and Q factors) and hybrid integration of s-SWCNTs into photonics resonators were important step towards obtaining the laser effect. In this chapter, the measurements in pulsed regime for a s-SWCNTs integrated in a micro-disk resonators have been presented. These measurements have shown for the first time that the intensity output follows a nonlinear dependence with the pumping power. At the same time, an increasing in the Q factor of the resonance peaks is observed. These two items follow the adequate tendency but they have not exceeded the values to ensure that the laser effect has been achieved. In principle, the non linear behavior of the intensity output vs pumping power could find its origin in thermo-optic effect or amplified spontaneous emission. These promising results are not enough to clearly demonstrate the lasing effect. We are still working on carbon nanotubes laser. It is worth mentioning that the behavior shown in this chapter is reproducible and the sample did not burn at high power.

Coherent measurements and more experiments are required to conclude on the possibilities to achieve lasing effect with CNTs.

6
Electroluminescence and photodetection in CNT

This chapter is dedicated to the development of integrated devices based on electrically driven carbon nanotubes. As it is explained in chapter 3, the optimized solution to work with metallic contacts is the solution based on Laser ablation SWCNTs, purified by Dr. Arianna Filoramo in CEA-Saclay. The semiconducting SWCNTs resulting in this solution are long enough to provide contact between two metals. Due to chiralities of this solution the results presented in this chapter are in the telecomunication band around 1.5 μm wavelength.

The two first parts of this chapter are devoted to surface emitter and detector. Specifically, in the section 6.1 the electroluminescence results are presented, while the detection results are reported in the section 6.2. The last part of this chapter (section 6.3) shows the preliminary results on an integrated optical link based on carbon nanotubes.

All the results shown in this chapter have been obtained thanks to the close collaboration with the team of Dr. Arianna Filoramo from CEA-Saclay. The manufacture and the characterization of the samples have been realized using the cleanrooms and measurement equipments at C2N and CEA-Saclay.

6.1. Electroluminescence

As discussed in chapter 2, electroluminescence results from the radiactive recombination of electrons and holes in response to the passage of an electric current. In semiconducting SWCNTs, electroluminescence can be produced by two processes: impact excitation or carrier recombination. In the impact excitation process, only one kind of carriers (electrons or holes) is injected in the semiconducting SWCNT. These carriers are scattered in the defects producing electron-hole pairs, which can recombine to emit photons. This is the dominant effect in unipolar FET devices (Field Effect Transistor) [57, 141]. The use of large bias in these devices inevitably mixes the excitonic states with those of the band-to-band continuum, which leads to spectral weight transfer from the excitonic peak to the continuum and therefore yields a much broader electroluminescence spectrum [57]. On the other hand, the carrier recombination process relies on the introduction of both types of carriers (electrons and holes) in the semiconducting SWCNT. The emission occurs when the electron and hole inside the SWCNT are recombined. This is the dominant physical effect in ambipolar FET devices [24, 142].

The electrical behavior of a FET based on undoped semiconducting SWCNTs is determined by the metal/SWCNTs interactions. Depending on the metal of choice, different physical phenomena can occur in the metal/SWCNTs interface. These phenomena can range from p-type or n-type doping on the SW-CNTs to a 1D Schottky barrier behavior [143]. The use of proper asymmetric contacts favors the electron injection/extraction in one contact and the hole injection/extraction in the other. This way, both electrons and holes are simultaneously introduced into the nanotube. As it is widely reported in the bibliography, the metals of choice to implement asymmetric contacts in SWCNTs are platinum and scandium. Pt contact with a work function of 5.68 eV, higher than SWCNTs work function (4.25 eV), induces a p-type doping in the SWCNTs. Conversely, scandium (Sc) contact with lower work function (3.5 eV) produces a n-type doping [143, 144]. Sc can make an ohmic contact with the conduction band of s-SWCNTs while Pd forms an ohmic contact with the valence band [55]. Figure 6.1 shows the local density of states (LDOS) for the proposed asymmetric contacts configuration.

Field effect transistors based on a single nanotube have been widely developed in recent years, successfully achieving nanoscale integration [145–147]. Under a high driving current, arrays of parallel semiconducting SWCNTs are preferred. Proper alignment of the CNTs is required regardless the configuration. Among the methods for nanotube alignment [148–150], we decided to use the dielectrophoresis (DEP) method. Dielectrophoresis leverages the appearance of a force on a dielectric object when it is placed in a non-uniform electric field. In the

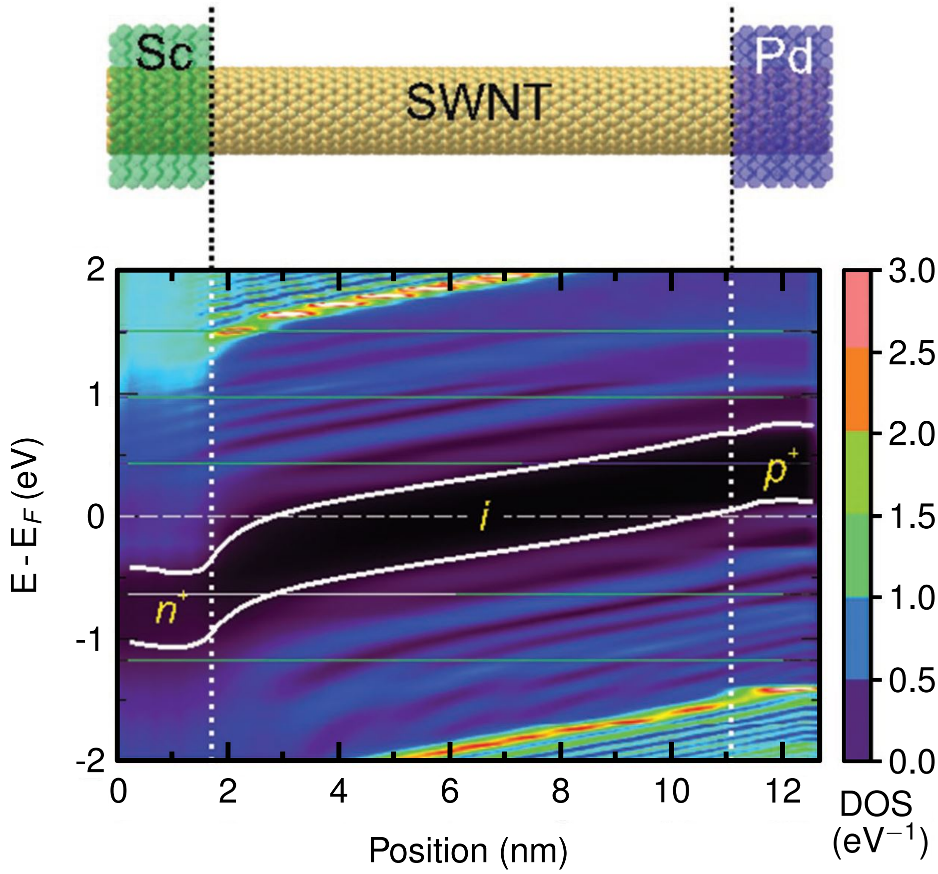

Figure 6.1.: Local density of states for asymmetric contact configuration.

case of an object with a high aspect ratio, such as carbon nanotubes, the dielectrophoretic force aligns the nanotubes along the electric field lines [95]. The exact location of the nanotube array can be determined thanks to the definition of electrodes.

In this work, we have opted for an ambipolar FET configuration for the source that results in a narrower electroluminescence spectrum. We implemented asymmetric contacts of Pt-Sc that maximize the injection of electrons and holes at both ends of the SWCNT. We have decided to work with arrays of SWCNTs to improve the driving current and increase the number of generated photons.

The sample has been fabricated using a Si p^{++} substrate covered with a 150 nm thick SiO_2 film. The electrodes have been patterned using e-beam lithography with a positive resist (PMMA-A6). For the first electrodes, a double step deposition is performed. Firstly, 4 nm of Ti is deposited as adhesion layer. Then, we deposit 40 nm of Pt. These two depositions are performed with a Plassys

MEB 450 system. The lift-off of the metal was performed with acetone, followed by an IPA rinse. Then, the deposition of semiconducting SWCNTs by dielectrophoresis is carried out. The voltage bias is provided by two channels of a TABOR WW1074 function generator. The signals were combined to provide a 20 V peak-to-peak with a sinusoidal wave of 500 kHz. A drop of 10 μL was deposited over the polarized pads. The deposition time was set at 30 s to ensure the drop does not evaporate before the end of the process. The evaporation time ranges from 1 to 2 minutes at room temperature and ambient pressure. After that, the sample is cleaned with toluene to remove the excess of polymer. Figure 6.2 shows an AFM image of the semiconducting SWCNTs deposited by dielectrophoresis. The top and bottom parts correspond to Pt electrodes. We have estimated an average nanotube density between 20 and 30 SWCNTs μm^{-1}.

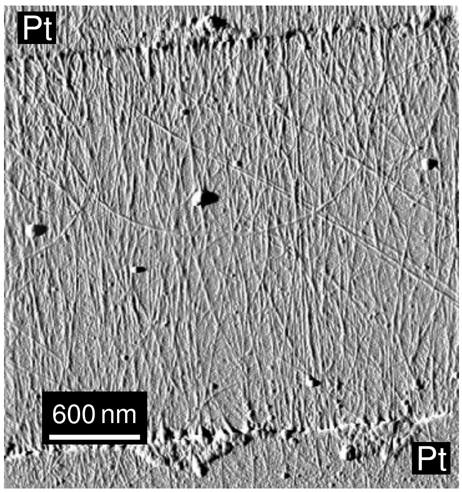

Figure 6.2.: AFM image of semiconducting SWCNTs deposited by dielectrophoresis. The top and bottom regions correspond to the Pt electrodes used for dielectrophoresis. The average SWCNTs density was estimated between 20 and 30 SWCNTs μm^{-1}.

Figure 6.3-a shows the schematic view of the first step of lithography followed by the SWCNTs deposition. Once the DEP process is complete, a second stage of lithography is performed to obtain a device with asymmetric contacts, as depicted in Fig. 6.3-b. The lithography is done following the aforementioned steps. For this metal, a layer of 40 nm of Sc, which provides the asymmetric contact for SWCNTs is deposited followed by a deposition of 30 nm of Al to slow down the oxidation of the Sc surface.

To perform the electroluminescence measurements the drain and gate voltage

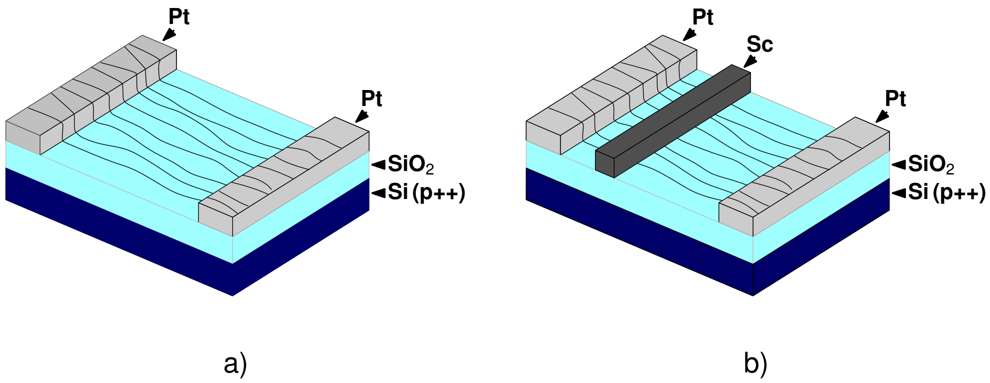

Figure 6.3.: Schematic view of SWCNT transistor. a) Unipolar FET with symmetric contact (Pt-Pt). b) Ambipolar FET employing asymmetric electrodes (Pt-Sc).

bias are provided by two Yokogawa 7651 power supplies. The current in the device, I_{ds}, is amplified by a Standford Research SR5770 current amplifier. The current (I_{ds}) and the voltages (V_{ds} and V_{gs}) are recorded by a LabVIEW home-made program. The electroluminescence signal is collected by a long working distance NIR Mitutuyo objetive and an ACTON SP2500 spectrometer with a nitrogen cooled InGaAs detector.

Figure 6.4-a shows the schematic cross section using symmetric contacts (Pt-Pt) configuration. Figure 6.4-b compares the luminescence spectrum obtained by optically exciting the nanotubes from the top (photoluminescence in red line) and by carrier injection (electroluminescence reported in black line). The photoluminescence spectrum is obtained by optically pumping with Ti:Sa laser at 870 nm wavelength, through a NIR 100x objective. The redshift of the emission indicates that most carriers are injected in the nanotubes with smaller band gap. In our devices, small carrier injection in other SWCNTs can be forced by using different bias conditions (see Fig. 6.4-c). In addition, we observed that the recorded electroluminescence emission is weaker and stronger drain bias voltage is needed in order to observe EL. The use of large bias inevitably mixes the excitonic states with those of the band-to-band continuum, which yields a much broader EL spectrum [57, 151, 152]. We observed that the efficiency of the electroluminescence effect in symmetric contact is very poor. To mitigate this issue we studied the asymmetric (Sc-Pt) configuration. Figure 6.5-a shows a simplified schema of a surface emitter with asymmetric contacts (Sc-Pt). In Fig. 6.5-b we compare the measured emission when the device is excited from the surface

(photoluminescence in red) and when it is excited by carrier injection (electroluminescence in black). As in the previous case, we observed a red shift in EL emission because most of the carrier are injected through nanotubes with smaller band gap [144]. As we can see in Fig. 6.5-c, the carrier injection can be tunned by using different bias conditions, in which the gate bias operates onto two different Schottky barriers.

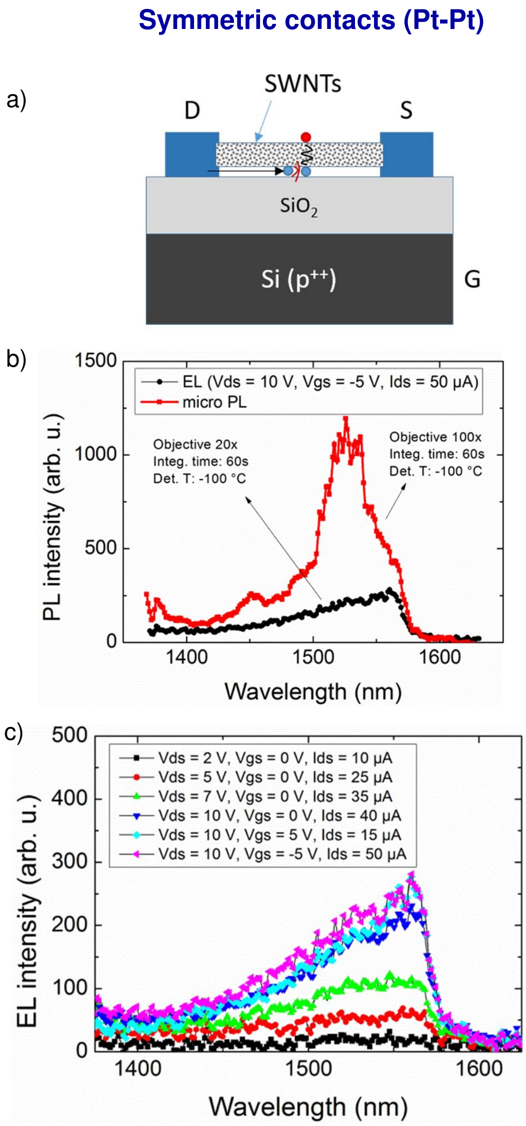

Figure 6.4.: Schema and measurements for a symmetric contacts device. a) Illustration of a symmetric contacts (Pt-Pt) emitter on surface. b) Electroluminescence and micro photoluminescence spectra as a function of the wavelength. c) Electrolumoniscence spectrum as a function of the bias condition.

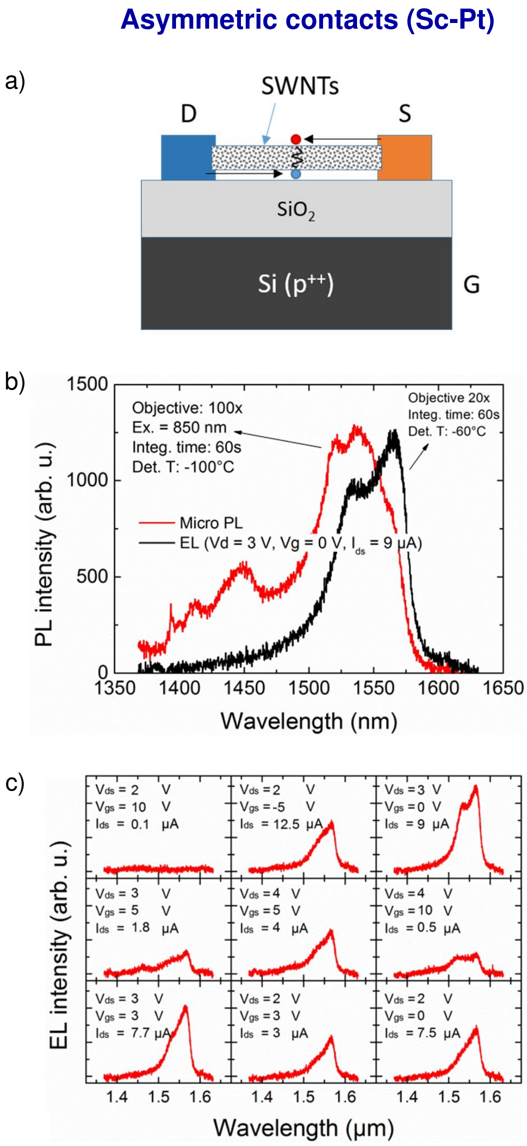

Figure 6.5.: Schema and data for a device with asymmetric contacts. a) Schematic view of an asymmetric contacts (Sc-Pt) emitter on surface. b) Electroluminescence and micro photoluminescence spectra as a function of the wavelength. c) Electrolumoniscence spectrum as a function of the bias condition.

These results show that the device works as a photoemitter in air condition and room temperature in the telecommunications wavelength range (around 1.5 μm). We observed that the electroluminesce obtained in asymmetric devices is substantially more efficient than the one in the symmetric configuration.

It is worth mentioning that because of the non calibrated setup it is not possible to obtain a precise EL efficiency value.

6.2. Photodetection

The emitter device presents a built-in voltage between both asymmetric contacts that makes it very interesting also for photodetection, as it requires no bias and no doping. Then, the measurements carried out in photodetection mode are shown hereafter.

The Fig. 6.6-a shows the schematic top view of a photodetector in asymmetric configuration. The analyzed dimensions are: channel length (C_l) and channel width (C_w). Figure 6.6-b shows the optical microscope image of one of the final devices.

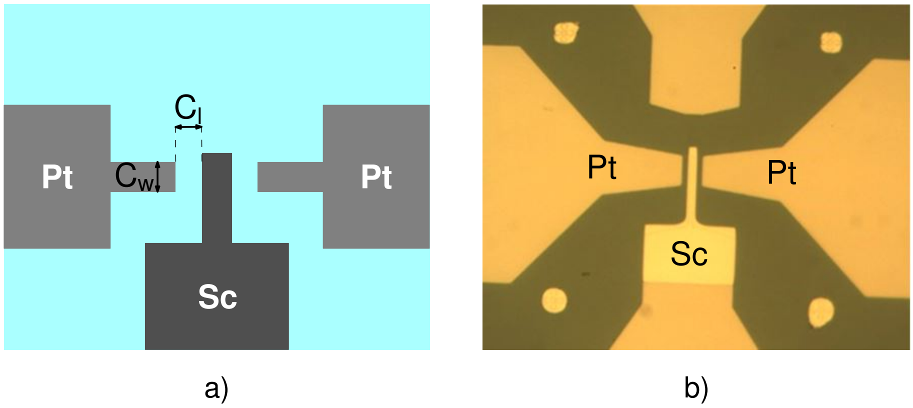

Figure 6.6.: a) Schematic top view for an photodetector in asymmetric (Sc-Pt) configuration. b) Optical microscope image of one photodetector in asymmetric configuration.

A polarized infrared light is provided by a tunable laser from Yenista. The infrared light is in the range from 1.25 μm to 1.68 μm wavelength, matching the S_{11} transition of Laser ablation semiconducting SWCNTs [144]. The light is modulated by an optical chopper (Standford SR540) which allows synchronous detection. Light is sent to the sample through a cleaved optical fiber. The fiber is placed as close as possible to the surface of the device to illuminate the SWCNTs based photodetector. The generated current is amplified with a low noise current amplifier (Standford SR570) and a lock-in amplifier (Standford Research, SR830). The gate and drain voltage bias are fixed by two Yokogawa 7651 power supply sources.

Figure 6.7 shows the I-V curve for an asymmetric (Pt-Sc) photodetector in dark and under illumination conditions. The illumination current is recorded when the surface of the device is illuminated with an infrared light around 1.5 μm wavelength with a power density of 10 μW μm^{-2}. The open circuit voltage, V_{OC}, of 0.3 V corresponds to the SWCNTs band gap [144]. The non-zero slope at small bias of the I-V curve under illumination evidences the presence of a small shunt resistance.

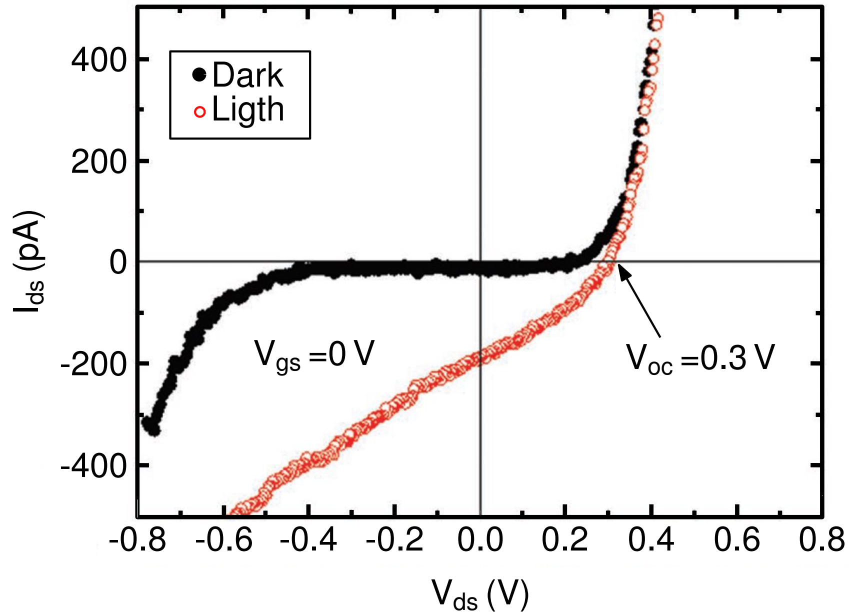

Figure 6.7.: Photodiode I-V curve characteristics with asymmetric contacts (Pt-Sc) in dark and under illumination. The illumination wavelength is ∽ 1.5 μm and the gate is grounded.

Figure 6.8, shows the spectra of the photocurrent as a function of the wavelength for an asymmetric (Pt-Sc) device with channel length (C_l) and channel width (C_w) of 1.5 μm and 10 μm, respectively. The laser light in the telecomunication wavelength range is shaded onto the active region with an optical fiber while the photocurrent is recorded. The polarization of the incident light is parallel to the aligned s-SWCNTs. During the photocurrent measurements the device is under no bias condition ($V_{ds} = V_{gs} = 0$). The spectrum for light ON (red line) shows a clear peak around 1660 nm which matches with the absorption peak of one of the chiralities present in the solution, as shown in the dry absorption spectra represented in blue line. The photocurrent spectrum is clearly dominated by small energy band gap nanotubes. This is consistent with the fact that SWCNTs with smaller gap are favored in photocurrent by the smaller Schottky barrier at the contact [144]. Furthermore, the purification process where sonication and ultracentrifugation steps are used could affect the length distribution following the nanotube diameters. Larger diameter nanotubes are harder to break [153, 154]. After the purification process only larger diameter, corresponding to smaller band gap, are long enough to bridge the two contacts. In the case of light OFF (dark current), the device presents no dependence with the wavelength and its current is always lower that 10 nA.

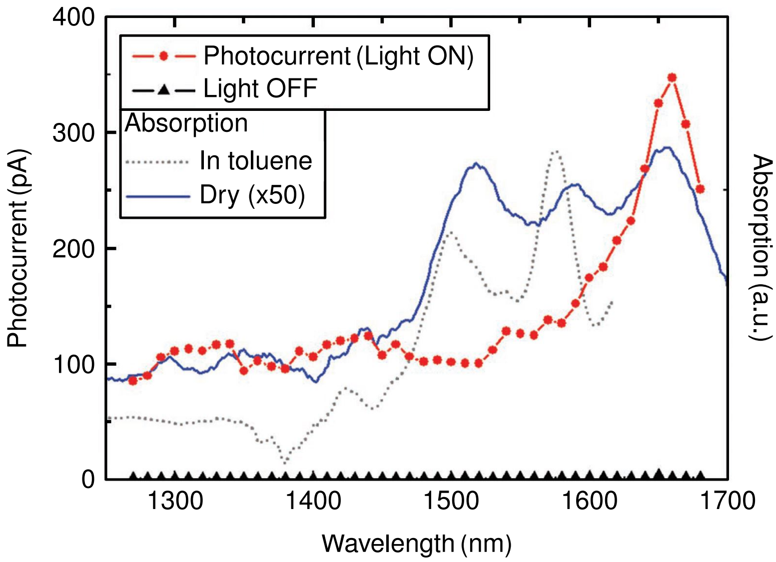

Figure 6.8.: Photocurrent spectrum as a function of the excitation wavelength for a photodiode with channel length (C_l) and channel width (C_w) of 1.5 μm and 10 μm, respectively. Red circles and black triangles in the measurements represent light and dark regimes, respectively. The current is collected without bias ($V_{ds} = V_{gs} = 0$) and with a 10 μW μm^{-2} excitation power. Blue line and gray dotted line represent the absorbance spectrum for a SWCNTs in solution and dropcasted SWCNTs on a sapphire substrate, respectively.

Figure 6.9 clearly shows a strong response of the photocurrent to the light polarization, with a maximum photocurrent when the polarization is parallel to the drain-source direction i.e. the light polarization parallel to the CNT. The photocurrent level along this direction is more than five times larger than in the perpendicular direction, which indicates the high degree of alignment of the nanotubes. We performed two independent measurements of polarization effect, shown in Fig. 6.9.

The response of the induced current to the polarization also excludes the possibility that the observed current is related to a photo-thermoelectric effect, since this effect does not present polarization dependence.

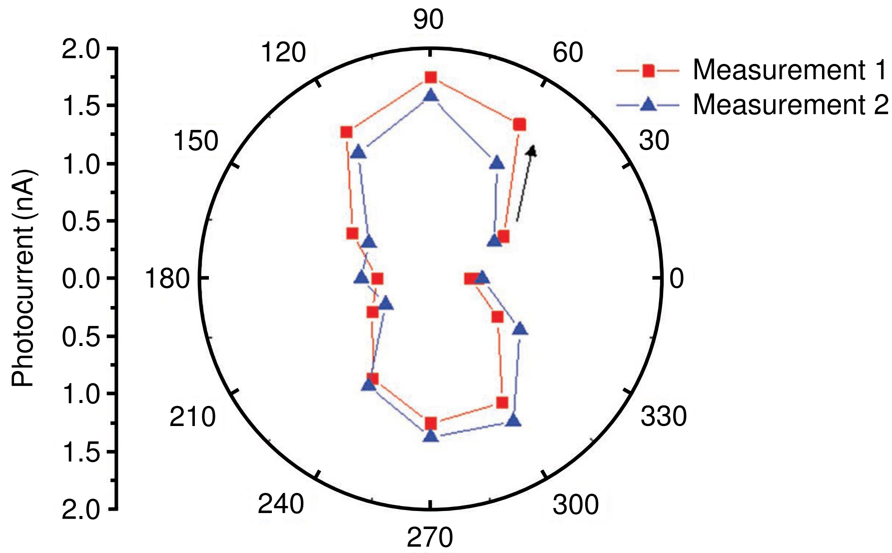

Figure 6.9.: Two measurements of the photocurrent at zero bias ($V_{ds} = V_{gs} = 0$) for an asymmetric (Pt-Sc) photodetector with respect to the light polarization for a wavelength of $\backsim 1.65\,\mu$m. Channel length and width are of 1 μm and 20 μm, respectively. The vertical direction represents the drain to source direction.

With these measurements we have demonstrated that the same device can work as a photodetector and light source. The photodetector works at zero bias condition thanks to the use of asymmetric contacts which form a built-in voltage and provide ambipolar carrier collection.

6.3. Integrated transceiver

As it is showed in the two previous sections, we have successfully demonstrated the implementation of surface LED and photodetector based on SWCNTs FET. Exploiting the same physical effects, we present here the preliminary results on an integrated optical link in planar photonics technology.

Within an industrial project with the company ST Microelectronic (Crolles), we fabricated SiN waveguides on the 300 mm silicon nitride technology.

The technology (see Fig. 6.10-b) consists in silicon bulk wafers with 1.4 μm thick silicon dioxide layer. A 600 nm thick silicon nitride layer is deposited at low temperature via plasma enhanced chemical vapor deposition (PECVD). The patterning of the silicon nitride layer is performed using 248 nm deep-ultraviolet (deep-UV) optical photolithography, and dry etching process. A planarization layer of ∽600 nm thick silicon dioxide is deposited.

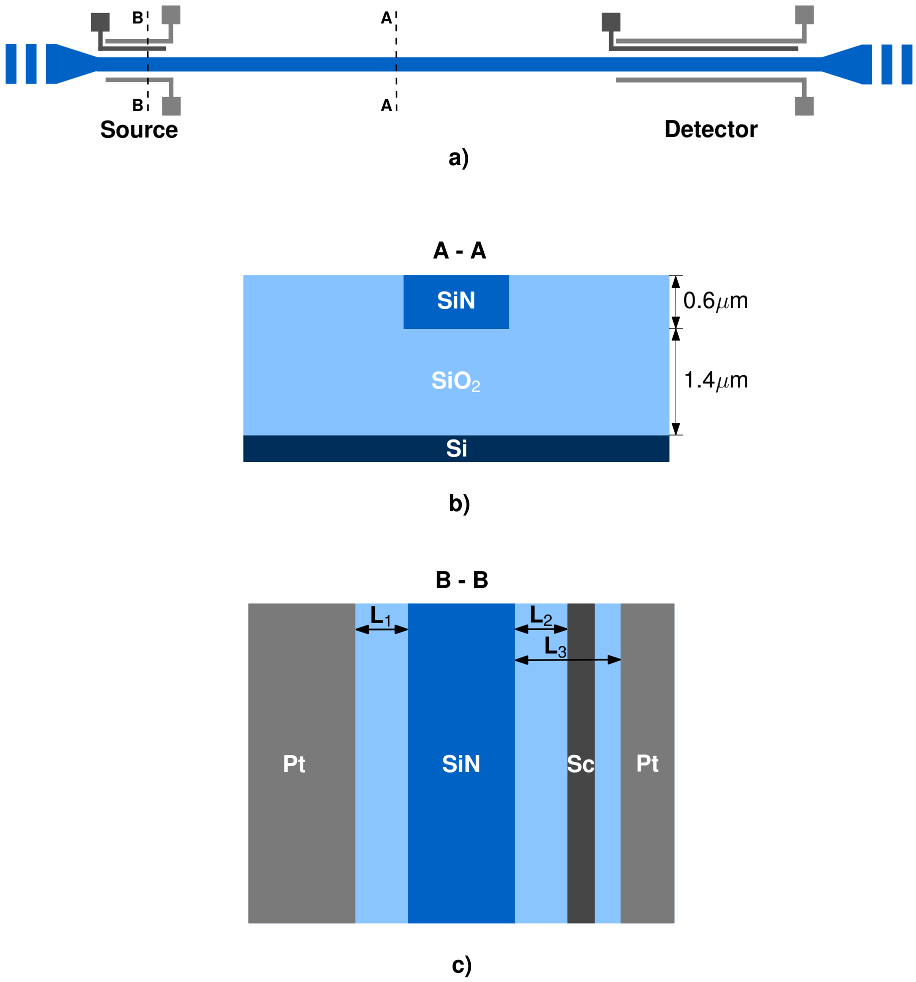

Figure 6.10.: Schematic representation of: a) complete link, with grating coupler for input and output, source and detector and interconnection waveguide. For simplicity, SWCNTs have not been represented. b) Cross section of strip SiN waveguide in A - A line and c) top view for source/detector configuration on a planar silicon nitride technology in B - B line.

We have started by designing the waveguide cross section. We designed the waveguide width to guarantee single mode behavior in the wavelengths of interest (∼ 1.5 μm - 1.6 μm). In Fig. 6.11, the effective index of each mode is represented as a function of the waveguide width. The simulations have been done using Mode Solutions of Lumerical [119] considering wavelength of 1550 nm and 100 nm thick cladding with refractive index of 1.5, corresponding to semiconducting SWCNTs sorted by polymer [108]. As we clearly see in Fig. 6.11

the waveguide presents multimode behavior for width larger than 900 nm. So, we choose a waveguide width of 700 nm as a good trade off between propagation losses, optical mode confinement and single mode operation. For this waveguide dimensions, the dielectric energy confinement for the E_x component for TE mode, $\xi_{cladd,x}$, of $\sim 7\,\%$ has been calculated.

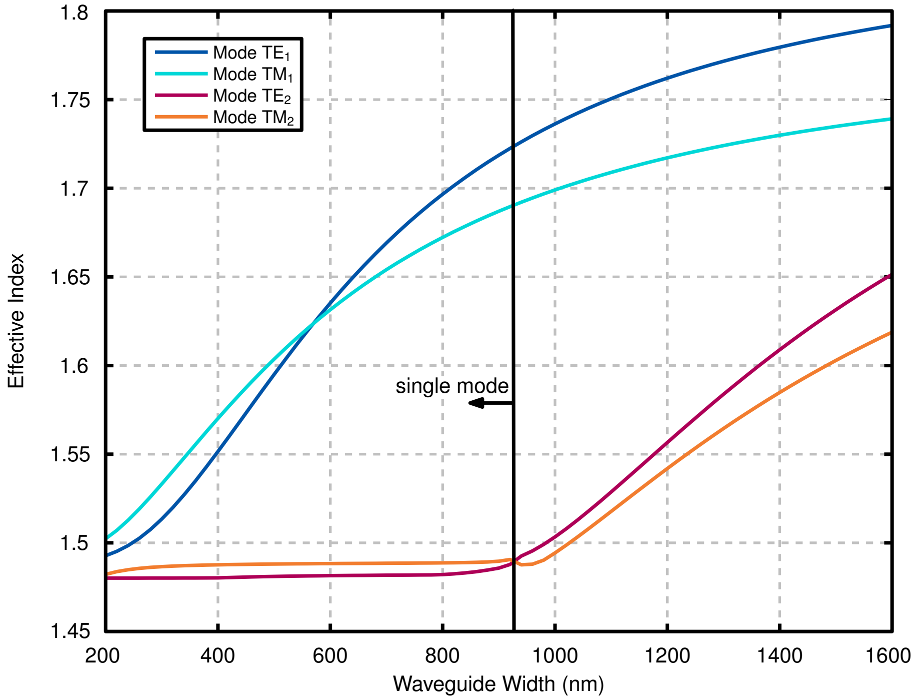

Figure 6.11.: Simulated effective index as a function of the waveguide width. Simulations performed at 1550 nm.

Figure 6.10-c represents the schematic top view distribution of electrodes for source and detector in asymmetric configuration. The waveguide is centered between Pt and Sc contacts. Pt electrodes are placed on both sides of the waveguide at a distance L_1 and L_3 to perform the DEP of semiconducting SWCNTs. A third electrode in Sc, located on one side at a distance L_2, forms the asymmetric contact. In Fig. 6.10-a, the schematic view of the target optical link is presented. This link includes: input/output grating coupler, interconnection waveguide, one source and one detector. To reduce the propagation loss due to the metallic contacts, we performed some simulations. We employed the structure represented in the inset of Fig. 6.12. Figure 6.12 reports the optical losses for TE mode as a function of the distance electrodes considering waveguide in the middle. The simulation has been carried out with Mode Solutions of Lumerical

for a wavelength of 1550 nm. As we can see the losses are negligible for a distances larger than 4 μm. To keep low losses even in the presence of misalignment during the fabrication process, we select a distance between electrodes of 5 μm. This will correspond with the distance between asymmetric contact (Pt-Sc).

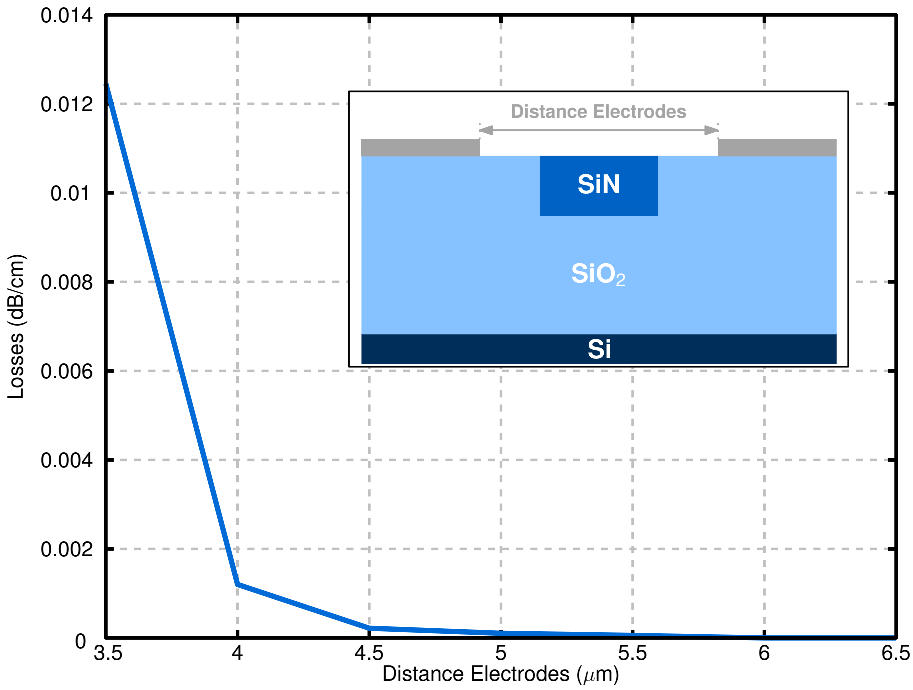

Figure 6.12.: Calculated optical losses as a function of distance electrodes for TE at 1550 nm. Inset: cross section of the simulated structure.

The fabrication of the passive devices is realized by ST Microelectronics in Crolles, France. I fabricated the electrodes in the clean rooms of C2N and CEA-Saclay. Similar technological process that the one presented in previous sections is performed. A first lithography is realized to deposit the symmetric contacts (Pt-Pt) with $L_1 = 2$ μm and $L_3 = 3.3$ μm. After that, the semiconducting SWCNTs are deposited by DEP with the same parameters that previous samples. Once the nanotubes are deposited, a second lithography level is realized to obtain asymmetric contact (Pt-Sc) at a distance of $L_2 = 2$ μm. We have fabricated four different links with sources having lengths of 20 μm, 60 μm, 140 μm and 180 μm. We fixed the detector length to 500 μm. The separation between source and detector was 2.3 mm. We deposited nanotubes in all the links except in the one with the source length of 20 μm, which we used as a reference link to characterize the level of parasitic crosstalk current.

The SEM view of one of the fabricated links is shown in Fig. 6.13. In Fig. 6.13-a, we can see the complete optical link including source, detector and waveguide. The dotted line indicates the waveguide position. Figure 6.13-b reports one light source. We clearly distinguish the platinum electrodes used for DEP and a narrower scandium electrode, used to form the asymmetric contacts. Figure 6.13-c presents the carbon nanotube array aligned between Sc and Pt electrodes.

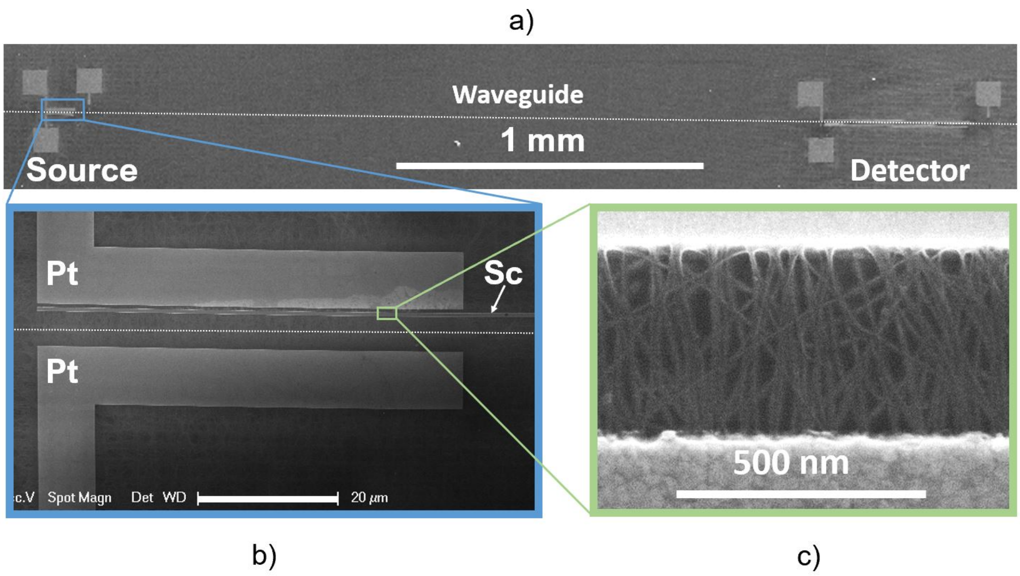

Figure 6.13.: SEM images for one of the fabricated devices. a) General view of completed optical link. Dotted line represents the waveguide position. b) Zoom of the optical source. Two symmetric contacts (Pt-Pt) are employed to perform DEP and a third electrode (Sc) is conceived to form asymmetric contact (Pt-Sc). c) Aligned nanotubes array.

To characterize the sample, the setup represented in Fig. 6.14 is built. The bench is divided in three different sections: i) photonics to perform optical characterization, comprising a tunable laser, automatic data acquisition system, CT400 from Yenista and optical chopper from Stanford. ii) I/O Chip conceived to inject/extract light in/from the devices and also to polarize source and detector. This part of the setup comprises an standard grating coupler setup and DC probes, and iii) electronics part to provide voltage to bias and to collect generated signals from the devices. This part is formed by two low noise current amplifiers (Standford SR570), a lock-in amplifier (Standford Research, SR830) and two Yokogawa 7651 power supply sources.

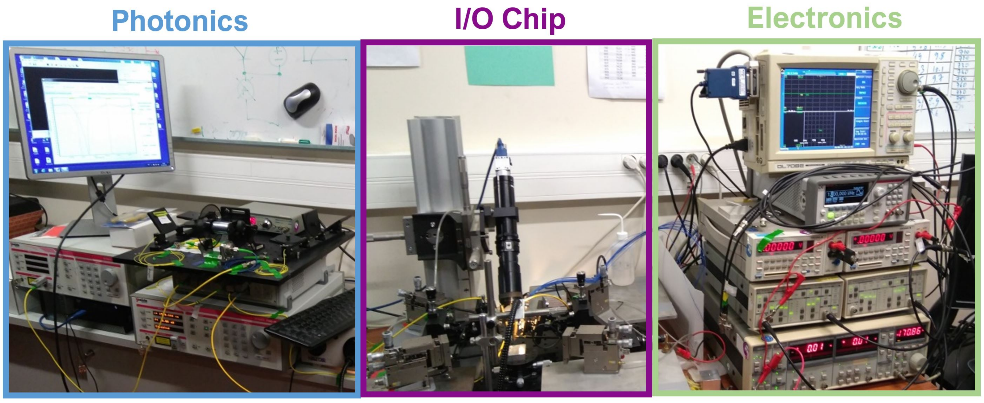

Figure 6.14.: Image for the setup for the optical link characterization. The setup is composed by three parts: i) Photonics to perform optical characterization. ii) I/O to inject/extract the light in/from the devices and iii) electronics to polarize and collect the generated signals.

First, we characterized the optical waveguide and gratings. The light from a tunable laser passes through polarization rotator and is injected in the input grating with an optical fiber. The light is collected with a second fiber at the output grating. The response of the device is collected using an automatic data acquisition system, CT400 from Yenista. From the measurement of the insertion loss we can estimate the coupling efficiency of one grating, represented in Fig. 6.15-a.

The maximum coupling efficiency is -21 dB, obtained at 1580 nm. With this configuration we monitor the current detected by the detector. To do this, we inject the light using one of the fiber-chip couplers. This light is routed by the waveguide and injected into the integrated SWCNT-based photodetector. We collect the generated photocurrent as a function of the injected wavelength. The detector responsivity is represented in Fig. 6.15-b. It is worth to mention that the responsivity shown in Fig. 6.15-b is not normalized by the grating response. If we consider the grating efficiency of -22 dB at 1600 nm we obtain a responsivity of $\sim 0.1\ \mu$A/mW.

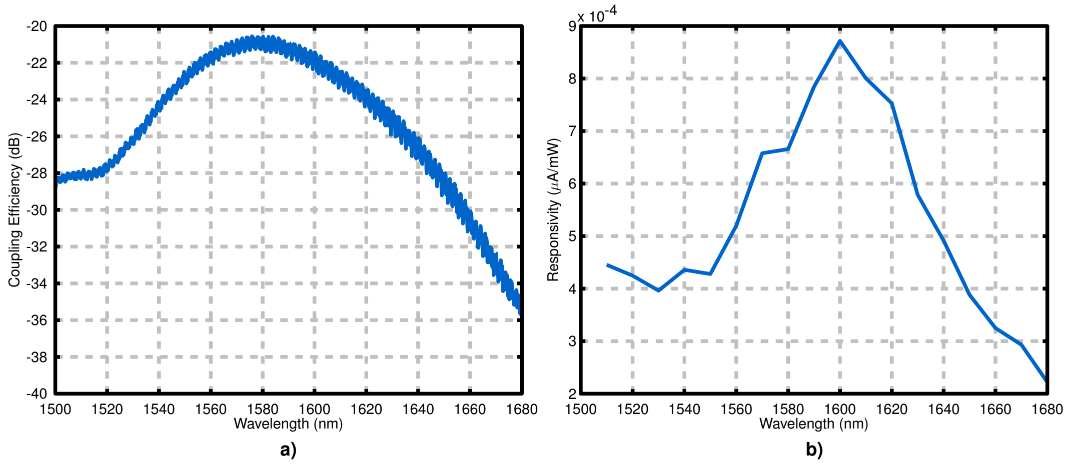

Figure 6.15.: a) Measured coupling efficiency for one the grating coupler. b) Measured detector responsivity as a function of the wavelength.

To characterize the complete link, the following set of measurements has been made: i) measurements are made for the reference link with no carbon nanotubes deposited by DEP. This measurement provided the level of parasitic cross-talk current in the device, source and detector. ii) Measurements for three different links with source length of 60 μm, 140 μm and 180 μm are performed to compare with the cross-talk level. The source is polarized by a Yokogawa 7651 power supply. The detector is working in zero bias condition. The current in the detector, $I_{detector}$, is amplified by a low noise Standford Research SR5770 current amplifier connected to a lock-in amplifier (Standford Research, SR830). The signal is rerecorded by a LabVIEW home-made program. This set of measurements are represented in Fig. 6.16. We can observe that in the case of reference device the detected photocurrent is in the order of pA. In contrast, in all the devices with SWCNTs, the photocurrent delivered by the photodetector is more than two orders of magnitude higher, yielding a nA level. Note that this photocurrent is generated by detecting light generated by the source and coupled into the waveguide. It can be noticed that for the 60 μm long source, the detected current increases proportionally to the voltage applied at the source. The larger electroluminescence signal, the larger amount of absorbed light in the detector, and the larger photocurrent. We can also observe that for longer sources (140 μm and 180 μm) the photocurrent is greater than the one for 60 μm long source. The longer device, the larger number of nanotubes, the higher photocurrent. On the other hand, we can not observe higher photocurrent for the longer device (source of 180 μm). This could be attributed to the fact that part of the light generated at the beginning of the device may be absorbed during the propagation along the source (where the SWCNT are). Another cause may be the presence of larger amount of residual polymer, reducing the quality of the metallic contacts with s-SWCNTs for 180 μm long device. We also observed that the current for the device of 140 μm is not proportional to the applied voltage. The current decays for voltages greater than 3 V. This fact could be due to a degradation of the Sc contact.

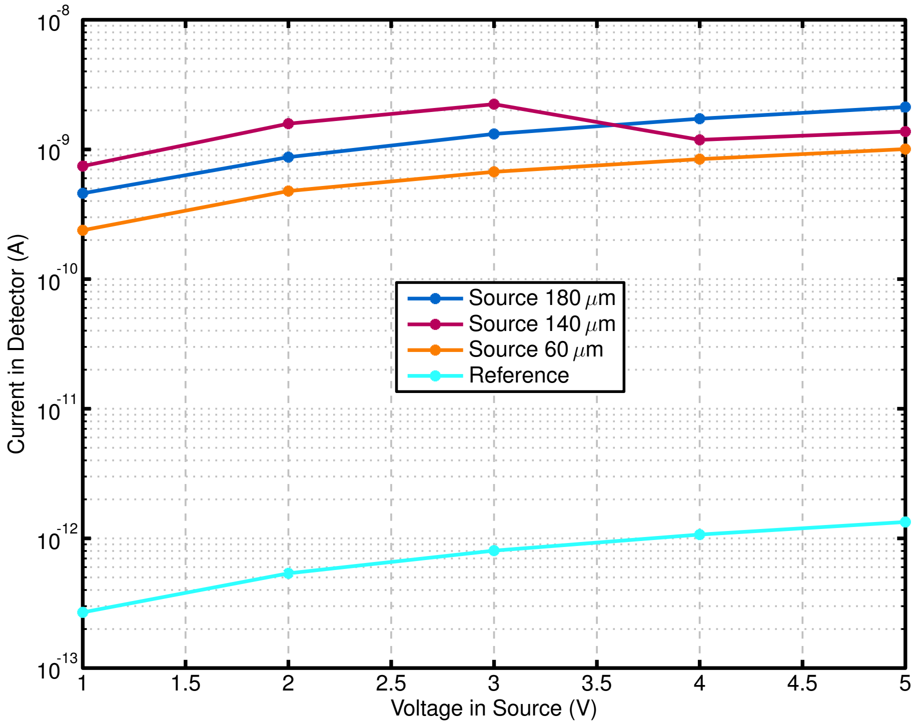

Figure 6.16.: Detector photocurrent as a function of the voltage bias in the source for four different device length (60 μm, 140 μm and 180 μm). The measurements are performed using synchronous detection.

6.4. Conclusions

In this chapter the results for electrically driven SWCNTs devices are presented. First, experimental results for emitter and detector alone based on SWCNTs array deposited by DEP and using asymmetric contact are shown. These results clearly demonstrate that the use of asymmetric contacts improves the performance of both emitter and detector. The photocurrent measurements present a strong dependence on the light polarization, which indicates the high degree of alignment of the nanotubes and also excludes the possibility that the observed photocurrent is related to a photo-thermoelectric effect. The life time of Sc contact is limited by oxidation [55]. Due to this short life time the performance of the device degrades substantially after three days. The detrimental effect of the oxidation process could be alleviated by proper encapsulation, e.g. with a film of poly(methyl methacrylate) (PMMA) [55]. Another root for improvement is the optimization of the contact geometry. In the current version s-SWCNTs are deposited on top of the Pt contacts. Those only s-SWCNTs on the surface of the Pt layer will be contacted. By depositing a second Pt layer on top of the s-SWCNTs the number of contacted s-SWCNTs can be increased, thereby improving the performance of the device. In the last part of this chapter, we show for the first time, the design, fabrication and experimental demonstration of a waveguide-integrated SWCNT photodetector and an optical link based on semiconducting SWCNTs LED and photodetector integrated on SiN photonics platform. The responsivity of the fabricated photodetector is estimated to be $\sim 0.1\,\mu$A/mW, while the link exhibits photocurrents in the order of nA/V. The same optimization strategies described for the surface emitters and receivers could be applied to improve the performance of the waveguide-integrated LED and photodetector.

7 Nonlinear effects in SWCNTs

This chapter is devoted to the study of the nonlinear optical properties of semiconducting SWCNTs. In particular third order nonlinear optical properties have been analyzed. At the beginning of the chapter a small review of nonlinear optics is presented. The second part reports on several experiments carried out on hybrid SiN waveguides covered by different SWCNTs solutions. In the third part, a theoretical model is employed to analyze the experimental results. At the end of the chapter conclusions are given.

The results presented in this chapter have been obtained thanks to the collaboration with Nicolas Dubreuil of the Charles Fabry laboratory of the Institut d'Optique Graduate School (IOGS) and the analysis work of Samuel Serna PhD student in the group. A complete theoretical study allowing the analysis of third-order nonlinear effects is the result of the work reported in [155, 156].

7.1. Nonlinear optics

As explained in the section 2.3.4, the nonlinear phenomena can be described by a series expansion of the macroscopic polarization as a function of the electric field, as

$$P = \varepsilon_0\chi^{(1)}E + \varepsilon_0\chi^{(2)}E^2 + \varepsilon_0\chi^{(3)}E^3 + \cdots , \tag{7.1}$$

where ε_0 is dielectric permittivity of free space. $\chi^{(1)}$ is the first order coefficient, the origin of linear effects. $\chi^{(i)}$ with $i > 1$ correspond to the nonlinear susceptibilities. In this work, we focus on the study of the third order susceptibility, $\chi^{(3)}$, which is responsible for the Kerr effect and the two photon absorption (TPA). $\chi^{(3)}$ is a complex number defined by

$$\chi^{(3)} = \chi_R^{(3)} + i\chi_I^{(3)}, \tag{7.2}$$

where the imaginary part ($\chi_I^{(3)}$) is related with the coefficient of the nonlinear absorption, β_{TPA}, as follows

$$\beta_{\text{TPA}} = \frac{3\omega}{2\varepsilon_0 c^2 n_0^2} \mathbb{Im}\left\{\chi^{(3)}\right\}, \tag{7.3}$$

and, its real part ($\chi_R^{(3)}$) is related to nonlinear refractive index or Kerr nonlinearity, defined as

$$n_2 = \frac{3}{4n_0^2 \varepsilon_0 c} \mathbb{Re}\left\{\chi^{(3)}\right\}, \tag{7.4}$$

where ω is the laser radiation frequency, ε_0 is dielectric permittivity of free space, c the speed of light in vacuum and n_0 is the linear refractive index.

One of the consequences of the Kerr effect is the self-phase modulation (SPM). This phenomenon introduces a symmetrical spectral broadening in the optical pulses. Using this effect, we are able to measure the nonlinear phase shift, ϕ_{NL}, induced by the Kerr medium and therefore to quantify the nonlinear refractive index, n_2 (sign and amplitude).

Considering a material without losses ($\chi^{(3)}$ real) the expression for the nonlinear phase shift can be written as [155]

$$\phi_{NL}(z,t) = \frac{2\pi}{\lambda_0} n_2 I(t) z. \tag{7.5}$$

ϕ_{NL} is proportional to the temporal distribution of the intensity, and increases with the propagation distance, z, in the Kerr medium. The frequency variation of the pulse is a function of this phase shift, defined by $\delta\omega(t) = -d\phi_{NL}(t)/dt$. The temporal shape of the pulse is not modified, but the nonlinear phase shift creates a frequency chirp that depends on the sign of n_2 and the temporal derivative of the intensity. In Fig. 7.1, an illustrative example, extracted from [155], is represented. The input signal follows the envelope of a cardinal sinus (Fig. 7.1-a). Figure 7.1-b shows $\delta\omega$ for $n_2 > 0$ (blue box) and $n_2 < 0$ (red box). Figure 7.1-c plots the output signal after propagating through a medium with $n_2 > 0$ (blue box) or $n_2 < 0$ (red box). The positive Kerr effect induces a red shift of the impulse front and a blue shift at the end of the pulse (Fig. 7.1-c top). The opposite frequency shift is then obtained for a medium with negative Kerr effect (Fig. 7.1-c bottom).

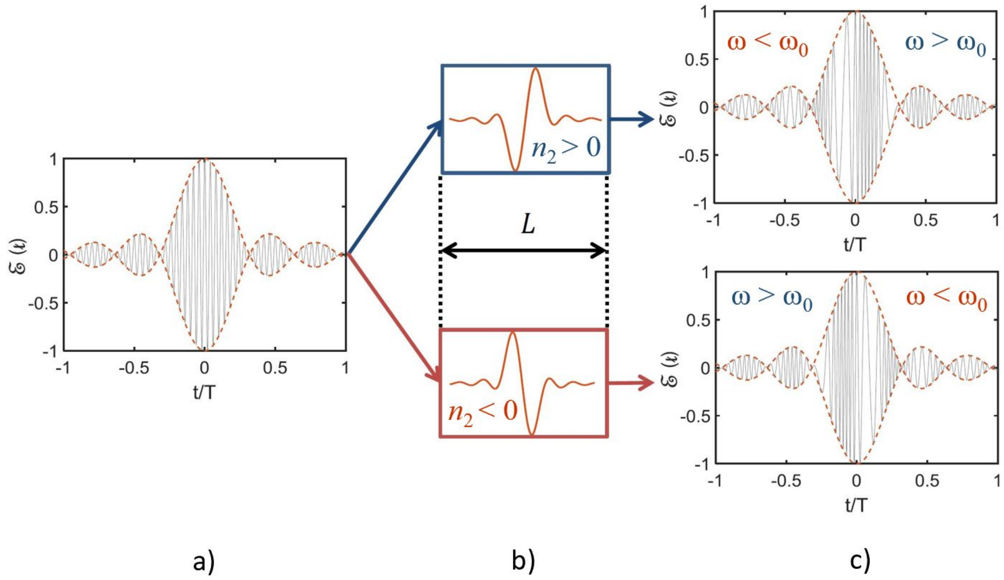

Figure 7.1.: a) Temporal representation of the input signal. b) Representation of $\delta\omega$ for a Kerr medium with $n_2 > 0$ (top) and $n_2 < 0$ (bottom) and length L. c) Temporal representation for the output. Figure extracted from [155].

7.2. Measurements

Considering the large nonlinear third order coefficients of silicon ($n_2 \sim 2 \times 10^{-18}$ m^2/W [156]), silicon nitride (SiN) with $n_2 \sim 2.4 \times 10^{-19}$ m^2/W [157] is chosen as platform to perform nonlinear characterizations of hybrid waveguide with semiconducting SWCNTs layers. The waveguides were fabricated on SiN wafers with 400 nm thick silicon nitride film over 2 μm thick buried oxide layer. The photonic structures were defined by electron beam lithography (NB-4 system, 80kV) followed by inductively coupled plasma etching (SF_6 gas). Before the carbon nanotube deposition, the facets of the samples are protected with polymethyl methacrylate (PMMA A-10), annealed at 100°C during 3 minutes. Then, the semiconducting SWCNTs solution is deposited by drop casting onto the sample. The sample is annealed 20 minutes at 180°C. After that, the sample is cleaned with acetone to totally remove the PMMA at the facets and guarantee low insertion loss. Figure 7.2-a represents the schematic top view of the hybrid SiN waveguide with semiconducting SWCNTs layer. In Fig. 7.2-b the schematic cross section is represented. And finally, Fig. 7.2-c shows the optical image after the semiconducting SWCNTs deposition. Dark region corresponds to the SWCNTs layer.

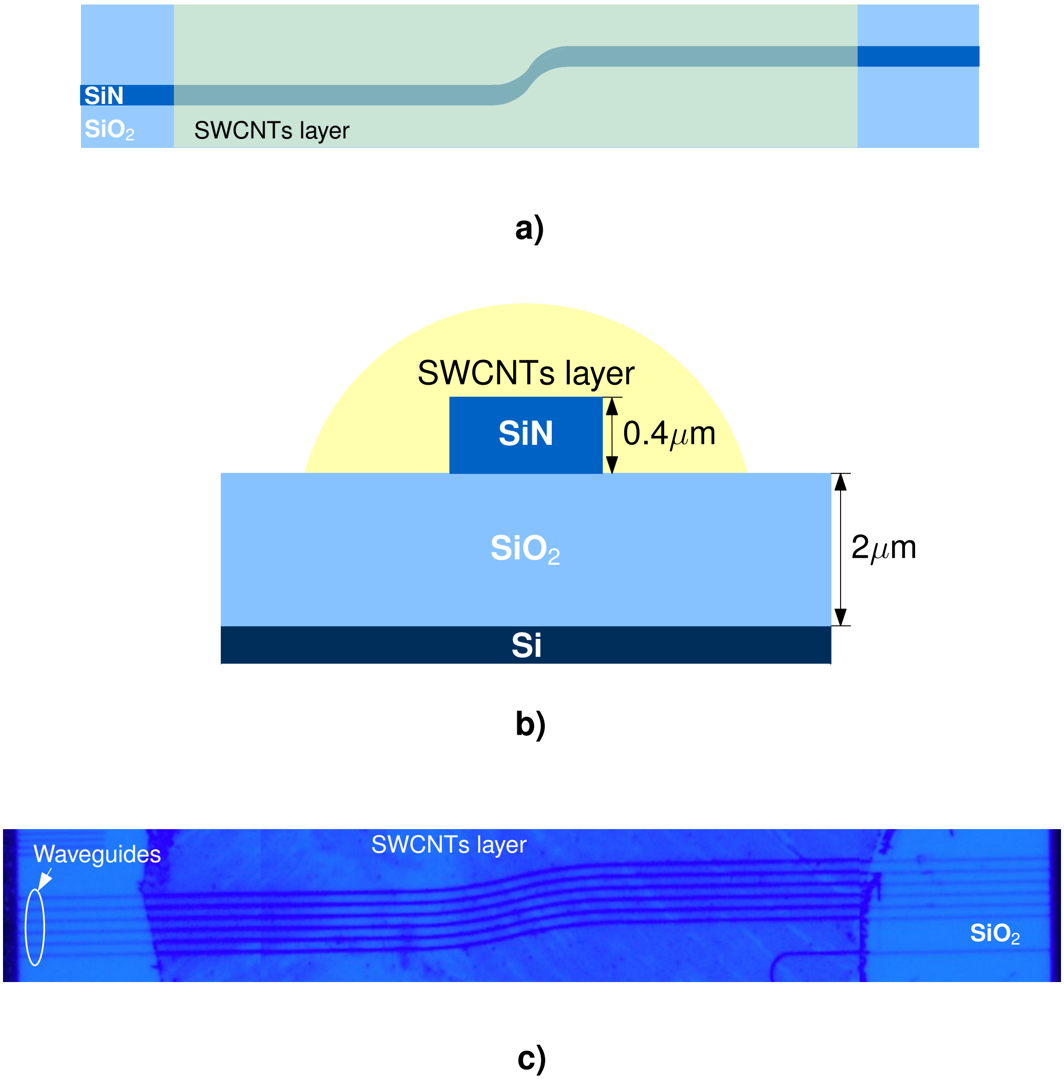

Figure 7.2.: Schematic view for hybrid SiN waveguide with semiconducting SWCNTs layer: a) top view and b) cross section. c) Optical image for a fabricated hybrid SiN waveguide after the semiconducting SWCNTs deposition. The dark region corresponds to the SWCNTs deposited.

A schematic view of the setup developed by Nicolas Dubreil from LCF and Samuel Serna from our group, used for the nonlinear characterization, is represented in Fig. 7.3. As a laser source, we used a mode-locked erbium-doped fiber laser, with pulses of 150 fs, repetition rate of 50 MHz and average power of 182 mW. The output signal is collimated and sent through a grating based stretcher that changes its temporal and frequency characteristics. The spectral shape is quasi-rectangular with a width of 7.3 nm centered at 1580 nm wavelength. The dispersion can be adjusted by $\phi^{(2)}$ coefficient.

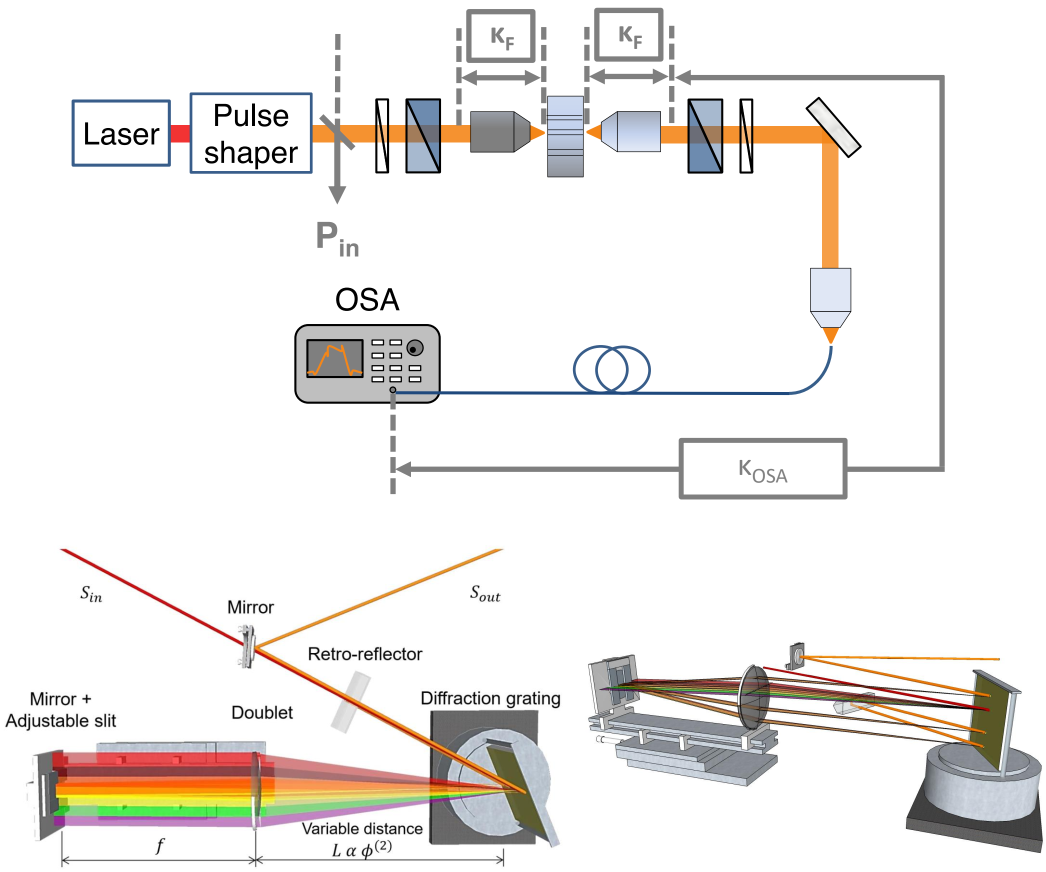

Figure 7.3.: Setup for nonlinear characterization developed by N. Dubreuil in IOGS. Detailed view of pulse shaper. Figures extracted of [155].

The laser is injected into a waveguide through a 20x objective. Two systems formed by $\lambda/2$ and a polarization beam splitter (PBS) are placed at the input and output of the sample to control the polarization state, TE in our case.

To estimate the nonlinear phase shift, ϕ_{NL}, the self phase modulation (SPM) effect on the pulses through their propagation in a nonlinear Kerr medium (waveguide) is simulated. In the case of a material without two photon absorption

(TPA) and considering the particularities of the employed setup, the nonlinear phase shift, ϕ_{NL}, can be written as [155]:

$$\phi_{NL} = \frac{k_0 n_2}{A_{NL}} P_p L_{eff} = \gamma^{wg} \kappa_F \eta P_{in} L_{eff}, \tag{7.6}$$

where $L_{eff} = (1 - e^{-\alpha L})/\alpha$ is the waveguide effective length, L is the waveguide length and α is the linear propagation loss in cm^{-1}. The coupling efficiency at the facets, κ_F, is calculated from the experimental data P_{out}= κ_l P_{in} in the absence of TPA and considering identical coupling efficiencies at both facets ($\kappa_{FA} = \kappa_{FB} = \kappa_F$). The parameter η links incident peak power and the incident average power through $P_p = \kappa_F \eta P_{in}$ where $\eta = 1/[F \int_0^{1/F} |U(t)|^2]dt$ with $U(t)$ is the temporal pulse shape and F the repetition rate of the laser. The parameter $\gamma^{wg} = k_0 n_2 / A_{NL}$ represents the waveguide nonlinear susceptibility. The nonlinear area, A_{NL}, is defined as

$$A_{NL} = \frac{(\int \int Re[e \wedge h^*] z d^2 r)^2}{\varepsilon_0^2 c^2 \int \int_{S_{NL}} n_0^2 |e|^4 d^2 r}, \tag{7.7}$$

where e and h are the electric and magnetic fields, z is the unit vector in the direction of propagation and S_{NL} is the nonlinear area in the material.

To determine the nonlinear refractive index, n_2, we start by characterizing the TPA. To do this, we measured the output power (P_{out}) as a function of the input power (P_{in}). If the variation of the output power presents a linear dependence on the input power (P_{out}= κ_l P_{in}), it means that the TPA is negligible and the coefficient κ_l is the coupling coefficient of the system defined as

$$\kappa_l = \kappa_{in} \kappa_{out} e^{-\alpha L}, \tag{7.8}$$

where κ_{in} and κ_{out} are the input and output couping coefficients with $\kappa_{in} = \kappa_F$ and $\kappa_{out} = \kappa_F \, \kappa_{OSA}$. Here $\kappa_{OSA} = 25 \pm 4\%$ is the coupling efficiency between free space and the optical fiber at the input of the OSA. The coefficient α is the linear propagation loss and L the waveguide length.

We calculated the spectral broadening of the pulses, 2σ, produced by self-phase modulation for an injected power (P_{in}), defined by the root mean squared (r.m.s.) as

$$2\sigma = 2\sqrt{\frac{\int \lambda^2 P(\lambda) d\lambda}{\int P(\lambda) d\lambda} - \left(\frac{\int \lambda P(\lambda) d\lambda}{\int P(\lambda) d\lambda} \right)^2}. \tag{7.9}$$

The values of the calculated broadening of the experimental spectra are used as a convergence criterion for the simulation of pulse propagation through a non-linear waveguide that presents Kerr effect. The output spectra is numerically calculated following the Fourier transform of the pulse envelope at the waveguide output, given by $A(L,t) = U(t)exp[i\phi_{NL}(L,t)]$ where $\phi_{NL}(L,t) = \phi_{NL}|U(t)|^2$ with $U(t) = sinc(at)$ envelope shape with $a = 2.317\,\mathrm{ps}^{-1}$ to match with the autocorrelation measurement in the input pulse. The dispersion effect has been neglected. In fact, the dispersion length ($L_D = T_0^2/|\beta_2|$) is equal to 1.48 m much longer that the waveguide length of 10 ± 0.5 mm. In our case, with absence of TPA and low linear losses we can consider the pulse intensity $I_0 = |U(0,t)|^2$ constant along the propagation z. This way, we can semianalytically obtain the strength of the nonlinear phase shift by using the peak to valley difference of the 2σ calculated. When the broadening of the simulated spectrum 2σ is equivalent to that calculated on the experimental spectrum, we can then extract the nonlinear phase shift ϕ_{NL} from the function $A(L,t)$ and then calculate the nonlinear refractive index n_2.

We started the experiments by the nonlinear characterization of the silicon nitride waveguide with no cladding. First, we employed the Fabry-Perot method to estimate the propagation losses, obtaining $\alpha = 0.8\,\mathrm{cm}^{-1}$ at 1550 nm. Next, the output power is characterized as a function of the input power. As we can see in Fig. 7.4, P_{out} vs. P_{in} follows a linear trend, which indicates the absence of two photon absorption (TPA). Using the linear regression we can identify the coupling coefficient of the system, $\kappa_l = 0.002794$, resulting in $\kappa_F = 30 \pm 4$ % with $\kappa_{OSA} = 25 \pm 4$ %. We have calculated L_{eff}= 0.69 cm considering $\alpha = 0.8\,\mathrm{cm}^{-1}$ and L = 10 ± 0.5 mm.

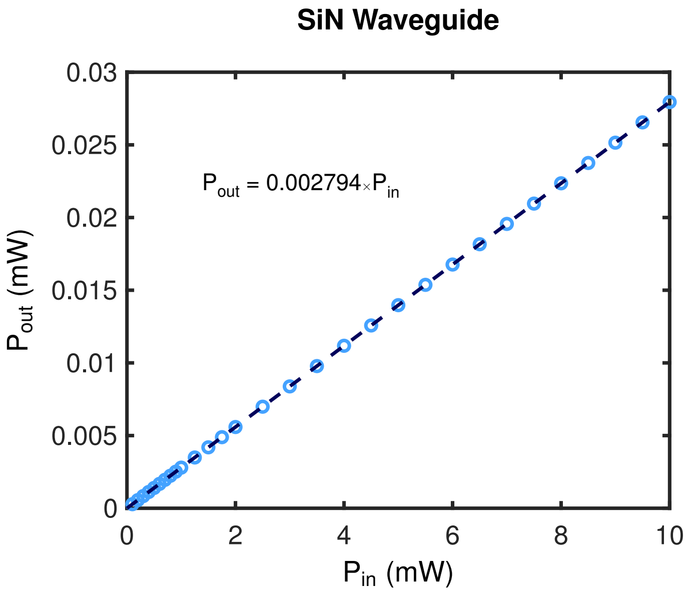

Figure 7.4.: Characterization of a SiN waveguide. The output power as a function of the input power shows a linear relationship verifying the absence of TPA.

In order to obtain n_2 we proceed as follows:

- The output spectrum is measured as a function of the second order dispersion for different input powers.
- The spectral broadening of the pulses, 2σ, is estimated from the measurements for each input power, employing the equation 7.9.
- We numerically simulate the output spectrum for different nonlinear phase shifts, ϕ_{NL}, until the peak-to-peak value in the simulated 2σ curve matches the peak-to-peak value extracted from the measurements.
- Once the nonlinear phase shift is fitted, the nonlinear refractive index (n_2), is obtained from equation 7.6.

Following the process described above, we performed the measurements of the output spectra as a function of the second order dispersion for the input power of: 0.1 mW, 2.5 mW, 5 mW, 7 mW and 10 mW. As an example, Fig. 7.5-a shows the measured output spectra as a function of the second order dispersion for the maximum power, 10 mW. Figure 7.5-b shows the spectral broadening of the pulses, 2σ, for the different input powers using equation 7.9. Figure 7.5-d shows the simulated 2σ as a function of the dispersion for different values of ϕ_{NL}.

Comparing the simulations (Fig. 7.5-d) with the measurements (Fig. 7.5-b) we obtained ϕ_{NL}= 0.16 rad. Note that the high 2σ level estimated for pump power of 0.1 mW is an effect of measurement noise. The measured signal for this pump power is comparatively low, making the estimation of the 2σ highly sensitive to experimental variations and noise. Figure 7.5-c represents the simulated output spectra when ϕ_{NL}= 0.16 rad. These results are in good agreement with the measurements represented in Fig. 7.5-a. Taking into account the geometry of the waveguide (width = 800 nm and height = 400 nm), and the air cladding, we have calculated the nonlinear area employing the equation 7.7, obtaining a value of $A_{NL} = 0.695\,\mu$m^2. Considering ϕ_{NL}= 0.16 rad and $A_{NL} = 0.695\,\mu$m^2, from equation 7.6 we extracted a nonlinear refractive index for the SiN waveguide of $n_2^{SiN} \approx 2.87\times10^{-19}$ m^2/W, in a good agreement with the previous data reported in the literature [157].

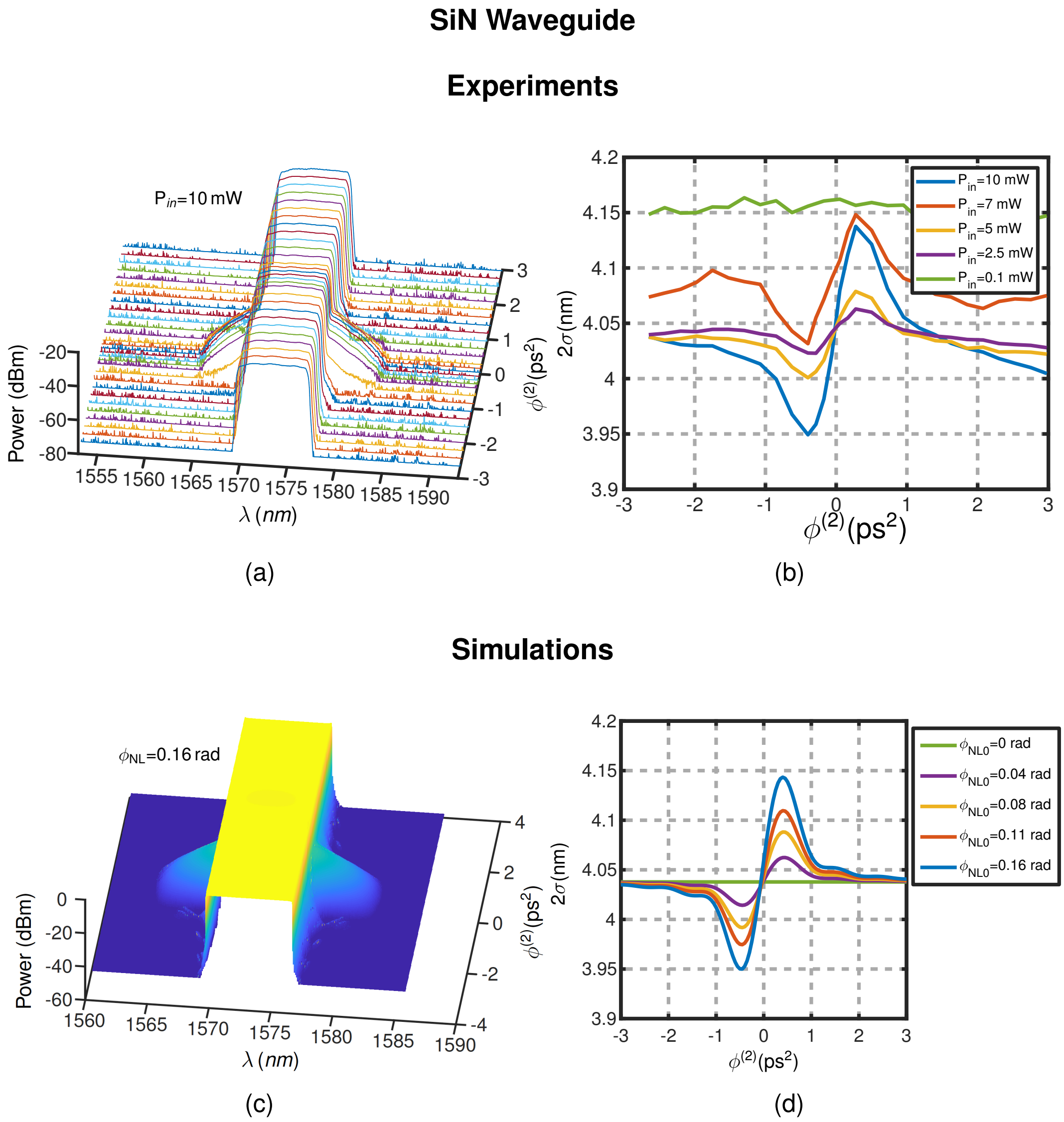

Figure 7.5.: Measurements and simulations for silicon nitride waveguide without cladding. a) Output spectra as a function of the second order dispersion for na input power of 10 mW. b) Spectral broadening of the pulses, 2σ, calculated from the experimental data. c) and d) simulated spectrum considering the experimental conditions.

Once our characterization method is validated, we established a set of measurements to determine the influence by chirality in the nonlinear refractive index. The measurements are made on the same waveguide following the order:

1. **Characterization of SiN waveguide covered by polymer (PFO)**. These measurements help us quantify the effect of the polymer on the nonlinear refractive index. This is important since the solutions of carbon nanotubes

presented in this work are mainly composed of polymer.

2. **Characterization of SiN waveguide covered by HiPco solution**. Allows us to study the effect of the different chiralities present in this solution.

3. **Characterization of SiN waveguide covered by CoMoCat solution**. Finally we employ a semiconducting SWCNTs solution with a single predominant chirality.

It is worth to mention that we are not going to directly characterize the nonlinear refractive index of the different bulk materials (PFO, HiPco, CoMoCAT). We are going to characterize hybrid waveguides composed by SiN and semiconducting SWCNTs. In this kind of waveguide,s the semiconducting SWCNTs are placed onto the waveguides. For this reason, the interaction between optical mode and material is produced through the evanescent field of the waveguide optical mode. Considering the waveguide topology, the calculated percentage of the optical mode in the cladding is 30 %. Also, this cladding is basically composed of PFO with a few quantity of semiconducting SWCNTs randomly distributed. Therefore not all of the SWCNTs are parallel to the electric field where they present the maximum interaction [53]. For the reasons listed above, the measured nonlinear refractive index in hybrid waveguides is smaller than that in the bulk material.

A) Characterization of SiN waveguide covered by polymer (PFO).

The nonlinear characterizations of the same SiN waveguide covered by polymer, PFO, are first carried out. We prepared a new solution following the same steps as for solution D, described in chapter 3, without adding the SWCNTs powder. Employing the Fabry-Perot method, we have estimated the propagation losses in $\alpha = 2.84 \pm 0.40\,\mathrm{cm}^{-1}$, obtaining a $L_{eff} = 0.27\,\mathrm{cm}$. As we can see in Fig. 7.6, P_{out} as a function of P_{in} follows a linear function which indicates no presence of TPA. From this measurement, we obtain the coupling coefficient in the sample facet, $\kappa_F = 13\,\%$.

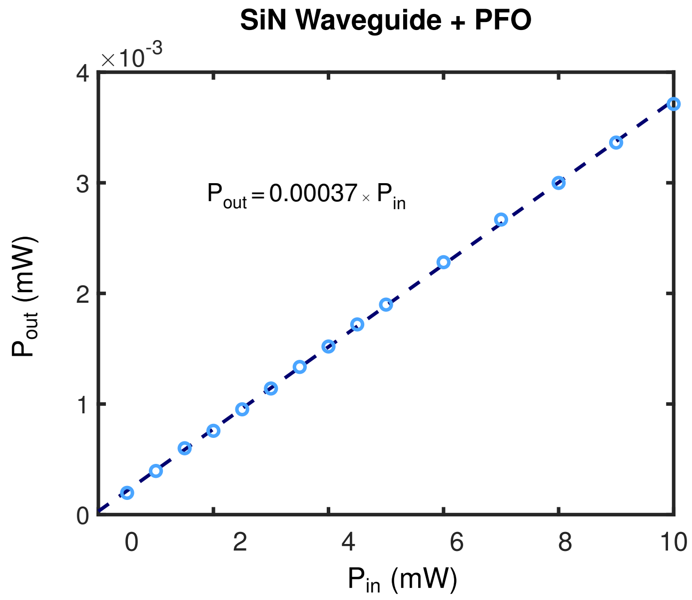

Figure 7.6.: Characterization of a SiN waveguide covered by PFO solution. The output power as a function of the input power shows a linear relationship verifying the absence of two photon absorption (TPA).

Figure 7.7-a shows the measured output spectra as a function of the second order dispersion for the maximum power, 10 mW. The corresponding 2σ calculated from the experiments for the different input powers is shown in Fig. 7.7-b. The simulated 2σ as a function of the dispersion for different values of ϕ_{NL} is represented in Fig. 7.7-d. The nonlinear phase shift ϕ_{NL}=0.03 rad is extracted comparing the peak-to-peak value from simulations (Fig. 7.7-d) and measurements (Fig. 7.7-b). In this case we have calculated the nonlinear area considering as a cladding the refractive index of 1.6 that correspond to the PFO [108], resulting in $A_{NL} = 0.879\,\mu\text{m}^2$. In this situation, we have obtained a $n_2^{SiN+PFO} \approx$ 2.6×10^{-19} m^2/W practically the same as in the previous case, so we can consider that the nonlinear contribution of PFO on the cladding is negligible for the nonlinear refractive index of the hybrid SiN waveguide at this wavelength range.

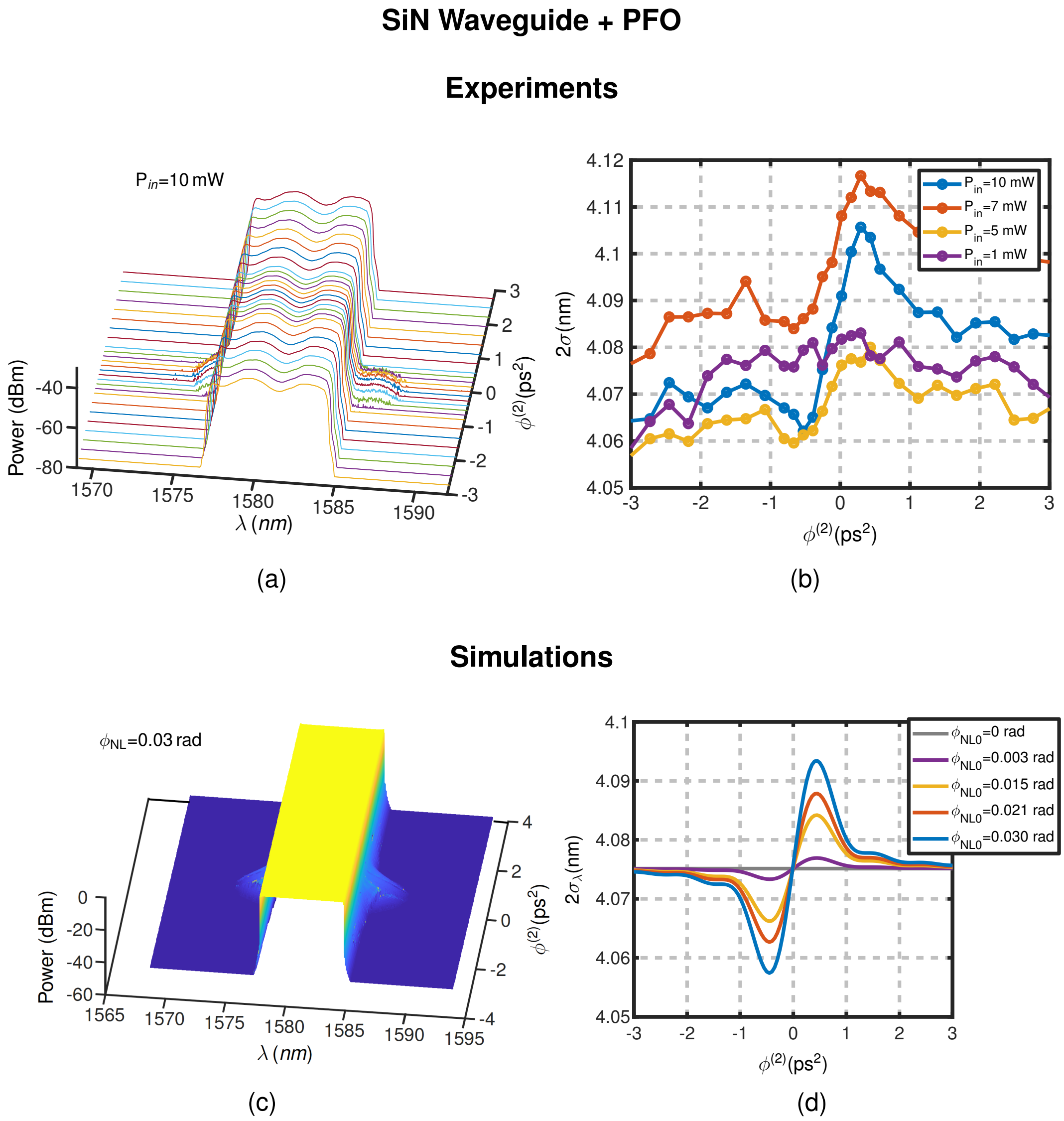

Figure 7.7.: Measurements and simulations for silicon nitride waveguide covered by PFO. a) Output spectra as a function of the second order dispersion for a input power of 10 mW. b) Spectral broadening of the pulses, 2σ, calculated from the experimental data. c) and d) simulated spectrum considering the experimental conditions.

B) Characterization of SiN waveguide covered by HiPco solution.

In the previous measurements we have seen that the influence on nonlinear coefficient of the polymer is negligible, therefore we can guarantee that the results obtained in the measurements using the HiPco solution are exclusively due to the different chiralities comprised in the solution.

After cleaning the sample with piranha solution, the HiPco solution (solution D presented in chapter 3) is deposited.

The propagation losses have been estimated with the Fabry-Perot method in $\alpha = 2.84 \pm 0.40\,\mathrm{cm}^{-1}$, leading to a $L_{eff} = 0.27$ cm. From the measurements of P_{out} vs P_{in}, represented in Fig. 7.8, we observed that both magnitudes follow a linear relationship that means the waveguide presents no TPA. By linear regression κ_l = 0.0003473 is identified, resulting in $\kappa_F \sim 16\%$.

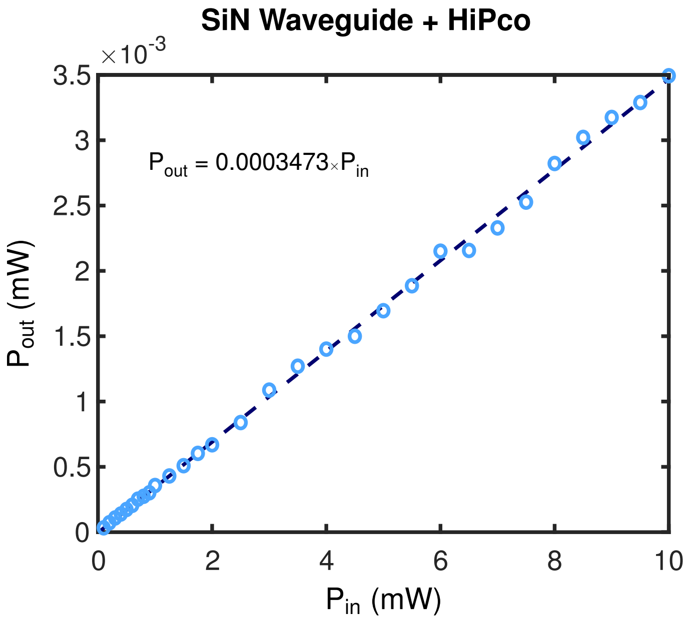

Figure 7.8.: Characterization of a SiN waveguide covered by HiPco semiconducting SWCNTs solution. The output power as a function of the input power shows a linear relationship verifying absence of TPA.

As in the previous case, the nonlinear area is $A_{NL} = 0.879\,\mu\mathrm{m}^2$. Figure 7.9-a shows the output spectra as a function of the second order dispersion when the input power is 14.5 mW. In Fig. 7.9-b the calculated 2σ from the experiments for the different power under analysis is presented. Figure 7.9-d shows the simulated 2σ curve as a function of the dispersion for different values of the nonlinear phase shift, ϕ_{NL}. Comparing the peak-to-peak value from simulations (Fig.7.9-d) and measurements (Fig.7.9-b), the ϕ_{NL}= -0.116 rad is extracted. Figure 7.9-c plots the simulated output spectra when ϕ_{NL}= -0.116 rad, in good agreement with the measurements (Fig. 7.9-a). With nonlinear phase shift of ϕ_{NL}= -0.116 rad and equation 7.6 we obtained a negative nonlinear refractive index for a hybrid SiN waveguide covered by HiPco SWCNTs of $n_2^{SiN+HiPco} \approx$ -

5.82×10^{-19} m^2/W. This value is very different to the one obtained from SiN waveguide characterization. Then we can conclude that the HiPco SWCNTs induced a negative Kerr effect.

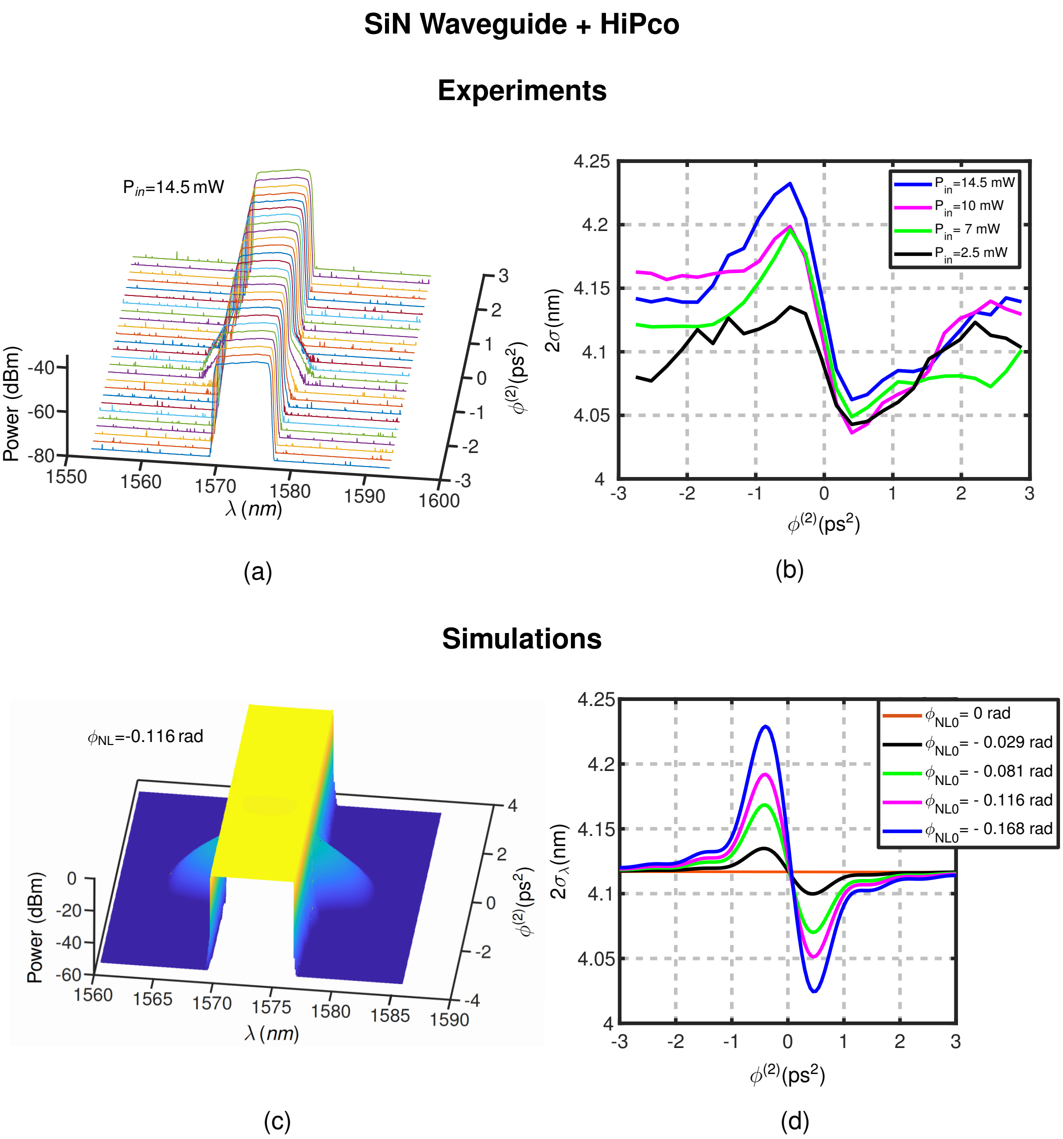

Figure 7.9.: Measurements and simulations for silicon nitride waveguide covered by HiPco SWCNTs solution. a) The output spectra as a function of the second order dispersion for a input power of 14.5 mW. b) Spectral broadening of the pulses, 2σ, calculated from the experimental data. c) and d) simulated spectrum considering the experimental conditions.

C) Characterization of SiN waveguide covered by CoMoCAT solution.

We performed the nonlinear characterization of the same waveguide, in this case covered by semiconducting SWCNTs CoMoCAT solution. Before the semiconducting SWCNTs deposition the sample is cleaned with piranha solution. As in the previous cases, the propagation losses have been estimated in $\alpha = 2.84 \pm 0.40\,\mathrm{cm}^{-1}$ with a calculated $L_{eff} = 0.27\,\mathrm{cm}$. In Fig. 7.10 P_{out} as a function of P_{in} is represented. It follows a linear relationship that indicate no presence of two photon absorption. Using the linear regression $\kappa_l = 0.0002995\,\%$ is extracted, leading to $\kappa_F \sim 14\%$.

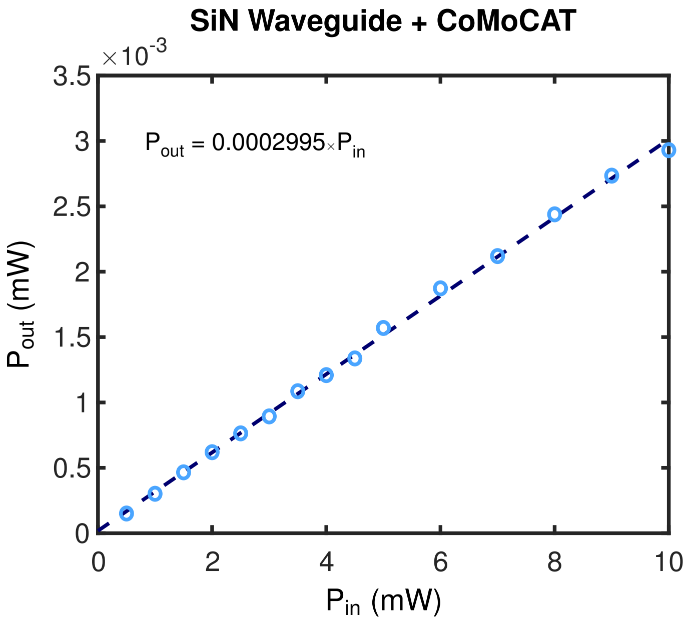

Figure 7.10.: Characterization of a SiN waveguide covered by CoMoCAT semiconducting SWCNTs solution. The output power as a function of the input power shows a linear relationship verifying absence of TPA.

Figure 7.11-a shows the output spectra as a function of the second order dispersion at the power of 10 mW. The experimental 2σ as a function of the dispersion for different excitation power are represented in Fig. 7.11-b. Figure 7.11-d presents the simulated 2σ for different values of the nonlinear phase shift, ϕ_{NL}. Comparing simulations (Fig. 7.11-d) and measurements (Fig. 7.11-b), $\phi_{NL} = 0.039\,\mathrm{rad}$ is extracted. As before, the calculated nonlinear area is $A_{NL} = 0.879\,\mu\mathrm{m}^2$. Considering the preceding values and equation 7.6, we determine a positive nonlinear refractive index for hybrid SiN waveguide covered by CoMoCAT solution of $n_2^{S_iN+CoMoCAT} \approx 5.32 \times 10^{-19}\,\mathrm{m}^2/\mathrm{W}$. This value, different to the one obtained in SiN waveguide and has an opposite sign in compar-

ison of SiN waveguide covered with HiPco solution.

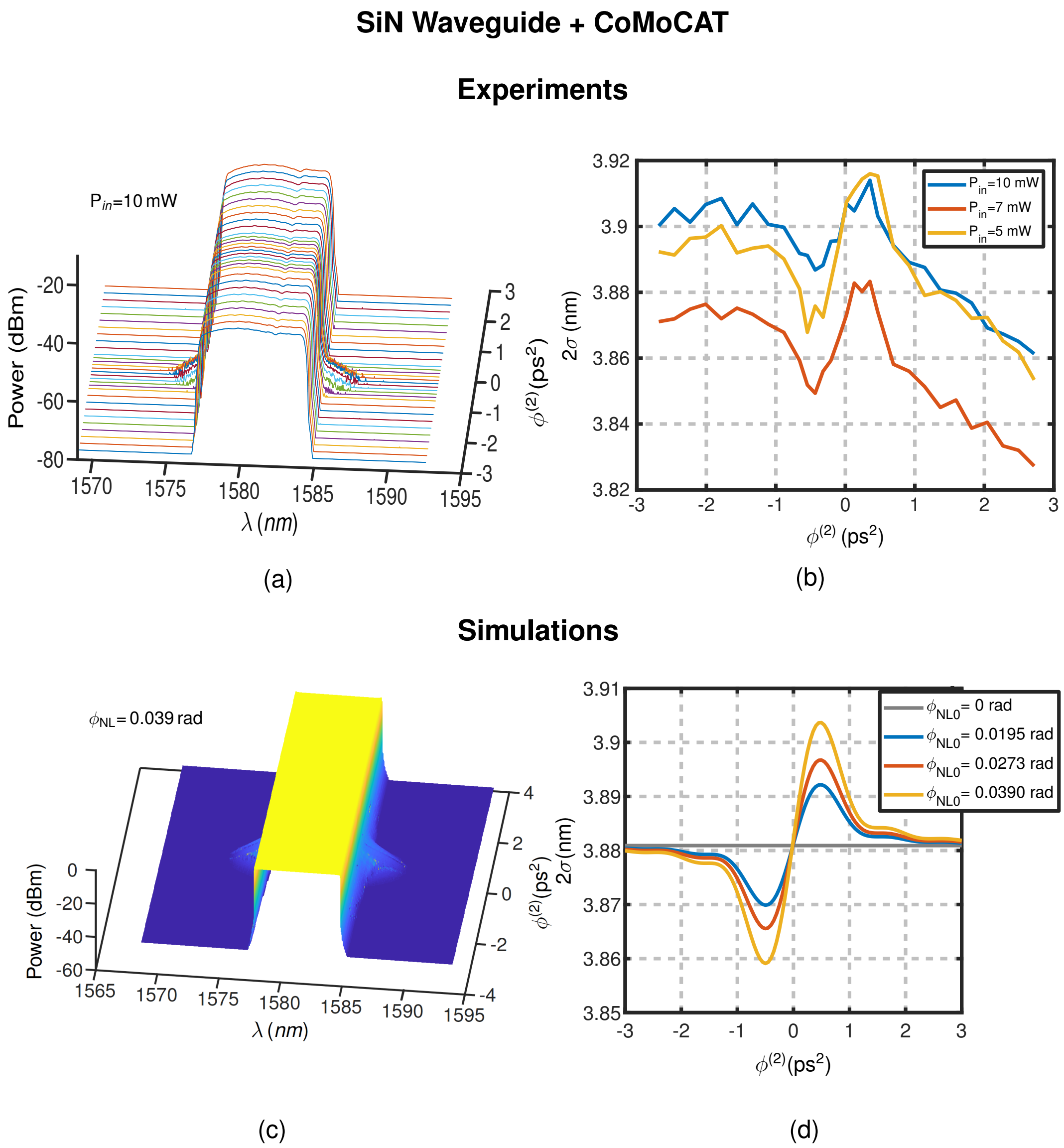

Figure 7.11.: Measurements and simulations for silicon nitride waveguide covered by CoMoCAT solution. a) The output spectra as a function of the second order dispersion for a input power of 10 mW. b) Spectral broadening of the pulses, 2σ, calculated from the experimental data. c) and d) simulated spectrum considering the experimental conditions.

7.3. Discussion and analysis of kerr effect in SWCNTs

To qualitatively explain the nonlinear experiments presented above, showing negative n_2 for HiPco SWCNTs solution and positive n_2 for CoMoCAT SWCNTs solution, we used a generic model describing nonlinear coefficient of semiconductor materials. This model relates the value of n_2 to the value of the semiconductor bandgap. Note that this model was not developed for SWCNTs but for semiconducting materials in general. This approach is based on the two band model and the Kramers-Krönig relation to predict the non-resonant third order nonlinear effects of semiconductors and wide-gap solids at given wavelengths with respect to the material energy bandgap [158]. The expression is defined by

$$n_2(\omega) = \frac{40\pi\sqrt{E_p}}{cn_0^2E_g^4}K'G_2\left(\frac{\hbar\omega}{E_g}\right), \tag{7.10}$$

where E_g is the gap energy of the material, n_0 refractive index of the material, $E_p = 21\,\mathrm{eV}$ and K' is 1.5×10^{-8} when the energies are in eV. The dispersion function G_2 depends on the contributions from different physical origins: two-photon transitions (TPA and Raman (R)), linear Stark (LS), quadratic Stark (QS) and a divergent term (DT).

Figure 7.12-a presents the normalized optical absorption for the CoMoCAT solution developed in chapter 3. As we can see, this solution is constituted by a predominant semiconducting SWCNTs chirality, (7,5), with absorption near 1040 nm (that corresponds with an energy gap of ~ 1.181 eV). We calculated the theoretical Kerr coefficient for this solution applying equation 7.10 for a pump wavelength of 1580 nm. The theoretical Kerr index is $n_2^{(7,5)} \sim 3.386\times10^{-17}\mathrm{m}^2/\mathrm{W}$ as it is represented in Fig. 7.12-c in dark blue. We performed the same calculation for the chiralities present in HiPco solution. As it is shown in 7.12-b, this solution presents five different chiralities with energy gap comprised between 0.90 eV and 1.2 eV. The calculated Kerr coefficients are represented in light blue in Fig. 7.12-c. In this case, we observed that chiralities with gap wavelength below 1150 nm present n_2 positive, while the rest are negative. The n_2 values of SWCNTs are expected to be one order of magnitude larger than the n_2 of silicon [156] and two orders larger than the one of silicon nitride [157]. Even larger values have been predicted in the literature [78–80] but for differ-

ent class of nanotubes and excitation wavelengths. Considering the absorption spectrum for CoMoCAT and HiPco solution, represented in Fig. 7.12-a and -b, respectively, we can extract the relative concentration of each nanotube chirality in the solution. By weighting the contribution of each nanotube with respect to their relative presence in the solution (peak value), we have obtained a contribution from the ensemble such that: $n_2^{CoMoCAT} \sim n_2^{(7,5)} \sim 3.386\times10^{-17}$m^2/W and $n_2^{HiPco} = 0.6 \times n_2^{(10,2)} + 0.72 \times n_2^{(9,4)} + n_2^{(8,6)} + 0.47 \times n_2^{(8,7)} + 0.36 \times n_2^{(9,7)} = -2.24 \times 10^{-17}$m^2/W at 1.55 μm. Due to the different contribution of each chirality, we obtained a negative nonlinear refractive index for HiPco solution. The sign of n_2 predicted by this model, positive for CoMoCAT and negative for HiPco, is in very good agreement with the experimental results. Note that this simple model considers the effect in ideal bulk s-SWCNT material, neglecting the effects of having an hybrid SiN waveguide with randomly distributed SWCNTs. The difference in magnitude between theoretical and experimental values can be attributed to these non-idealities. Given that bandgap engineering plays an important role in the third order optical nonlinearities, we are able to deliberately tailor the effective nonlinear optical response in hybrid SWCNT-on-SiN integrated waveguides.

These results show that the flexible bandgap tunning in s-SWCNT opens new degrees of freedom to control the nonlinear properties of integrated waveguides, allowing the implementation of effective Kerr nonlinear indices with possitive and negative sign.

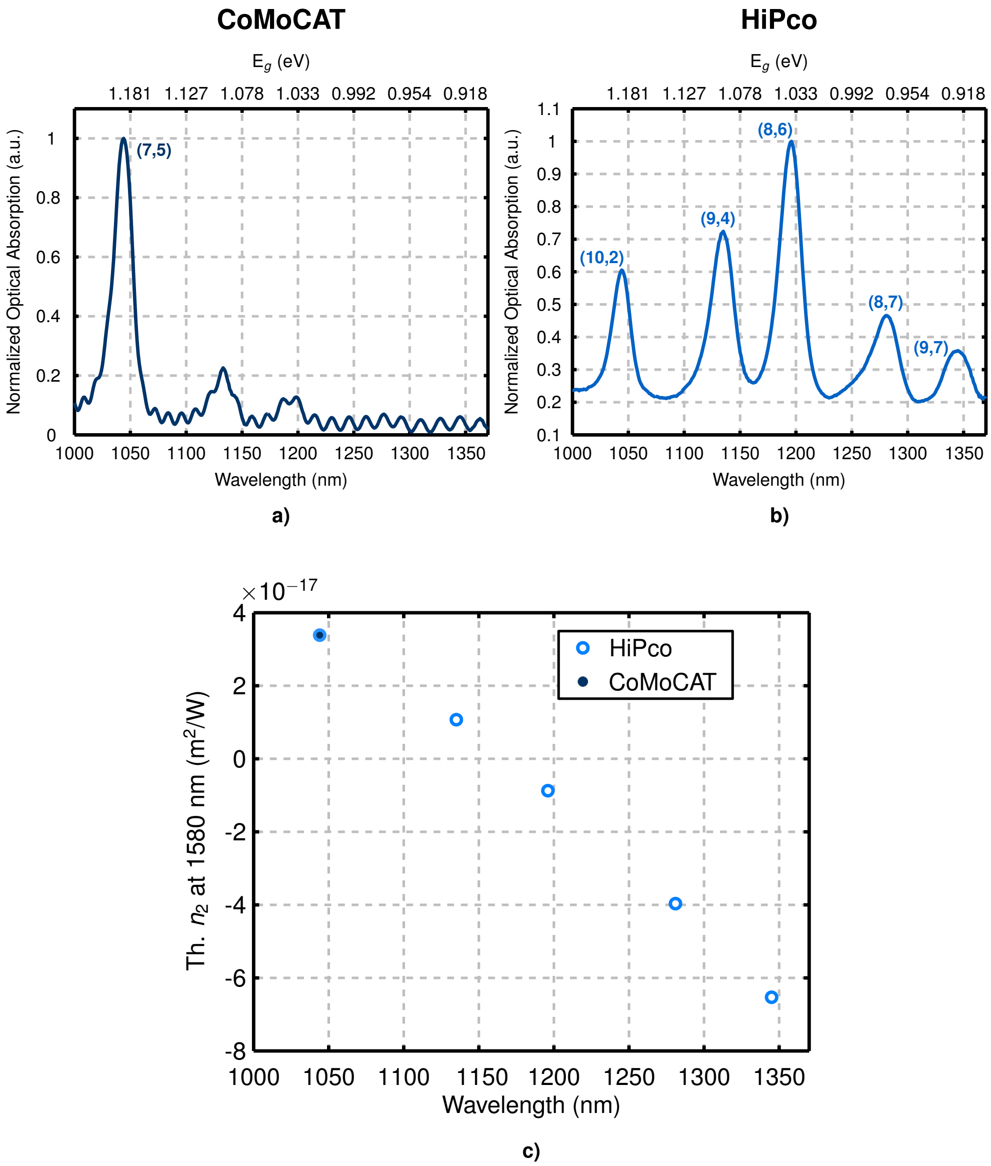

Figure 7.12.: Normalized optical absorption for CoMoCAT in a) and HiPco in b) solution prepared during this thesis work. c) Theoretical estimation of the Kerr coefficient of each chirality present in CoMoCAT and HiPco solution represented in dark blue and light blue, respectively.

7.4. Conclusions

In this chapter, we have performed the nonlinear characterizations of hybrid SiN waveguide covered by SWCNTs. We have determined that the nonlinear refractive index of hybrid SiN waveguides covered by CoMoCAT solution is positive while being negative for the waveguides covered by HiPco solution. We have explained these results employing a generic theoretical model for semiconductor materials. That allowed us to theoretically relate the sign of the nonlinear coefficient and the SWCNT chirality. We report here the first experimental demonstration of negative nonlinear refractive index for hybrid waveguide of SiN and SWCNTs layers. These results represent, to the best of our knowledge, the first demonstration of a negative nonlinear refractive index in integrated devices. These results open a new route for the development of the future all-optical ultra fast circuits based in third order non linear effects. These key results offer promising routes to compensate unwanted refractive nonlinear effects or to enhance them towards Kerr modulation in integrated waveguides.

8

Conclusions and Prospects

In this thesis a complete work about the integration of s-SWCNTs on Si photonics platform has been presented. This manuscript began with an overview of the structure and optical properties of carbon nanotubes, with a especial mention on the purification methods and deposition techniques. A significant amount of time has been employed to optimize the semiconducting SWCNTs solutions. Different deposition techniques, integration schemes and photonics structures have been analyzed. First experimental demonstrations of key functionalities based on optical and electrical excitation, as well as non linear phenomena have been reported.

In this work, a large number of s-SWCNTs solutions emitting from 1 μm to $1.6\,\mu$m has been developed. More specifically, a solution based on CoMoCAT SWCNTs compound for almost a single chirality with emission at $\sim 1\mu$m. A second solution based on HiPco SWCNTs to cover the datacom wavelength range, centered at $\sim 1.3\,\mu$m, and a solution based on Laser ablation SWCNTs, with emission at $\sim 1.5\,\mu$m, to cover the telecom wavelength range. CoMoCAT and HiPco solutions have been developed to work with optical excitation, while Laser ablation solution has been conceived to work with electrical injection. The first year of my PhD has been mainly dedicated to improve the concentration in the HiPco solution. In this work, a double selection process (polymer extraction followed by ultraconcentration step) has been optimized to increase the semiconducting SWCNTs concentration. We have obtained an improvement of ~ 45 times of the s-SWCNTs concentration with respect the previous thesis works.

In parallel with the solution optimization, we have demonstrated photoluminescence resonant enhancement in different photonic structures. First, we have analyzed different waveguide geometries to improve the light matter interaction. We have presented the first experimental demonstration of integration of carbon nanotubes with slot ring resonators. We have also studied the integration with small mode volume cavities, showing the first integration with 2D hollow-core photonic crystals. We have analyzed the polarization effect. We have shown that, contrary to the common knowledge, it is possible to exploit the longitudinal electric field component in TM modes to efficiently interact with the s-SWCNTs aligned parallel to the chip surface. We have proposed a novel selective deposition process, implementing interaction windows on a HSQ cladding to reduce the losses from the non excited carbon nanotubes. We have presented first preliminary results on the collinear excitation of s-SWCNTs using the silicon nitride on insulator platform. This collinear excitation approach will allow us to have both pump and PL signal resonant enhancement in micro-resonators.

Working on micro-disk resonators in TM polarization, we have shown for the first time nonlinear behavior in the collected PL signal as a function of the pumping power. We have simultaneously observed an superlinear emission and spectral narrowing of the emission peak after a given pump power threshold. These features are reproducible in different micro-disk resonators with different radii. These results are an important first step towards the demonstration of an integrated laser based on CNTs. Measurements of second order photon correlation are planned to further elucidate the origin of this behavior and confirm the lasing effect.

Using electrical injection, we have demonstrated emitter and detector on surface using arrays of s-SWCNTs aligned by DEP. We have demonstrated that the use of asymmetric contact (Sc-Pt) improves the performance of both emitter and detector. We have also shown that the photocurrent present a strong dependence with the light polarization, which indicates the high degree of nanotube alignment and also excludes the possibility that the observed photocurrent is related to a photo-thermoelectric effect. We have designed, fabricated and measured the first optical link based on semiconducting SWCNTs integrated on SiN photonics platform. We have estimated a responsivity of $\sim 0.1\ \mu$A/mW.

We have also theoretically analyzed and experimentally validated the evolution of nonlinear refractive index (Kerr effect) as a function of SWCNT chirality. We have determined that the nonlinear refractive index of SWCNTs HiPco is negative, while being positive for CoMoCAT. We have presented first experimental demonstration of negative nonlinear refractive index for hybrid waveguide of SiN and SWCNTs layers. This key results offer promising routes to compensate unwanted refractive nonlinear effects or to enhance them towards Kerr modulation in integrated waveguides.

The first objective after this work is to conclude the laser demonstration. To do so, we will work on the sample presented in chapter 5 performing measurements of second order photon correlation ($g^{(2)}(0)$), to discern between thermal emission ($g^{(2)}(0) \sim 2$) and lasing effect ($g^{(2)}(0) \sim 1$).

In addition, we will analyze this effect in: i) small mode volume cavities, presented in section 4.3 and ii) SiN ring resonator fabricated in collaboration with St Microelectronic that present Q factors larger than 1000000.

As a long term objectives, I propose to study several points to further improve the hybrid integration of SWCNTs with photonic devices. Indeed, taking into account the advantages of the deposition by DEP, resulting arrays of s-SWCNTs well aligned and with location control, we can substantially improve light interaction between optical mode and SWCNTs, avoiding parasitic absorption of the signal.

After the preliminary promising results of the collinear excitation in the waveguides, we will extend it to the disk and ring resonators to study the photoluminescence resonance enhancement when the wavelength of the pump also resonates in the structure.

I also propose to use the same integration approach to integrate electrical pumping of SWCNTs on ring resonators and cavities to demonstrate the first laser based on SWCNTs with electrical injection.

The promising results on nonlinear effect variation with SWCNT chirality open a new route to compensate unwanted refractive nonlinear effects or to enhance them towards Kerr modulation in integrated waveguides. We have also explained that this nonlinear coefficient is lower than theoretically expected, due to the lack control on the alignment and placed of SWCNTs. To further control the nonlinear refractive index in hybrid waveguides, I propose to deposit s-SWCNTs by DEP which will allow us to increase the nonlinear refraction index per unit of length. This improvement may allow a fine control of the nonlinear refractive index of hybrid photonic guides.

In the long term, the demonstration of an optical laser with SWCNTs on a Si photonics platform would open a whole new range of opportunities to develop a new generation of hybrid photonics circuits with immense potential for applications in Datacom, sensing and quantum photonics.

A
Publication list

International Journal Papers

1. C. Alonso-Ramos, X. Le Roux, D. Benedikovic, V. Vakarin, **E. Durán-Valdeiglesias**, D. Pérez-Galacho, E. Cassan, D. Marris-Morini, P. Cheben, L. Vivien, "Diffraction-less propagation beyond the sub-wavelength regime: a new type of nanophotonic waveguide," Sci. Rep., 9 (1), 5347 (2019).

2. D. González Andrade, C. Lafforgue, **E. Durán-Valdeiglesias**, X. Le Roux, M. Berciano, E. Cassan, D. Marris-Morini, A. V. Velasco, P. Cheben, L. Vivien, C. Alonso-Ramos, "Polarization- and wavelength-agnostic nanophotonic beam splitter," Sci. Rep., 9 (1), 3604 (2019).

3. J. Zhang, X. Le Roux, **E. Durán-Valdeiglesias**, C. Alonso-Ramos, D. Marris-Morini, L. Vivien, S. He, E. Cassan, "Generating Fano resonances in a single-waveguide silicon nanobeam cavity for efficient electro-optical modulation," ACS Photonics 5(11), 4229 (2018).

4. S. Guerber, C. Alonso-Ramos, D. Benedikovic, **E. Durán-Valdeiglesias**, X. Le Roux, N. Vulliet, E. Cassan, D. Marris-Morini, C. Baudot, F. Boeuf, L. Vivien, "Broadband polarization beam splitter on a silicon nitride platform for O-band operation," IEEE Photon. Technol. Lett. 30(19), 1679 (2018).

5. **E. Durán-Valdeiglesias**, W. Zhang, C. Alonso-Ramos, S. Serna, X. Le Roux, D. Maris-Morini, N. Caselli, F. Biccari, M. Gurioli, A. Filoramo, E.

Cassan, L. Vivien, "Tailoring carbon nanotubes optical properties through chirality-wise silicon ring resonators," Sci. Rep. 8(1), 11252 (2018).

6. M. Balestrieri, A.?S. Keita, **E. Durán-Valdeiglesias**, C. Alonso?Ramos, W. Zhang, X. Le Roux, E. Cassan, L. Vivien, V. Bezugly, A. Fediai, V. Derycke, A. Filoramo, "Polarizationn-sensitive single-wall carbon nanotubes all-in-one photodetecting and emitting device working at 1.55 μm," Adv. Funct. Mater., 1702341 (2017).

7. T. H. C. Hoang, **E. Durán-Valdeiglesias**, C. Alonso-Ramos, S. Serna, W. Zhang, M. Balestrieri, A.-S. Keita, N. Caselli, F. Biccari, X. Le Roux, A. Filoramo, M. Gurioli, L. Vivien, E. Cassan, "Narrow-linewidth carbon nanotube emission in silicon hollow-core photonic crystal cavity," Opt. Lett. 42(11), 2228 (2017).

8. F. Biccari, F. Sarti, N. Caselli, A. Vinattieri, **E. Durán-Valdeiglesias**, W. Zhang, C. Alonso-Ramos, T. H. C. Hoang, S. Serna, X. Le Roux, E. Cassan, L. Vivien, M. Gurioli, "Single walled carbon nanotubes emission coupled with a silicon slot-ring resonator," J. Lumin. (2016).

9. J. D. Sarmiento-Merenguel, A. Ortega-Moñux, J.-M. Fédéli, J. G. Wangüemert-Pérez, C. Alonso-Ramos, **E. Durán-Valdeiglesias**, P. Cheben, I. Molina-Fernández, R. Halir, "Controlling leakage losses in subwavelength grating silicon metamaterial waveguides," Opt. Lett. 41(15), 3443 (2016).

10. F. La China, N. Caselli, F. Sarti, F. Biccari, U. Torrini, F. Intonti, A. Vinattieri, **E. Durán-Valdeiglesias**, C. Alonso-Ramos, X. Le Roux, M. Balestrieri, A. Filoramo, L. Vivien, M. Gurioli, "Near-field imaging of single walled carbón nanotubes emitting in the telecom wavelength range," Journal of Applied Physics 120 (12), 123110 (2016).

11. J. D. Sarmiento-Merenguel, A. Ortega-Moñux, J.-M. Fédéli, J. G. Wangüemert-Pérez, C. Alonso-Ramos, **E. Durán-Valdeiglesias**, P. Cheben, I. Molina-Fernández, R. Halir, "Controlling leakage losses in subwavelength grating silicon metamaterial waveguides," Opt. Lett. 41(15), 3443-3446 (2016).

12. **E. Durán-Valdeiglesias**, W. Zhang, A. Noury, C. Alonso-Ramos, T. H. C. Hoang, S. Serna, X. Le Roux, E. Cassan, N. Izard, F. Sarti, et al., "Integration of carbon nanotubes in silicon strip and slot waveguide micro-

ring resonators," IEEE Transactions on Nanotechnology 15(4), 583-589 (2016).

13. F. La China, F. Intonti, N. Caselli, F. Lotti, F. Sarti, A. Vinattieri, A. Noury, X. Le Roux, W. Zhang, E. Cassan, C. Alonso-Ramos, **E. Durán-Valdeiglesias**, N. Izard, L. Vivien, M. Gurioli, "Near-field Fano-imaging of TE and TM modes in silicon microrings," ACS Photonics 2(12), 1712-1718 (2015).

14. J.D. Sarmiento-Merenguel, R. Halir, X. Le Roux, C. Alonso-Ramos, L. Vivien, P. Cheben, **E. Durán-Valdeiglesias**, I. Molina-Fernández, D. Marris-Morini, D.-X. Xu, J.H. Schmid, S. Janz, A. Ortega-Moñux, "Demonstration of integrated polarization control with a 40 dB range in extinction ratio," Optica 2(12), 1019-1023 (2015).

15. J. M. Ávila-Ruiz, A. Moscoso-Mártir, **E. Durán-Valdeiglesias**, L. Moreno-Pozas, J. de-Oliva-Rubio, I. Molina-Fernández, "Six-port-based architecture for phase noise measurement in the UWB band," Journal of Electrical and Computer Engineering 2014, 3 (2014).

16. J. M. Ávila-Ruiz, L. Moreno-Pozas, **E. Durán-Valdeiglesias**, A. Moscoso-Mártir, J. de-Oliva-Rubio, I. Molina-Fernández, "Frequency locked loop architecture for phase noise reduction in wideband low-noise microwave oscillators," IET Microwaves, Antennas & Propagation 7(11), 869-875 (2013).

International Conferences

1. D. Oser, X. Le Roux, F. Mazeas, D. Pérez-Galacho, D. Benedikovic, **E. Durán-Valdeiglesias**, V. Vakarin, O. Alibart, P. Cheben, S. Tanzilli, L. Labonté, D. Marris-Morini, E. Cassan, L. Vivien, C. Alonso-Ramos, "Harnessing sub-wavelength and symmetry engineering for the implementation of high-performance silicon Bragg grating filters," International Conference on Transparent Optical Networks (ICTON), July 2019, Angers, France (Invited).

2. C. Alonso-Ramos, P. Cheben, R. Halir, J.H. Schmid, J. ?tyroky?, D. Benedikovic, A. Ortega-Moñux, A. Sánchez-Postigo, D. González-Andrade, J.

G. Wangu?emert-Pérez, I. Molina-Fernández, A. V. Velasco, A. Herrero-Bermello, J. M. Luque-González, D. Pereira-Martín, J. Lapointe, S. Janz, D.-X. Xu, D. Melati, Y. Grinberg, S. Wang, M. Vachon, M. Kamandar Dezfouli, R. Cheriton, V. Vakarin, M. Dado, D. Oser, F. Mazeas, D. Pérez-Galacho, X. Le Roux, **E. Durán-Valdeiglesias**, L. Labonte, S. Tanzilli, E. Cassan, D. Marris-Morini, L. Vivien, "Recent advances on nanostructured metamaterial silicon photonics," Progress In Electromagnetics Research Symposium (PIERS), June 2019, Rome, Italy (Invited).

3. C. Alonso-Ramos, P. Cheben, J. Schmid, D. Oser, X. Le Roux, F. Mazeas, D. Pérez-Galacho, D. Benedikovic, **E. Durán-Valdeiglesias**, V. Vakarin, O. Alibart, S. Tanzilli, L. Labonté, D. Marris-Morini, J. ?tyroky?, J.G. Wanguemert-Pérez, I. Molina-Fernández, A. Ortega-Moñux, R. Halir, M. Dado, E. Cassan, F. Boeuf, C. Baudot, L. Vivien, "High-performance fiber-chip grating couplers and wavelength filters based on subwavelength engineering in silicon," Progress In Electromagnetics Research Symposium (PIERS), June 2019, Rome, Italy (Invited).

4. D. Oser, X. Le Roux, F. Mazeas, D. Pérez-Galacho, D. Benedikovic, **E. Durán-Valdeiglesias**, V. Vakarin, O. Alibart, P. Cheben, S. Tanzilli, L. Labonté, D. Marris-Morini, E. Cassan, L. Vivien, C. Alonso-Ramos "High-performance silicon Bragg filters based on sub-wavelength, symmetry and modal engineering," IEEE International Frequency Control Symposium & European Frequency and Time Forum (IFCS-EFTF), April 2019, Orlanso, USA (Invited).

5. **E. Durán-Valdeiglesias**, W. Zhang, C. Alonso-Ramos, T. H. C. Hoang, S. Serna, X. Le Roux, M. Balestrieri, D. Maris-Morini, N. Caselli, F. Biccari, M. Gurioli, A. Filoramo, E. Cassan, L. Vivien, "Shaping on-chip optical properties of hybrid silicon carbon nanotube photonics circuits," SPIE Photonics West, Feb. 2019, San Francisco, USA (Invited).

6. D. Oser, X. Le Roux, F. Mazeas, D. Pérez-Galacho, D. Benedikovic, **E. Durán-Valdeiglesias**, V. Vakarin, O. Alibart, P. Cheben, S. Tanzilli, L. Labonté, D. Marris-Morini, E. Cassan, L. Vivien, C. Alonso-Ramos, "High-performance silicon Bragg filters exploiting sub-wavelength and symmetry engineering," SPIE Photonics West, Feb. 2019, San Francisco, USA (Invited).

7. C. Alonso-Ramos, D. Perez-Galacho, X. Le Roux, D. Benedikovic, F. Mazeas, W. Zhang, S. Serna, V. Vakarin, **E. Durán-Valdeiglesias**, N. Belabas-Plougonven, L. Labonte, S. Tanzilli, P. Cheben, E. Cassan, D. Marris-Morini, L. Vivien, "Subwavelength engineered silicon photonics," International Workshop on Advanced Materials Science and Nanotechnology (IWAMSN), November 2018, Ninh Binh, Vietnam (Invited).

8. D. Oser, X. Le Roux, F. Mazeas, D. Pérez-Galacho, D. Benedikovic, **E. Durán-Valdeiglesias**, V. Vakarin, O. Alibart, P. Cheben, S. Tanzilli, L. Labonté, D. Marris-Morini, E. Cassan, L. Vivien, C. Alonso-Ramos "High-performance on-chip Bragg grating filters," Asia Communications and Photonics Conference (ACP), October 2018, Hangzhou, China (Invited).

9. E, Cassan, W. Zhang, **E. Durán-Valdeiglesias**, X. Le Roux, S. Serna, N. Caselli, F. Biccari, C. Alonso-Ramos, A. Filoramo, M. Gurioli, L. Vivien, "Hybrid integration of carbon nanotube emitters into silicon photonic nanoresonators," SPIE Photonics West, Feb. 2018, San Francisco, USA (Invited).

10. **E. Durán-Valdeiglesias**, W. Zhang, T.-H.-C. Hoang, C. Alonso-Ramos, X. Le Roux, S. Serna, M. Balestrieri, D. Marris-Morini, E. Cassan, F. Intonti, F. Sarti, N. Caselli, F. La China, M. Gurioli, A. Filoramo, L. Vivien, "Integration of carbon nanotubes on silicon photonic micro-cavities and resonators," IEEE International Conference on Group IV Photonics (GFP), August 2017, Berlin, Germany.

11. **E. Durán-Valdeiglesias**, W. Zhang, C. Alonso-Ramos, X. Le Roux, S.Serna, H.C. Hoang, M. Balestrieri, D. Marris-Morini, E. Cassan, F. Intonti, F. Sarti, N.Caselli, F. La China, M. Gurioli, A. Filoramo, L. Vivien "Hybrid integration of carbon nanotubes in silicon photonics resonators," European Conference on Integrated Optics (ECIO), May 2017, Eindhoven, Netherlands.

12. W. Zhang, **E. Durán-Valdeiglesias**, S. Serna, N. Caselli, F. Biccari, C. Alonso-Ramos, X. Le Roux, A. Filoramo, M. Gurioli, L. Vivien, E. Cassan, "Efficient excitation of silicon photonic cavity modes from carbon nanotube photoluminescence," Asia Communications and Photonics Conference (ACP), November 2017, Guangdong, China.

13. P. Cheben, C. Alonso-Ramos, J.H. Schmid, R. Halir, A. Sánchez-Postigo, A. Ortega-Moñux, G. Wangüemert-Pérez, I. Molina-Fernández, J.M. Luque-González, J.D. Sarmiento-Merenguel, D.-X. Xu, S. Janz, J. Lapointe, S. Wang, M. Vachon, X. Le Roux, **E. Durán-Valdeiglesias**, D. Benedikovic, J. Litvík, M. Dado, D. Pérez-Galacho, S. Guerber, D. Oser, F. Mazeas, W. Zhang, S. Serna, V. Vakarin, L. Labonte, S. Tanzilli, J. Soler Penadés, M. Nedeljkovic, G.Z. Mashanovich, F. Bœuf, C. Budot, E. Cassan, D. Marris-Morini, L. Vivien, "Subwavelength engineered metamaterial silicon photonic devices," Asia Communications and Photonics Conference (ACP), November 2017, Gangzhou, China (Invited).

14. C. Alonso-Ramos, X. Le Roux, D. Benedikovic, V. Vakarin, **E. Durán-Valdeiglesias**, D. Oser, D. Pérez-Galacho, E. Cassan, D. Marris-Morini, P. Cheben, L. Vivien, "Bragg grating filter for suspended silicon waveguides," IEEE International Conference on Group IV Photonics (GFP), August 2017, Berlin, Germany.

15. P. Cheben, C. Alonso-Ramos, J.H. Schmid, R. Halir, A. Sánchez-Postigo, A. Ortega-Moñux, J.G. Wangüemert-Pérez, I. Molina-Fernández, J.M. Luque-Gonzalez, J.D. Sarmiento-Merenguel, D.-X. Xu, S. Janz, J. Lapointe, S. Wang, M. Vachon, X. Le Roux, **E. Durán-Valdeiglesias**, D. Benedikovic, D. Marris-Morini, L. Vivien, J. Litvík, M. Dado, "Subwavelength grating metamaterial engineering for silicon nanophotonic devices," Pacific Rim Conference on Lasers and Electro-Optics (CLEO-PR), November 2017, Singapore (Invited).

16. P. Cheben, D. Benedikovic, C. Alonso-Ramos, J.H. Schmid, R. Halir, A. Ortega-Moñux, J.G. Wangüemert-Pérez, I. Molina Fernández, J.M. Luque-Gonzalez, J.D. Sarmiento-Merenguel, D.-X. Xu, S. Janz, S. Wang, M. Vachon, X. Le Roux, **E. Durán-Valdeiglesias**, D. Marris-Morini, L. Vivien, A.V. Velasco, M. Dado, "Subwavelength index engineered integrated photonic devices," IEEE International Conference on Optical Communications and Networks (ICOCN), August 2017, Wuzhen, China (Invited).

17. C. Alonso-Ramos, D. Pérez-Galacho, D. Oser, X. Le Roux, D. Benedikovic, F. Mazeas, W. Zhang, S. Serna, V. Vakarin, **E. Durán-Valdeiglesias**, L. Labonte, S. Tanzilli, P. Cheben, E. Cassan, D. Marris-Morini, and L.

Vivien, "Nanostructured Si photonics for applications in the near- and mid-infrared," International Conference on Metamaterials, Photonic Crystals and Plasmonics (META), July 2017, Seoul, South Korea (Invited).

18. C. Alonso-Ramos, D. Pérez-Galacho, X. Le Roux, D. Benedikovic, F. Mazeas, W. Zhang, S. Serna, V. Vakarin, **E. Durán-Valdeiglesias**, L. Labonté, S. Tanzilli, P. Cheben, E. Cassan, D. Marris-Morini, L. Vivien, "Near-IR and mid-IR subwavelength engineered Si photonics," Photonics North, June 2017, Ottawa, Canada (Invited).

19. C. Alonso-Ramos, X. Le Roux, D. Benedikovic, V. Vakarin, **E. Durán-Valdeiglesias**, D. Pérez-Galacho, E. Cassan, D. Marris-Morini, P. Cheben, L. Vivien, "Mid- and near-IR silicon waveguides for sensing applications," SPIE Microtechnologies, May 2017, Barcelona, Spain (Invited).

20. **E. Durán-Valdeiglesias**, W. Zhang, C. Alonso-Ramos, X. Le Roux, S. Serna, T. H. C. Hoang, D. Marris-Morini, E. Cassan, F. Intonti, F. Sarti, N. Caselli, F. La China, M. Gurioli, M. Balestrieri, A. Filoramo, L. Vivien, "Hybrid integration of Carbon nanotubes in silicon photonic structures," SPIE Photonics West, Feb. 2017, San Francisco, US (Inivited).

21. C. Alonso-Ramos, D. Pérez-Galacho, X. Le Roux, D. Benedikovic, F. Mazeas, W. Zhang, S. Serna, V. Vakarin, **E. Durán-Valdeiglesias**, N. Belabas-Plougonven, L. Labonté, S. Tanzilli, P. Cheben, E. Cassan, D. Marris-Morini, L. Vivien, "Subwavelength Si photonics for near- and mid-infrared applications," SPIE Photonics West, Feb. 2017, San Francisco, US (Inivited).

22. C. Alonso-Ramos, X. Le Roux, D. Benedikovic, V. Vakarin, **E. Durán-Valdeiglesias**, D. Pérez-Galacho, E. Cassan, D. Marris-Morini, P. Cheben, L. Vivien, "Bragg grating filter for hybrid near- and mid-infrared silicon membrane waveguides," International Conference on Nanophotonics and Micro/Nano Optics, December 2016, Paris, France.

23. **E. Durán-Valdeiglesias**, W. Zhang, C. Alonso-Ramos, T. H. C. Hoang, S. Serna, F. Sarti, F. La China, X. Le Roux, M. Balestrieri, A.-S. Keita, H. Yang, E. Cassan, D. Marris-Morini, A. Filoramo, V. Bezugly, M. Gurioli, L. Vivien, "Carbon nanotubes for hybrid silicon photonics," International

Conference on Nanophotonics and Micro/Nano Optics, December 2016, Paris, France.

24. W. Zhang, **E. Durán-Valdeiglesias**, M. Balestrieri, S. Serna, C. Alonso-Ramos, X. Le Roux, A. Filoramo, L. Vivien, E. Cassan, "Enhanced carbon nanotubes light emission integrated with photonic SOI ring resonators," Asia Communications and Photonics Conference, November 2016, Wuhan China.

25. C. Alonso-Ramos, D. Pérez-Galacho, X. Le Roux, D. Benedikovic, F. Mazeas, W. Zhang, S. Serna, V. Vakarin, **E. Durán-Valdeiglesias**, N. Belabas-Plougonven, L. Labonté, S. Tanzilli, P. Cheben, E. Cassan, D. Marris-Morini, L. Vivien, "Subwavelength engineered silicon photonics," Nouveaux systèmes périodiques / Instrumentation diffractive, Journées du CCT-CNES et du GT2 ? GDR Ondes, Nov. 2016, Toulouse, France (Invited).

26. C. Alonso-Ramos, **E. Durán-Valdeiglesias**, W. Zhang, H.C. Hoang, S. Serna, X. Le Roux, E. Cassan, F. Sarti, U.Torrini, M. Balestrieri, A.-S. Keita, H. Yang, V. Bezugly, A. Vinattieri, G. Cuniberti, A. Filoramo, M. Gurioli, L. Vivien, "Hybrid integration of carbon nanotubes in silicon photonic structures," International Conference on Information Optics and Photonics (CIOP), August 2016, Shanghai, China (Keynote).

27. **E. Durán-Valdeiglesias**, W. Zhang, H.C. Hoang, C. Alonso-Ramos, S. Serna, F. Sarti, F. La China, X. Le Roux, H. Yang, E. Cassan, A. Filoramo, V. Bezugly, M. Gurioli, L. Vivien, "Hybrid integration of carbon nanotubes in silicon," Progress In Electromagnetics Research Symposium (PIERS), August 2016, Shanghai, China (Invited).

28. C. Alonso-Ramos, J. D. Sarmiento-Merenguel, R. Halir, X. Le Roux, L. Vivien, P. Cheben, **E. Durán-Valdeiglesias**, I. Molina-Fernández, D. Marris-Morini, D.-X. Xu, J. H. Schmid, S. Janz, A. Ortega-Moñux, "Silicon-on-insulator integrated tunable polarization controller with a 40 dB range in extinction ratio," Progress In Electromagnetics Research Symposium (PIERS), August 2016, Shanghai, China (Invited).

29. J. D. Sarmiento-Merenguel, A. Ortega-Moñux, J.-M. Fédéli, J. G. Wangüemert-Pérez, C. Alonso-Ramos, **E. Durán-Valdeiglesias**, P. Cheben, I. Molina-

Fernández, R. Halir, "On leakage losses in subwavelength grating devices," International Conference on Metamaterials, Photonic Crystals and Plasmonics (META), July 2016, Malaga, Spain.

30. J. D. Sarmiento-Merenguel, C. Alonso-Ramos, R. Halir, X. Le Roux, L. Vivien, P. Cheben, **E. Durán-Valdeiglesias**, I. Molina-Fernández, D. Marris-Morini, D.-X. Xu, J. H. Schmid, S. Janz, A. Ortega-Moñux, "Integrated polarization controller with 40 dB polarization extinction ratio range in the C-Band," European Conference on Integrated Optics (ECIO), May 2016, Warsow, Poland.

31. **E. Durán-Valdeiglesias**, W. Zhang, H. C. Hoang, C. Alonso-Ramos, S. Serna, X. Le Roux, E. Cassan, M. Balestrieri, A.-S. Keita, F. Sarti, F. Biccari, U. Torrini, A. Vinattieri, H. Yang, V. Bezugly, G. Cuniberti, A. Filoramo, M. Gurioli, L. Vivien, "Integration of carbon nanotubes in slot waveguides," SPIE Photonics Europe, April 2016, Brussels, Belgium.

32. J. D. Sarmiento-Merenguel, C. Alonso-Ramos, R. Halir, X. Le Roux, L. Vivien, P. Cheben, **E. Durán-Valdeiglesias**, I. Molina-Fernández, D. Marris-Morini, D.-X. Xu, J. H. Schmid, S. Janz, A. Ortega-Moñux, "Silicon-on-insulator integrated tunable polarization controller," SPIE Photonics Europe, April 2016, Brussels, Belgium.

33. F. Sarti, N. Caselli, F. La China, F. Biccari, U. Torrini, F. Intonti, A. Vinattieri, **E. Durán-Valdeiglesias**, W. Zhang, A. Noury, C. Alonso-Ramos, H. C. Hoang, S. Serna, X. Le Roux, E. Cassan, N. Izard, H. Yang, V. Bezugly, G. Cuniberti, A. Filoramo, L. Vivien, M. Gurioli, "Coupling of semiconductor carbon nanotubes emission with silicon photonic micro ring resonators," SPIE Photonics Europe, April 2016, Brussels, Belgium.

34. **E. Durán-Valdeiglesias**, W. Zhang, H. C. Hoang, C. Alonso-Ramos, A. Noury, S. Serna, X. Le Roux, E. Cassan, N. Izard, L. Vivien, "Hybrid integration of carbon nanotubes into silicon slot photonic structures," SPIE Photonics West, Feb. 2016, San Francisco, US.

35. **E. Durán-Valdeiglesias**, W. Zhang, A. Noury, C. Alonso-Ramos, H. C. Hoang, S. F Serna-Otalvaro, X. Le Roux, E. Cassan, N. Izard, F. Sarti, U.Torrini, H. Yang, A. Filoramo, V. Bezugly, M. Gurioli, L. Vivien, "In-

tegration of carbon nanotubes in silicon resonators," IEEE International Conference on Nanotechnology, July 2015, Rome, Italy.

36. A. Noury, **E. Durán-Valdeiglesias**, W. Zhang, F. Sarti, C. Alonso-Ramos, F. La China, H. C. Hoang, X. Le Roux, H. Yang, E. Cassan, N. Izard, A. Filoramo, V. Bezugly, M. Gurioli, L. Vivien, "Recent advances in carbon nanotube photonics on silicon platform," Progress In Electromagnetics Research Symposium (PIERS), July 2015, Prague, Czech Republic (Invited).

37. C. Alonso-Ramos, A. Noury, **E. Durán-Valdeiglesias**, W. Zhang, F. Sarti, F. La China, H.C. Hoang, X. Le Roux, H. Yang, E. Cassan, N. Izard, A. Filoramo, V. Bezugly, M. Gurioli, L. Vivien, "Light emission coupling from carbon nanotubes in silicon photonic structures," International Conference on Nanotechnology and Nanoscience, June 2015, Paris, France.

38. **E. Durán-Valdeiglesias**, C. Alonso-Ramos, W. Zhang, S. Serna, F. Sarti, F. La China, H.C. Hoang, X. Le Roux, H. Yang, E. Cassan, A. Noury, N. Izard, A. Filoramo, V. Bezugly, M. Gurioli, L. Vivien, "Hybrid Si photonics: Carbon nanotubes Integration on silicon," Workshop Progress in Photonics, October 2015, Florence, Italy (Workshop).

39. A. Noury, **E. Durán-Valdeiglesias**, C. Alonso-Ramos, W. Zhang, S. Serna, F. Sarti, F. La China, H.C. Hoang, X. Le Roux, H. Yang, E. Cassan, N. Izard, A. Filoramo, V. Bezugly, M. Gurioli, L. Vivien, "Recent advances in hybrid integration of carbon nanotubes on silicon," Optoelectronics and Communications Conference (OECC), July 2015, Shanghai, China (Invited).

40. F. Sarti, F. Biccari, F. Fioravanti, U. Torrini, A. Vinattieri, M. Gurioli, A. Filoramo, V. Derycke, V. Bezugly, H. Yang, G. Cuniberti, X. Le Roux, A. Noury, W. Zhang, N. Izard, **E. Durán-Valdeiglesias**, C. Alonso-Ramos, E. Cassan, L. Vivien, "Carbon nanotubes for efficient emission at telecom wavelengths on silicon photonic structures," EMRS spring meeting, 20150511 ? 20150515, Lille, France.

41. F. Sarti, F. Biccari, F. Fioravanti, U. Torrini, A. Vinattieri, M. Gurioli, A. Filoramo, V. Derycke, V. Bezugly, H. Yang, G. Cuniberti, X. Le Roux, A. Noury, W. Zhang, N. Izard, **E. Durán-Valdeiglesias**, C. Alonso-Ramos,

E. Cassan, L. Vivien, "Integration of carbon nanotubes on silicon for efficient emission at telecom wavelengths," Workshop on nanotube optics and nanospectroscopy, 20150601 ? 20150604, Kloster Banz, Germany.

42. M. Rahman, **E. Durán-Valdeiglesias**, V. Vakarin, J. Frigerio, J. M. Ramírez, D. Chrastina, P. Chaisakul, X. Le Roux, L. Vivien, G. Isella, D. Marris-Morini, "Investigation of Ge/SiGe Quantum Well properties by room temperature photoluminescence," EMRS spring meeting, 20150511 ? 20150515, Lille, France.

43. A. Moscoso-Mártir, J. M. Ávila-Ruiz, **E. Durán-Valdeiglesias**, L. Moreno-Pozas, Í. Molina-Fernández, A. Ortega-Moñux, J. de-Oliva-Rubio, "Butler matrix based six-port passive junction," IEEE Topical Conference on WiSNet, January 2014, California, USA.

Bibliography

[1] E. A. Marcatili, "Dielectric rectangular waveguide and directional coupler for integrated optics," *Bell Syst. Tech. J.*, vol. 48, no. 7, p. 2071, 1969.

[2] R. Soref and J. Lorenzo, "Single-crystal silicon: a new material for 1.3 and 1.6 μm integrated-optical components," *Electron. Lett.*, vol. 21, no. 21, p. 953, 1985.

[3] A. Rickman, "The commercialization of silicon photonics," *Nat. Photonics*, vol. 8, no. 8, p. 579, 2014.

[4] A. G. Rickman, G. T. Reed, and F. Namavar, "Silicon-on-insulator optical rib waveguide circuits for fiber optic sensors," in *Distributed and Multiplexed Fiber Optic Sensors III*, vol. 2071. International Society for Optics and Photonics, 1993, p. 190.

[5] J. Sun, E. Timurdogan, A. Yaacobi, E. S. Hosseini, and M. R. Watts, "Large-scale nanophotonic phased array," *Nature*, vol. 493, no. 7431, p. 195, 2013.

[6] J. S. Fandiño, P. Muñoz, D. Doménech, and J. Capmany, "A monolithic integrated photonic microwave filter," *Nat. Photonics*, vol. 11, no. 2, p. 124, 2017.

[7] D. Van Thourhout and J. Roels, "Optomechanical device actuation through the optical gradient force," *Nat. Photonics*, vol. 4, no. 4, p. 211, 2010.

[8] K. Fang, M. H. Matheny, X. Luan, and O. Painter, "Optical transduction and routing of microwave phonons in cavity-optomechanical circuits," *Nat. Photonics*, vol. 10, no. 7, p. 489, 2016.

[9] H. Wen, A. Daruwalla, and F. Ayazi, "Resonant pitch and roll silicon gyroscopes with sub-micron-gap slanted electrodes: Breaking the barrier toward high-performance monolithic inertial measurement units," *Microsyst. Nanoeng.*, vol. 3, p. 16092, 2017.

[10] J. W. Silverstone, D. Bonneau, J. L. OBrien, and M. G. Thompson, "Silicon quantum photonics," *IEEE J. Sel. Top. Quantum Electron.*, vol. 22, no. 6, p. 390, 2016.

[11] H. Lin, Z. Luo, T. Gu, L. C. Kimerling, K. Wada, A. Agarwal, and J. Hu, "Mid-infrared integrated photonics on silicon: a perspective," *Nanophotonics*, vol. 7, no. 2, p. 393, 2017.

[12] C. Baudot, A. Fincato, D. Fowler, D. Pérez-Galacho, A. Souhaité, S. Messaoudène, R. Blanc, C. Richard, J. Planchot, C. De-Buttet *et al.*, "Daphne silicon photonics technological platform for research and development on WDM applications," in *Silicon Photonics and Photonic Integrated Circuits V*, vol. 9891. International Society for Optics and Photonics, 2016, p. 98911D.

[13] J. Leuthold, C. Koos, and W. Freude, "Nonlinear silicon photonics," *Nat. Photonics*, vol. 4, no. 8, p. 535, 2010.

[14] C. V. Poulton, A. Yaacobi, D. B. Cole, M. J. Byrd, M. Raval, D. Vermeulen, and M. R. Watts, "Coherent solid-state LIDAR with silicon photonic optical phased arrays," *Opt. Lett.*, vol. 42, no. 20, p. 4091, 2017.

[15] X. Zhang, G. Zhou, P. Shi, H. Du, T. Lin, J. Teng, and F. S. Chau, "On-chip integrated optofluidic complex refractive index sensing using silicon photonic crystal nanobeam cavities," *Opt. Lett.*, vol. 41, no. 6, p. 1197, 2016.

[16] M.-C. M. Lee and M. C. Wu, "Tunable coupling regimes of silicon microdisk resonators using MEMS actuators," *Opt. Express*, vol. 14, no. 11, p. 4703, 2006.

[17] G. Crosnier, D. Sanchez, S. Bouchoule, P. Monnier, G. Beaudoin, I. Sagnes, R. Raj, and F. Raineri, "Hybrid indium phosphide-on-silicon nanolaser diode," *Nat. Photonics*, vol. 11, no. 5, p. 297, 2017.

[18] B. B. Bakir, A. Descos, N. Olivier, D. Bordel, P. Grosse, E. Augendre, L. Fulbert, and J. Fédéli, "Electrically driven hybrid Si/III-V Fabry-Pérot lasers based on adiabatic mode transformers," *Opt. Express*, vol. 19, no. 11, p. 10 317, 2011.

[19] D. Thomson, A. Zilkie, J. E. Bowers, T. Komljenovic, G. T. Reed, L. Vivien, D. Marris-Morini, E. Cassan, L. Virot, J.-M. Fédéli *et al.*, "Roadmap on silicon photonics," *J. Opt.*, vol. 18, no. 7, p. 073003, 2016.

[20] J. Hartmann, A. Abbadie, A. Papon, P. Holliger, G. Rolland, T. Billon, J. Fédéli, M. Rouviere, L. Vivien, and S. Laval, “Reduced pressure–chemical vapor deposition of Ge thick layers on Si (001) for 1.3–1.55-μm photodetection,” *J. Appl. Phys.*, vol. 95, no. 10, p. 5905, 2004.

[21] L. Vivien, A. Polzer, D. Marris-Morini, J. Osmond, J. M. Hartmann, P. Crozat, E. Cassan, C. Kopp, H. Zimmermann, and J. M. Fédéli, “Zero-bias 40Gbit/s germanium waveguide photodetector on silicon,” *Opt. Express*, vol. 20, no. 2, p. 1096, 2012.

[22] P. Avouris, M. Freitag, and V. Perebeinos, “Carbon-nanotube photonics and optoelectronics,” *Nat. Photonics*, vol. 2, no. 6, p. 341, 2008.

[23] P. Avouris, Z. Chen, and V. Perebeinos, “Carbon-based electronics,” in *Nanoscience And Technology: A Collection of Reviews from Nature Journals*. World Scientific, 2010, p. 174.

[24] J. Misewich, R. Martel, P. Avouris, J. Tsang, S. Heinze, and J. Tersoff, “Electrically induced optical emission from a carbon nanotube FET,” *Science*, vol. 300, no. 5620, p. 783, 2003.

[25] G. Guo, K. Chu, D.-S. Wang, and C.-G. Duan, “Linear and nonlinear optical properties of carbon nanotubes from first-principles calculations,” *Phys. Rev. B*, vol. 69, no. 20, p. 205416, 2004.

[26] V. A. Margulis and T. Sizikova, “Theoretical study of third-order nonlinear optical response of semiconductor carbon nanotubes,” *Physica B*, vol. 245, no. 2, p. 173, 1998.

[27] A. D. Franklin, M. Luisier, S.-J. Han, G. Tulevski, C. M. Breslin, L. Gignac, M. S. Lundstrom, and W. Haensch, “Sub-10 nm carbon nanotube transistor,” *Nano Lett.*, vol. 12, no. 2, p. 758, 2012.

[28] J. Tang, Q. Cao, G. Tulevski, K. A. Jenkins, L. Nela, D. B. Farmer, and S.-J. Han, “Flexible CMOS integrated circuits based on carbon nanotubes with sub-10 ns stage delays,” *Nat. Electron.*, vol. 1, no. 3, p. 191, 2018.

[29] É. Gaufrès, “Carbon nanotubes photonics on silicon,” Theses, Université Paris Sud - Paris XI, Dec. 2010.

[30] A. Noury, "Carbon nanotube hybrid photonic," Theses, Université Paris Sud - Paris XI, Sep. 2014.

[31] S. Reich, C. Thomsen, and J. Maultzsch, *Carbon nanotubes: basic concepts and physical properties*. John Wiley & Sons, 2008.

[32] S. Roche, E. Akkermans, O. Chauvet, F. Hekking, J. Issi, R. Martel, G. Montambaux, and P. Poncharal, "Understanding carbon nanotubes from basics to applications," *Springer Lecture Notes in Physics*, vol. 677, 2006.

[33] S. Iijima, "Helical microtubules of graphitic carbon," *Nature*, vol. 354, no. 6348, p. 56, 1991.

[34] J.-P. Salvetat, J.-M. Bonard, N. Thomson, A. Kulik, L. Forro, W. Benoit, and L. Zuppiroli, "Mechanical properties of carbon nanotubes," *Appl. Phys. A*, vol. 69, no. 3, p. 255, 1999.

[35] K. Sun, M. A. Stroscio, and M. Dutta, "Thermal conductivity of carbon nanotubes," *J. Appl. Phys.*, vol. 105, no. 7, p. 074316, 2009.

[36] T. W. Odom, J.-L. Huang, P. Kim, and C. M. Lieber, "Structure and electronic properties of carbon nanotubes," *J. Phys. Chem. B* vol. 104, no. 13, p. 2794, 2000.

[37] H. Kataura, Y. Kumazawa, Y. Maniwa, I. Umezu, S. Suzuki, Y. Ohtsuka, and Y. Achiba, "Optical properties of single-wall carbon nanotubes," *Synth. Met.*, vol. 103, no. 1-3, p. 2555, 1999.

[38] S. Kruss, A. J. Hilmer, J. Zhang, N. F. Reuel, B. Mu, and M. S. Strano, "Carbon nanotubes as optical biomedical sensors," *Adv. Drug Deliv. Rev.*, vol. 65, no. 15, p. 1933, 2013.

[39] N. M. Iverson, P. W. Barone, M. Shandell, L. J. Trudel, S. Sen, F. Sen, V. Ivanov, E. Atolia, E. Farias, T. P. McNicholas *et al.*, "In vivo biosensing via tissue-localizable near-infrared-fluorescent single-walled carbon nanotubes," *Nat. Nanotechnol.*, vol. 8, no. 11, p. 873, 2013.

[40] Y. Yang, L. Ding, H. Chen, J. Han, Z. Zhang, and L.-M. Peng, "Carbon nanotube network film-based ring oscillators with sub 10-ns propagation time and their applications in radio-frequency signal transmission," *Nano Res.*, vol. 11, no. 1, p. 300, 2018.

[41] S. Park, M. Vosguerichian, and Z. Bao, "A review of fabrication and applications of carbon nanotube film-based flexible electronics," *Nanoscale*, vol. 5, no. 5, p. 1727, 2013.

[42] A. Jeantet, Y. Chassagneux, C. Raynaud, P. Roussignol, J.-S. Lauret, B. Besga, J. Estève, J. Reichel, and C. Voisin, "Widely tunable single-photon source from a carbon nanotube in the Purcell regime," *Phys. Rev. Lett.*, vol. 116, no. 24, p. 247402, 2016.

[43] S. Khasminskaya, F. Pyatkov, K. Słowik, S. Ferrari, O. Kahl, V. Kovalyuk, P. Rath, A. Vetter, F. Hennrich, M. M. Kappes *et al.*, "Fully integrated quantum photonic circuit with an electrically driven light source," *Nat. Photonics*, vol. 10, no. 11, p. 727, 2016.

[44] A. D. Franklin, "Electronics: The road to carbon nanotube transistors," *Nature*, vol. 498, no. 7455, p. 443, 2013.

[45] S. Iijima and T. Ichihashi, "Single-shell carbon nanotubes of 1-nm diameter," *Nature*, vol. 363, no. 6430, p. 603, 1993.

[46] T. Sugai, H. Yoshida, T. Shimada, T. Okazaki, H. Shinohara, and S. Bandow, "New synthesis of high-quality double-walled carbon nanotubes by high-temperature pulsed arc discharge," *Nano Lett.*, vol. 3, no. 6, p. 769, 2003.

[47] J. Prek, J. Drbohlavova, J. Chomoucka, J. Hubalek, J. Ondrej, V. Adam, and R. Kizek, "Methods for carbon nanotubes synthesis - review," *J. Mater. Chem.*, vol. 21, p. 15 872, 2011.

[48] J. Liu, S. Fan, and H. Dai, "Recent advances in methods of forming carbon nanotubes," *MRS bulletin*, vol. 29, no. 4, p. 244, 2004.

[49] Y. Maeda, M. Kanda, M. Hashimoto, T. Hasegawa, S.-I. Kimura, Y. Lian, T. Wakahara, T. Akasaka, S. Kazaoui, N. Minami *et al.*, "Dispersion and separation of small-diameter single-walled carbon nanotubes," *J. Am. Chem. Soc.*, vol. 128, no. 37, p. 12 239, 2006.

[50] C. Kane and E. Mele, "Ratio problem in single carbon nanotube fluorescence spectroscopy," *Phys. Rev. Lett.*, vol. 90, no. 20, p. 207401, 2003.

[51] F. Wang, G. Dukovic, L. E. Brus, and T. F. Heinz, "The optical resonances in carbon nanotubes arise from excitons," *Science*, vol. 308, no. 5723, p. 838, 2005.

[52] R. B. Weisman and S. M. Bachilo, "Dependence of optical transition energies on structure for single-walled carbon nanotubes in aqueous suspension: an empirical Kataura plot," *Nano Lett.*, vol. 3, no. 9, p. 1235, 2003.

[53] J. Lefebvre, J. Fraser, P. Finnie, and Y. Homma, "Photoluminescence from an individual single-walled carbon nanotube," *Phys. Rev. B*, vol. 69, no. 7, p. 075403, 2004.

[54] A. Fediai, D. A. Ryndyk, G. Seifert, S. Mothes, M. Claus, M. Schröter, and G. Cuniberti, "Towards an optimal contact metal for CNTFETs," *Nanoscale*, vol. 8, no. 19, p. 10 240, 2016.

[55] S. Wang, Q. Zeng, L. Yang, Z. Zhang, Z. Wang, T. Pei, L. Ding, X. Liang, M. Gao, Y. Li *et al.*, "High-performance carbon nanotube light-emitting diodes with asymmetric contacts," *Nano Lett.*, vol. 11, no. 1, p. 23, 2010.

[56] D. Yu, H. Liu, L.-M. Peng, and S. Wang, "Flexible light-emitting devices based on chirality-sorted semiconducting carbon nanotube films," *ACS Appl. Mater. Interfaces*, vol. 7, no. 6, p. 3462, 2015.

[57] J. Chen, V. Perebeinos, M. Freitag, J. Tsang, Q. Fu, J. Liu, and P. Avouris, "Bright infrared emission from electrically induced excitons in carbon nanotubes," *Science*, vol. 310, no. 5751, p. 1171, 2005.

[58] Z. Ma, S. Liang, Y. Liu, F. Wang, S. Wang, and L.-M. Peng, "On-chip polarized light emitters based on (6,5) chirality-sorted carbon nanotube aligned arrays," *Appl. Phys. Lett.*, vol. 108, no. 6, p. 063114, 2016.

[59] E. Gaufres, N. Izard, X. Le Roux, D. Marris-Morini, S. Kazaoui, E. Cassan, and L. Vivien, "Optical gain in carbon nanotubes," *Appl. Phys. Lett.*, vol. 96, no. 23, p. 231105, 2010.

[60] N. Izard, S. Kazaoui, K. Hata, T. Okazaki, T. Saito, S. Iijima, and N. Minami, "Semiconductor-enriched single wall carbon nanotube networks applied to field effect transistors," *Appl. Phys. Lett.*, vol. 92, no. 24, p. 243112, 2008.

[61] Y.-R. Shen, "The principles of nonlinear optics," *New York, Wiley-Interscience*, 1984.

[62] R. W. Boyd, "Nonlinear optics", *Academic press*, 2003.

[63] E. L. Wooten, K. M. Kissa, A. Yi-Yan, E. J. Murphy, D. A. Lafaw, P. F. Hallemeier, D. Maack, D. V. Attanasio, D. J. Fritz, G. J. McBrien *et al.*, "A review of lithium niobate modulators for fiber-optic communications systems," *IEEE J. Sel. Top. Quantum Electron.*, vol. 6, no. 1, p. 69, 2000.

[64] S. Yamashita, "A tutorial on nonlinear photonic applications of carbon nanotube and graphene," *J. Light. Technol.*, vol. 30, no. 4, p. 427, 2012.

[65] L. De Dominicis, S. Botti, L. Asilyan, R. Ciardi, R. Fantoni, M. Terranova, A. Fiori, S. Orlanducci, and R. Appolloni, "Second-and third-harmonic generation in single-walled carbon nanotubes at nanosecond time scale," *Appl. Phys. Lett.*, vol. 85, no. 8, p. 1418, 2004.

[66] S. Konorov, D. Akimov, A. Ivanov, M. Alfimov, S. Botti, R. Ciardi, L. De Dominicis, L. Asilyan, A. Podshivalov, D. Sidorov-Biryukov *et al.*, "Femtosecond optical harmonic generation as a non-linear spectroscopic probe for carbon nanotubes," *J. Raman Spectrosc.*, vol. 34, no. 12, p. 1018, 2003.

[67] S. Garnov, S. Solokhin, E. Obraztsova, A. Lobach, P. Obraztsov, A. Chernov, V. Bukin, A. Sirotkin, Y. Zagumennyi, Y. Zavartsev *et al.*, "Passive mode-locking with carbon nanotube saturable absorber in Nd: $GdVO_4$ and Nd: $Y_{0.9}Gd_{0.1}VO_4$ lasers operating at 1.34 μm," *Laser Phys. Lett.*, vol. 4, no. 9, p. 648, 2007.

[68] A. Martinez and Z. Sun, "Nanotube and graphene saturable absorbers for fibre lasers," *Nat. Photonics*, vol. 7, no. 11, p. 842, 2013.

[69] K.-N. Cheng, Y.-H. Lin, and G.-R. Lin, "Single-and double-walled carbon nanotube based saturable absorbers for passive mode-locking of an erbium-doped fiber laser," *Laser Phys.*, vol. 23, no. 4, p. 045105, 2013.

[70] T. Wang, C. Zou, Z. Yan, Q. Huang, C. Mou, K. Zhou, M. AlAraimi, A. Rozhin, and L. Zhang, "Tunable mode locked erbium-doped fiber laser based a tilted fiber grating and carbon nanotube saturable absorber," in

Lasers and Electro-Optics Pacific Rim (CLEO-PR), 2017 Conference on. IEEE, 2017, pp. 1–2.

[71] E. P. Ippen, “Principles of passive mode locking,” *Appl. Phys. B*, vol. 58, no. 3, p. 159, 1994.

[72] S. Kivistö, T. Hakulinen, A. Kaskela, B. Aitchison, D. P. Brown, A. G. Nasibulin, E. I. Kauppinen, A. Härkönen, and O. G. Okhotnikov, “Carbon nanotube films for ultrafast broadband technology,” *Opt. Express*, vol. 17, no. 4, p. 2358, 2009.

[73] S. Reich, C. Thomsen, and J. Maultzsch, "Carbon nanotubes",*Wiley-VCH, Weinheim*, 2004.

[74] D. Li, H. Jussila, L. Karvonen, G. Ye, H. Lipsanen, X. Chen, and Z. Sun, “Polarization and thickness dependent absorption properties of black phosphorus: new saturable absorber for ultrafast pulse generation,” *Sci. Rep.*, vol. 5, p. 15899, 2015.

[75] L. Kong, Z. Qin, G. Xie, Z. Guo, H. Zhang, P. Yuan, and L. Qian, “Black phosphorus as broadband saturable absorber for pulsed lasers from 1 μm to 2.7 μm wavelength,” *Laser Phys. Lett.*, vol. 13, no. 4, p. 045801, 2016.

[76] H. Song, Q. Wang, D. Wang, and L. Li, “Passively Q-switched wavelength-tunable 1-μm fiber lasers with tapered-fiber-based black phosphorus saturable absorbers,” *Results Phys.*, vol. 8, p. 276, 2018.

[77] L. Vivien, E. Anglaret, D. Riehl, F. Hache, F. Bacou, M. Andrieux, F. Lafonta, C. Journet, C. Goze, M. Brunet *et al.*, “Optical limiting properties of singlewall carbon nanotubes,” *Opt. Commun.*, vol. 174, no. 1, p. 271, 2000.

[78] J.-S. Lauret, C. Voisin, G. Cassabois, J. Tignon, C. Delalande, P. Roussignol, O. Jost, and L. Capes, “Third-order optical nonlinearities of carbon nanotubes in the femtosecond regime,” *Appl. Phys. Lett.*, vol. 85, no. 16, p. 3572, 2004.

[79] D. Shimamoto, T. Sakurai, M. Itoh, Y. A. Kim, T. Hayashi, M. Endo, and M. Terrones, “Nonlinear optical absorption and reflection of single wall carbon nanotube thin films by Z-scan technique,” *Appl. Phys. Lett.*, vol. 92, no. 8, p. 081902, 2008.

[80] N. Kamaraju, S. Kumar, A. Sood, S. Guha, S. Krishnamurthy, and C. Rao, "Large nonlinear absorption and refraction coefficients of carbon nanotubes estimated from femtosecond Z-scan measurements," *Appl. Phys. Lett.*, vol. 91, no. 25, p. 251103, 2007.

[81] X. Liu, J. Si, B. Chang, G. Xu, Q. Yang, Z. Pan, S. Xie, P. Ye, J. Fan, and M. Wan, "Third-order optical nonlinearity of the carbon nanotubes," *Appl. Phys. Lett.*, vol. 74, no. 2, p. 164, 1999.

[82] A. Maeda, S. Matsumoto, H. Kishida, T. Takenobu, Y. Iwasa, M. Shiraishi, M. Ata, and H. Okamoto, "Large optical nonlinearity of semiconducting single-walled carbon nanotubes under resonant excitations," *Phys. Rev. Lett.*, vol. 94, no. 4, p. 047404, 2005.

[83] M. C. Hersam, "Progress towards monodisperse single-walled carbon nanotubes," *Nat. Nanotechnol.*, vol. 3, no. 7, p. 387, 2008.

[84] S. Nagasawa, M. Yudasaka, K. Hirahara, T. Ichihashi, and S. Iijima, "Effect of oxidation on single-wall carbon nanotubes," *Chem. Phys. Lett.*, vol. 328, no. 4-6, p. 374, 2000.

[85] Y. Miyata, T. Kawai, Y. Miyamoto, K. Yanagi, Y. Maniwa, and H. Kataura, "Chirality-dependent combustion of single-walled carbon nanotubes," *J. Phys. Chem. C*, vol. 111, no. 27, p. 9671, 2007.

[86] C.-M. Yang, K. H. An, J. S. Park, K. A. Park, S. C. Lim, S.-H. Cho, Y. S. Lee, W. Park, C. Y. Park, and Y. H. Lee, "Preferential etching of metallic single-walled carbon nanotubes with small diameter by fluorine gas," *Phys. Rev. B*, vol. 73, no. 7, p. 075419, 2006.

[87] P. G. Collins, M. S. Arnold, and P. Avouris, "Engineering carbon nanotubes and nanotube circuits using electrical breakdown," *Science*, vol. 292, no. 5517, p. 706, 2001.

[88] D. A. Heller, R. M. Mayrhofer, S. Baik, Y. V. Grinkova, M. L. Usrey, and M. S. Strano, "Concomitant length and diameter separation of single-walled carbon nanotubes," *J. Am. Chem. Soc.*, vol. 126, no. 44, p. 14 567, 2004.

[89] R. Krupke, F. Hennrich, M. M. Kappes, and H. Lohneysen, “Surface conductance induced dielectrophoresis of semiconducting single-walled carbon nanotubes,” *Nano Lett.*, vol. 4, no. 8, p. 1395, 2004.

[90] M. S. Arnold, A. A. Green, J. F. Hulvat, S. I. Stupp, and M. C. Hersam, “Sorting carbon nanotubes by electronic structure using density differentiation,” *Nat. Nanotechnol.*, vol. 1, no. 1, p. 60, 2006.

[91] J.-Y. Hwang, A. Nish, J. Doig, S. Douven, C.-W. Chen, L.-C. Chen, and R. J. Nicholas, “Polymer structure and solvent effects on the selective dispersion of single-walled carbon nanotubes,” *J. Am. Chem. Soc.*, vol. 130, no. 11, p. 3543, 2008.

[92] F. Chen, B. Wang, Y. Chen, and L.-J. Li, “Toward the extraction of single species of single-walled carbon nanotubes using fluorene-based polymers,” *Nano Lett.*, vol. 7, no. 10, p. 3013, 2007.

[93] M. J. O’connell, S. M. Bachilo, C. B. Huffman, V. C. Moore, M. S. Strano, E. H. Haroz, K. L. Rialon, P. J. Boul, W. H. Noon, C. Kittrell *et al.*, “Band gap fluorescence from individual single-walled carbon nanotubes,” *Science*, vol. 297, no. 5581, p. 593, 2002.

[94] R. D. Deegan, O. Bakajin, T. F. Dupont, G. Huber, S. R. Nagel, and T. A. Witten, “Contact line deposits in an evaporating drop,” *Phys. Rev. E*, vol. 62, no. 1, p. 756, 2000.

[95] M. Dimaki and P. Bøggild, “Dielectrophoresis of carbon nanotubes using microelectrodes: a numerical study,” *Nanotechnology*, vol. 15, no. 8, p. 1095, 2004.

[96] A. Nish, J.-Y. Hwang, J. Doig, and R. J. Nicholas, “Highly selective dispersion of single-walled carbon nanotubes using aromatic polymers,” *Nat. Nanotechnol.*, vol. 2, no. 10, p. 640, 2007.

[97] F. Chen, B. Wang, Y. Chen, and L.-J. Li, “Toward the extraction of single species of single-walled carbon nanotubes using fluorene-based polymers,” *Nano Lett.*, vol. 7, no. 10, p. 3013, 2007.

[98] K. S. Mistry, B. A. Larsen, and J. L. Blackburn, “High-yield dispersions of large-diameter semiconducting single-walled carbon nanotubes with tunable narrow chirality distributions,” *ACS Nano*, vol. 7, no. 3, p. 2231, 2013.

[99] M. Tange, T. Okazaki, and S. Iijima, "Selective extraction of semiconducting single-wall carbon nanotubes by poly (9, 9-dioctylfluorene-alt-pyridine) for 1.5 μm emission," *ACS Appl. Mater. Interfaces*, vol. 4, no. 12, p. 6458, 2012.

[100] E. Gaufres, N. Izard, L. Vivien, S. Kazaoui, D. Marris-Morini, and E. Cassan, "Enhancement of semiconducting single-wall carbon-nanotube photoluminescence," *Opt. Lett.*, vol. 34, no. 24, p. 3845, 2009.

[101] J.-Y. Hwang, A. Nish, J. Doig, S. Douven, C.-W. Chen, L.-C. Chen, and R. J. Nicholas, "Polymer structure and solvent effects on the selective dispersion of single-walled carbon nanotubes," *J. Am. Chem. Soc.*, vol. 130, no. 11, p. 3543, 2008.

[102] Kataura, *http://www.photon.t.u-tokyo.ac.jp/ maruyama/kataura/kataura.html*.

[103] M. S. Dresselhaus, A. Jorio, M. Hofmann, G. Dresselhaus, and R. Saito, "Perspectives on carbon nanotubes and graphene Raman spectroscopy," *Nano Lett.*, vol. 10, no. 3, p. 751, 2010.

[104] F. Sarti, F. Biccari, F. Fioravanti, U. Torrini, A. Vinattieri, V. Derycke, M. Gurioli, and A. Filoramo, "Highly selective sorting of semiconducting single wall carbon nanotubes exhibiting light emission at telecom wavelengths," *Nano Res.*, vol. 9, no. 8, p. 2478, 2016.

[105] M. C. Estevez, M. Alvarez, and L. M. Lechuga, "Integrated optical devices for lab-on-a-chip biosensing applications," *Laser Photonics Rev.*, vol. 6, no. 4, p. 463, 2012.

[106] A. Densmore, D.-X. Xu, P. Waldron, S. Janz, P. Cheben, J. Lapointe, A. Delâge, B. Lamontagne, J. Schmid, and E. Post, "A silicon-on-insulator photonic wire based evanescent field sensor," *IEEE Photon. Technol. Lett.*, vol. 18, no. 23, p. 2520, 2006.

[107] V. R. Almeida, Q. Xu, C. A. Barrios, and M. Lipson, "Guiding and confining light in void nanostructure," *Opt. Lett.*, vol. 29, no. 11, p. 1209, 2004.

[108] M. Campoy-Quiles, P. Etchegoin, and D. D. Bradley, "Exploring the potential of ellipsometry for the characterisation of electronic, optical, morphologic and thermodynamic properties of polyfluorene thin films," *Synth. Met.*, vol. 155, no. 2, p. 279, 2005.

[109] J. G. Wangüemert-Pérez, P. Cheben, A. Ortega-Moñux, C. Alonso-Ramos, D. Pérez-Galacho, R. Halir, I. Molina-Fernández, D.-X. Xu, and J. H. Schmid, "Evanescent field waveguide sensing with subwavelength grating structures in silicon-on-insulator," *Opt. Lett.*, vol. 39, no. 15, p. 4442, 2014.

[110] A. Noury, X. Le-Roux, L. Vivien, and N. Izard, "Controlling carbon nanotube photoluminescence using silicon microring resonators," *Nanotechnology*, vol. 25, no. 21, p. 215201, 2014.

[111] A. Noury, X. Le Roux, L. Vivien, and N. Izard, "Enhanced light emission from carbon nanotubes integrated in silicon micro-resonator," *Nanotechnology*, vol. 26, no. 34, p. 345201, 2015.

[112] T. K. Leeuw, D. A. Tsyboulski, P. N. Nikolaev, S. M. Bachilo, S. Arepalli, and R. B. Weisman, "Strain measurements on individual single-walled carbon nanotubes in a polymer host: Structure-dependent spectral shifts and load transfer," *Nano Lett.*, vol. 8, no. 3, p. 826, 2008.

[113] M. Barkelid, G. A. Steele, and V. Zwiller, "Probing optical transitions in individual carbon nanotubes using polarized photocurrent spectroscopy," *Nano Lett.*, vol. 12, no. 11, p. 5649, 2012.

[114] E. Gaufres, N. Izard, A. Noury, X. Le Roux, G. Rasigade, A. Beck, and L. Vivien, "Light emission in silicon from carbon nanotubes," *ACS Nano*, vol. 6, no. 5, p. 3813, 2012.

[115] E. Durán-Valdeiglesias, W. Zhang, A. Noury, C. Alonso-Ramos, S. Serna, X. L. Roux, E. Cassan, N. Izard, F. Sarti, U. Torrini, F. Biccari, A. Vinattieri, M. Balestrieri, A.-S. Keita, H. Yang, V. Bezugly, G. Cuniberti, A. Filoramo, M. Gurioli, and L.Vivien, "Integration of carbon nanotubes in silicon strip and slot waveguide micro-ring resonators," *IEEE Trans. Nanotechnol.*, vol. 15, no. 4, p. 583, 2016.

[116] R. Miura, S. Imamura, R. Ohta, A. Ishii, X. Liu, T. Shimada, S. Iwamoto, Y. Arakawa, and Y. Kato, "Ultralow mode-volume photonic crystal nanobeam cavities for high efficiency coupling to individual carbon nanotube emitters," *Nat. Commun.*, vol. 5, p. 5580, 2014.

[117] T. H. C. Hoang, E. Durán-Valdeiglesias, C. Alonso-Ramos, S. Serna, W. Zhang, M. Balestrieri, A.-S. Keita, N. Caselli, F. Biccari, X. Le Roux *et al.*, "Narrow-linewidth carbon nanotube emission in silicon hollow-core photonic crystal cavity," *Opt. Lett.*, vol. 42, no. 11, p. 2228, 2017.

[118] R. Osgood, N. Panoiu, J. Dadap, X. Liu, X. Chen, I.-W. Hsieh, E. Dulkeith, W. Green, and Y. Vlasov, "Engineering nonlinearities in nanoscale optical systems: physics and applications in dispersion-engineered silicon nanophotonic wires," *Adv. Opt. Photonics*, vol. 1, no. 1, p. 162, 2009.

[119] M. Solutions, "version 4.0, lumerical solutions," *Inc. Available: http://www. lumerical. com.*

[120] W. Bogaerts, P. De Heyn, T. Van Vaerenbergh, K. De Vos, S. Kumar Selvaraja, T. Claes, P. Dumon, P. Bienstman, D. Van Thourhout, and R. Baets, "Silicon microring resonators," *Laser Photonics Rev.*, vol. 6, no. 1, p. 47, 2012.

[121] W. Zhang, S. Serna, X. Le Roux, L. Vivien, and E. Cassan, "Highly sensitive refractive index sensing by fast detuning the critical coupling condition of slot waveguide ring resonators," *Opt. Lett.*, vol. 41, no. 3, p. 532, 2016.

[122] F. La China, F. Intonti, N. Caselli, F. Lotti, F. Sarti, A. Vinattieri, A. Noury, X. Le Roux, W. Zhang, E. Cassan *et al.*, "Near-field fano-imaging of TE and TM modes in silicon microrings," *ACS Photonics*, vol. 2, no. 12, p. 1712, 2015.

[123] O. Painter, R. Lee, A. Scherer, A. Yariv, J. O'brien, P. Dapkus, and I. Kim, "Two-dimensional photonic band-gap defect mode laser," *Science*, vol. 284, no. 5421, p. 1819, 1999.

[124] S. Strauf, K. Hennessy, M. Rakher, Y.-S. Choi, A. Badolato, L. Andreani, E. Hu, P. Petroff, and D. Bouwmeester, "Self-tuned quantum dot gain in photonic crystal lasers," *Phys. Rev. Lett.*, vol. 96, no. 12, p. 127404, 2006.

[125] A. Di Falco, L. O Faolain, and T. Krauss, "Dispersion control and slow light in slotted photonic crystal waveguides," *Appl. Phys. Lett.*, vol. 92, no. 8, p. 083501, 2008.

[126] W. Jun, P. Chao, L. Yan-Ping, and W. Zi-Yu, "Light localization in slot photonic crystal waveguide," *Chin. Phys. Lett.*, vol. 26, no. 1, p. 014209, 2009.

[127] T. H. C. Hoang, "Planar slot photonic crystal cavities for on-chip hybrid integration," Theses, Université Paris-Saclay, Mar. 2017.

[128] C. Caër, "Slot Photonic Crystal Waveguides : towards a silicon photonics with a localized exaltation of the electromagnetic field," Theses, Université Paris Sud - Paris XI, Sep. 2013.

[129] C. Caër, S. Combrié, X. Le Roux, E. Cassan, and A. De Rossi, "Extreme optical confinement in a slotted photonic crystal waveguide," *Appl. Phys. Lett.*, vol. 105, no. 12, p. 121111, 2014.

[130] T. H. C. Hoang, W. Zhang, S. F. Serna-Otálvaro, C. Caër, X. Le Roux, L. Vivien, and E. Cassan, "SOI slotted photonic crystal cavities spanning from 1.3 to 1.6 μm with $\mathrm{Q/V}$ factors above 800 000," *IEEE Photonics Technol. Lett.*, vol. 27, no. 20, p. 2138, 2015.

[131] C. Alonso-Ramos, A. Ortega-Moñux, L. Zavargo-Peche, R. Halir, J. de Oliva-Rubio, I. Molina-Fernández, P. Cheben, D.-X. Xu, S. Janz, N. Kim *et al.*, "Single-etch grating coupler for micrometric silicon rib waveguides," *Opt. Lett.*, vol. 36, no. 14, p. 2647, 2011.

[132] T. Tamir and S.-T. Peng, "Analysis and design of grating couplers," *J. Appl. Phys.*, vol. 14, no. 3, p. 235, 1977.

[133] Europractice, *http://www.europractice-ic.com*.

[134] I. D. Samuel, E. B. Namdas, and G. A. Turnbull, "How to recognize lasing," *Nat. Photonics* , vol. 3, no. 10, p. 546, 2009.

[135] O. Svelto and D. C. Hanna, *Principles of lasers*. Springer, 1998, vol. 4.

[136] A. E. Siegman, *Lasers*. University Science Books, 1986.

[137] L. Reeves, Y. Wang, and T. F. Krauss, "2D material microcavity light emitters: To lase or not to lase?" *Adv. Opt. Mater.*, vol. 6, no. 19, p. 1800272, 2018.

[138] N. Koukourakis, C. Bückers, D. Funke, N. Gerhardt, S. Liebich, S. Chatterjee, C. Lange, M. Zimprich, K. Volz, W. Stolz *et al.*, "High room-temperature optical gain in Ga (NAsP)/Si heterostructures," *Appl. Phys. Lett.*, vol. 100, no. 9, p. 092107, 2012.

[139] G. T. Reed and C. J. Png, "Silicon optical modulators," *Mater. Today*, vol. 8, no. 1, p. 40, 2005.

[140] A. Hugi, G. Villares, S. Blaser, H. Liu, and J. Faist, "Mid-infrared frequency comb based on a quantum cascade laser," *Nature*, vol. 492, no. 7428, p. 229, 2012.

[141] L. Marty, E. Adam, L. Albert, R. Doyon, D. Menard, and R. Martel, "Exciton formation and annihilation during 1D impact excitation of carbon nanotubes," *Phys. Rev. Lett.*, vol. 96, no. 13, p. 136803, 2006.

[142] S. Wang, Z. Zhang, L. Ding, X. Liang, J. Shen, H. Xu, Q. Chen, R. Cui, Y. Li, and L.-M. Peng, "A doping-free carbon nanotube CMOS inverter-based bipolar diode and ambipolar transistor," *Adv. Mater.*, vol. 20, no. 17, p. 3258, 2008.

[143] A. Fediai, D. A. Ryndyk, G. Seifert, S. Mothes, M. Claus, M. Schröter, and G. Cuniberti, "Towards an optimal contact metal for CNTFETs," *Nanoscale*, vol. 8, no. 19, p. 10 240, 2016.

[144] M. Balestrieri, A.-S. Keita, E. Duran-Valdeiglesias, C. Alonso-Ramos, W. Zhang, X. Le Roux, E. Cassan, L. Vivien, V. Bezugly, A. Fediai *et al.*, "Polarization-sensitive single-wall carbon nanotubes all-in-one photodetecting and emitting device working at 1.55 μm," *Adv. Funct. Mater.*, vol. 27, no. 38, p. 1702341, 2017.

[145] A. D. Franklin, M. Luisier, S.-J. Han, G. Tulevski, C. M. Breslin, L. Gignac, M. S. Lundstrom, and W. Haensch, "Sub-10 nm carbon nanotube transistor," *Nano Lett.*, vol. 12, no. 2, p. 758, 2012.

[146] Q. Cao, S.-J. Han, J. Tersoff, A. D. Franklin, Y. Zhu, Z. Zhang, G. S. Tulevski, J. Tang, and W. Haensch, "End-bonded contacts for carbon nanotube transistors with low, size-independent resistance," *Science*, vol. 350, no. 6256, p. 68, 2015.

[147] C. Qiu, Z. Zhang, M. Xiao, Y. Yang, D. Zhong, and L.-M. Peng, “Scaling carbon nanotube complementary transistors to 5-nm gate lengths,” *Science*, vol. 355, no. 6322, p. 271, 2017.

[148] L. Ding, A. Tselev, J. Wang, D. Yuan, H. Chu, T. P. McNicholas, Y. Li, and J. Liu, “Selective growth of well-aligned semiconducting single-walled carbon nanotubes,” *Nano Lett.*, vol. 9, no. 2, p. 800, 2009.

[149] X. He, W. Gao, L. Xie, B. Li, Q. Zhang, S. Lei, J. M. Robinson, E. H. Hároz, S. K. Doorn, W. Wang *et al.*, “Wafer-scale monodomain films of spontaneously aligned single-walled carbon nanotubes,” *Nat. Nanotechnol.*, vol. 11, no. 7, p. 633, 2016.

[150] Y. Joo, G. J. Brady, M. S. Arnold, and P. Gopalan, “Dose-controlled, floating evaporative self-assembly and alignment of semiconducting carbon nanotubes from organic solvents,” *Langmuir*, vol. 30, no. 12, p. 3460, 2014.

[151] M. Freitag, V. Perebeinos, J. Chen, A. Stein, J. C. Tsang, J. A. Misewich, R. Martel, and P. Avouris, “Hot carrier electroluminescence from a single carbon nanotube,” *Nano Lett.*, vol. 4, no. 6, p. 1063, 2004.

[152] F. Xia, M. Steiner, Y.-m. Lin, and P. Avouris, “A microcavity-controlled, current-driven, on-chip nanotube emitter at infrared wavelengths,” *Nat. Nanotechnol.*, vol. 3, no. 10, p. 609, 2008.

[153] J. P. Casey, S. M. Bachilo, C. H. Moran, and R. B. Weisman, “Chirality-resolved length analysis of single-walled carbon nanotube samples through shear-aligned photoluminescence anisotropy,” *ACS Nano*, vol. 2, no. 8, p. 1738, 2008.

[154] W. Li, F. Hennrich, B. S. Flavel, M. M. Kappes, and R. Krupke, “Chiral-index resolved length mapping of carbon nanotubes in solution using electric-field induced differential absorption spectroscopy,” *Nanotechnology*, vol. 27, no. 37, p. 375706, 2016.

[155] S. Serna, “Design and characterization of silicon photonic structures for third order nonlinear effects,” Theses, Université Paris-Saclay, Nov. 2016.

[156] S. Serna and N. Dubreuil, "Bi-directional top-hat D-scan: single beam accurate characterization of nonlinear waveguides," *Opt. Lett.*, vol. 42, no. 16, p. 3072, 2017.

[157] K. Ikeda, R. E. Saperstein, N. Alic, and Y. Fainman, "Thermal and Kerr nonlinear properties of plasma-deposited silicon nitride/silicon dioxide waveguides," *Opt. Express*, vol. 16, no. 17, p. 12 987, 2008.

[158] M. Sheik-Bahae, D. C. Hutchings, D. J. Hagan, and E. W. Van Stryland, "Dispersion of bound electron nonlinear refraction in solids," *IEEE J. Quantum Electron.*, vol. 27, no. 6, p. 1296, 1991.

ÉCOLE DOCTORALE
Physique et ingénierie : électrons, photons, sciences du vivant (EOBE)

Titre : Etude de composants optiques et optoélectroniques à base de nanotubes de carbone

Mots clés : Nanotubes carbone, photonique silicium, optoélectronique

Résumé : La photonique silicium est reconnue comme la technologie à même de répondre aux nouveaux défis des interconnexions optiques. Néanmoins, la photonique silicium doit faire face à d'importants défis. En effet, le Si ne peux pas émettre ou détecter de la lumière dans la plage de longueurs d'onde des télécom (1,3 µm à 1,5 µm). Par conséquent, les sources et les détecteurs sont mis en œuvre avec du Ge et des matériaux III-V. Cette approche multi-matériaux complique la fabrication des dispositifs et augmente le coût final du circuit. Cependant, les nanomatériaux ont été identifiés comme alternative pour la mise en œuvre d'émetteurs-récepteurs moins chers et plus petits.

Cette thèse est dédiée à l'étude et au développement de dispositifs optiques et optoélectroniques sur la plateforme photonique silicium basés sur l'utilisation de nanotubes de carbone mono paroi (SWCNT). L'objectif principal est de démontrer les blocs fonctionnels de base qui ouvriront la voie à une nouvelle technologie photonique dans laquelle les propriétés actives proviennent des nanotubes de carbone.

Les nanotubes de carbone ont été étudiés comme matériaux pour la nanoélectronique avec la démonstration de transistors ultra-compacts à hautes performances. De plus, les SWCNTs semi-conducteurs (s-SWCNTs) sont également des matériaux très intéressants pour la photonique. Les s-SWCNTs présentent une bande interdite directe qui peut être ajustée dans la gamme de longueurs d'onde du proche infrarouge en choisissant le bon diamètre. Les s-SWCNT présentent une photoluminescence et une électroluminescence, pouvant être exploitées pour la mise en œuvre de sources de lumière. Ils présentent également diverses bandes d'absorption pour la réalisation de photodétecteurs. Ces propriétés font que les nanotubes de carbone sont des candidats très prometteurs pour le développement de dispositifs optoélectroniques pour la photonique.

Le premier objectif de la thèse était l'optimisation des solutions de nanotubes de carbone. Une technique de tri par ultra-centrifugation assistée par polymère a été optimisée, donnant des solutions de haute pureté en s-SWCNT. Sur cette base, plusieurs solutions de s-SWCNTs ont été élaborées pour obtenir des SWCNTs émettant dans les longueurs d'onde comprise entre 1µm et 1,6µm.

Le deuxième objectif était d'étudier l'interaction des s-SWCNT avec des guides d'onde silicium et des résonateurs optiques. Plusieurs géométries ont été étudiées dans le but de maximiser l'interaction des s-SWCNT avec le mode optique en exploitant la composante transverse du champ électrique. D'autre part, une approche alternative a été proposée et démontrée en utilisant la composante longitudinale du champ électrique. En utilisant la composante longitudinale, une amélioration de la photoluminescence, un seuil d'émission avec la puissance de pompe ainsi qu'un rétrécissement de la largeur spectrale des résonances dans les microdisques ont été observés. Ces résultats sont un premier pas très prometteur vers la démonstration d'un laser intégré à base de SWNTs.

Le troisième objectif était d'étudier les dispositifs optoélectroniques à base de s-SWCNTs. Plus spécifiquement, une diode électroluminescente (DEL) et un photodétecteur ont été développés, permettant la démonstration du premier lien optoélectronique sur puce basé sur les s-SWCNT.

Le dernier objectif de la thèse était d'explorer le potentiel de s-SWCNT pour l'optique non linéaire. Il a été démontré expérimentalement, qu'en choisissant la chiralité des s-SWCNTs, le signe du coefficient Kerr pouvait être soit positif ou négatif. Cette capacité unique ouvre un nouveau degré de liberté pour contrôler les effets non linéaires sur puce, permettant de compenser ou d'améliorer les effets non linéaires pour des applications variées.

Université Paris-Saclay
Espace Technologique / Immeuble Discovery
Route de l'Orme aux Merisiers RD 128 / 91190 Saint-Aubin, France

ÉCOLE DOCTORALE
Physique et ingénierie : électrons, photons, sciences du vivant (EOBE)

Title: Study of optical and optoelectronic devices based on carbon nanotubes

Keywords: Carbon nanotube, silicon photonics, optoelectronics

Abstract: Silicon photonics is widely recognized as an enabling technology for next generation optical interconnects. Nevertheless, silicon photonics has to address some important challenges. Si cannot provide efficient light emission or detection in telecommunication wavelength range (1.3µm-1.5µm). Thus sources and detectors are implemented with Ge and III-V compounds. This multi-material approach complicates device fabrication, offsetting the low-cost of Si photonics. Nanomaterials are a promising alternative route for the implementation of faster, cheaper, and smaller transceivers for datacom applications.

This thesis is dedicated to the development of active silicon photonics devices based on single wall carbon nanotubes (SWCNTs). The main goal is to implement the basic building blocks that will pave the route towards a new Si photonics technology where all active devices are implemented with the same technological process based on a low-cost carbon-based material, i.e. SWCNT.

Indeed, carbon nanotubes are an interesting solution for nanoelectronics, where they provide high-performance transistors. Semiconducting SWCNT exhibit a direct bandgap that can be tuned all along the near infrared wavelength range just by choosing the right tube diameter. s-SWCNTs provide room-temperature photo- and electro- luminescence and have been demonstrated to yield intrinsic gain, making them an appealing material for the implementation of sources. SWCNTs also present various absorption bands, allowing the realization of photodetectors.

The first objective of this thesis was the optimization of the purity of s-SWCNT solutions. A polymer-sorting technique has been developed and optimized, yielding high-purity s-SWCNT solutions. Based on this technique, several solutions have been obtained yielding emission between 1µm and 1.6µm wavelengths.

The second objective was the demonstration of efficient interaction of s-SWCNT with silicon photonics structures. Different geometries have been theoretically and experimentally studied, aiming at maximizing the interaction of s-SWCNT with optical modes, exploiting the electric field component transversal to light propagation. An alternative approach to maximize the interaction of s-SWCNT and the longitudinal electric field component of waveguide modes was proposed. Both, a power emission threshold and a linewidth narrowing were observed in several micro disk resonators. These results are a very promising first step to go towards the demonstration of an integrated laser based on CNTs.

The third objective was to study optoelectronic SWCNT devices. More specifically, on-chip light emitting diode (LED) and photodetector have been developed, allowing the demonstration of the first optoelectronic link based on s-SWCNT. s-SWCNT-based LED and photodetector were integrated onto a silicon nitride waveguide connecting them and forming an optical link. First photodetectors exhibited a responsivity of 0.1 mA/W, while the complete link yielded photocurrents of 1 nA/V.

The last objective of the thesis was to explore the nonlinear properties of s-SWCNT integrated on silicon nitride waveguides. Here, it has been experimentally shown, for the first time, that by choosing the proper s-SWCNT chirality, the sign of the nonlinear Kerr coefficient of hybrid waveguide can be positive or negative. This unique tuning capability opens a new degree of freedom to control nonlinear effects on chip, enabling to compensate or enhancing nonlinear effects for different applications.

Université Paris-Saclay
Espace Technologique / Immeuble Discovery
Route de l'Orme aux Merisiers RD 128 / 91190 Saint-Aubin, France